UNIVERSITY OF
LIVERPOOL

Electronic structure at the cores of dislocations in transition metals

Thesis submitted in accordance with the requirements of the University of Liverpool for the degree of Doctor in Philosophy

by

Hema Venkata Veerendra Suneel Motru

February 2010

ABSTRACT

Study about core of screw dislocations in transition metals has been the topic of primary interest for many years. The dependence of flow stress over temperature has been anomalous in the case of bcc metals and so the interest to study bcc transition metals has led to the observation of screw dislocation cores, which are attributed to the varied behaviour of bcc metals at low temperatures. Research carried out by modelling of screw dislocation cores did rarely take into account the all important d-bands and the destruction of the local symmetry in the bcc transition metals. The ability to analyse materials at atomic resolution combined with high resolution electron energy loss spectroscopy is the possible solution to look at the screw dislocation cores. The changes associated at the core of dislocation due to distortion of local symmetry seem to alter the electronic structure.

The aim of this research is to identify local electronic structural changes using electron energy loss spectroscopy and lattice structural changes by imaging the cores of dislocations at atomic resolution. This topic was investigated in pure molybdenum and iron samples and the cores of ½[111] screw dislocations were analysed in them. Two types of dislocation cores were investigated for their electronic structure using theoretical simulations and the experimental results were used to attempt

and identify the type of core configuration. Fe samples were used to identify changes in the electronic structure near dislocation cores. Microscopic techniques involving TEM, STEM and SuperSTEM at Daresbury laboratories were used for this purpose. Fe samples due to their magnetism were prepared carefully for reduced magnetic field in the electron microscopes. The reported results include atomic resolution images recorded at SuperSTEM supported by high resolution EELS at the cores of dislocations and from a dislocation-free region.

The results were compared in both Mo and Fe which revealed electronic structural changes on and off the dislocation core. The objective then is to find out density of empty states and bond length changes in the core region. Simulations of dislocation core in bcc metals have been used to generate EELS spectra by FEFF8 codes and to compare the changes ($M_{4,5}$ edges in Mo and $L_{2,3}$ in Fe) in the generated spectrum with experimental spectra. The variations in the spectra near the Mo-$M_{4,5}$ and Fe-$L_{2,3}$ energy edges revealed the presence of local electronic structural change at the cores of dislocations that are attributed to the electronic transitions, lattice strain at the core and the density of unoccupied states available in transition metals. These variations are used to attempt and predict the core configuration that is practically preferred. The experimental conditions set a challenge for the interpretation of the obtained results and limit the workable regions of the ELNES for screw cores which is still a bottle neck.

Acknowledgements

I would like to take this opportunity to thank my supervisors Professor David Bacon and Professor Peter Goodhew who have guided me throughout this work. I am especially grateful to Dr. Andrew Bleloch for his time, help and guidance on this research. I would like to thank Professor Mick Brown from University of Cambridge for his support throughout this work.

I would like to thank Dr. Robert Murray at University of Liverpool who trained me on TEM and Dr. Buddhika Mendis who helped me at SuperSTEM. I would like to thank my family and friends who have supported me all the way through. I am especially grateful to Mr. Dave Atkinson at University of Liverpool for his support in all times. Finally I would like to acknowledge the financial support provided by EPSRC.

CONTENTS

Chapter 1

Introduction

Chapter 1

INTRODUCTION

1.1 Introduction

Study of dislocations in transition metals had been an interesting research topic for several decades; especially since the screw dislocation cores were attributed to the changes in the plasticity of bcc metals [1]. The technology of working with bcc metals like iron and molybdenum developed through the years but the science behind the properties of these metals is not fully understood. For many years, the changes in properties of bcc metals subjected to external stresses were studied at macroscopic level using plastic deformation concept. The atomic level changes that would cause the change in properties were yet to be investigated using microscopic approach.

Dislocations are important crystal defects that affect the properties of materials at atomic level. It is widely reported from research over the years that screw dislocation cores are responsible for the change in bulk properties of bcc metals when subjected to applied stress [1-3]. In order to understand this phenomenon, the presence of two types of core configurations called hard core and easy core have been studied extensively using computer simulations. Easy core and hard core configurations have different stacking sequence of atoms around the dislocation core[4]. Due to the difference in the arrangement of atoms around the core for each core configuration, the core energy varies due to which lighter impurity atoms like hydrogen [5, 6], carbon and nitrogen can segregate to dislocation cores. The presence of such impurities at the

core of dislocation can alter the deformation behaviour and hence control the properties of bulk bcc metals[7].

The presence of Cottrell atmospheres in iron is an example where carbon or nitrogen atoms segregate to dislocation core, pin the dislocation, and prevent its motion further. BCC materials deform plastically when these dislocations get unpinned, usually with the application of external stress[1]. Even in a case where Cottrell atmospheres are absent, the dislocation core in itself can be an interesting region to study for electronic structure change. This is due to the variation of bond lengths, bond angles at the core and the overall energy of the dislocation compared to that of perfect crystal region. The study of electronic structure at the dislocation cores therefore can help in predicting deformational behaviour of bcc metals. It can also provide information about chemical environment at the core with reference to the bulk metal. Therefore it is considered an interesting topic to study and understand the dislocation core structures at microscopic level.

1.2 Significance

Most bcc metals like iron (at room temperature), tungsten, molybdenum are widely used for common applications, while metals like tantalum vanadium and chromium are used for specialized applications under high strain rates and low temperatures. Molybdenum and iron are the two bcc transition metals studied in this research. Molybdenum is commonly used in high temperature electrical applications like electrodes and in aircraft parts due to its ability to withstand high temperatures without softening[8]. It is also a common alloying element in high speed steels like M42. Molybdenum is used in special applications in defence and nuclear medicine industries (as Mo-99 stable isotope)[9].

Iron is the most extensively used structural material and strength is an important factor for all structural materials. The strength of materials to a large extent is controlled by the presence of dislocations, impurities, voids and other alloying elements in them. The presence of screw dislocations can affect the overall strength and ductility of the material and cores of screw dislocations control the plasticity at low temperatures. Mo and Fe being the materials widely used for such structural and high performance applications have to be rigorously tested for their properties like mechanical strength under conditions like low temperatures and high stresses. In material science, the failure of structural components can be understood by the study of defects like dislocations in them and knowledge about the properties of defects under given conditions can help reduce the time and cost for testing materials. In addition it can prevent unexpected failure of materials during usage. Hence it is a significant aspect in a wider context of science to understand the effect of dislocations and their cores on the properties of bcc metals Mo and Fe.

1.3 Aims and Objectives

This project aims at understanding the electronic structure of dislocation cores in body centred cubic transition metals molybdenum and iron. Molybdenum and iron being transition metals have the ability to exhibit variable valences in different environments under given conditions like temperature and applied stress.

The research work involved in this project attempts to analyse screw and mixed dislocation cores in Mo and Fe through aberration-corrected atomic resolution electron microscopy and high resolution electron energy loss spectroscopy.

One of the important aims is to calculate the electronic structure of screw and mixed dislocation cores using theoretical simulation methods and distinguish theoretical electronic structure from the experimental electronic structures. In addition, theoretical simulations are aimed to assess whether the two different types of screw dislocation cores: the easy core and the hard core can be distinguished in terms of electronic structure. Comparison of easy and hard core electronic structures with experimental results can reveal the type of core configuration that is practically preferred in bcc transition metals Mo and Fe.

The electronic structure from screw and mixed dislocation cores is studied in terms of electron energy loss near edge structure (ELNES) and density of states (DOS). It is compared with ELNES and DOS of a perfect crystal. This comparison will reveal the electronic structure changes that can be expected from the experimental ELNES. The comparison between the theoretical ELNES from different atoms around the core will also be presented in order to understand the sensitivity of electronic structure to the dislocation core configuration.

The other aim of this project is to attempt to explain the subtle electronic changes in the 'd' band of transition metals at a dislocation core and the impact they can have on the overall energetics of the core structure. The presence of local asymmetry at the core can influence the electronic transitions, which can be recorded using electron energy loss spectroscopy. The electronic transitions are responsible for the variable co-ordination number of the element and can dictate the ability to form different compounds. For example transition metal like iron can exhibit either Fe^{2+} or Fe^{3+} valence state depending upon its surrounding chemical environment. In order to address this interesting problem, the available experimental techniques were made into a possible solution. These techniques involved electron microscopy of screw dislocations in bcc

transition metals molybdenum and iron using conventional transmission electron microscope and aberration corrected high resolution scanning transmission electron microscope equipped with electron energy loss spectrometer (1.0 Å resolution SuperSTEM).

If the transitions occurring in the d-band due to varied symmetry at the screw dislocation core can be recorded and compared with those of pure metal without dislocation, in other words a perfect crystal region, then the energy changes attributed to bond angles and inter-atomic interactions in the above discussed simulations can be deduced. The electron energy loss spectrum at core edges probes unoccupied states. The information about density of unoccupied states at a specific core loss edge can be used to find the electronic transitions between different angular momentum states. The comparison between the density of unoccupied states from perfect region and dislocation core can be used to determine the presence of any additional states in either case. This is considered a direct experimental approach to the problem. Hence, comparison of electron energy loss spectrum at atomic resolution from the screw dislocation core with that of a perfect crystal region (non-defect region) will provide the answer experimentally.

1.4 Experimental Approach

The experiments were planned to take advantage of the aberration corrected STEM (SuperSTEM 1 at Daresbury[10]) with its high resolution electron energy loss spectrometer. The experimental results obtained with this instrument are compared in this work with spectra generated by computational models utilising well established atomistic simulation programs called FEFF8.4[11]. Aberration corrected STEM helps to obtain atomic resolution image that can efficiently provide information about atomic arrangement, lattice distortion and possible

chemical and surface contaminations at the dislocation core. Electron energy loss spectrometer (EELS) records spectra from selective regions or atoms in and around the core and provides local chemical, electronic and structural information[12]. Selected absorption energy edges for molybdenum ($M_{4,5}$) and iron ($L_{2,3}$) in the spectra were used to identify characteristic changes in the case of dislocation and perfect crystal. Excitations from core electron levels of specific atoms were recorded at different absorption edges in the spectrum.

Care was taken to avoid extra information from the other elements being included in the spectra by choosing selective absorption edges. The information about the type of chemical bonds and the co-ordination around the excited atom can be obtained from the fine structure above these absorption edges. This is also referred in terms of site-specific symmetry projected local density of states (LDOS)[13] .

1.5 Thesis Outline

This thesis presents experimental results in comparison to theoretical calculations of electronic structure at dislocation core. ELNES from screw and mixed dislocation cores will be presented and theoretical ELNES will be calculated instead of only DOS. The experimental and theoretical comparison makes this thesis different from the DOS and atomistic simulation work done by most other research groups on dislocation cores in bcc metals.

The review of literature that is relevant to the work described in this thesis will be presented in chapter 2. The significance of dislocations in bcc materials in general, the effect of dislocations on material properties, and previous research undertaken in this subject will be discussed. Electron microscopy of dislocations and theoretical calculations to study

the electronic structure at dislocation cores will be discussed with reference to the research work presented in this thesis.

The theoretical aspects of electron interactions with sample and the inelastic scattering processes are explained in Chapter 3 called "Electron scattering and EELS". It also includes the description of instrumentation like TEM, STEM and EELS that were used to achieve the experimental results. The need for high resolution imaging and EELS to this research work is discussed with reference to the advantages and limitations of other available experimental techniques.

It is very important that the experiments be compared with the theoretical results so that an agreement or disagreement is obtained. This will guide the future analysis, discussion and possible explanation for the results. Hence, theoretical models were generated using ATOMS® and served as input into FEFF8, an automated software which creates a model EELS spectrum for a defined cluster of atoms with given parameters. FEFF8 calculates EELS spectra using self consistent, real space multiple scattering formalism and provides information about site-specific symmetry-projected local density of states for a given system[13]. The advantages and limitations of using FEFF8 over other conventional and different methods are critically discussed in Chapter 4 "Theoretical Simulation Methods".

Specimen preparation was a challenging task for the work described in this thesis. Experimental procedures for the preparation of thin and contamination-free molybdenum and iron samples as well as the basic operating parameters of electron microscopes like TEM and STEM are explained in Chapter 5 "Experimental Technique". The images recorded in both microscopes are presented. Application of different strategies to obtain good surface finish and a thin transparent sample for microscopy

using electropolishing and other intermediate methods are discussed. Other details include storage instructions for molybdenum to prevent oxide formation on surface and working with magnetic samples like bcc Fe. The problems involved in analysing the samples in microscopes like carbon contamination and sample degradation are discussed and the preferable solutions to overcome these problems are suggested.

The parameters that were identified and used to simulate ELNES spectra for perfect crystals of both Mo and Fe are presented in chapter 6 "Theoretical Techniques". Comparison of theoretical and experimental ELNES from perfect crystal is done to confirm the accuracy of the simulation method for iron and molybdenum. The various parameters used for ELNES modelling are justified with reasons. The agreement of perfect ELNES spectra is explained and the problems involved in calculations are highlighted.

In Chapter7 "Theoretical Results", the simulated spectra for various dislocation core models are compared with each other and also with the spectra from perfect crystal. The simulated ELNES spectra for different atoms in the shells surrounding the core are presented showing how sensitive the ELNES changes are to the location away from the core. The observed changes are interpreted in terms of unoccupied DOS for the Mo -$M_{4,5}$ and Fe $L_{2,3}$ core loss edges. The approximations that were used for prior atomistic calculations from which the core model was generated as well as for the simulations of the spectra are discussed.

The experimental results from SuperSTEM are included in chapter 8 for molybdenum and chapter 9 for iron. The imaging results, experimental ELNES data from the EELS are discussed for a dislocation core and a perfect crystal region. The methods used for analysis are explained which include geometric phase analysis, Fourier filtering, spectrum imaging and

adjustments like energy calibration by drift tube correction. The experimental ELNES results are then clearly compared with theoretical results and any observed ELNES change is discussed along with a justification for the comparison of both results. The factors that could affect the experimental results like background subtraction, sample drift and noise are also discussed. Finally it is assessed whether the two dislocation core models can be distinguished by comparing the experimental and theoretical results.

The conclusions from this research work are presented in the final chapter and the results obtained in this project are assessed. Any future experimental modifications that might be possible are suggested. Further possible research aspects that can be undertaken on this topic in future are suggested. Study of screw dislocations in magnetic materials like Fe is a topic of renewed interest and different ways to minimise the effects of magnetism induced by the magnetic samples in the electron microscope are explored. Segregation of impurity atoms among the dislocation core atom sites and inclusion of impurity atoms for further FEFF calculations are also suggested.

References:

[1] M. S. Duesbery, V. Vitek, Acta Materialia 46 (1998) 1481-1492.

[2] L. Hollang, M. Hommel, A. Seeger, Physica Status Solidi a-Applied Research 160 (1997) 329-354.

[3] V. Vitek, Philosophical Magazine 84 (2004) 415-428.

[4] D. Hull, D. J. Bacon, Introduction to dislocations, Butterworth Heinemann, Oxford, 2001, p. vii, 242 p.

[5] A. Juan, B. Irigoyen, S. Gesari, Applied Surface Science 172 (2001) 8-17.

[6] M. V. Rodríguez, P. J. Ficalora, Materials Science and Engineering 85 (1987) 43-52.

[7] D. R. Trinkle, C. Woodward, Science 310 (2005) 1665-1667.

[8] J. Emsley, Nature's building blocks: an A-Z guide to the elements, Oxford University Press, Oxford, 2001, p. viii, 538 p.

[9] A. Gottschalk, Annual Review of Medicine 20 (1969) 131-139.

[10] SuperSTEM, http://superstem.co.uk/, in: Daresbury,UK, 2004.

[11] FEFF, FEFF wiki: http://leonardo.phys.washington.edu/feff/wiki in: 2009.

[12] D. B. Williams, C. B. Carter, Transmission electron microscopy: a textbook for materials science, Plenum, New York; London, 1996, p. xxvii, 729p.

[13] M. S. Moreno, K. Jorissen, J. J. Rehr, Micron 38 (2007) 1-11.

Chapter 2

Literature Review

Chapter 2

LITERATURE REVIEW

This chapter would review the literature about different aspects that are of importance to this thesis. In this chapter the relevant literature about dislocations in general, their effect on the deformation behaviour of b.c.c. transition metals with reference to plasticity will be presented. It is followed by the literature review of theoretical and experimental studies done on crystallographic and electronic structure at dislocation cores and their combination. Literature about broader context of research topics will be reviewed initially, followed by all important topics relevant to this thesis.

2.1 Dislocations in materials

A perfect crystal is a three dimensional arrangement of atoms separated by a definite distance between them in a given orientation depending upon its crystal structure. A dislocation is a local disturbance in the perfect array of atoms. Dislocation is a line defect in crystalline material that governs its deformational behaviour. Plastic deformation of metals and other crystalline solids under applied stress is usually affected by the motion of dislocations in them. The presence of dislocation in crystalline materials affects their physical properties dominated by the elastic strain field spreading over a few atomic spacings around the centre of the dislocation[1]. The centre of the dislocation is known as the core of the dislocation and plays an important role in plastic deformation by affecting the arrangement of atoms around it. Mechanical properties like strength and ductility are highly dependent on the arrangement of dislocation core atoms[2].

2.2 Types of dislocations

The two common types of dislocations are edge dislocation and screw dislocation. An edge dislocation contains an extra half-plane of atoms (ABCD) in an otherwise perfect crystal as shown in figure 2.1a.

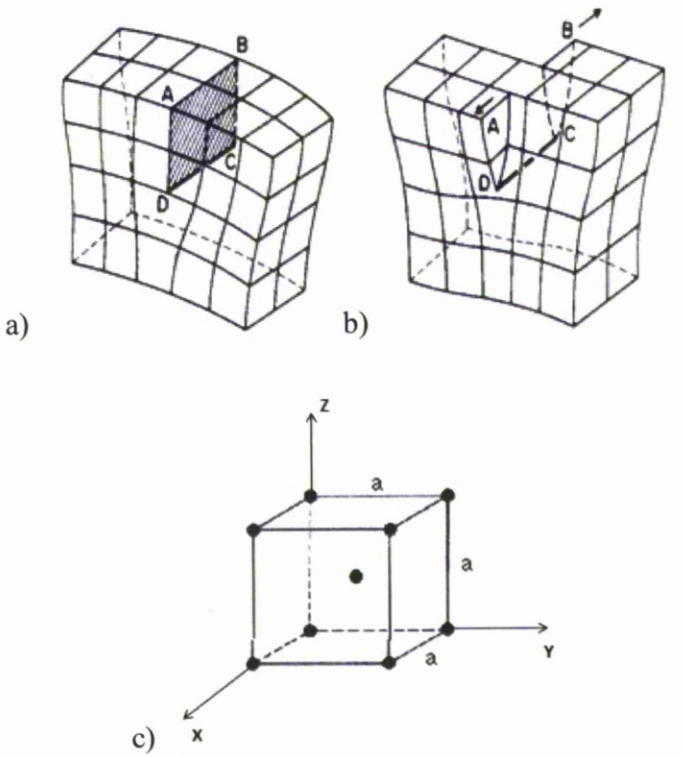

Figure 2.1a) Edge dislocation showing the extra half plane of atoms[3], 2.1b) screw dislocation showing the dislocation line direction[3], 2.1c) body centred cubic unit cell.

DC is the positive edge dislocation where the distortion of the planes is the greatest. The inclusion of an extra-half plane in the bottom half of a perfect crystal will generate a negative edge dislocation.

A screw dislocation is produced by shearing the two halves of the crystal along directions A and B as shown in the figure 2.1b. DC is the screw

dislocation. A Burgers circuit defines the type of dislocation. "A Burgers circuit is any atom-atom path taken in a crystal containing dislocations which forms a closed loop"[3]. The Burgers vector is the missing lattice vector that can complete the circuit. Burgers vector for an edge dislocation is normal to the dislocation line and the Burgers vector for a screw dislocation is parallel to the dislocation line. The sites where atoms are situated in a b.c.c. crystal are the corners and the centre with coordinates ½, ½, ½, as shown in figure 2.1c. The closed pack direction in b.c.c. structures is along <111>. The burgers vector **b** defined for a screw dislocation in <111> direction is the lattice vector from the origin to the centre of the b.c.c. cell with displacements of a/2 each in x, y and z directions. The notation used is **b** = ½ [111] and the length (or magnitude) b of the vector is $\sqrt{3}$ a /2, where 'a' is the lattice parameter of the b.c.c. crystal. In Mo and Fe, slip occurs in close packed <111> directions and the crystallographic slip planes are {110} {112} and {123}[3]. <111> slip directions are present for each of these planes and it is important to understand that three {110} three {112} and six {123} planes intersect in the same <111> direction[4]. These planes can determine the behaviour of screw dislocation motion under applied stress. {110} is the most densely packed plane and the most common slip planes are {110} and {112}, but the slip appears to be macroscopically non-crystallographic in b.c.c. metals like iron when it is deformed at room temperatures[3].

2.3 Plastic deformation in b.c.c. metals

It has been generally accepted that plastic deformation in b.c.c. metals at low temperatures is controlled to a great extent by lattice friction[5]. The tensile test experiments done on b.c.c. metals iron and molybdenum proved that the flow stress of b.c.c. metals increased strongly with decreasing temperature and at sufficiently low temperatures the b.c.c.

metals failed by brittle fracture[6]. It is reported that the graph of flow stress at different temperatures for b.c.c Mo showed a "hump" in the curve which is attributed to the dependence of kink-pair formation enthalpy on resolved shear stress and has a direct relation to the motion of screw dislocations in the metal[6, 7].

"Schmid's law states that in uniaxial straining, extensive plastic deformation sets in when the resolved shear stress in the active slip system reaches a critical value (the so-called critical shear stress) that is independent of the crystallographic direction of the straining axis"[8]. In f.c.c. metals, the critical shear stress obeys Schmid's law to a good approximation but depends on the perfection of the crystals. In the case of b.c.c. metals the low-temperature critical shear stress appears to strongly violate Schmid's law[1]. The elastic theory can correctly define the long range strain fields of a dislocation with respect to the dislocation line and the Burger's vector, and therefore cannot be the reason for the violation of Schmid's law. Therefore the core of the screw dislocation must have the ability to affect critical shear stress and thereby influencing the deformational properties of the bcc metal as a whole.

It was shown by the atomistic calculations done by Takeuchi and Kuramoto[9] that for some type of the interatomic force a screw dislocation in the b.c.c. lattice can take a core configuration which results in a camel-hump Peierls potential[7]. This concept has been confirmed by atomistic simulations from other research works. It is now accepted that the plasticity in b.c.c. metals is governed by the movement of screw dislocations overcoming Peierls potential and the velocity of screw dislocations is dependent upon the nucleation of kink pairs under applied stress. This causes the change in the flow stress behaviour for bcc metals like Mo and Fe.

The plastic flow stress τ_c measured at different temperatures T, as reported by Suzuki et.al[7] are shown below for Mo and b.c.c. Fe.

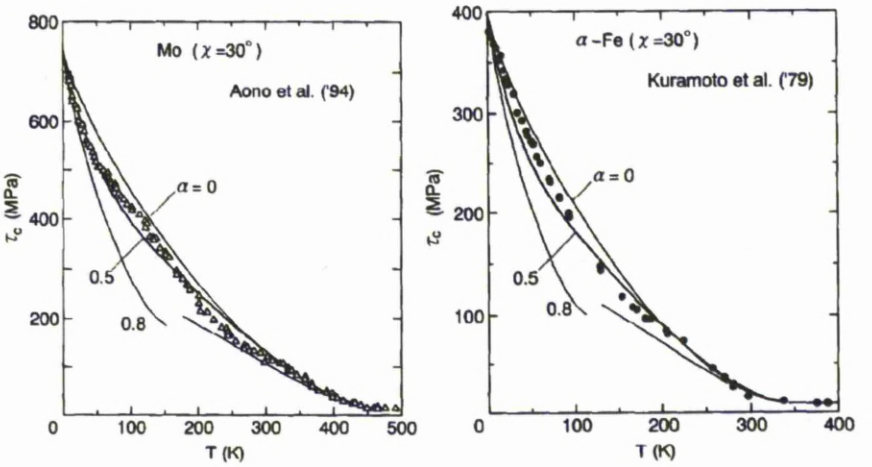

Fig2.2. Plastic flow stress τ_c for Mo and Fe crystals in 30° orientation with different periods of Peierls potential (α) and temperatures, T.[7]

2.4 Screw dislocation core

The centre of the dislocation is called the dislocation core and is an important factor that controls the movement of dislocations under applied stress. It was reported that the core of screw dislocation has a non-planar character as revealed in computer simulations[3]. Screw dislocation cores in b.c.c. metals are responsible for very high flow stress at low temperature[6]. It was shown by many research groups that the screw dislocation core is distributed in several non-parallel crystallographic planes of the <111> zone[5, 10, 11]. A concise and descriptive explanation of various findings from experimental and theoretical calculations was given by Vitek *et.al* in their 2004 publication[4]. The results of two atomistic calculations for screw dislocation core in Mo were compared. One of them was calculated with Finnis-Sinclair type many-body central force potentials while the other was calculated with

bond order potentials that include angular dependence of interatomic interactions. They have demonstrated that both core structures vary in symmetry but led to very similar responses of the dislocation to applied stresses since the strained crystal loses the original symmetry, and thus the distinction between the two types of cores vanished[4]. It was found that the core structure of ½[111] screw dislocations in b.c.c. metals like Mo and Fe was not only responsible for the unusually high lattice friction stress (also called the Peierls stress) but also for the orientation dependence of the yield stress. This seems to apply in common to all b.c.c. metals and the reason was explained to be the mismatch of atomic columns at the core of screw dislocation. This asymmetry causes significant changes in the overall energy of that localised core region.

Two basic types of core structures found to exist after studying screw dislocations in Mo by different computer simulation methods are the 3 fold and 6 fold core structures. The use of Finnis Sinclair potentials and pseudo-potentials for simulations resulted in 3 fold core structure while the 6 fold structure was observed when tight-binding and density functional theory (DFT) methods were adopted. These two types of core structures were compared by Futoshi Shimizu *et.al* [12] while calculating core properties and Peierls stress using first principles based on DFT method. A 6 fold core structure and a Peierls stress of 1.8 GPa were reported for a simple shear strain along (-110) <111> direction.

For many years, two types of screw dislocation core configurations were predicted by computer modelling research groups, called easy core and hard core [11, 13]. The main difference between the two types of configurations was the stacking sequence with reference to the perfect crystal. Easy core was found to have ABCBCA.., while hard core had ABCCAB. The stacking sequence for the two types of screw cores with respect to perfect crystal is shown in Figure 2.3.

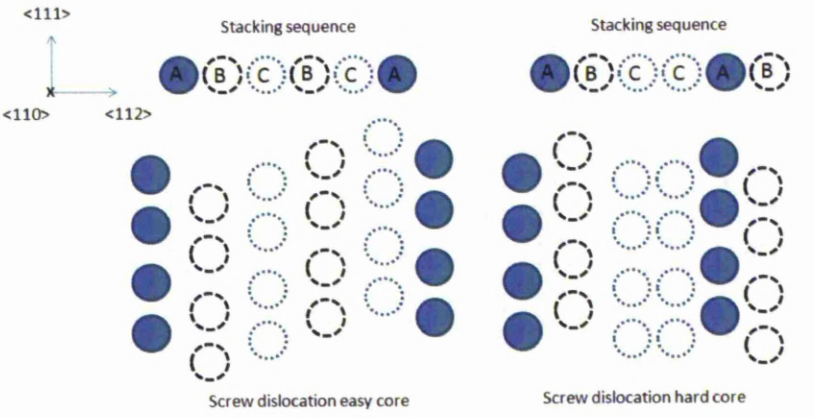

Figure 2.3 Easy and hard screw dislocation core configurations.

In an attempt to understand the screw dislocation core and its behaviour on the flow stress, atomistic calculations have been carried out by several research groups and some of them included density functional theory (DFT) methods[10]. Such calculations have reported that the core does not confine itself to one atomic plane and is non-planar with the possibility of motion through the planes by forming kink pairs[14]. "In materials with strong dislocation-lattice coupling, dislocations are known to move by forming double kinks and having them extend (spread) laterally along the line"[14]. Left kink and right kinks that allow the motion of screw dislocation in b.c.c. Mo are shown in figure 2.3.

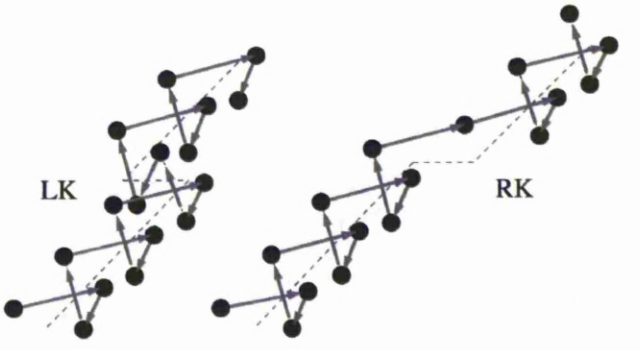

"Fig.2.3. LK (left kink) and RK (right kink) in ½ [111] screw dislocation in b.c.c. Mo. Only the atoms nearest to the geometric centre of the

dislocation are shown, connected by arrows representing relative atomic displacements in the direction of **b** with breaks (kinks) in the helical sequence. Helix period is equal to Burgers vector **b** and the arrows are scaled by their maximum length of **b**/3. LK appears as a step with W-shaped pattern of arrows, with two extra atoms in the helical sequence, whereas in RK, only one extra atom appears"[14].

"Ductility is controlled at the atomic level by dislocation kink motion. Band structure energy controls kink motion, so valence electrons control shearing motions involved with ductility"[15]. This idea was supported by results from cyclic deformation experiments done on high purity molybdenum crystals of different crystal orientations under different strain rates and temperatures[6].

It was also reported that the ½[111] screw dislocation core in b.c.c. metals spreads into three {110} and {112} planes of the [111] zone and does not split into partials like f.c.c metals[16]. Based on interatomic potential calculations, two core configurations were reported, easy core and hard core. The easy core dislocation was found to be stable and to have smaller core energy than the hard core dislocation for Mo both in DFT calculations and interatomic potential calculations [10, 17]. These calculations have also shown that larger displacements along the dislocation line created larger bond angle difference between atoms of different <111> planes and the strain energy variation at the core was dependent upon bond angles between atoms.

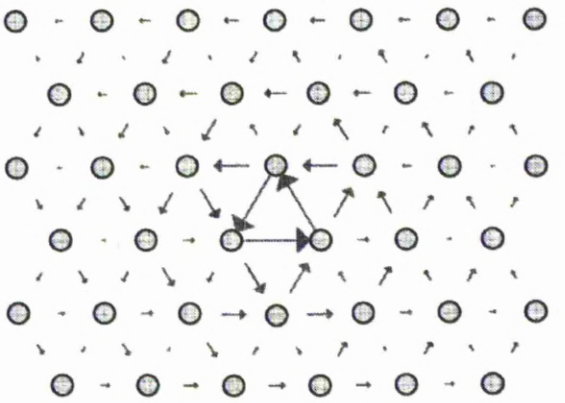

Figure 2.4 A non-degenerate screw dislocation core in <111> calculated using bond order potentials; circles are atomic positions and the magnitude of arrows indicate the magnitude of displacement of atoms along <111>. Image source[4].

The criterion for studying screw dislocations in b.c.c. molybdenum varied from one research group to the other in terms of the fundamental potentials and the boundary conditions that were employed to generate core structure. Similarly screw dislocation cores have been studied in b.c.c. Fe by using various computer simulation methods. In the case of α-Fe, a comparison was done by Ventelon *et.al.*[18] between the cluster and dipole approaches for core structure and Peierls potential calculation from first principles using Mendeleev potentials. It was observed that both approaches confirmed the presence of a non-degenerate core in agreement with Duesbery-Vitek criterion[1]. "In both cases the degenerate core is found to decay to the non-degenerate structure. The hard core is metastable with an energy less than 50 meV/**b** above that of the easy core in the cluster approach"[18]. The relaxed easy core according to their calculations using both approaches did not show a sign of broken symmetry along <110> axes or splitting along <211> direction, thereby confirming that easy core structure exhibits non-degenerate configuration[18]. Edge components of less than 0.1 Å were noticed at

the relaxed core. However, in similarity to Mo[19], the motion of a dislocation with a non-degenerate core in b.c.c iron seems to occur by glide at low temperatures through nucleation and propagation of kink-pairs in a {110} glide plane[20]. The differential displacement (DD) map obtained by Ventelon *et.al* for a relaxed easy core using cluster approach is shown in figure 2.5.

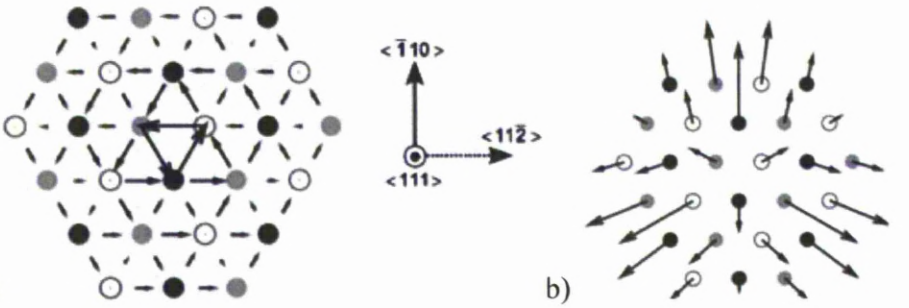

Fig. 2.5(**a**) Differential displacement map of relaxed easy core (**b**) Displacement field vectors in the {111} plane or edge components magnified by a factor of 50. Image reference[18].

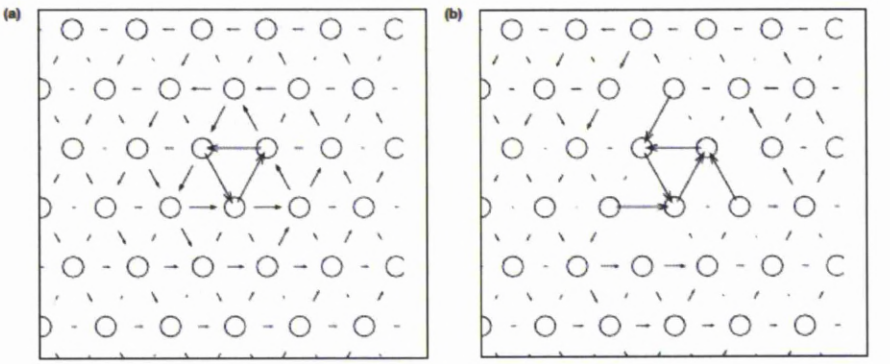

Fig.2.6. Dislocation core structures in α-Fe: a) DD map for non-degenerate core obtained using Mendeleev interatomic potentials and b) degenerate core obtained using Simonelli et al. potential, as reported by Chaussidon *et al.* [20].

In this research work, the dependence of energy on the bond angles and bond lengths was considered as one of the factors for the expected difference in electronic structure at core. However, Mendeleev interatomic potentials were used for core structure simulations due to their availability and their tested credibility towards easy core calculations although they do not account for magnetism and bond angle dependence to a great extent. Furthermore, the reason for electronic structure change occurring at cores was assumed to be due to partially filled 'd' band in transition metals and their sensitivity towards local atomic environment. Their variable occupancy due to excitation of core atom sharing a different atomic environment with respect to perfect crystal can alter the density of states and hence change the electronic structure. This aspect is not considered in the above reported atomistic calculations. Electron microscopy analysis involving high resolution electron energy loss spectra can provide the answer by recording the changes in electronic structure at the dislocation cores in transition metals.

2.5 Electron Microscopy

Electron microscopy has evolved into a powerful science for characterising materials over a wide range starting from simple crystalline solids and extending to complex biological materials. High resolution microscopes equipped with spectrometers that can analyse materials at atomic level generated interest to study the electronic structure at the cores of dislocations in transition metals. Structural defects in the materials were thought to change the electronic structure because of the variation in bond lengths and bond angles. This change in electronic structure can be noticed by comparing it with the electronic structure of perfect crystal. While semiconductors are an example for this

kind of electronic structural change, highly deformed metals also have the potential to exhibit this varied behaviour.

Screw dislocation cores in b.c.c metals have been studied using electron microscopes by a few research groups mainly with an interest in core configurations and to measure the displacements at the core. The study of ½[111] screw dislocation in Mo done by Sigle[21], using high resolution transmission electron microscopy (HRTEM) revealed the non-planar dissociation of the screw dislocation core which is responsible for the high flow stress of bcc metals at low temperatures. It was shown that image contrast is dominated by surface relaxations induced by the Eshelby twist. Eshelby twist is the torsional deformation experienced by a material that contains end-on screw dislocations in order to make the surface of the foil stress-free. This twist induces relaxation to the atoms at the surface and at screw dislocation core. The upper and lower surfaces have opposite relaxation directions due to which small edge components result and can be noticed at atoms close to the core. These relaxations reported by Sigle[21] were attributed to the influence of non-planar core dissociation rather than theoretical relaxations described by Eshelby and Stroh[22]. Molecular dynamics (MD) simulations were used by him to interpret HRTEM images of defects which lead to shear stress components on the surface. The HRTEM image of screw dislocation in Mo and the Eshelby twist from MD simulations presented by Sigle in his work are shown in figure 2.5.

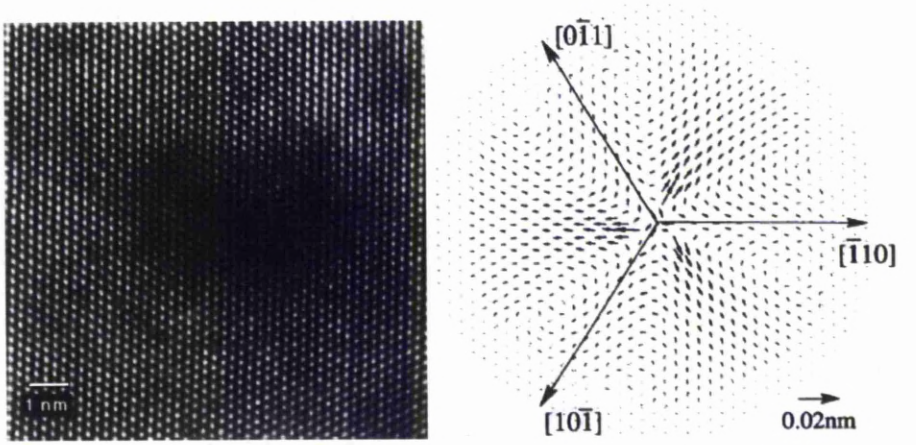

Fig.2.5. a) Screw dislocation core in Mo. b) Eshelby twist calculated by MD simulations. {Images reference[21]}

The in-plane displacements of atoms around screw dislocation core were calculated by Hemker *et. al.*[23] from high resolution electron microscopy HREM images expecting the displacements to be of the order of 10 picometres or less. However, the atomic displacements were found to be due to the surface relaxation by Eshelby twist thereby masking the finer atomic displacements of the screw dislocation core. Methods like removal of large displacements from Eshelby twist and Nye tensor plots that map the resultant Burgers vector at each point of distorted crystal were used by Mendis *et. al* [24], but the signal from core could not be observed from the HREM images. The images of screw dislocations in Mo described by Mendis *et.al.* in their work are shown in Figure 2.6.

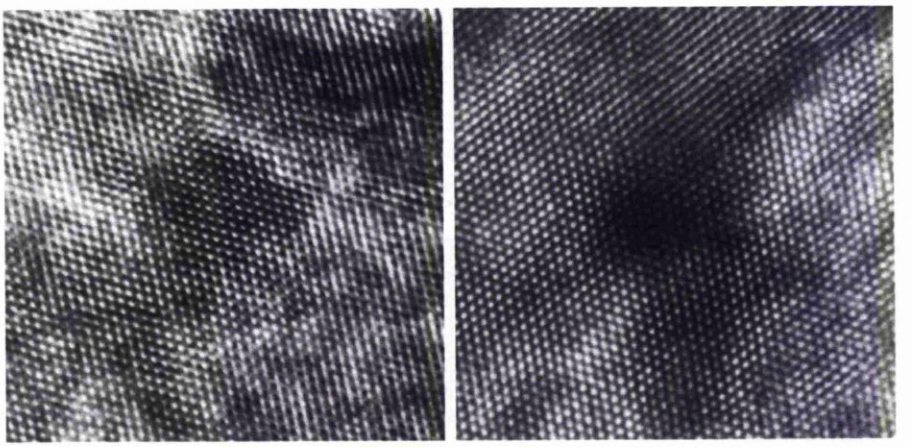

Fig.2.6. HREM images of screw dislocations in molybdenum as presented by Mendis *et.al.*[24].

The characterisation of dislocation cores in single crystal Mo through HREM experimental approach by Hemker *et. al.*[25] confirmed the three fold screw dislocation core previously reported by Sigle, but did not report the use of EELS as a method to study the electronic structure. It was briefly described that the problems associated with the position of energy edges and the instrumental noise did not favour the experimental EELS analysis by HREM. Therefore they adopted a much simpler image simulation approach using Nye tensor plots for the removal of Eshelby twist[26]. However they concluded that a mottled contrast existed in Nye tensor plots arising from experimental noise that masked true structure of dislocation core[25]. This reported problem aroused an interest to study dislocation cores at atomic resolution using EELS and hence paved the way for experiments conducted in this research using instruments like SuperSTEM that can provide 1.0 Å resolution, spherical aberration correction and reduced noise levels equipped with an atomic resolution electron energy loss spectrometer. It has to be noted here that the HREM image analysis methods like geometric phase analysis (GPA) adopted by

Hemker *et. al.*[25] have been used in this research work with a similar objective to identify screw dislocation cores.

2.6 Electronic structure of transition metals

The electronic structure of a material can be explained through band structure which describes occupied and unoccupied states and the Fermi energy E_f that divides them, in an ideal case. The occupied states lie below the Fermi energy while the unoccupied states lie above it. Fermi energy, occupied and unoccupied states for an infinite system are shown in figure 2.7.

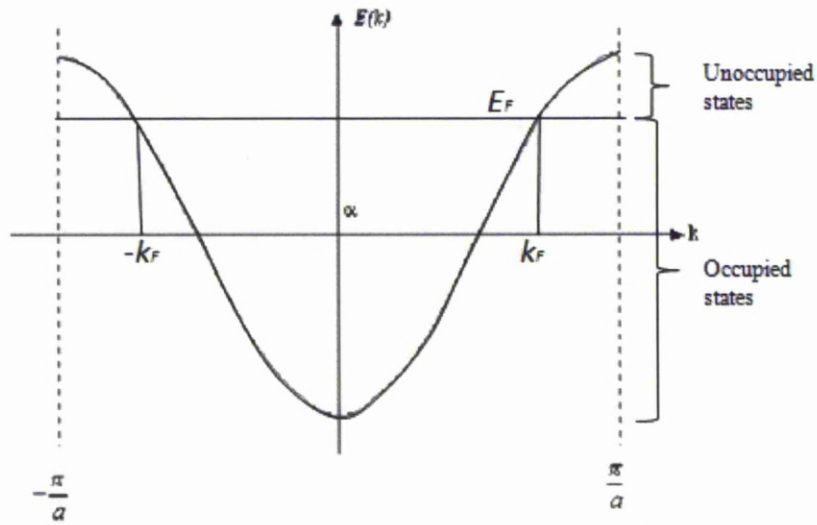

Fig.2.7. The Eigen value spectrum (or band structure) depicting the Fermi energy E_F, occupied and unoccupied states for an infinite ring of atoms with atomic spacing '*a*' and energy α. *k* is the wave vector lying between $-\pi/a$ and π/a. The band structure outside this wave vector period is a repetition of this period.

Fermi energy, by definition is the energy of the highest occupied state at 0° K and is determined by the number of electrons per atom. The Fermi

energy of molybdenum determined from experimental data was reported to be 6.5eV[27] and 4.5 Ry^{-1}[28]. E_f of iron was reported to be 21 Ry^{-1} [28], but the value was found to vary depending upon the impurity level and the conditions under which structure calculations were performed.

The electronic structure is interpreted in terms of the density of states (DOS) and hence it is important to understand them with reference to *k* space. The density of states in *k*-space is the number of states that can fit in a unit distance along the k-axis in an Eigen value spectrum Density of states in k-space, $d(k) = Na/2\pi$, where N is the finite number of atoms in the ring with atomic spacing *a*.[29]. The density of states for each atom or local density of states can also be expressed as a function of energy E rather than wave vector and for each atom they are given as

$$d(E) = \frac{1}{\pi} \frac{1}{(4\beta^2-(E-\alpha)^2)^{1/2}} \qquad (2.1)[29]$$

where α and β are the Hamiltonian matrix elements and can be useful in calculating the overall Fermi energy of a given system. The total density of states D(E) is simply a multiple of this entity by the total number of atoms N. It is important to determine the local density of states as to the total density of states since local density of states vary with local environment and inequivalent atomic sites will have different densities of states[29-31]. This is a significant aspect in the study of electronic structure at dislocation cores since the core atoms can occupy inequivalent sites for a given core configuration. Hence, the DOS for each atom in the dislocation core can vary depending on its local environment.

In semiconductors and insulators there exists a bandgap between the unoccupied (i.e. conduction band) and occupied states (i.e. valence band) while in metals there is no gap between occupied and unoccupied states,

but are distinguished by the presence of Fermi energy between them. Under the influence of external electromagnetic field, the electrons in occupied states can make transitions between different energy levels of the occupied states or can make a transition to the unoccupied states[32, 33]. In order to conserve the momentum and energy of the transition the excitation process results in various post-processes that could be recorded out of which the electron energy loss is a significant one that provides a signature of the local environment of the metal atom. The electron energy loss (EELS) signal that corresponds to transitions from core levels into empty states in the valence band probes the density of unoccupied states and therefore is useful in determining the electronic structure from highly spatially resolved features in a sample.

Transition metals are considered to be interesting materials to study for their electronic structure since they have d-bands different from the rest of the metals. "Their densities of states are characterised by a partially filled narrow d band, superimposed on a broad free electron-like s-p band"[29]. This is schematically shown in figure 2.8.

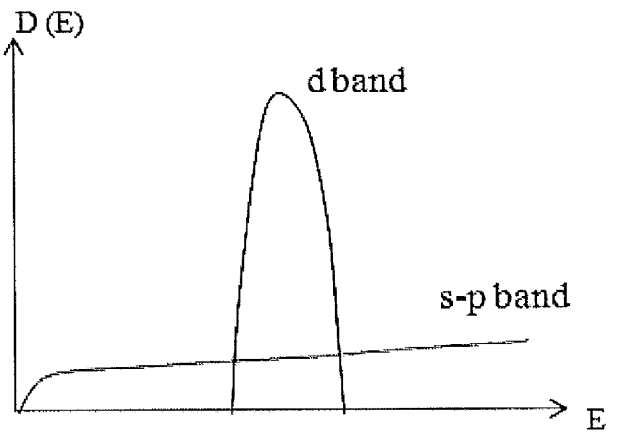

Fig.2.8. Schematic diagram showing narrow d-band superimposed on s-p band in the density of states for a transition metal.

The filling of the d-band measured by its width is responsible for most of the properties exhibited by transition metals as recognised by Friedel[30] in his d-band model. An example of such property is magnetism occurring among 3d transition metal series, attributed to the changes in spin alignment due to the narrowness of d-band. Friedel's model considered that filling of the d-band has an effect on the cohesive energy across the transition metal series and the properties of transition metal series were calculated using second moment approximation. Cohesive energy of a transition metal is a sum of attractive bond energy and overall repulsive pair potentials.

$$E_{coh} = E_{bond} + E_{rep} \qquad (2.2)$$

The calculated and experimental cohesive energies calculated by Friedel[30] and Pettifor[34] were found to have shown a significant variation for all 4d transition metal series. The experimental d-band width for Mo was 10eV and the cohesive energy was approximately 6eV per atom while the theoretical calculations have shown the cohesive energy to be 2eV higher[29]. This variation between experimental and theoretical cohesive energies was the smallest for Mo in comparison to other metals of 4d series. The sp and d-band hybridisation that can increase cohesive energy was attributed for the observed change although its effect on the overall cohesive energy was neglected[29]. The relation between bond length and cohesive energy is shown in figure 2.9.

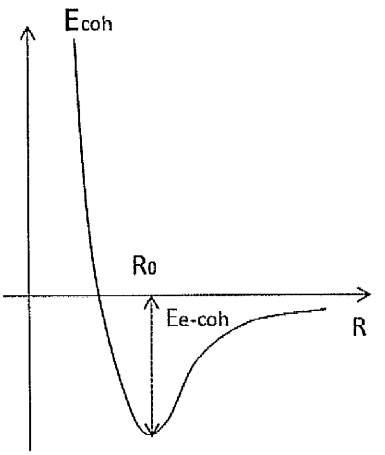

Fig.2.9. Cohesive energy plotted as a function of bond length.

In figure 2.9, E_{coh} is the cohesive energy for the d-bandwidth, R is the bond length, R_0 is the equilibrium bond length where the repulsive potentials balance the attractive bond energy and $E_{e\text{-}coh}$ is the corresponding equilibrium cohesive energy.

The change in cohesive energy includes the contribution from bond energy which again depends on the local atomic environment with respect to interatomic distance, bond length and bond angles. This is an interesting aspect since the bonding energy variations occurring due to bonding of different atoms from inequivalent sites at a distorted symmetry region like dislocation core, can vary the density of states and hence can also alter the electronic structure.

2.7 Electronic structure at dislocation cores

The theoretical study of electronic structure at dislocation cores in b.c.c metals Mo and α-Fe was previously done by J. Th. M. De Hosson in 1978 and 1980 using a self consistent field multiple scattering model. However, these calculations were done for <100> edge dislocation in both Mo and α-Fe[35, 36]. Screw dislocation cores were difficult to

analyse with the experimental and theoretical techniques available at that time since the dislocation line direction for screw is along the axis of the electron beam, whereas atomistic simulations required lot of computational power. This could be the reason for a significantly less number of investigations done on the electronic structure of screw dislocation cores both experimentally and theoretically. Although the electronic structure of <100> edge dislocation was presented for Mo, a review of the results can provide an insight into the changes that could be predicted from a screw dislocation core. A small difference in orbital energies of Mo was reported for edge dislocation core as compared to perfect crystal[35]. Electron density redistribution around the dislocation was observed which was due to a small change in electronic occupation. This was observed even in the case of α-Fe and the electrons seem to shift away from the extra half plane[36]. Edge dislocation core being a region with major displacements of atoms when compared to screw dislocation core, was reported to have exhibited minute changes in the electronic structure with reference to perfect crystal. Therefore the microscope and the EELS spectrometer have to be highly sensitive to record these minute electronic structure changes at the screw core.

Electronic structure at screw core in b.c.c. Fe was reported by Juan *et. al,* 2001 using atom superposition and electron delocalization orbital cluster method (ASED-MO) and no changes in DOS from screw core were reported[37]. However the experimental comparison was never done with pure b.c.c. Fe. The density of states at edge dislocation cores were reported to contain localised electronic states in b.c.c. Fe when the calculations were done using discrete variational method with in density functional theory DFT[38]. The localised electronic states in Fe were attributed to the decrease in the co-ordination number around the central atom, local symmetry arrangement of the core and the contribution of d

electrons to the localised electronic states. The changes that occur in the d-band in transition metals due to local symmetry destruction at the core were scarcely considered in the atomistic models used for studying the changes in density of states (DOS). It is therefore, a very interesting topic to research the changes due to transitions in the d band that occur in b.c.c. transition metals taking into consideration the localised asymmetry at the screw dislocation core.

2.8 Near Edge Structure changes

Energy Loss Near Edge Structure (ELNES) changes can be expected at the screw dislocation core due to high lattice strain observed at the screw dislocation core. At the screw dislocation core the bond lengths and the bond angles are different to that of perfect crystal because the atoms from different planes bond together at the core, in other words screw core tends to be non co-planar. The easy core was reported to have less core energy in Mo making it stable[11]. Murray *et.al* [39] found the hard core in Fe to be 0.12 eV/Angstrom higher in energy than the easy core. In their calculations for Mo, the hard core was found to be unstable. Hence it would be more interesting to know the type of core configuration exhibited by screw dislocations observed through experiments.

The ELNES near core loss edges $M_{4,5}$ for Mo and $L_{2,3}$ for Fe will be presented in this thesis for perfect crystal and at dislocation cores. Molybdenum M_4 edge is the resultant of $3d^{3/2}$ electron transition while M_5 is the resultant of $3d^{5/2}$ electron transition to unoccupied states above Fermi energy. The p states dominate in the energy range of $M_{2,3}$. Electronic configuration for molybdenum and the electron binding energies for different orbitals are shown in figure 2.10. The dipole selection rule dictates that the transition could happen from d states to either p or f states[33]. This was true if the 3d dipole transitions were

thought to occur, resulting in the $M_{4,5}$ edge. However the non-dipole ($\Delta\ell \neq \pm 1$) 3d to 4d transitions were also reported to show sharp peaks before the $M_{4,5}$ edge (227eV) in molybdenum[40].

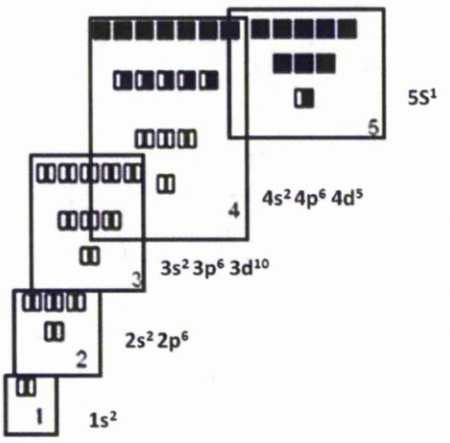

Label	Orbital	eV
K	1s	20000
L_I	2s	2866
L_{II}	$2p_{1/2}$	2625
L_{III}	$2p_{3/2}$	2520
M_I	3s	506.3
M_{II}	$3p_{1/2}$	411.6
M_{III}	$3p_{3/2}$	394
M_{IV}	$3d_{3/2}$	231.1
M_V	$3d_{5/2}$	227.9
N_I	4s	63.2
N_{II}	$4p_{1/2}$	37.6
N_{III}	$4p_{3/2}$	35.5

Fig.2.10. Ground state electronic configuration of molybdenum and the electron binding energies for different energy states are shown.

It was suggested that the non dipole transitions gain importance when there was a high density of dipole-forbidden states in the near threshold region and that these monopole (i.e. non-dipole) excitations were dependant on the scattering wave vector ***q***. The monopole transition (3d→4d) with final angular momentum (ℓ=2) increased significantly with ***q***, while the dipole allowed (3d→4f) transition decreased with ***q*** [40]. "In general strongest non-dipole features will be seen where a ($\Delta\ell \neq \pm 1$) transition reaches empty states in a shell which is just being filled and therefore has a high density of states just above the Fermi level"[41].

Ground state electronic configuration of iron is [Ar] $3d^6$ $4s^2$ and its variable oxidation states are +2 and +3. The metallic behaviour is exhibited by iron due to the transfer of one 4s electron into d-band while the remaining 4s electron couples with similar 4s electron from the neighbouring atom. Fe $L_{2,3}$ core loss edge corresponds to the energy lost

when a transition occurs between the spin-orbit split 2p level and unoccupied states in the 3d-band. L2 edge consists of transitions from $2p^{1/2}$ to $3d^{3/2}$ and L3 edge is the result of transitions from $2p^{3/2}$ to both $3d^{3/2}$ and $3d^{5/2}$. The electronic configuration of iron and the transitions relevant to EELS core loss edges are shown in figure 2.11. The electron binding energies of different energy states are also shown.

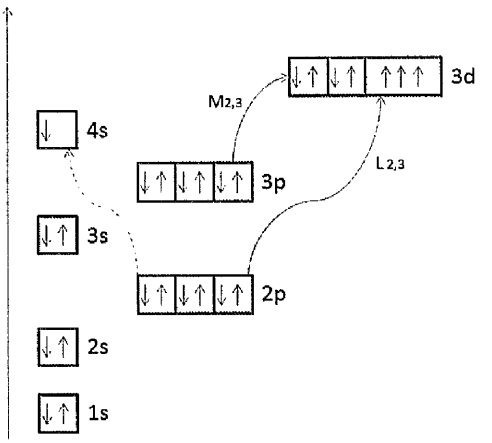

Shell	Orbital	Binding energy(eV)
K	1s	7112
L_I	2s	844.6
L_{II}	$2p_{1/2}$	719.9
L_{III}	$2p_{3/2}$	706.8
M_I	3s	91.3
M_{II}	$3p_{1/2}$	52.7
M_{III}	$3p_{3/2}$	52.7

Fig.2.11. Schematic of the electronic configuration of metallic iron showing the filling of d-band from other energy levels and their corresponding core loss edges. The dotted line indicates dipole-allowed but energetically unfavoured transition. EELS signal which probes unoccupied states can be used to complement the occupied states and the sum of occupied and unoccupied states gives the number of electrons in d-band, also known as occupancy. It was shown by Leapman *et.al.* that the area under L_2 and L_3 white lines can be used to interpret the d-band occupancy[42]. In the later years, Pearson *et.al* has shown that the sum of all unoccupied energy states is directly proportional to the sum of the areas under L_2 and L_3 white lines[43, 44]. Therefore the white line intensity ratios will be calculated for screw dislocation core and compared with perfect crystal as well as experimental values.

Screw dislocation core, a region of different energy configuration with respect to rest of the crystal may either increase or decrease the transitions from core states (3d for Mo-$M_{4,5}$ and 2p for Fe-$L_{2,3}$) to unoccupied states. The higher the number of transitions the larger would be the difference noticed in the difference spectrum. Hence comparison of (p+f) DOS plots of screw dislocation core and perfect crystal will reveal the change in density of states in Mo while (s+d) plots reveal the DOS changes in α-Fe. Theoretically simulated ELNES spectra can be compared directly with the experimental ELNES for different core configurations with respect to perfect crystal. This approach makes it possible to identify the practically preferred dislocation core configuration and interpret the differences in terms of electronic structure.

References

[1] M. S. Duesbery, V. Vitek, Acta Materialia 46 (1998) 1481-1492.
[2] J. a. W. Weertman, J. R. Weertman, Elementary Dislocation Theory, pp. ix. 213. Macmillan Co.: New York; Collier-Macmillan: London, 1964, p. 8º.
[3] D. Hull, D. J. Bacon, Introduction to dislocations, Butterworth Heinemann, Oxford, 2001, p. vii, 242 p.
[4] V. Vitek, Philosophical Magazine 84 (2004) 415-428.
[5] J. W. Christian, Second International Conference on the Strength of Metals and Alloys, Asilomar Conference Grounds, Pacific Grove California, 30 August-4 September, 1970 : Conference proceedings, ASM press, 1970, p. 31-70.
[6] L. Hollang, M. Hommel, A. Seeger, Physica Status Solidi a-Applied Research 160 (1997) 329-354.
[7] T. Suzuki, H. Koizumi, H. O. K. Kirchner, Acta Metallurgica et Materialia 43 (1995) 2177-2187.
[8] E. Schmid, Proceedings on International Congress of Applied Mechanics (1924) 342.
[9] S. Takeuchi, E. Kuramoto, Journal of the Physical Society of Japan 38 (1975) 480-487 p.
[10] S. Ismail-Beigi, T. A. Arias, Physical Review Letters 84 (2000) 1499-1502.
[11] C. Woodward, S. I. Rao, Philosophical Magazine A 81 (2001) 1305 - 1316.

[12] F. Shimizu, S. Ogata, H. Kimizuka, T. Kano, J. Li, H. Kaburaki, Journal of the Earth Simulator 7 (2007) 17–21.
[13] V. Vitek, Philosophical Magazine 18 (1968) 773-786.
[14] V. V. Bulatov, J. F. Justo, W. Cai, S. Yip, Physical Review Letters 79 (1997) 5042-5045.
[15] Y. M. Huang, J. C. H. Spence, O. F. Sankey, Physical Review Letters 74 (1995) 3392.
[16] V. Vitek, Crystal Lattice Defects 5 (1974) 1-34.
[17] W. Xu, J. A. Moriarty, Journal of Computer-Aided Materials Design 3 (1996) 245-252.
[18] L. Ventelon, F. Willaime, Journal of Computer-Aided Materials Design 14 (2007) 85-94.
[19] T. E. Jones, M. E. Eberhart, D. P. Clougherty, C. Woodward, Physical Review Letters 101 (2008) 085505.
[20] J. Chaussidon, M. Fivel, D. Rodney, Acta Materialia 54 (2006) 3407-3416.
[21] W. Sigle, Philosophical Magazine A 79 (1999) 1009 - 1020.
[22] J. D. Eshelby, A. N. Stroh, Philosophical Magazine 42 (1951) 1401.
[23] B. G. Mendis, Y. Mishin, C. S. Hartley, K. J. Hemker, Philosophical Magazine 86 (2006) 4607 - 4640.
[24] B. Mendis, Y. Mishin, C. Hartley, K. Hemker, HREM imaging of screw dislocation core structures in bcc metals., in: Mater. Res. Soc. Symp. Proc., vol 839, 2005, pp. 73-78.
[25] K. J. Hemker, Characterization of Dislocation Core Structures in BCC Metals, in: U.S. Air force office of scientific research reports, 2004, pp. 1-16.
[26] B. G. Mendis, K. J. Hemker, Ultramicroscopy 108 (2008) 855-864.
[27] I. M. Duma, B. L. Mel'nichuk, Z. V. Stasyuk, Russian Physics Journal 35 (1992) 1123-1126.
[28] P. Mohn, Magnetism in the solid state : an introduction, Springer, Berlin ; [London], 2006, p. xi, 229 p.
[29] A. P. Sutton, Electronic structure of materials, Oxford University Press, Oxford, 1993, p. xii,260p.
[30] J. Friedel, Advances in Physics 3 (1954) 446-507.
[31] A. P. Sutton, Contemporary Physics 30 (1989) 219-222.
[32] U. Mizutani, Introduction to the electron theory of metals, Cambridge University Press, Cambridge, 2001, p. xii, 590 p.
[33] R. M. Martin, Electronic structure: basic theory and practical methods, Cambridge University Press, Cambridge, 2004, p. xxiii, 624 p.
[34] D. G. Pettifor, T. Henry Ehrenreich and David, A Quantum-Mechanical Critique of the Miedema Rules for Alloy Formation, in: Solid State Physics, vol Volume 40, Academic Press, 1987, pp. 43-92.
[35] J. T. M. D. Hosson, International Journal of Quantum Chemistry 14 (1978) 469-482.
[36] J. T. M. D. Hosson, International Journal of Quantum Chemistry 18 (1980) 575-582.
[37] A. Juan, B. Irigoyen, S. Gesari, Applied Surface Science 172 (2001) 8-17.

[38] L.-q. Chen, C.-y. Wang, T. Yu, Computational Materials Science 38 (2006) 39-44.
[39] M. S. Daw, LDA Calculations of Dislocation Mobility in Fe & Mo, in: Department of Energy, Scientific and Technical Information Reports., Dept of Physics & Astronomy, Clemson University, Clemson, 2006, pp. 1-8.
[40] J. M. Auerhammer, P. Rez, Physical Review B 40 (1989) 2024.
[41] C. C. Ahn, O. L. Krivanek, EELS Atlas - A reference guide of electron energy loss spectra covering all table elements, in: 1998.
[42] R. D. Leapman, L. A. Grunes, P. L. Fejes, Physical Review B 26 (1982) 614.
[43] D. H. Pearson, C. C. Ahn, B. Fultz, Physical Review B 47 (1993) 8471.
[44] D. H. Pearson, B. Fultz, C. C. Ahn, Applied Physics Letters 53 (1988) 1405-1407.

Chapter 3

Electron scattering and EELS

Chapter 3

ELECTRON SCATTERING AND EELS

When fast moving electrons travel through a thin specimen that is transparent to electrons, they either scatter or remain unaffected by the specimen. Scattering of fast electrons can be classified into two types: elastic and inelastic scattering. Elastic scattering refers to the scattering of electrons with negligible energy loss but may deflect from their original travelling path. Such electrons are coherent. This means that the energy loss to the sample due to coherent elastically-scattered electrons may be negligible in the experiment. Scattering is defined to be inelastic when the fast electron loses a measurable amount of energy. Inelastically scattered electrons are usually incoherent.

In this chapter, electron interaction with the sample and the inelastic scattering which gives a spectrum of measurable energy loss will be considered. The dependence of inelastic scattering on differential cross section will be discussed while taking into account other factors like specimen thickness and scattering angles. Different regions in the electron energy loss spectrum which are a resultant of different processes during the electron-sample interaction will be discussed. The techniques and the devices used to measure the energy loss are also considered.

3.1 Introduction to electron scattering

When fast electrons with high energy are incident upon thin solid specimens like metals, they can scatter at different angles due to electrostatic attraction of the positive nucleus. This kind of scattering is known as elastic scattering and is dependent upon the atomic number of the metal. The distance between the travelling electron and the nucleus is

an important consideration which will decide the scattering angle. The amount of energy that is transferred can be negligible for an experimental result from this kind of scattering. Yet it is important to understand it as a process which indirectly contributes towards the measuring of the electron energy loss. The process of interaction and the resulting scattering is shown in figure 3.1.

Electrons that undergo inelastic scattering as well as elastic scattering will result in a non-uniform angular and spatial distribution which will provide the chemical and structural information about the specimen. Angular distribution of such scattering gives diffraction patterns while spatial distribution provides the contrast for the image in an electron microscope.

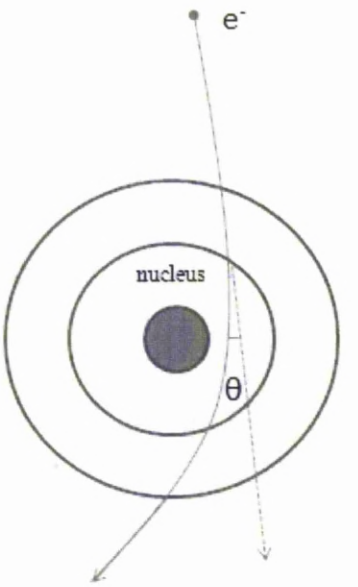

Fig.3.1.High energy electron scattering due to attraction from the nucleus.

Elastic scattering usually is loosely defined as a scattering process with no energy loss and the collective intensity of such scattering gives information about the specimen's atomic number. The sample used in

this research work is a single crystal of pure molybdenum rather than any interface and hence the interference of numerous electron scattering events from different materials is not considered in this thesis.

3.2 Theory of inelastic scattering

When a high energy electron interacts with an atom in the specimen, it loses energy by penetrating into the inner shells after passing through the loosely bound outer shells. The resultant scattering due to this interaction of incident electron with inner and outer shell atomic electrons is known as inelastic scattering. Inelastic scattering can result in a distribution of electrons scattered at high scattering angles and wide range of energy losses. Hence the processes of inelastic scattering are classified into processes that generate x-rays, secondary electrons and processes that can be a result of collective interaction of many atoms.

The electron energy losses that result due to inelastic scattering process can be measured over a wide energy range and are often displayed as electron energy loss spectra. The elastic scattering process including the unscattered electrons is responsible for the zero loss peak in the spectrum while inelastic scattering process contributes to the rest of the spectrum. These spectra give local chemical and structural information about the material. They are also useful in understanding the bonding between atoms. Any changes observed in the fine structure above the edge threshold can be understood as a result of local symmetry or structural changes like changes in bond angles and interatomic distance. The study of dislocations presented in this thesis hence considers the electron energy loss changes at the dislocation core in molybdenum and iron as an important result. It gives an efficient guidance to understand the local symmetry and structural changes at the dislocation core. In this research work, electron energy loss near edge structure at $M_{4,5}$ edge of molybdenum and $L_{2,3}$ edge of iron will be discussed.

3.3 The inelastic scattering cross section

Interaction cross section, σ is an important factor that determines the probability of any electron to undergo any kind of interaction. The difference in interaction cross section is dependent upon energy of the incident electron. Beam energy thus has a very significant role in determining the possibility of particular type of interaction as well as scattering process. Larger cross sections can lead to better chances of scattering. Apart from this, scattering angle and the atomic number of the specimen can affect scattering process, as discussed before. The figure 3.2 shows the electron scattering and the illustration of scattering semiangle θ, and the incremental solid angle, $d\Omega$.

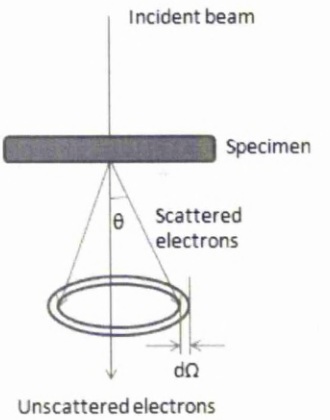

Fig.3.2 Image showing electron scattering by semiangle θ and incremental solid angle $d\Omega$.

Scattering is less at high energies and high angles while it is more for heavier atoms than lighter atoms. The angular distribution of scattering from an atom is given by differential cross section ($d\sigma / d\Omega$).

It can be written as:

$$d\sigma / d\Omega = (1/ 2\pi \sin\theta) (d\sigma/d\theta) \qquad [3.1]$$

From this equation it can be said that the value of interaction cross section increases with decreasing semiangle θ.

Now, the total cross section for all angles up to θ can be calculated by integrating equation 3.1. This gives

$$\sigma_\theta = 2\pi \int_0^\pi \frac{d\sigma}{d\Omega} sin\theta \, d\theta \qquad [3.2]$$

Thus by knowing the differential cross section, the values of interaction cross section, σ can be calculated easily for any atom in the specimen.

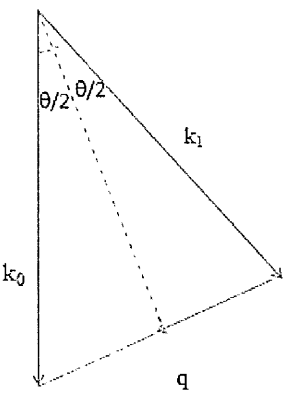

Fig.3.3.Wave vectors of an incident electron; k_0 is the wave vector before scattering; k_1 is the wave vector after scattering; q is the scattering vector.

According to *Bethe* [1] theory, for inelastic scattering processes, the [dσ / dΩ] must describe the transition for each atomic electron as the transition from initial (ψ_0) to final (ψ_n) states of wave function. From the figure 3.3, if k_0 is the pre-scattering wave vector, k_1 the post scattering wave vector and q, the scattering vector, then using first *Born* [2] approximation, the differential cross section for a transition *n* can be written as,

$$\frac{d\sigma_n}{d\Omega} = \left(\frac{m_0}{2\pi\hbar^2}\right)^2 \frac{k_1}{k_0} \left| \int V(r)\psi_0\psi_n \exp(iq.r) d\tau^2 \right| \qquad [3.3]$$

If we consider energies less than 300 keV, the above equation becomes,

$$\frac{d\sigma_n}{d\Omega} = \frac{4\gamma^2 R}{E_n q^2} \frac{k_1}{k_0} f_n(q) \qquad [3.4]$$

where $f_n(q) = \frac{E_n}{R} \frac{|\varepsilon_n(q)|^2}{(qa_0)^2}$ is defined as the generalised oscillator strength (GOS), R is the Rydberg energy; E_n is the energy loss during transition.

The electron energy loss spectrum can be considered as a continuous function of energy loss, E, by using the GOS per unit excitation energy $\frac{df(q,E)}{dE}$. The dependence of scattering on angle and energy can then be specified by a double differential cross section which is given by,

$$\frac{d^2\sigma}{d\Omega dE} = \frac{4\gamma^2 R}{Eq^2} \frac{k_1}{k_0} \frac{df}{dE}(q,E) \qquad [3.5]$$

In order to understand the angular distribution of inelastic scattering, scattering angle θ must be related with scattering vector q. Upon approximation, where scattering angle θ <<1, E<<E_0, and k_1/k_0 =1, the scattering vector q can be written as

$$q^2 = k_0^2 (\theta^2 + \theta_E^2) \qquad [3.6]$$

and the characteristic angle of scattering is given by,

$$\theta_E = \frac{E}{(E + m_0c^2)(\upsilon / c^2)} \qquad [3.7]$$

Using above, the double differential cross section can be written as,

$$\frac{d^2\sigma}{d\Omega dE} \approx \frac{8a_0{}^2R^2}{Em_0{}^2\upsilon^2}\left(\frac{1}{\theta^2 + \theta_E{}^2}\right)\frac{df}{dE} \qquad [3.8]$$

v is the velocity of the incident electron. The above equation shows the angular dependence of scattering at low angles as well as the energy loss measured in the electron energy loss spectrum.

3.4 Dielectric formulation:

Inelastic scattering in a solid that occurs from inner atomic shells can be described by *Bethe* [1] theory, while the inelastic scattering from the outer shell electrons can be complex due to the changes induced in the chemical bonding by the valence electrons. An alternate approach to this problem is to use the interaction of a transmitted electron in the whole solid, explained in terms of dielectric response function ϵ (q, ω).The electron scattering power of an infinite medium was given by Ritchie in 1957[3]. The relation between double differentiated inelastic cross section and the dielectric response as explained by him is given by,

$$\frac{d^2\sigma}{d\Omega dE} \approx \frac{\mathrm{Im}\left[-1/\varepsilon(q,E)\right]}{\pi^2 a_0 m_0 \upsilon^2 n_a}\left(\frac{1}{\theta^2 + \theta_E{}^2}\right) \qquad [3.9]$$

The imaginary part of the function is known as energy loss function and provides complete description of the medium through which the fast electron passes. Equations 3.8 and 3.9 can be shown to be equivalent provided,

$$\frac{df}{dE}(q,E) = \frac{2E}{\pi E_a^2}\,\mathrm{Im}\left[\frac{-1}{\varepsilon(q,E)}\right] \qquad [3.10]$$

E_a, the plasmon energy which corresponds to one free electron per atom is given by $E_a^2 = \left(\frac{\hbar^2 n_a e^2}{\varepsilon_0 m_0}\right)$.

Due to little variation of ϵ (q, E) with **q** for spectra that are acquired with small collection angles, it can be replaced with optical permittivity of the specimen $\epsilon(0, E)$ at an angular frequency, $\omega = E/\hbar$. With this relation, the electron energy loss spectra can be compared directly with the optical information. Other information about the energy dependence on real (ϵ_1) and imaginary (ϵ_2) parts of $\epsilon(0, E)$ can also be studied.

3.5 Multiple Scattering:

The dependence of scattering on the thickness of the specimen can be used to understand the probability of scattering events. In a thin specimen ($t/\lambda < 3$) the scattering probability (either elastic or inelastic depending on the process lambda was chosen to represent) is low and the chance of having more than one scattering event becomes negligible. In a thick specimen ($t/\lambda > 5$), the probability of having more than one scattering event (multiple scattering) is high, and thus individual peaks may not be clearly distinguished in the EELS spectrum.

A *Landau* distribution is produced due to combination of multiple inner and outer shell processes, and is recognised by the broad peaks near the high energy loss region in the spectrum[4]. The specimen thickness can be nearly proportional to the maximum probable energy loss given by (t/λ) E_p where E_p is the main energy peak in a single scattering distribution.

3.6 Dislocation contrast

When dislocations in a material are studied using the electron microscope, it is often required to know the dislocation density in the sample and whether they are edge, screw or mixed dislocations. If a dislocation of particular type is studied, the parameters that can be determined are the dislocation line direction, and the Burgers vector's direction and magnitude.

Theoretically, the dependence of the contrast on the type of dislocation can be understood using the displacement field equation[5]. The displacement field in an isotropic solid is given by:

$$\mathbf{R} = \frac{1}{2\pi}\left(\mathbf{b}\phi + \frac{1}{4(1-\nu)}\{\mathbf{b}_e + \mathbf{b}\times\mathbf{u}(2(1-2\nu)\ln r + \cos 2\phi)\}\right) \quad [3.11]$$

Where r is the distance of the displaced atom from the dislocation core at angle Φ, ν is the Poisson's ratio, **b** is the Burgers vector, $\mathbf{b}_e$ is the edge component of the Burgers vector and **u** is the unit vector along the dislocation line. Consider the two cases, edge and screw dislocation.

1. Screw dislocation: $\mathbf{b}_e = 0$; **b** is parallel to **u**, so **b** x **u** = 0. Using this criterion, equation 3.11 can be written as $\mathbf{R} = \mathbf{b}\frac{\phi}{2\pi}$ [3.12]

   From equation 3.12 the displacement field is dependent upon the angle that the dislocation makes with a column of atoms under incident beam far from the dislocation i.e. in a perfect crystal region. Since the angle is a variable of the depth at which the dislocation core is present below the crystal surface, the displacement field is present both above and below the dislocation and so it affects the whole column of atoms that are considered here. From the above two equations we can express that **g.R**

is proportional to **g.b**, where **g** is the diffraction vector. Therefore contrast from a dislocation is always interpreted in terms of **g.b**.

2. Edge dislocation: **b** = $\mathbf{b}_e$ and **g.R** has two terms **g.b** and **g.bxu**. The Bragg diffracting planes associated with **g** bend because of the displacement field **R**. The introduction of the second term implies the buckling of the glide plane due to edge dislocation[6].

In both these cases (screw and edge) **g.R** is responsible for contrast from the dislocation and therefore is important while imaging dislocations in a TEM. A general formula involving the Burgers vector then would be **g.b** = n. If **g** is determined from the experiment, and the value of n is known, then the Burgers vector **b** can be easily found.

By theory, if **g.b** = 0 then there should not be any contrast because the diffracting planes will be parallel to displacement field vectors. This is termed as *invisibility criterion*. But practically, dislocations can still be visible when the beam is nearly parallel to their line direction. This is true in the case of screw dislocation where **g.b**= 0. The reason for this is the Eshelby twist and the relaxation of the surface[7]. One more rule that dictates the contradiction to invisible contrast from dislocations when **g.b** = 0 is that **g.bxu** $\geq$0.64[5].

Important factors that affect the dislocation contrast are:

1. Sign and magnitude of the deviation parameter, the spatial distance at which the dislocation core is situated from the column of atoms under the probe[8].

2. The depth of the dislocation core from the surface of the sample, and the thickness of the sample.

3. The sign and magnitude of the Burgers vector **b**, **(g.b)** product as well as **(g.b) x u**.

Contrast from an edge dislocation is due to bending of the diffracting planes on either side of the dislocation with variable intensity. Screw dislocations with line direction parallel to the beam appear with faint intensity as sharp projections from the surface of the foil and with no projected length along the surface of the foil. An example for this is shown in image 3.4. This contrast can be observed even in the atomic resolution images which will be presented in the results chapter.

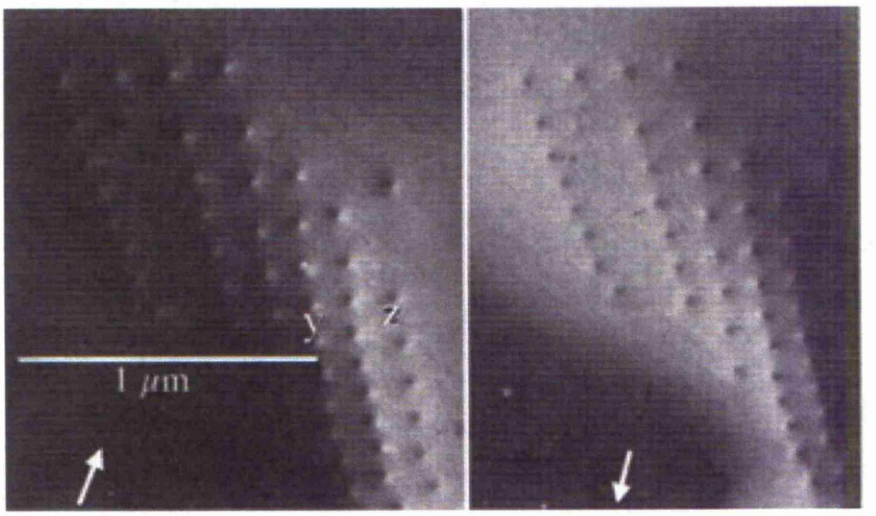

Fig.3.4. TEM image of screw dislocations normal to the foil in platinum[8]. Left image shows the anticlockwise (left-handed) screw character while the right image shows clockwise (right-handed) character and contrast change can be seen in comparison.

3.7 Instrumentation

This section will discuss instrumentation involved in electron microscopy with specific reference to imaging dislocations in TEM, aberration corrected STEM and challenges associated with electron microscopy of

magnetic samples. Transmission electron microscope and Scanning Transmission Electron Microscope used in this study will be discussed with reference to the study of dislocations and their limitations with respect to the requirements of the project. Electron energy loss spectrometers and the features of EELS spectrum will be discussed with reference to theory. The need for high resolution aberration corrected microscope equipped with electron energy loss spectrometer (SuperSTEM) as a tool to study dislocation cores in this research will be explained, followed by its own advantages and limitations.

3.7.1 Electron Microscopes

The transmission electron microscope is an important tool for studying dislocations in materials. When an electron beam interacts with a crystal containing a dislocation in a TEM, it produces alternative bright and dark contrast from the dislocation region in the image. This is due to bending of the lattice planes near the dislocation which cause a change in the diffraction conditions. Dislocation character can be understood by studying the contrast in the TEM image.

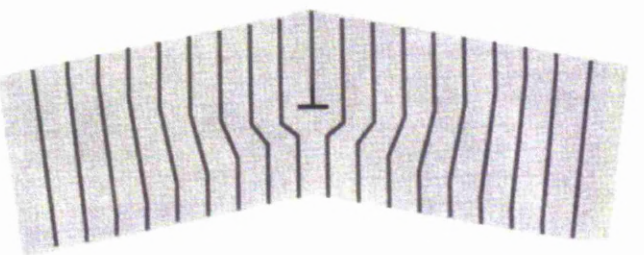

Fig.3.5. Bending of diffracting planes at an edge dislocation[5].

Figure 3.5 shows the bending of the lattice planes near an edge dislocation that could result in change of diffracting conditions.

By definition contrast is the change in intensity between two adjacent but similar areas[5]. Scattering by the specimen changes the uniform electron beam intensity into a non-uniform distribution and the presence of dislocations in the sample adds to a further change in intensity. A diffraction pattern records the non-uniform intensity after scattering by differentiating the transmitted beam from the scattered beam as per Bragg's diffraction conditions. An important parameter in understanding the contrast arising from a dislocation is "deviation parameter" denoted by "s". Deviation parameter is a vector in reciprocal space that measures the deviation from exact Bragg condition[5]. Planes near a dislocation are bent into Bragg diffraction condition, where deviation parameter of the incident beam, s=0. Regions far from dislocation are tilted away from Bragg condition ($s \neq 0$). This would cause the image contrast to be displaced from its projected position. Therefore it is important to understand the ways of imaging a dislocation in an electron microscope.

The two common methods of imaging in an electron microscope are bright field (BF) imaging and dark field (DF) imaging. BF uses the direct beam to form the image while DF uses one of the diffracted beams. The selection of the beam is done by an objective aperture in a TEM while it is done by bright field (BF) and high angle annular dark field (ADF) detectors in a STEM.

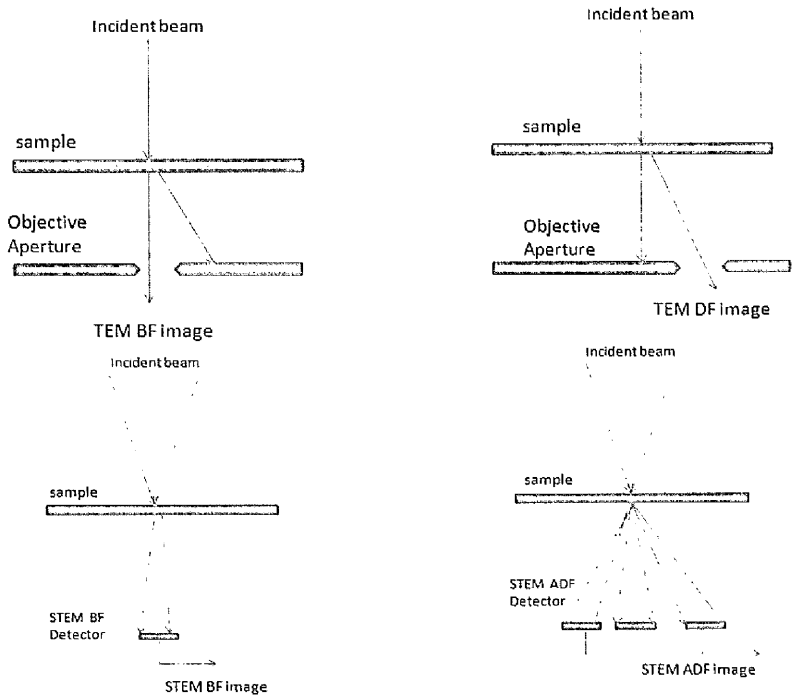

Fig.3.6. Bright field and dark field imaging in a TEM and BF and ADF imaging in a STEM.

The darker areas in a bright field image will appear bright in a dark field image. Dislocation contrast in a TEM can be understood by tilting the specimen to two beam conditions. In this condition one of the diffracted beams is made strong by tilting precisely. This can give information about the specific orientation of the region of interest in the sample. The best contrast from dislocations can be obtained by tilting the specimen close to Bragg condition with a small positive deviation parameter **s**, but not to exact Bragg condition where s=0. Further tilting increases the **s** value and the contrast starts to diminish along with narrowing of dislocation features in the image. Other important points to take care of that can help improve contrast from a dislocation in a TEM are a parallel beam (i.e. small convergence angle), two beam conditions and a single strong direct or diffracted beam reaching the objective aperture.

3.7.2 Electron Energy Loss Spectrometer

When an electron beam travels through a thin specimen, the fast incident electron may undergo various processes as described in the previous sections 3.1 and 3.2. Inelastically scattered electrons contain information which if collected separately can provide spatial chemical and structural information about the specimen. A spectrometer is the device which collects the inelastically scattered electrons which undergo energy loss of different magnitudes and scattered at different angles. Two common types of spectrometers are spectrometer by GATAN which is designed for use with energy loss measurement and the other one is omega filter which is mainly used for energy filtered imaging. Both are magnetic spectrometers, GATAN in post-column and omega filter usually in-column. The spectrometer used for the work in this thesis is a magnetic prism spectrometer by GATAN fitted to the aberration corrected SuperSTEM. A schematic diagram of how a GATAN spectrometer works is shown in the figure 3.7.

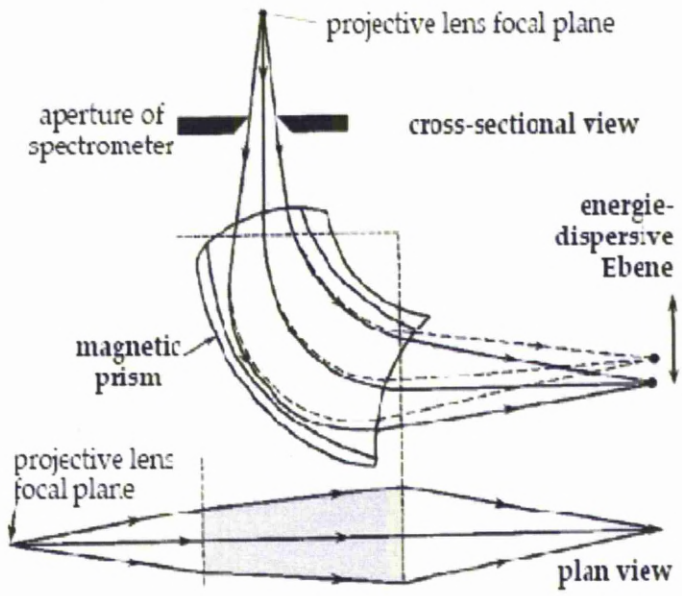

Fig.3.7. Principle of EELS spectrometer[5].

Fast travelling electrons are allowed into the spectrometer using apertures of various sizes. These electrons travelling through a drift tube get deflected by more than 90^0 by a surrounding strong magnetic field. High energy loss electrons get more deflected than electrons with low energy loss. This results in the formation of a spectrum with the distributed counts of electrons (commonly referred as intensity) as a function of energy loss in electron volts. The spectrometer focuses off axis and on axis electrons onto the dispersion plane where the spectrum image can be recorded. The spectrometer is an asymmetric lens and hence needs adjustment with focus. Electrons which lose no energy form the zero loss peak and this peak can be adjusted for focus using the quadrupoles until it becomes sharp.

There are two methods in which the spectrum can be collected, namely serial collection system and parallel collection system. In a serial collection system the focus is done using the slit in the dispersion plane while in parallel system, the quadrupoles can be directly used for focus. The acquisition of the spectrum in serial system (SEELS) is done by building up one channel at a time, while in parallel system (PEELS or commonly EELS) it is done by acquiring all channels at the same time. The parallel collection spectrometer consists of a scintillator coupled to a semiconductor photodiode array which show individually varying responses. PEELS has more advantage than SEELS in being more efficient in collection over given integration time and detects whole spectrum at one time rather than one channel at a time.

The EEL spectra presented in this thesis were collected by a Gatan parallel EEL detector, with the spectrometer fitted on the top of the SuperSTEM. A thermostatically cooled scintillator-charge coupled device (CCD) with greater sensitivity than a photo diode array is used in this spectrometer. The advantages of using such a device are achieving

better resolution measured as point spread function, quicker acquisition times and high sensitivity. Some important factors which may be optimised are collector aperture, acquisition time, energy dispersion and the number of channels used. These optimisations will be discussed in detail in chapter 5 which will describe the experimental techniques used.

3.8 Theory of electron energy loss spectrum

The electron energy loss spectrum can be classified into three main regions as shown in the figure 3.8. The region I shown in the figure is the zero loss peak which consists of the information about elastically scattered electrons. Inelastically scattered electrons form the rest of the spectrum. Region II is known as low loss region and region III is known as core loss region. When incident electrons interact with the shared (nearly-free) electrons in the outer-shells, the resultant region is the low loss region and plasmon peaks are the most important feature of this region. When the incident electron interacts with the inner shell atomic electrons, the resultant region is the core loss region.

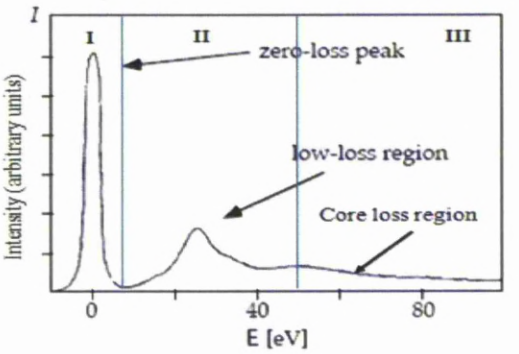

Fig.3.8 Electron energy loss spectrum showing its three main regions.

It can be observed in the spectrum that the background reduces as the energies increase gradually along the spectrum and the edges correspond to different scattering processes. The core loss region contains

superimposed ionisation edges while there could also be contribution of the noise from the instrument to the background. To avoid this, background from a spectrum taken in vacuum can be subtracted from the real spectrum. The remaining background could be the effect of many scattering events. In the low loss region the intensity is shown to decrease as E^{-3}, by integrating the equation 3.9, and assuming $\beta > \theta_E$

$$\frac{d\sigma}{dE} \propto \mathrm{Im}\left(\frac{-1}{\varepsilon}\right)\ln\left(\frac{\beta}{\theta_E}\right) \qquad [3.13]$$

As there is a low probability of many scattering events in the high energy loss region, a single electron approach is taken and hence the intensity dependence is governed by a power law, for which the intensity $d\sigma / dE$, becomes,

$$\frac{d\sigma}{dE} \propto E^{-s}, \qquad [3.14]$$

where s depends on the size of the collection aperture. The intensity of the core loss region is found to be concentrated at smaller scattering angles than the background, as the inner shell electrons are more tightly bound than the outer shell electrons. Hence by choosing smaller collection apertures, the edge signal to background energy ratio can be altered to better values. Background removal is one of the initial and important steps when analysing the information recorded in the EEL spectrum.

3.9 Features of an EEL Spectrum

The various types of energy losses in a typical EEL spectrum have been discussed in the section 3.8. This section focuses on the specific regions

of EEL spectra that will be used for analysis in this thesis. A specimen with thickness of less than about 100 nm studied in a 100 keV microscope for electron energy loss, will produce a sharp and intense feature called the zero loss peak at 0 eV which contains information about elastically scattered electrons collected from the specimen. The resolution of the spectrum is often affected by the energy spread of the electron source which results in broadening the characteristic features of the zero loss peak. Phonons in solids produce the lowest electron energy losses of the order of 10 to 100 meV and are often not resolved within the zero loss peak.

The often-delocalized outermost atomic shell electrons extending over a multiple atomic distances are responsible for the low loss region of the EEL spectrum which typically extends from a few (~5) eV to about 50 eV. This region has predominantly aggregate effect of excitations from valence electrons known as plasmons. The energy of plasmon peaks can reveal the valence state and the density of valence electrons while the width of the peak informs about the decay rate. Low loss region can also reveal the all important feature known as interband transitions in insulating materials, which are defined by valence electron excitations to low energy unoccupied states above the *Fermi* level. The main use of low loss region in general is the determination of specimen thickness and also to measure the dielectric response function of the material which in turn is helpful in determination of band gap.

As shown in figure 3.8, the high loss region extends anywhere above 50 eV to thousands of eV and edges in this region are a result of electron excitations from localised orbitals to unoccupied states above the Fermi level of the specimen material. High loss region contains edges which are called ionisation edges and are caused due to excitation of inner shell electrons. This region can provide vital atomic information about the

solid. This region is useful for quantitative analysis as the number of atoms present is directly proportional to the intensity under the ionisation edge. Hence these edges are recorded for various materials and are used as a standard reference for most materials studied by EELS.

Specific edge shapes can be attributed to the excitation processes from different shells and the interaction of electrons with one another. In the case of solids, chemical bonding may change the unoccupied electronic states near Fermi level and may lead to complex density of states (DOS). Such changes in basic atomic shape up to several tens of eV constitute the fine structure on inner shell ionisation edges commonly termed as energy loss near edge structure (ELNES). The ELNES region can provide information about atomic bonding, coordination number and the local electronic structure associated with very specific atomic regions in the specimen. In the work presented in this thesis the ELNES region of the EEL spectrum is used to analyse metals like molybdenum and iron for any associated electronic changes near the dislocation core regions.

As the energy loss region increases gradually beyond the ELNES region, a region of weaker and extended energy losses known as extended energy loss fine structure (EXELFS) is observed. The amplitude of these excitations helps in determining the coordination number while the period helps in deducing the bond distances. The basic difference between the ELNES and the EXELFS region is the kinetic energy of the ejected electron. The near edge region produces a low kinetic energy electron which interacts with a larger volume leading to multiple elastic scattering. EXELFS region electrons are ejected with high kinetic energy resulting in single elastic scattering event and hence providing only limited information.

The application of the dipole rule to different transitions near core loss edges becomes necessary if the electrons are collected at small scattering angles. The angular momentum then defines the probability of observing a specific electron transition. This means different edges of the same metal can have different symmetries of the final state, for example an $L_{2,3}$ edge can access both unoccupied *s* and *d* like DOS. Transition metals have partially filled d-band superimposed on s-p bands and are interesting materials to study for electronic changes. In this thesis, the transition metals molybdenum and iron will be analysed for any changes in electronic structure near dislocation core using EEL spectra.

3.10 Spatial localisation of EELS signal: (low loss and core loss)

Screw dislocation cores are extremely localised regions of the order of a few angstroms. The variation in interatomic spacing at the core can give an idea of the location of the core, but the more important contrast variation is helpful in identifying it from the dark field image. The atomic displacements near the core have been reported to be less than 10 picometres[9]. The typical electron wavelength in a TEM is of the order of 0.02 Å, yet the spatial resolution of such a microscope is 1–2 Å which is not sufficient to probe dislocation cores[10]. Therefore only atomic resolution imaging with aberration correction can solve the problem of noise that was reported by HREM experiments. In this context, the identification of electronic structure at the core can be done by a high energy resolution energy loss spectrometer which is sensitive enough to record the variations from atoms that vary their atomic positions by a fraction of an angstrom. Moreover only core loss edges can be used to detect the differences in EELS signal from dislocation core since low loss signals should have been delocalised over 1 nm scale and hence are less sensitive.

The delocalisation of inelastic scattering process limits the spatial resolution of EELS due to the extension of electronic field effects characterised by the angular distribution. The degree of delocalization decreases from a few nanometers to sub-nanometer order with increasing energy-loss[11]. This is because the spatial decay of the electronic fields is faster at high energy losses. In the scale of energy losses from 300-1000eV, localization can reach 1-2Å[12]. The characteristic delocalization length can be larger than the interatomic spacing at lower energies thereby effecting the image resolution and making the interpretation difficult[13]. Hence, the electronic structure differences from a localised core can only be interpreted by the variation in the ELNES region at the specified core loss edge.

It should also be noted here that the time for EELS acquisition should be around 1 to 10 seconds taking account a typical sample drift rates of about 5Å per minute[10]. The noise levels should be less than the signal in order to identify the significant changes in the signals. "For EELS work, the main benefit of correctors is likely to be the very large increases in signal at a resolution of 1–2 Å rather than deep, sub-angstrom spatial resolution"[10]. This is one of the key advantages of having aberration correctors in the STEM.

3.11 Magnetic samples in microscopes

Magnetic samples can be troublesome to use in an electron microscope. Ferromagnetic materials have been interesting materials for microscopy but the magnetism from the sample affecting the beam is a major problem. The electrons used for imaging after they pass through the magnetic sample can be deflected from the optic axis because the electron beam is deflected as it passes through the sample. Ferromagnetic materials produce deflections through their internal magnetisation and

surface leakage fields[14]. The images will be recorded with severe aberrations and will cause big shifts in the features in the recorded image.

In particular the astigmatism in the microscope cannot be corrected effectively than when compared to non-magnetic samples. Setting the eucentric height for a magnetic sample is another problem. When the sample is tilted, it will be pulled onto either side trying to align itself parallel to the beam, and can rotate, flip out of the holder or change its position and height. If the sample is allowed to flip or rotate, it can fall out of the holder and stick to the pole piece in which case the microscope has to be disassembled. The ways in which the effect of magnetic field from the sample could be corrected will be discussed in the experimental techniques chapter.

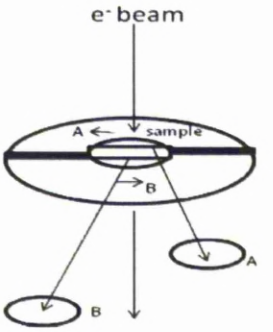

Fig.3.9. Deflection of incident beam into A and B at the domain boundary due to Lorentz deflections.

Aberration corrected electron microscopes can help solve the problem to a certain extent by correcting some of the aberrations introduced by the sample. There are other important steps to make the analysis of magnetic samples in electron microscopes easier. One of the possible ways is to prepare the sample as thin as possible with the smallest possible magnetic material in it. This will help reduce the total magnetic field strength of

the sample that perturbs the electron beam. The sample should have sufficient support to resist the torque from the interaction of the sample field with the objective lens field.

Correcting astigmatism in the area of interest could also help but translation or tilting of the sample will change the astigmatism again. This is because the magnetic field varies depending upon the position of the sample. This local correction can be done with considerable experience in using the microscope with magnetic samples. The magnetic samples discussed in this thesis are used for experimental analysis both in TEM and SuperSTEM.

3.12 Aberration corrected STEM (SuperSTEM)

Aberrations are common in all practical lenses and electron microscope lenses are no exception. They are crucial factors that limit the resolution of the instrument. Better design and alignment of the lenses in the microscope can reduce these aberrations to a significant extent.

The two common types of aberration in electron optical lenses are chromatic and spherical aberrations. Different possible approaches of reducing these aberrations in the electron microscopes have been proposed while the use of multipole lenses was accepted. The two types of multipole lenses were quadrupole-octupole (QO) and hexapole correctors. The SuperSTEM-1 used for the work described in this thesis contains a quadrupole-octupole corrector[15]. Figure 3.10 shows a schematic cross-section of an aberration corrected STEM. The components of the aberration corrected STEM are electron source, a stable electron optical column, sample stage, aberration correctors, optics for beam control and a high resolution EELS spectrometer.

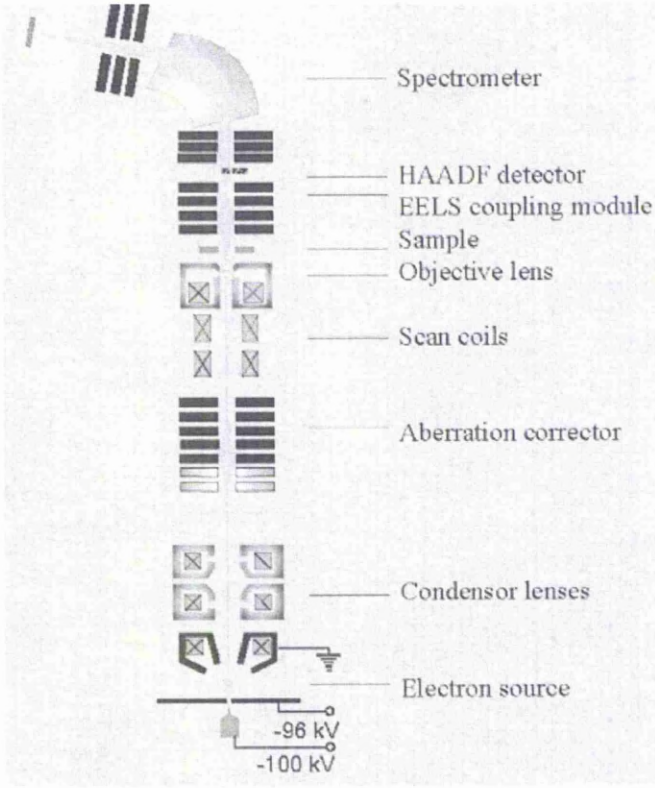

Fig.3.10. Cross-section of an Aberration corrected SuperSTEM with essential components.

3.13 Features of the SuperSTEM instrument

The SuperSTEM consists of a base microscope VG HB 501 FEG STEM with a cold-field emission source. This instrument located at Daresbury laboratory was used for the high resolution imaging and EELS experiments described in this thesis. This is due to its capability to perform imaging and EELS at high energy resolution. The performance of the instrument is dependent on its cold field emission source with an energy spread of 0.3 eV. This reduces the chromatic aberration caused by the energy spread of the source.

SuperSTEM-1 has a spherical aberration corrector fitted to the objective lens which allows the formation of a sub-Angstrom probe. This is essential for characterising materials atom by atom for their chemical geometrical and electronic information. Ultra-high resolution high angle annular dark field (HAADF) imaging combined with atomic resolution EELS is best suited for analysing the dislocation core region in metals. The SuperSTEM operates at 100 kV and requires a thin sample of 20~30 nm thickness with clean surface free from oxides and any possible contamination. The current density is 0.1nA in a 1.0 Angstrom beam which is 10^6 A/cm^2. It is equipped with Gatan Enfina spectrometer with 90^0 magnet prism. It is supported by ultra-high vacuum system with a typical column value of 5 x 10^{-8} mbar and a typical gun vacuum of 3 x 10^{-11} mbar. SuperSTEM is fitted so that it is free of mechanical movement and is sensitive to external vibrations.

3.14 Dislocation core study using SuperSTEM

Dislocation cores are atomic misfit regions generating a lattice strain in the surrounding areas of the crystal. The miniature displacements or (tiny edge components) of the atomic planes in the case of an end-on screw dislocation can collectively produce visible dislocation contrast on the surface and are a remarkable tool to identify the core region. The Eshelby twist masks some of the lattice contrast that can be obtained from a high resolution microscope. Resolving the atomic columns in the HAADF image therefore becomes necessary to identify the core of a screw dislocation. This is the reason why SuperSTEM was chosen as an experimental device that can help studying the dislocation cores. Moreover high resolution electron energy loss spectroscopy is a useful tool to identify the possible transitions involved in Mo and Fe due to excitation process and any changes to the electronic configuration of the

atoms near the core. These reasons justify the use of SuperSTEM for studying the electronic structure at dislocation cores in transition metals.

References:

[1] H. Bethe, Annalen der Physik 397 (1930) 325-400.
[2] M. Inokuti, Reviews of Modern Physics 43 (1971) 297-&.
[3] R. H. Ritchie, Physical Review 106 (1957) 874.
[4] R. F. Egerton, Electron energy-loss spectroscopy in the electron microscope, Plenum Press, New York, 1996.
[5] D. B. Williams, C. B. Carter, Transmission electron microscopy : a textbook for materials science, Plenum, New York ; London, 1996, p. xxvii,729p.
[6] A. H. S. Cottrell, Dislocations and Plastic Flow in Crystals, pp. ix. 223. Clarendon Press: Oxford, 1953, p. 8º.
[7] J. D. Eshelby, A. N. Stroh, Philosophical Magazine 42 (1951) 1401.
[8] P. B. Hirsch, Electron microscopy of thin crystals, Butterworths, London, 1965, p. 558p.
[9] B. G. Mendis, Y. Mishin, C. S. Hartley, K. J. Hemker, Philosophical Magazine 86 (2006) 4607 - 4640.
[10] D. A. Muller, Nat Mater 8 (2009) 263-270.
[11] K. Kimoto, T. Asaka, T. Nagai, M. Saito, Y. Matsui, K. Ishizuka, Nature 450 (2007) 702-704.
[12] D. A. Muller, J. Silcox, Ultramicroscopy 59 (1995) 195-213.
[13] L. J. Allen, S. D. Findlay, M. P. Oxley, C. Witte, N. J. Zaluzec, Ultramicroscopy 106 1001-1011.
[14] R. D. Heidenreich, Fundamentals of Transmission Electron Microscopy. [With illustrations.], pp. xiv. 414. Interscience Publishers: New York, 1964, p. 8º.
[15] A. Bleloch, A. Lupini, Materials Today 7 (2004) 42-48.

Chapter 4

Theoretical simulation methods

Chapter 4

THEORETICAL SIMULATION MEHODS

4.1 Introduction

In this chapter the theoretical simulation methods used to generate theoretical ELNES spectra are presented. The background to different atomistic simulations will be reviewed briefly and the results obtained with different models will be critically discussed. The emphasis is on the theoretical explanation of spectra generated from the software and also on the application based variations. Different formalisms like band structure (BS) and real space multiple scattering (RSMS) methods that are available for atomistic calculations are discussed. Theoretical background of XAS (x-ray absorption structure) is described including the approach taken to calculate EELS from XANES (X-ray absorption near edge structure). Calculations that can be performed using FEFF software are discussed considering the practical aspects required for this research. FEFF is named after the effective scattering amplitude f_{eff} and can calculate effective scattering phase shifts Φ_k, effective scattering amplitudes f_{eff}, structure factor χ (k), and most importantly absorption coefficient μ.

There are advantages and limitations of using multiple scattering calculations in FEFF over other methods. Theoretical spectra are used to observe local electronic changes in the ELNES of various periodic and non-periodic systems including pure metals and complex compounds. Optimisation of parameters like path distance, radius of the cluster and the electronic configuration of Fe-$L_{2,3}$ and Mo-$M_{4,5}$ edges which play an

important role in calculating the fine structure is explained. Important steps taken in EELS data fitting, adjusting for peak broadening and energy shift have also been discussed with respect to theoretical and experimental spectra.

4.2 Atomistic Simulation Methods

A significant number of atomistic calculations have been done to understand the screw dislocation core structure and its behaviour under applied stress. The core configurations and the methods used have been reviewed in Literature Review chapter.

In early years, the atomistic simulations done by using potentials such as Finnis-Sinclair[1] and Johnson[2] have revealed the non-planar nature of the screw dislocation in bcc metals and that the screw dislocation can dissociate into three {110} planes associated with the dislocation line vector. The finite displacements of atoms along the dislocation line when projected onto {111} plane perpendicular to the dislocation line were found to have small components of 1ess than 10 picometres in magnitude[3]. The interatomic potentials like Finnis Sinclair were known to have the limitation for not accounting the bond angle changes at the core and that they represent only the radial force of the interacting atoms. Bond order potentials which consider the bond angle variations have been employed to study dislocation cores[4]. The core was found to be compact in this case while the core dissociated in the case of Finnis-Sinclair potentials. These atomic simulations have shown that the resultant screw core configuration is dependent on the type of potentials used but both agreed that screw cores have the ability to control the low temperature deformation properties in bcc metals.

In this research the co-ordinates which serve as input for theoretical ELNES simulations are obtained from the dislocation cores generated using Mendeleev interatomic potentials. It is also important to briefly discuss the other kinds of EELS modelling methods available in the context of theoretical ELNES simulations.

4.3 EELS simulation methods:

Theoretical simulation of EELS is a good way of understanding the fine structure of materials that is a fingerprint of their electronic states. This is a significant tool in material science because of the option to choose parameters that closely compare with real experiments. A suitable example for this would be the theoretical ELNES study of a well defined cluster of Mo atoms with no carbon edges, but practically carbon contamination is a problem in microscopes. Various simulation methods for EELS simulation are available with their own advantages and limitations but can suit the need for a given problem in material science.

The theoretical approaches widely used for calculating electronic structure are band structure method, multiple scattering approach, molecular orbitals approach, and multiplets method. The band structure is applicable to periodic structures where a repetition of the given unit cell is preferred. Multiple scattering methods are used for a given number of shells (3 to 7 shells) within a definite radius(~5 Å) while molecular orbitals methods become much more precise in defining the local electronic structure with only a few shells (1or 2 shells to a radius ~2Å). Multiplet calculations are generally done for a single atom and its crystal field. Band structure and multiple scattering methods are preferred for metals and semiconductors to study their valences, bonding changes and structure changes in the presence of a defect. The study of dislocation cores, the regions with damaged symmetry, can be done using multiple

scattering calculations since band structure calculates periodic structures with symmetry. Some of the widely used codes to perform band structure calculations are Density Functional Theory (DFT), AB-INIT, CASTEP and WIEN2K. Most multiple scattering calculations are done using FEFF, CONTINUUM and ICXANES. FEFF calculates site-specific symmetry projected local density of states in a crystal with no symmetry. DFT calculations using pseudo-potentials can also be done for extended defects in a large crystal with 100's of atoms but they need intensive computation and time. In the case of a screw dislocation core where the defect does not extend a few atomic shells (although the strain field extends), multiple scattering calculations are the best methods for calculating ELNES. The additional benefit of using multiple scattering calculations using FEFF is that it can take core hole into account while calculating ELNES, although the core hole in metals is screened by valence electrons.

4.4 Multiple Scattering Calculations

Theoretical EELS spectra are calculated to identify near edge structure above the $M_{4,5}$ and $L_{2,3}$ edge threshold for Mo and Fe respectively. These spectra are used to interpret and analyse the local chemical, geometrical and electronic information from a range of few angstroms to an extent of a whole crystal and sometimes as a complete complex compound. The theory and practice of x-ray absorption techniques were used by many to calculate the fine structure from both periodic and non-periodic crystals[5]. Synchrotron experiments were carried out over the years to calculate the fine structure of many metallic and non metallic systems[6]. They are also working to explain the reason for the variations in the near edge structure in transition metals[7]. The work described in this thesis aims to explain the structural changes in the near-edge region of

calculated EEL spectra of transition metals, when they are deformed and contain screw dislocations along <111> dislocation line direction.

4.5 X-ray Absorption Fine Structure

XAFS experiments measure the x-ray absorption spectrum and study the structural information present in the spectrum. A typical XAFS spectrum of most common metals contain sharp peaks that represent the ionisation edges followed by a decreasing wiggly part with an increasing energy scale in eV. Given below is an example of copper metal data that has been taken from the reference provided with the FEFF software[8]. The wiggly part contains wealth of information about detailed electronic, geometric and vibrational characteristics of each individual material in the crystal with their unique signature. This is the reason why most x-ray absorption experiments are followed by a careful examination of this well defined structural region. This region of interest in the x-ray absorption spectrum has been classified into two well known and theoretically explainable parts known as XANES (x-ray absorption near edge structure) and EXAFS (extended x-ray absorption fine structure).

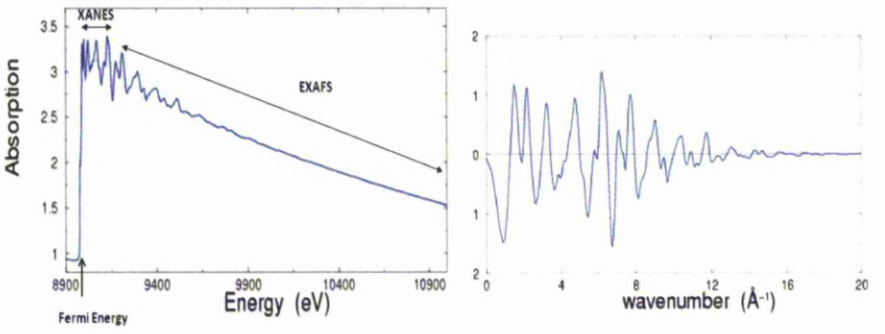

Fig 4.1 (Left) Typical x-ray absorption spectrum for Cu metal K-edge. (Right) Wiggly part which contains the structural information, where fine structure is plotted as a function of wave number.

X-ray absorption process defines the various regions observed in the x-ray absorption spectrum. The next section describes x-ray absorption, scattering and physical formalism of the involved processes.

4.6 X-ray absorption process:

When an x-ray of energy E is absorbed by a free atom, it may destroy a core electron with energy E_0 and emit a photo-electron of kinetic energy ($E-E_0$). The life time for the core hole being short and finite, it can be said that this state does not exist long and gets filled quickly which initiates the release of a fluorescent x-ray or an Auger electron. In other words, absorption is promoted by the availability of an empty final state.

The amount of x-ray energy can be influential in increasing the probability of promoting the core electron to a continuum eventually leading to a sharp increase in absorption. The physical process can also be said as the excitation of core electrons to the continuum states or high-energy requiring unfilled states. This excitation of deep core electrons above their binding energy accompanying the absorption of photons from the source can be measured as a function of energy. This is the x-ray absorption spectrum μ (E), which contains sharp steps at the core level binding energy followed by a declining smooth function of energy above the edge. Figure 4.2 shows the core level electron excitation process and subsequent events arising from it.

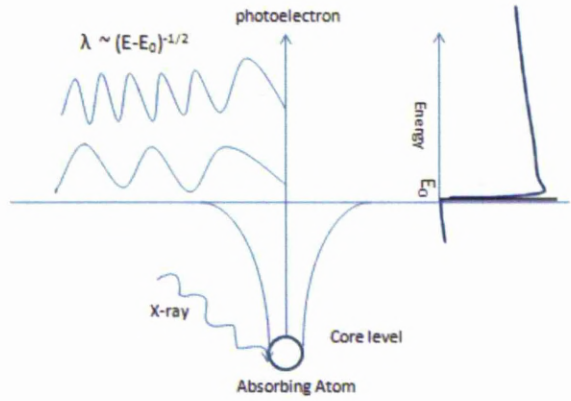

Fig 4.2 X-ray absorption process and XAFS spectrum

The sharp step in an experimental data can be broadened by instrument resolution and the life time of the core hole. The oscillatory fine structure (XAFS) is the contribution from XANES and EXAFS. The extended region which is about 50 to 2000 eV above absorption edge is the EXAFS region and provides information about the local geometry like the periodicity of the atoms in the crystal, distance to the nearest neighbours and their orientation[9]. XANES region (0- 50eV above the edge) consists of information about the free energy states above the Fermi level and the local electronic structure information like density of states (DOS). The electronic configuration data as well as spin and orbital momentum information can be deduced by carefully analysing this region. This region is of importance to this project as it can give detailed information about the fully unoccupied states with in a localised region; say from a few atoms in the cluster of definite radius. Knowledge of these occupied states will help the calculation of remaining occupied states from ℓ-DOS and vice versa. This can eventually predict the d-band transitions that are occurring in the transition metal samples due to core electron excitations at chosen energy edges. Comparison of transitions between a pure transition metal and those from a dislocation core region

in that transition metal will give detailed information about the electronic structural dependence of bulk properties in transition metals. The dependence of flow stress on the presence of screw dislocations and the effect of core symmetry on the properties of transition metals as a whole can be interestingly investigated with this approach.

4.7 Interpretation of XAS:

XAS process can be simplified for understanding in two processes. The first is the propagation of excited electron wave through the crystal and then getting scattered by the neighbouring atoms on its exit path. The second is the interference between the exiting excited-electron wave and the backscattered waves from the neighbouring atoms. The constructive or destructive interference caused due to variation in amplitudes of reflecting electron waves will be responsible for the strength of the transition between initial and final states.

This EXAFS process is explained by *J.J. Rehr* and *R.C. Albers* in their paper, as similar to waves in a pond of water being propagated when a central source of propagation was created, like throwing a stone in still water and when these propagating waves reach an obstacle on their way they get reflected, causing interference between outwardly propagating waves and reflected waves from obstacle[9]. A better description of the EXAFS process is shown in figure 4.3.

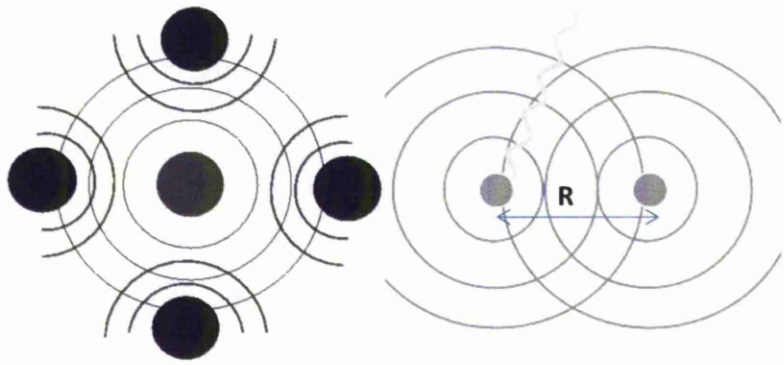

Fig 4.3 Pictorial description of EXAFS process; Interference between propagating and scattered electron waves.

Interatomic distance R can vary the total inelastic mean free path, λ, of the scattering waves significantly, leading to a phase shift and allowing for interference to occur between propagating and scattered electron waves. This interference is qualitatively interpreted to be the reason for the oscillatory fine structure in the x-ray absorption spectrum. Semi-quantitative agreement of XANES data from experiments with theoretical calculations have led to the development of an *ab initio* code FEFF8 intended for interpretation of XANES in terms of DOS. The theory of x-ray absorption formalism and XANES with equations will be discussed in the next section.

4.8 Theoretical Background:

4.8.1 Fermi's Golden Rule and Green's Function:

Fundamental multiple scattering (MS) theory of XAS is well established with published results (Rehr&Albers, 2000) using different approaches[9]. It is given by the Fermi's golden rule:

$$\tilde{\mu}(E) \propto \Sigma_f |\langle f|\hat{\boldsymbol{\epsilon}}\cdot\mathbf{r}|i\rangle|^2 \delta(E-E_f) \qquad (4.1)$$

The above equation explains the dipole-mediated transition of an electron in the core state $|i\rangle$ into an unoccupied state $|f\rangle$ due to the interaction between the incident photon and the core-state electron. $\hat{\boldsymbol{\epsilon}}$ is the polarisation vector of the incident electromagnetic field. $\tilde{\mu}(E)$ is the x-ray absorption coefficient which will provide information about the interaction and the resultant inelastic losses. Equation 4.1 is solved by using multiple scattering theory and Green's functions based on propagator formalism. This approach using Green's function is given by:

$$\mu(E) \propto -\frac{1}{\pi} \operatorname{Im} \langle i|\hat{\epsilon}^* \cdot r\, \mathbb{G}(r, r'; E)\hat{\epsilon} \cdot r'|i\rangle \Theta(E - E_F) \qquad (4.2)$$

This forms the basis for multiple scattering theory and the computation of Green's function will have to be done in order to predict the fine structure.

The theoretical calculations of fine structure are based on dipole approximation and the Fermi's Golden rule being limited to one electron approximation. The final-state rule is assumed to be true for these calculations, where the final states are calculated in the presence or absence of a core hole. Ionisation edges such as M_4 or M_5 and transition metals like Fe in particular are believed to show better adherence with experimental data when they are calculated as if the effect of core-hole is negligible[10, 11].

4.8.2 RSMS formalism and FEFF function

The approach taken for calculations in XAFS theory is often referred to as real space multiple scattering (RSMS) formalism or real space Green's function (RSGF) formalism. Band structure methods often tend to calculate the final states explicitly and are very computationally intensive. Moreover, the final states calculations are done efficiently for

highly symmetric systems like crystalline materials and periodic molecules. However when system like a dislocated crystal is considered they often tend to be ineffective in calculating the final states and particularly in the case of a transition metals where the final states have contribution of possible transitions. Using Green's function formalism, the x-ray absorption coefficient μ can be expressed in terms of a propagator in real space, as shown in equation 4.2. The term $\hat{\varepsilon}$ is the polarisation vector, while $\mathbb{G}(r, r'; E)$ is the propagator term which can be shown as the sum of different contributions from the environment through which the electron propagates.

Using the equation 4.2, absorption coefficient μ can be expressed as,

$$\mu = \mu_0(1 + \chi) \tag{4.3}$$

Where μ_0 is the atomic background and χ is the multiple scattering signal. χ gives the fine structure changes with respect to the atomic background and is commonly known as structure factor. This can be understood by rearranging the terms in equation 4.3 into,

$$\chi = (\mu - \mu_0)/\Delta\mu_0 \tag{4.4}$$

where $\Delta\mu_0$ is the jump in the smooth atomic-like background absorption which also includes the contribution from other nearby edges. It is the normalized value of total atomic background absorption at the primary edge for which the calculations are done. Fine structure is generally described as the sum of scattering contributions from all multiple scattering paths with in the radius of the atomic cluster. This can be generally expressed by the following equation:

$$\chi(k) = S_0^2 \sum_R \frac{|f_{\text{eff}}(k)|}{kR^2} \sin(2kR + \Phi_k) \exp(-2R/\lambda_k) \exp(-2\sigma^2 k^2) \tag{4.5}$$

Equation 4.5 which indicates scattering matrix formalism, calculates the effective scattering amplitude $f_{eff}(k)$ for curved wave calculations using the Green's function ideology of propagator G(E) and the resultant scattering. The important terms in the equation include amplitude reduction factor S_0^2, attributed to many-body effects, Φ_k the phase-shift, λ_k, the mean free path of the incident electromagnetic radiation, σ, the r.m.s variation in the effective path length or bond length R= $R_{path}/2$, and $k = [2(E - E_0)]^{1/2}$, the wave number measured from the threshold energy E_0. The term $\exp(-2\sigma^2 k^2)$ describes the Debye-Waller factors which include the dependence of the structural changes in the spectra to the temperature and disorder (for example, aperiodic systems and amorphous materials). The exponential term $\exp(-2R/\lambda_k)$, is the damping factor r, which indicates the finite life time of the photoelectron including core-hole life time.

In this research, ELNES spectra from atomic cluster with screw dislocation is being calculated and considering the similarity between XANES and ELNES spectra (which will be discussed in next section), the factors included for calculation of XANES spectra are generally applicable to the calculation of ELNES spectra. Debye-Waller factors [since $k^2 << 1/(\sigma^2)$ and constant T] contribution is negligible for XANES and the core-hole life time contribution to the XANES is considered not to a great extent for this research work, owing to the fact that the metals being considered are transition metals Mo and Fe and the energy edges being Mo-$M_{4,5}$ and Fe-$L_{2,3}$.

4.8.3 Application of FEFF for EELS

FEFF program was generally used for calculating x-ray absorption spectra. With the similarity of processes involved in the calculation of x-

ray and EEL spectra, updated versions of FEFF are being designed to include capability of generating EELS directly[7]. However, it is essential to understand the physics in relative terms to justify the application of FEFF for generating EELS. It also helps to recognise the importance of comparing experimental EELS to theoretical spectra produced by FEFF.

Fermi's golden rule is used again but now in terms of electrons as a starting point to identify the similarity between x-ray absorption spectra and EEL spectra. So, core-level electron energy loss spectra are given by Fermi's golden rule as:

$$\frac{\mathrm{d}^2\sigma}{\mathrm{d}\Omega\,\mathrm{d}\omega} = 4\gamma^2 a_0^{-2} q^{-4} \frac{k'}{k} S(q,\omega) \qquad (4.6)[12]$$

$$S(q,\omega) = \sum_f |\langle f|e^{iq\cdot r}|i\rangle|^2 \delta(\omega + E_i - E_f) \qquad (4.7)[12]$$

The term on the left hand side in equation 4.6 is the double differential scattering cross section with respect to scattering angle Ω, and energy loss ω, where $\gamma = 1/(1-\upsilon^2/c^2)^{1/2}$, υ is the incident velocity, $a_0 = 52.92 \times 10^{-12}$ m is the Bohr radius, q is the momentum transfer, (k'/k) is the ratio of wave vectors of the fast electron after and before scattering and is generally taken as unity. In the equation 4.7, the term $S(q, \omega)$ is the dynamic structure factor where $q.r$ is the dipole operator. Low q excitations often tend to account greatly to electron scattering cross section and hence the exponential term can be replaced by the dipole operator[13]. FEFF computational techniques can be used for both EELS and XAS since the formulation of XAS is analogous to EELS as shown by the above equations.

The x-ray absorption cross section in terms of structure factor according to FEFF is given by the following equation:

$$\mu(\varepsilon, \omega) = \frac{e^2}{4c\varepsilon_0} S(\varepsilon, \omega) \qquad (4.8)[12]$$

Comparing the equations 4.8 and 4.6, and deducing for the terms ϵ and **q**, the EEL spectra can be generated by multiplying the output x-ray absorption coefficient $\mu(E)$ and $\chi(k)$ of XAS with a factor f, given by:

$$f = 4\frac{\gamma^2}{a_0^2}\frac{k_f}{k_i}\frac{4c\varepsilon_0}{e^2} q^{-p}\omega^{-1} \qquad (4.9)[12]$$

Most of the terms in the equation 4.9 are already described before and their values given. The value of p will be 2 for dipole terms and 0 for quadrupole terms. Energy loss (ω) and impulse transfer are interesting terms in this equation and can be useful while doing analysis of the generated spectra. Energy loss factor helps compositional analysis when the cluster is a complex molecule with different individual atoms whose edges vary over wide range of energies. Impulse transfer (q) is dependent upon scattering angle and is helpful while calculating cross sections as a function of scattering angle[12]. Thus choosing the parameters effectively, theoretical EEL spectra can be generated and used for direct comparison with experimental spectra.

4.9 Scattering Paths and Multiple Scattering theory

Scattering paths represent the path taken by a photoelectron propagating out of the central atom, undergoing scattering by the nearest neighbouring atoms and then propagating back to the central atom. A scattering event includes the representation of all the paths that could be taken by the photoelectron before returning to the central atom. Multiple

scattering theories used for the calculation of XANES arise from the sum of the contribution of all such scattering events.

There are different ways of describing a scattering event. A scattering event can include either a single possible path that the propagating photoelectron could take or multiple possible paths before returning to the central atom. The following diagrams will explain different ways of scattering that can happen in a lattice and different individual scattering paths.

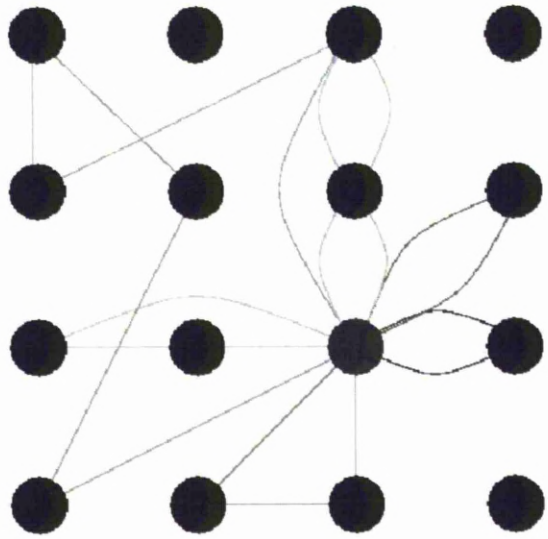

Fig.4.4 Multiple scattering in a lattice with single and multiple scattering paths originating from central atom (light), propagating to nearest neighbour atoms (dark), getting scattered and returning to central atom.

Fig.4.5. Single, double and triple scattering paths.

A single scattering path is similar to one scattering event in a single shell. A leg is the path between two atoms, so a single scattering event contains 2 legs; a double scattering event has 3 legs and so on.

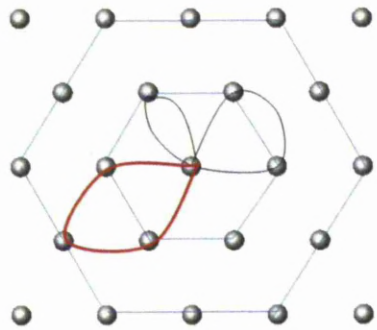

Fig. 4.6 Multiple scattering in a perfect bcc lattice in [111] direction with 2 shells of atoms showing single, double and triple scattering paths.

The full spectrum χ (k), defined by multiple scattering formalism is simply a sum of all the scattering paths and is given by:

$$\chi(k) = \sum_{\Gamma} \chi_{\Gamma}(k) \tag{4.6}$$

where $\chi_{\Gamma}(k)$ is the contribution computed from an individual scattering path and r may denote a single scattering path or a multiple scattering path of any order. The equation 4.5 is calculated for a given cluster of atoms with in a definite radius and all the essential parameters provided

as input, by an *ab initio* code known as FEFF. Finally, it fits these parameters into the equation 4.5 and calculates the x-ray absorption fine structure (XAFS) χ (E), local density of states ρ(E) and near edge spectra (XANES) μ(E), for that given cluster.

4.10 FEFF Program

FEFF is an *ab initio* code for simultaneous calculations of x-ray absorption spectra, electron energy loss spectra and electronic structure based on self consistent real space multiple-scattering formalism[14]. It permits the interpretation of the spectra in terms of structural and electronic properties of a material. FEFF8.4 is used for calculation of spectra in this thesis. Self consistent potentials are used and iteratively run for achieving convergence before full multiple scattering (FMS) calculations are done for the given cluster of atoms. The output from the calculations include XANES, LDOS and EELS (with additional calculations) spectra. The advantage of using FEFF8.4 is that it includes polarization dependence, core-hole effects, local field corrections, and does not require any crystal symmetry. FEFF is written in ANSI Fortran77, and typically requires a memory (RAM) of 500Mb for XANES calculations with a cluster of 100 atoms[15].

Apart from XANES μ (E) which can be used to calculate EELS spectra, FEFF8.4 calculates real space, site-specific, symmetry projected local density of states which will help identify the electronic configuration which affects the structure in the spectrum.

4.11 Features of FEFF

FEFF8.4 program is written with almost all complex parameters already included and is mostly parameter-free while the source code can also be

changed if needed to include any additional parameters like spin-dependence and the size of the cluster. Additional changes like Fermi energy E_f corrections, experimental broadening and Debye-Waller factors can be included as required. FEFF uses a self consistent field approach to electronic structure calculations. In this context, it is important to describe the self consistent approach.

FEFF starts calculating the potentials of free atoms ρ_0 (E) for each atom type as specified in the input file, using relativistic Dirac-Fock atom code considering as if the atoms are isolated in space[16].These potential calculations are iterated until the potentials function ρ(E) stops changing in value. The following equation explains the process of the self-consistency approach in calculating potentials and determining accurate Fermi energy:

$$\rho_\ell(E) = \rho_{0,\ell}(E)\left(1 + \chi_\ell(E)\right) \text{ where } \{l = 0,1,2,3..\} \qquad (4.7)$$

Once the above function achieves consistency in values, the iterations are finished and the final function ρ(E) is then integrated in energy. This integral will determine the Fermi energy and the charge transfer among the cluster of atoms. The energy where this integral equals the total number of valence electrons among the free atoms in the cluster is reported as the Fermi energy (with core-hole by default). The flow chart indicating the iterative procedure for achieving self consistent potentials is shown in figure 4.7.

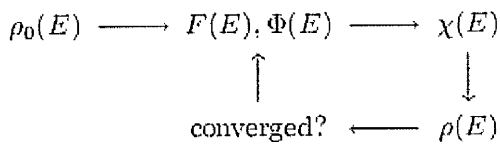

Figure 4.7 Flow chart of self-consistency iterative procedure.

For most systems, the Fermi energy is accurately estimated in both cases of the presence a core-hole and without a core-hole. This removes the necessity of fitting Fermi energy to an accurate energy scale, an important parameter that needs to be correct for the calculation of density of states without error. Moreover, the atomic configurations of most elements (Z<99) and their core-hole life times are included in the FEFF program by default, which increases the ease of use while calculating disordered structures with vacancies, dopants, or complex systems like molecules or metallic oxides. The electron mean free paths, self energy shifts, life-time contributions are all calculated automatically by FEFF using built-in atomic configurations and core-hole life times. The self consistency loop is important to make sure the calculations are correct and the convergence must be examined after every FEFF calculation.

4.12 Advantages and limitations of FEFF program

To summarise the features, FEFF can be used to calculate both electron energy loss and x-ray absorption spectra to interpret local electronic structure. It can be used to calculate XAFS, XANES, EELS, ELNES, EXELFS by full multiple scattering calculations and local projected density of states LDOS. FEFF can be altered to account for spin dependence in the calculation of spectra from magnetic materials like bcc iron. It is widely used for non-periodic systems like materials with defects and interfaces. It takes care of core-hole effects, instrumental broadening, Fermi energy and matches to experimental accuracy[9]. High spatial and energy resolution experimental spectra (ex: ELNES with 0.1 eV) acquired with aberration corrected sub-angstrom probe can take the comparisons between FEFF spectra and experimental spectra to a much better precision, for the spectra can be compared to angstrom level and hence are more interpretable than ever.

Although FEFF can calculate electronic structure to a good agreement with experimental data, it does have its own limitations. While EEL spectra include both low loss and core losses, FEFF can generate spectra limited to core level spectra above 10eV. The other limitation is that it cannot handle any fractional occupancy of atomic positions. Furthermore, it needs high computing power depending upon the cluster size. The various aspects of electron energy loss calculations using FEFF8 program and the key parameters used in those calculations are described in chapter 6. The results from theoretical ELNES simulations are presented in chapter7.

References:

[1] M. S. Duesbery, V. Vitek, Acta Materialia 46 (1998) 1481-1492.
[2] F. R. N. Nabarro, M. S. Duesbery, J. P. Hirth, Dislocations in solids v. 8, Amsterdam ; Oxford, 1989, p. 67
[3] B. G. Mendis, Y. Mishin, C. S. Hartley, K. J. Hemker, Philosophical Magazine 86 (2006) 4607 - 4640.
[4] V. Vitek, Philosophical Magazine 84 (2004) 415-428.
[5] E. D. Crozier, J. J. Rehr, R. Ingalls, X-ray absorption : principles, applications, techniques of exafs, sexafs and xanes, Wiley, New York, 1988, p. 375-384pp.
[6] A. P. Kaduwela, D. J. Friedman, C. S. Fadley, Journal of Electron Spectroscopy and Related Phenomena 57 (1991) 223-278.
[7] P. Rez, D. A. Muller, Annual Review of Materials Research 38 (2008) 535-558.
[8] B. Ravel, http://feff.phys.washington.edu/~ravel/, in: 2004.
[9] J. J. Rehr, R. C. Albers, Reviews of Modern Physics 72 (2000) 621.
[10] J. J. Rehr, A. L. Ankudinov, Coordination Chemistry Reviews 249 (2005) 131-140.
[11] S. Alam, J. Ahmed, Y. Matsui, Applied Surface Science 241 (2005) 199-204.
[12] A. L. Ankudinov, B. Ravel, J. J. Rehr, S. D. Conradson, Physical Review B 58 (1998) 7565.
[13] M. S. Moreno, K. Jorissen, J. J. Rehr, Micron 38 (2007) 1-11.
[14] FEFF, FEFF wiki: http://leonardo.phys.washington.edu/feff/wiki in: 2009.
[15] A. L. Ankudinov, C. E. Bouldin, J. J. Rehr, J. Sims, H. Hung, Physical Review B 65 (2002) 104107.
[16] FEFFTeam, FEFF8.4 User's Guide (provided with FEFF software), in: 2006.

Chapter 5

Experimental Techniques

Chapter 5

EXPERIMENTAL TECHNIQUES

In this chapter, sample preparation techniques used for making thin foil specimens for electron microscopy will be presented. Electron microscopy techniques used for analysing thin specimens in TEM and SuperSTEM will be discussed with relevant examples and figures where necessary.

The samples studied for the work presented in this thesis are high purity molybdenum and iron. The samples used for the initial work with TEM were polycrystalline while the later work with TEM and SuperSTEM include single crystal samples of molybdenum and iron.

5.1 Molybdenum sample preparation

Two types of material are used for the work described in this thesis.

1. Pure polycrystalline molybdenum.

2. Highly pure single crystal molybdenum.

5.1.1 Initial preparation

Polycrystalline molybdenum samples were prepared from thin metal foils provided by ADVENT RESEARCH MATERIALS®, based in Oxford, UK. Single crystal samples are grown specifically with an ultra high purity of 99.99% and are deformed under low temperatures (~ 40^0C) at high strain rates (compressed 10% along [-2 9 20] at 480/sec) using a Hopkinson bar for the generation of screw dislocations in <111> directions. The single crystal Mo was deformed at Lawrence Livermore

National Laboratory, University of California and supplied by John Hopkins University, Baltimore, U.S. This method was chosen for the reason that orientation-dependent deformation at low temperatures and high strain rates is a preferred way of generating screw dislocations in a pure single crystal molybdenum[1]. The single crystal sample is carefully cut by a thin diamond wafer blade, into two sections of large area with their surface perpendicular to a <111> direction. This is to ensure that the sample has screw dislocations end-on to the surface. The following figure shows the sectioning direction of the crystal and the screw dislocation line direction.

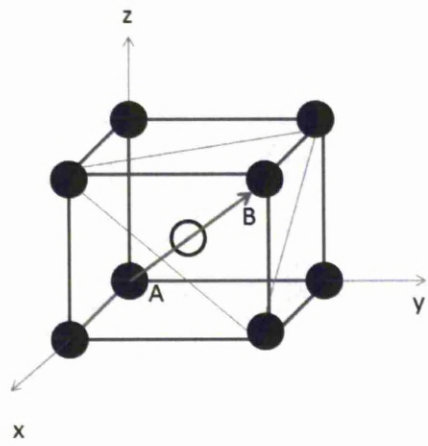

Figure5.1 $\bar{AB}$ is the <111> screw dislocation line direction; Sectioning of the samples is done so that sectioned surface is perpendicular to AB.

The sectioned bulk single crystal is further cut into thin foils of thickness 1mm using a slow speed cutting machine with a circular copper blade impregnated with diamond particles over its edge. The cutting speed is typically 200 rpm and the sample is cut for such a thickness that the damage done by cutting (~ 200μm) has to be added to the intended thickness of the sectioned specimen. This allows the damaged region to be removed first while grinding and polishing and preserves the deeper areas

of the specimen. A sectioned sample of 1 mm thickness might have 200μm of damage on either side below surface[2]. Once these foils are cut with required thickness, they are used the same way as any other thin foil for punching 3mm disc.

Polycrystalline and single crystal thin samples of 3mm diameter and 1 mm thickness are prepared from thin foils by mechanical punching using a disc punch. The disc punch can introduce deformation effects such as twinning if not used properly and hence care is taken by ensuring that the edges of the punch are sharp and the foil is supported with a soft material (couple of rubber O rings) underneath it. This is important because the sample might be affected by the deformation introduced by mechanical punching if proper care is not taken.

A hole is made at the centre of the disc in the final steps of sample preparation by electropolishing and is discussed in the next sections. Since electropolishing removes only the central region of the disc by chemical attack, no major mechanical deformation is introduced in the areas that are to be observed in the electron microscope. The sample cutting was done carefully so that the extent of deformation experienced by the sample is kept to a minimum.

It is important to know the composition of the bulk samples that are being sectioned into thin foils because the atomic level resolution EELS obtained from SuperSTEM can be affected by the presence of impurities in the core region of the dislocation. It is often reported that the dislocation cores serve as regions for segregation of lighter elements like carbon, hydrogen and nitrogen. These are called Cottrell atmospheres[3]. Hence the bulk sample materials are chosen such that they are of high purity (99.99%). The typical compositional analysis data (in ppm) for a polycrystalline molybdenum sample as provided by the company is given in Table 5.1.

Mo	C	Al, Ca, Cr, Cu, Fe, Mg, Mn, Ni, Pb, Si, Sn, Ti
99.95%	<20 ppm	<10 ppm per each element

Table5.1 Typical composition of elements in polycrystalline Mo sample.

5.1.2 Mechanical Grinding

In this research, all TEM and SuperSTEM samples of molybdenum were prepared as thin foils of 3mm diameter as described above, followed by subsequent thinning techniques involving mechanical grinding and electropolishing.

Samples punched as discs of 3mm diameter and 1mm thickness were mounted onto a grinding rig with the damaged surface open for grinding. The grinding rig was heated on a hotplate to about 110^0C for about 5 minutes, removed from the hot plate and transparent wax was melted onto it. The samples were placed on the surface of the molten wax, levelled using a plain glass slide and left for the wax to cool and set. Once the wax was set, the specimens got firmly embedded in wax and were strong enough to resist mechanical vibrations during grinding. The set samples were then mechanically ground from 1200 through to 4000 grit SiC paper for removing any surface oxides, damage and roughness.

When a fine finish was observed, the samples were washed with ethanol and examined in an optical microscope for surface roughness and measured for thickness. The samples were then polished on a fine polishing wheel from 5μ through to 1μ following standard metallographic polishing technique. Once the surface was shiny and scratch-free, the samples were soaked in acetone, turned onto other surface, stuck onto the rig with wax and mechanically ground and polished to a fine level of 1μ

and to a final thickness of 20μm. The fine-polished specimens were removed off the rig by soaking them in acetone, cleaned in ethanol and were finally thinned using twin jet electropolishing equipment.

5.1.3 Electropolishing

Electropolishing removes the surface layers of the sample, reduces the thickness uniformly and polishes the surface without causing mechanical deformation. The removal of metal from the surface is caused by slow dissolution of the metal when the sample is used as an anode and placed in an electrolytic solution operated under suitable conditions. Throughout this research, Struer's Tenupol Twin jet electropolishing equipment was used to electropolish molybdenum samples. Finely polished samples were carefully placed in the Twin Jet holder and the holder is placed in the electropolisher containing 12% sulphuric acid in methanol. Standard risk assessment and safety methods were followed during experiments with chemicals. Sulphuric acid is exothermic, corrosive and can damage skin or eyes upon contact. Care was taken not to contact any acids or harmful chemicals. The electrolytes used for electropolishing were prepared always by mixing acid slowly into methanol under continuous stirring. Liquid nitrogen was used to cool the electrolytes and care was taken while handling and disposal. Fume cupboards were always used during electropolishing to let the acidic fumes and nitrogen escape while working with them. Used electrolytes were always neutralised before disposal.

Sample	Electrolyte	Temperature	Voltage	Flow rate
Pure molybdenum	12% H_2SO_4 in methanol	-5 to -10°C	8 Volts	40 ml/min

Table5.2 Operating conditions used for electropolishing Mo samples.

Electropolishing creates thick viscous layer on the specimen surface and is responsible for removing large surface irregularities. A thin layer is formed under the thick layer which polishes the surface of the specimen to a finer scale and helps attain a lustrous and smooth surface finish. These layers are mainly controlled by the above parameters and the polishing time is dependent on the thickness of the sample. A molybdenum sample of 1mm thickness takes approximately four minutes to electropolish while a sample with 30μm thickness takes about a minute.

Very thin samples are prone to bend and curl during electropolishing due to the flow rate and such polished samples have a profile with sharp thickness change. The electropolisher is equipped with a sensor that measures the light from a laser which passes through the tiny hole created in the specimen and instructs the process to stop once a set transmitted light intensity is reached. This helps the creation of uniform thin areas with a tiny hole in the centre of the specimen.

The molybdenum samples were electropolished using the optimised parameters as given in table 5.3 to obtain thin shiny samples with a tiny hole in the centre. Care was taken to avoid surface deposits and creation of oxide layers on the polished sample. The polished samples were stored in membrane boxes placed in nitrogen-purged desiccators before being transferred to TEM or SuperSTEM.

Molybdenum samples can easily form oxides (MoO_3) when in contact with atmospheric oxygen and so polished samples were immediately used in TEM in order to obtain better results avoiding the problem of molybdenum oxidation.

The above discussed specimen preparation for molybdenum is shown as a process flow chart in figure 5.2.

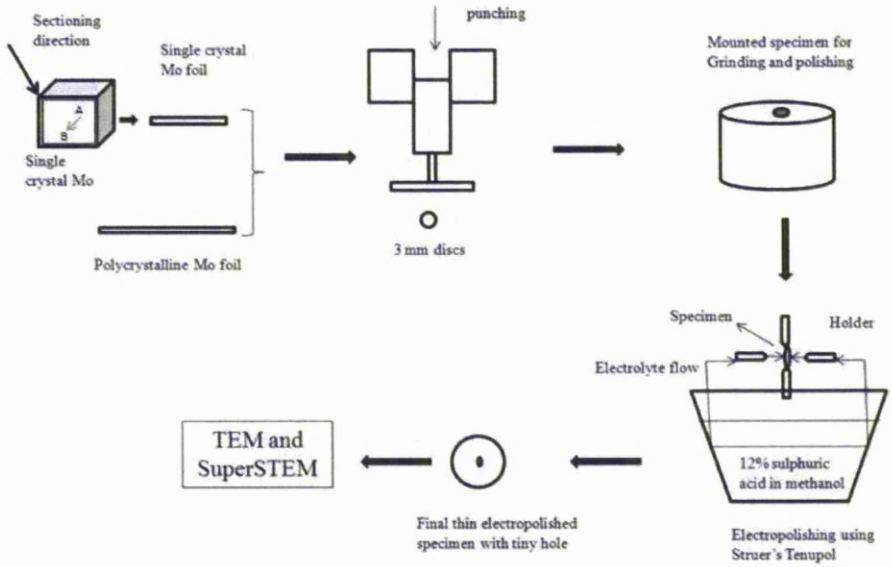

Figure 5.2 Schematic diagram of sample preparation techniques for molybdenum

5.1.4 Electropolishing results

The effect of electropolishing on the samples was studied when the samples were prepared by different electropolishing recipes. This was an important aspect taken into account since this research was involved with atomic resolution imaging and EELS. The chemical effect of electrolytes on the sample was an important consideration that could affect the results in this research work.

For example, if the EELS results were reporting the contribution of another element to the spectrum, they had to be confirmed by performing multiple EELS from other similar areas of the sample. If the contribution was confirmed by the EELS from other areas, then two questions had to be answered.

1. What was the effect of surface layers (like thin layer of oxide) to the overall EELS spectrum?

2. Where and how much in proportion was the contributing element present in the sample?

The possibility of answering the first question lies in the EELS spectrum itself. Careful EELS analysis by quantification would answer the first question. The second question if answered would confirm that the contributing elements were present in the bulk sample and were not from the surface layers or from other types of contamination. Hence it was important to prepare the samples with no surface contamination and this meant the use of appropriate electrolyte with optimised characteristics.

Initially polycrystalline samples punched out of the thin Mo foil were electropolished using 15% nitric acid in water in twin jet electropolishing equipment. Many samples were prepared with different values of parameters like voltage, temperature and flow rates. Their effect on the sample was assessed for the purpose of optimisation.

The samples electropolished by this electrolyte when observed in the TEM were found to have a strange texture on the surface. It was often observed in these samples that the electrolyte had deposited colonies of contaminants on the surface. The EELS from these samples often reported the existence of oxygen K edge at 532eV. The possibility for this could be that the surface of the sample was oxidised just after electropolishing. It has to be noted here that the samples were examined in the microscope within 2 days of sample preparation and stored in nitrogen purged desiccators avoiding contact with atmospheric oxygen that could lead to oxidation. Since the samples were also polycrystalline there were more favourable places in the sample like grain boundaries for enhanced oxidation. These samples were discarded due to contaminants and oxides over their surface. Therefore the electrolyte used for

electropolishing Mo samples was changed from 15% nitric acid in water to 12% sulphuric acid in methanol.

12% H_2SO_4 in methanol worked well with molybdenum samples as the surface finish was found to be much better with no contamination or oxidation. Hence this was used for both polycrystalline and single crystal Mo samples. The ELNES from molybdenum $M_{4,5}$ and $M_{2,3}$ edges were clearly visible than before and the contribution from oxygen has reduced to almost negligible extent. This was an important step in the research work that helped better EELS statistics. The optimised parameter values for the two types of electrolytes used in this research were shown in the table 5.3.

Sample	Mo (polycrystalline)	Mo (polycrystalline)	Mo (111 single crystal)
Electrolyte	15% HNO_3 in water	12% H_2SO_4 in Methanol	12% H_2SO_4 in Methanol
Voltage(V)	21.0	8.0	20.5
Current (mA)	270 - 300	45-65	220-240
Temperature(°C)	-5 to 0	-9 to -5	-5 to 0
flowrate (ml/sec)	25	40	38
Polishing time (min)	1 -2	6-8	≤1

Table 5.3 Optimised electropolishing characteristics of different samples

These parameters were important to obtain right surface finish and to ensure that the sample does not oxidise.

In general the following observations were helpful for optimisation. High voltage reduced the electropolishing time but the samples were heavily oxidised. The oxidation of the sample was identified by the change in surface colour from metallic to light blue. Increased flow rate reduced the current and hence increased the time for completion. When examined in TEM, samples prepared with high flow rate often revealed curly edges near the hole. Temperatures above 0° C would cause nasty surface with the hole created at the edge of the sample. Subzero temperatures were

often the key characteristic in the preparation of contaminant free Mo samples with shiny surface and tiny hole in the centre.

5.2 Iron Sample preparation

Two types of iron samples were investigated in this research work. The two samples were magnetic (bcc) iron, but one was polycrystalline and the other was [111] single crystal. The samples were checked with a magnet before they were prepared into thin specimens in order to estimate the direction of the magnetic field of the sample. They were then prepared into thin samples by techniques described in the following sections of this chapter.

The polycrystalline iron samples were prepared from 99.95% pure, annealed iron foils of 1 mm thickness. The impurities known from the information provided by the supplier were mainly carbon ($\leq$20ppm), copper (< 10ppm), chromium (< 8ppm), and manganese (<10ppm). Fe single crystal was specially grown in [111] direction and was highly pure with 99.99% purity. The impurities information however was not provided by the supplier of iron single crystal. Polycrystalline Fe samples were discarded for EELS analysis due to their relatively high impurities, random grain orientation, less probability of finding screw dislocations and easy formation of oxide layers on the surface.

Iron samples analysed in SuperSTEM were prepared from bcc Fe single crystal grown in <111> orientation. It was supplied by Metals and Oxides Ltd®, Cambridge, U.K. and was of ultra high purity (99.99%). Due to the magnetic nature of α-iron, the volume of iron in the final samples was reduced to a minimum. The problem of sample magnetism in the electron microscopes was discussed earlier in chapter 3.

5.2.1 Initial preparation

In order to reduce the effect of magnetic field from iron sample on the electron beam, the single crystal was chosen to be only 1mm in diameter and 1cm length. The iron single crystal was embedded in a hollow non-magnetic austenitic stainless steel tube of 3mm outer diameter, 1.03 mm inner diameter and 1.5 cm in length by brushing it with epoxy resin. Care was taken to allow the metals to be in contact for conduction, which is necessary for controlling charging of the specimen in the microscope.

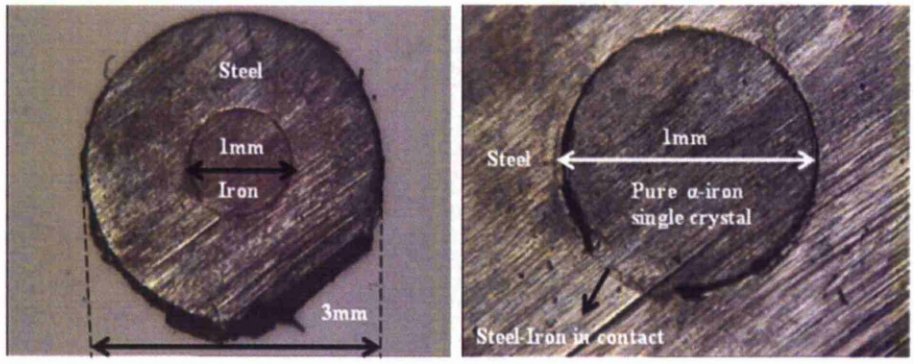

Figure5.3 Optical microscope images of embedded iron samples in steel at 5X and 20X magnification.

The epoxy was allowed to set and the sample material at this stage was a non-magnetic steel tube on the outside and magnetic iron in the inside stuck with epoxy resin. The steel tube and the iron crystal inside were checked for conduction and then sliced into thin discs using a diamond wafer blade in a slow speed cutting machine. The samples were then ground and polished by the procedure as described in section 5.12 to a fine polish size of 1 μ.

The sample thickness was measured between the successive grinding and polishing steps to ensure that both metals were being removed at a moderate level. Since the sample contains two metals with different

hardness values, the rate of removal of each metal can be different. Therefore it is necessary to check the sample for thickness at regular intervals while grinding and polishing.

5.2.2 Problem with electropolishing embedded iron sample

6% perchloric acid in methanol was used as an electrolyte and a low temperature of -60° C was maintained throughout the electropolishing process. The operating voltage was 8 and the flow rate 40 ml/min. The samples were then cleaned in methanol at -60° C to avoid thermal variation from a cold electrolyte bath to room temperature which might enhance the formation of iron oxides on the surface. The samples were then left in room temperature methanol for a few seconds followed by ethanol. The electropolished samples were stored in anhydrous ethanol for further use. The electropolished samples prepared by this process were not good enough to be used in SuperSTEM for high resolution imaging and EELS.

Sample	Electrolyte	Temperature	Voltage	Flow rate
Pure iron	6% perchloric acid + 94% methanol	-55 to -60°C	8 Volts	40 ml/min

Table5.2. Optimum operating conditions used for electropolishing Fe samples.

Electropolishing of finely polished iron samples embedded in austenitic steel did not offer much success with the twin jet electropolisher. It was observed that the samples were attacked by the electrolyte near the contact region between iron and steel during electropolishing. As a consequence, the hole was created in the iron-steel interface region rather than at the centre of the iron.

In most of the samples, the hole was created at the interface between iron and steel and was far away from the centre of the sample. In some cases the outer steel ring was electropolished leaving the iron simply attacked by the electrolyte chemically. This created an oxide layer on the iron and did not provide a good surface finish. Therefore the option of using a precision ion polishing system (PIPS) was considered for final thinning of the embedded iron samples instead of electropolishing.

5.2.3 Precision ion polishing system (PIPS)

The samples of iron used in this research were thinned using a dual beam precision ion polishing system PIPS. Use of dual beam PIPS is a well known technique of preparing samples for TEM and SuperSTEM. Thin samples of desired thickness for use in electron microscopy can be prepared by ion milling.

Embedded iron samples described in section 5.2.1 were reduced in thickness uniformly in PIPS till a small hole is made in the centre of iron.

PIPS thins the sample by firing argon (Ar) ions onto the surface and removing the surface layer by layer till sufficient thickness is reached. It was operated at 5 kV and at an angle of 5 degrees for thinning and 3 degrees for polishing. The ion beams were aligned prior thinning so that the hole is made only in iron at the centre of the sample. Due to the flexibility of using the sample again in PIPS to reduce the amount of iron to a minimum, this technique was chosen for preparing thin samples from embedded iron in steel.

The samples were thinned until they became electron transparent and the amount of iron within the sample was reduced to an extent that the effect of magnetic field from an iron sample would not affect the operation of the

electron microscope. The thinned samples were then removed from the PIPS and examined initially in TEM and later in SuperSTEM.

The next sections will explain the techniques involved using a TEM, SuperSTEM, EELS and other important techniques used for this research.

The specimen preparation techniques for samples of embedded iron in stainless steel are shown as a process flow chart in figure 5.4.

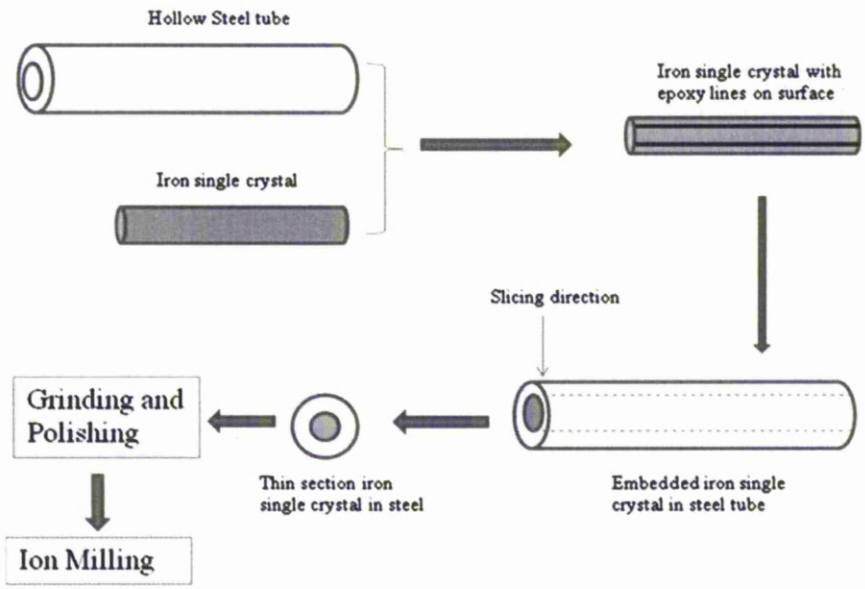

Figure 5.4 Schematic diagram of sample preparation techniques for iron

5.3 Electron microscopy

The initial part of the research work was carried out on polycrystalline samples which were studied using TEM, STEM and SuperSTEM while the latter part was on dislocations in single crystal Mo and Fe using TEM and SuperSTEM. The reason for changing the study from polycrystalline to single crystal specimens during this research will be discussed along with results.

One of the primary objectives of studying dislocations using TEM and STEM was to identify the character or type of the dislocation i.e. edge, screw or mixed. The other objectives included the verification of the grain orientation, thickness of the specimen near a hole, surface contamination and recording the amount of tilt required for orientating the sample to the [111] zone axis. The final objective was to locate and map the dislocations using a series of low magnification micrographs from TEM. This mapping was important because the areas with screw dislocations recorded using TEM can then be easily identified in SuperSTEM for imaging and EELS analysis.

5.3.1 Transmission Electron Microscope

The TEM that was used for experiments carried out on both molybdenum and iron was a JEOL 2000 FX transmission electron microscope operating at 200 kV. It was used to examine the final molybdenum samples prepared by electropolishing and iron samples prepared by ion milling. The specimen is illuminated with a parallel beam of electrons by adjusting the first two condenser lenses typically at a magnification of 12K – 20K. The microscope was aligned using the standard operating procedure provided by JEOL and then the sample was adjusted for the eucentric height. The features in the sample were resolved at this stage and all possible higher magnifications were used to observe dislocations in the samples. The transmission micrographs of dislocations were recorded using the camera below the phosphor viewing screen in the TEM.

5.3.2 Imaging screw dislocations in TEM

The techniques that were discussed in chapter 3 like two-beam technique were used to record a series of images of dislocations at different angles of X and Y tilts. A ½ [111] screw dislocation is faintly visible under parallel

beam because of the *invisibility criterion* (**g** . **b** = 0) and to record the contrast from the screw dislocation, the sample was tilted to a lowest possible angle close to zero tilt. A series of images were taken at possible different magnifications to confirm the line direction and Burgers vector. A low magnification image of the area with screw dislocations was taken in the TEM for identifying the same area when analysing the sample in SuperSTEM. These images will be presented in the next sections.

5.3.3 Electron diffraction

Electron diffraction patterns were important to align the sample along the [111] zone axis and to analyse the crystallographic information. The grains with <111> orientation were identified using electron diffraction patterns in polycrystalline samples and the patterns were recorded from the regions of interest at a specific camera length. These diffraction patterns were indexed to identify the crystallographic orientation of the sample. In iron samples, they were used to correct astigmatism caused due to the magnetic field from the sample. In addition they were helpful in identifying the presence of any oxide layers or carbon contamination in both Mo and Fe samples.

5.3.4 Grain orientation in polycrystalline samples

The first samples to be investigated using TEM were polycrystalline samples consisting of grains with random orientation. The orientation of interest for the work described in this thesis was [111] and the grains with such orientation were studied for the presence of any screw dislocations which were end-on (i.e. the dislocation line direction is parallel to the electron beam). The relative number of [111] grains in these polycrystalline samples was smaller than that of [110] grains. This was confirmed by the observation of diffraction patterns of most of the

thin grains while [111] grains were being searched for in the sample. It was also observed that grains close to [111] orientations were found in the thicker areas in most of the samples. Hence they were not effective for carrying out EELS analysis in SuperSTEM due to the possibility of plural scattering. Thicker sample also meant that the resolution in SuperSTEM would be affected consequently. It was thought that the manufacturing of thin foils from bulk materials by rolling could be the reason for the texture associated with the presence of a greater number of [110] grains[4]. Some of these samples were examined in TEM and STEM to study dislocations parallel to the surface of the foil in [110] grains as well as [111] grains and EELS was recorded from them.

5.3.5 TEM technique

The micrograph that shows dislocations inclined from top to the bottom surface of the foil with the grain orientation parallel to the beam direction [001] is shown in figure 5.5. The convergent beam diffraction pattern from this grain in shown in figure 5.6 and the electron diffraction pattern is shown in figure 5.7.

Figure 5.5 Bright field TEM micrograph showing dislocations inclined to the surface of the foil.

It can be observed from the image that the foil is bent which is evident from the contrast change in the image from bright to dark areas. The dislocations lie close to the grain boundary observed in the top right corner of the image and all of them are having projected length along the surface of the foil.

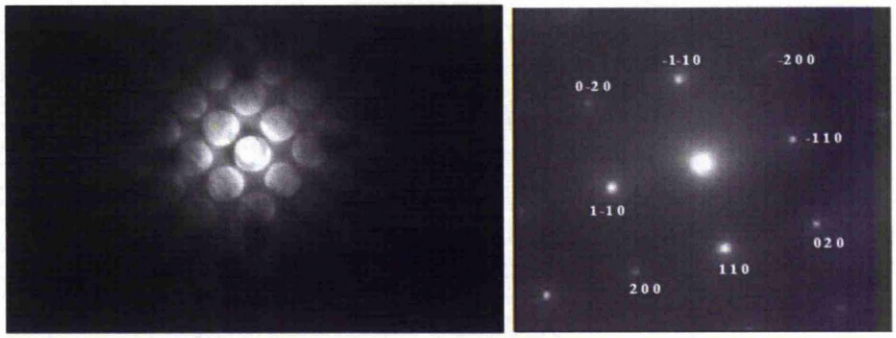

Figure 5.6 on the left shows a convergent beam electron diffraction (CBED) pattern of [001] zone axis; Figure 5.7 on the right is an electron diffraction pattern from the same grain showing bcc pattern.

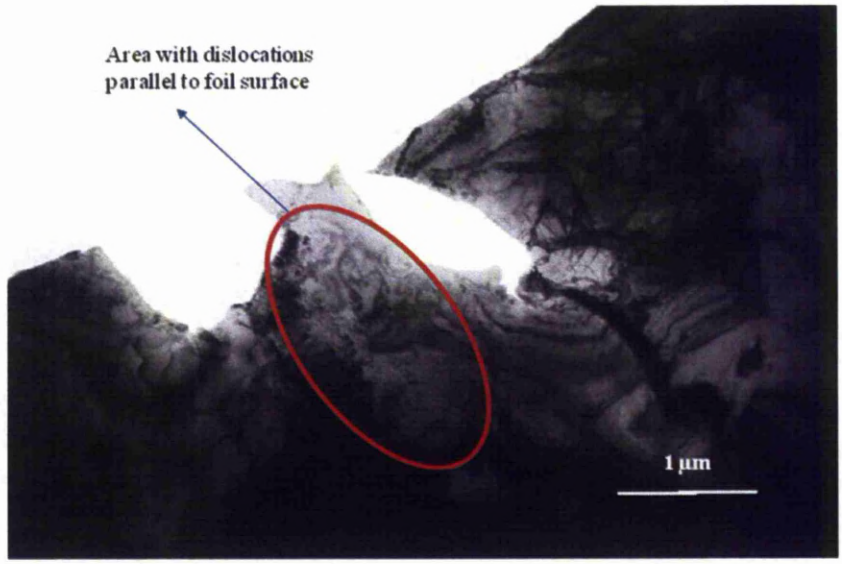

Figure 5.8 Low magnification bright field image showing thin grain containing dislocations with respect to the other regions of the sample.

The best probable areas for locating screw dislocations in these samples were near bend contours with their projected length perpendicular to the fold-directions arising from the bend contour. Dislocations of such kind are shown in figure 5.9 where a threefold symmetry is evident from the Kikuchi pattern and the dislocations are distributed along the length of the contours.

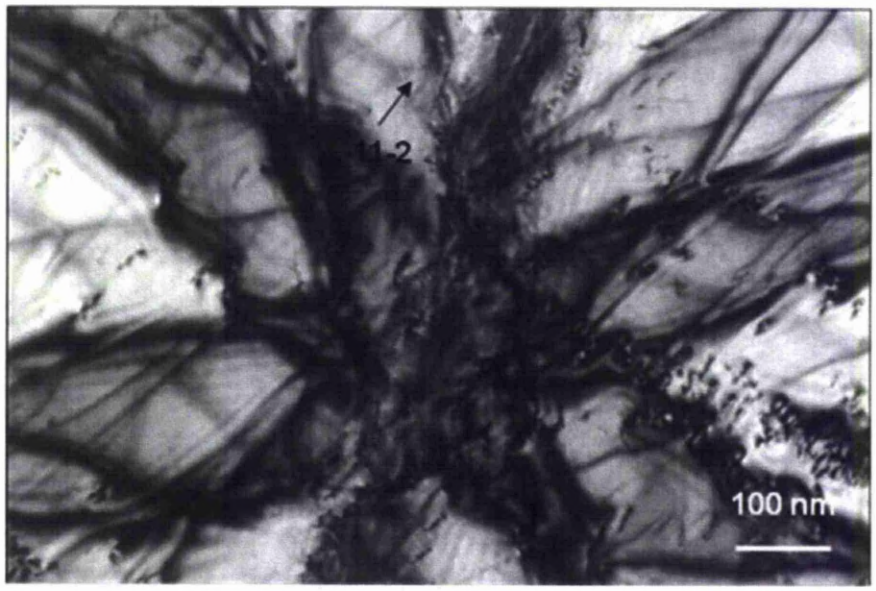

Figure 5.9 TEM bright field image showing screw dislocations near bend contour in a 111 grain.

Polycrystalline molybdenum samples were found to be complex ones for investigating the ½[111] screw dislocations since the number of [111] grains were minimal and the dislocations were mostly having length along the surface of the grains rather than being end-on. The problem often discussed in the case of end-on screw dislocations is the faint contrast from them in TEM bright field images since the dislocation line is parallel to the beam direction (**g**.**b** =0)[3, 5]. The **g** vector in the case of a screw dislocation is parallel to the line of no contrast, i.e. the line that

separates the darker and brighter areas of the contrast from screw dislocation[3]. This criterion was used to identify the character of the dislocations in the sample in TEM.

A quick method to identify the [111] grains in the sample was followed in which the CBED patterns from different grains were checked for the preferred <111> orientation by alternate translation and tilting. The JEOL 2000 FX has a limitation of 30 degrees of positive and negative tilt on X and Y axes. This was useful in tilting through different angles for identifying the reflection in which the dislocation becomes almost invisible and also in determining the Burgers vector. The tilt limit that was set for identifying the screw dislocations in this research work was 5 degrees which is similar to the available stage tilt range in SuperSTEM.

In summary it can be said that the TEM work involved with polycrystalline Mo samples was identification of the screw dislocations which are end-on or near to [111] zone axis within 5 degrees of X and Y tilt freedom in a thin, surface contamination-free 111 grain near the hole in the sample. Once a grain meeting these criteria was found it was mapped using low magnification bright field TEM images. The procedure followed for dislocations with screw character as explained above is shown in the figures 5.10, 5.11 and 5.12 respectively.

A. 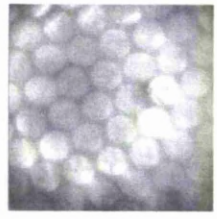 B. 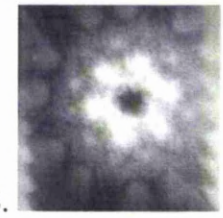

Figure 5.10 CBED pattern (A) with [111] zone axis and the respective Kikuchi pattern (B) indicating that the grain is in thicker area of sample.

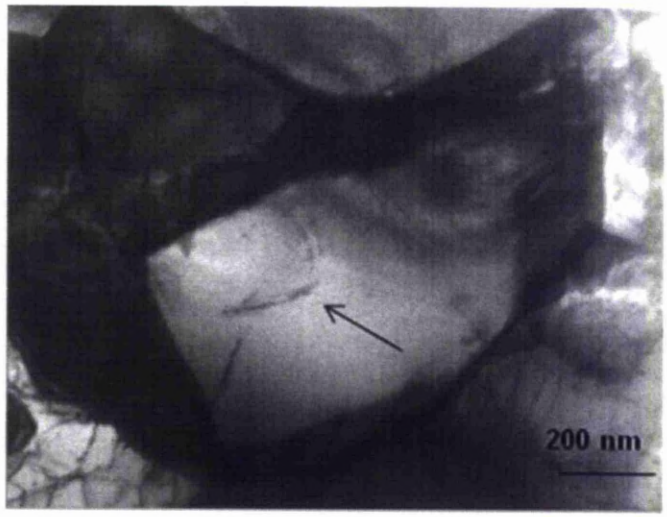

Fig 5.11 a) TEM bright field image showing a screw dislocation at the centre of a thick 111 grain at a positive tilt angle of 5 degrees.

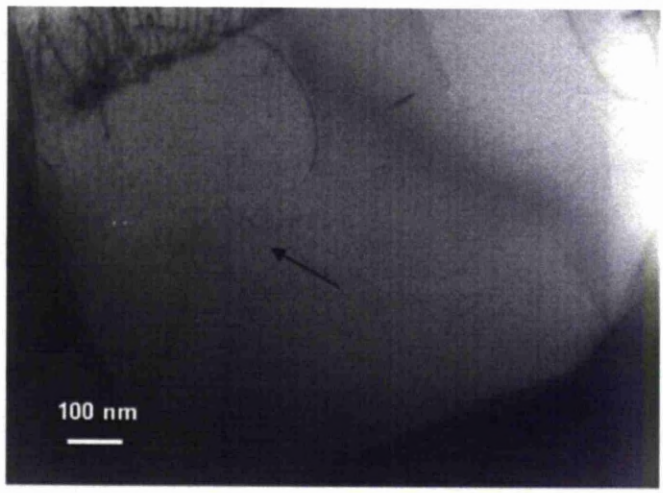

Figure 5.11 b) Screw dislocation vanishes when the grain is tilted to zero degrees or when then dislocation line is parallel to the beam direction.

When the sample is tilted from 0 degrees through to 5.5 degrees in the other direction (negative tilt), the dislocation starts to appear again in the bright field image. This is shown in the figures 5.11c and 5.11d. At an

angle of 2 degrees, it appears with the ends becoming visible and at 5.5 degrees the dislocation appears as it was in figure 5.11a.

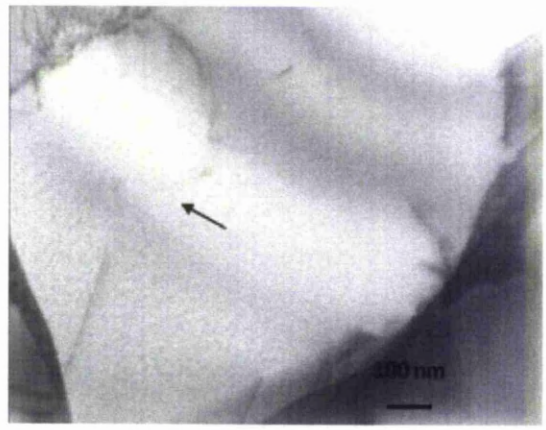

Figure 5.11c) TEM bright field image showing faintly visible ends of the dislocation.

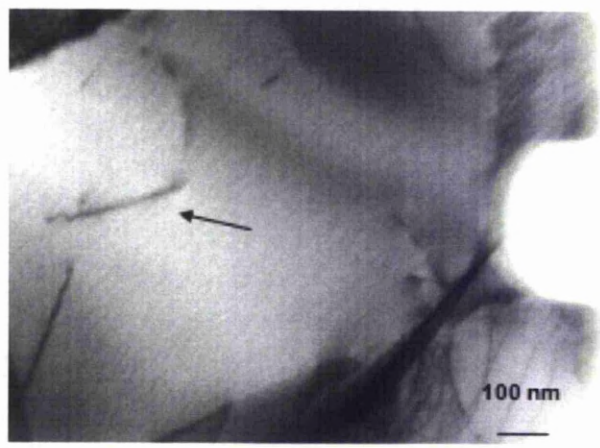

Figure 5.11 d) Screw dislocation reappears when the sample is tilted to 5.5 degrees in the opposite direction to that of 5.11a.

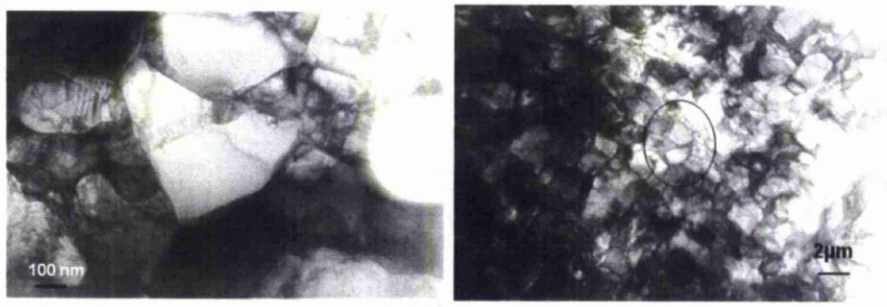

Figure.5.12 Low magnification bright field images of dislocation mapping.

5.3.6 STEM experiments

The samples with suitable thinner areas were analysed using STEM. They were checked for any possible surface contamination including molybdenum oxides. Molybdenum samples are readily oxidised when left in open atmosphere and form molybdenum trioxides which give a mottled surface finish to the samples.

In order to obtain best information from the dislocation core regions at high resolution, the oxide formation on the samples was avoided by storing the samples in gaseous nitrogen atmosphere. Apart from this it was possible to identify the near to end-on screw dislocations among other dislocations within a selected area of the polycrystalline sample. The density of dislocations in polycrystalline samples was also calculated using the images from STEM.

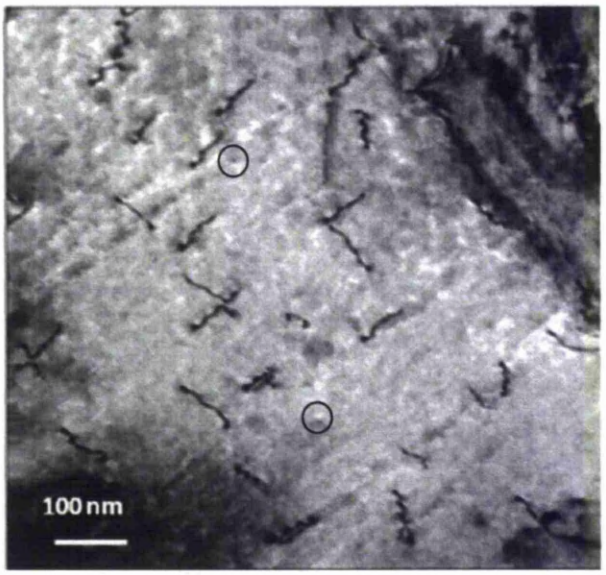

Figure 5.13 STEM bright field image of dislocations in [110] grain with projected length along the surface of the foil.

Dislocation density can be calculated by the number of dislocation lines intersected by a plane of unit area normal to them in cases where most of the dislocations are straight and parallel[6]. Consider figure 5.13 with dislocations where most of them are straight.

Approximate number of dislocations = 32

Area of consideration (from the image) = 800 x 800 (nm) ^{2},

$$= 64 \times 10^{-8} \text{ mm}^2.$$

Dislocation density therefore is, [(32) / (64 x 10^{-8})] mm^{-2},

$$= 5 \times 10^{7} \text{ mm}^{-2}.$$

It can be observed in figure 5.13 that there are two screw dislocations with negligible length but clearly visible. Observations such as this lead

to the conclusion that the density of near end-on screw dislocations is small compared to that of other dislocations.

Another area of the sample with dislocations straight and along the surface of [111] grains is shown in figure 5.14.

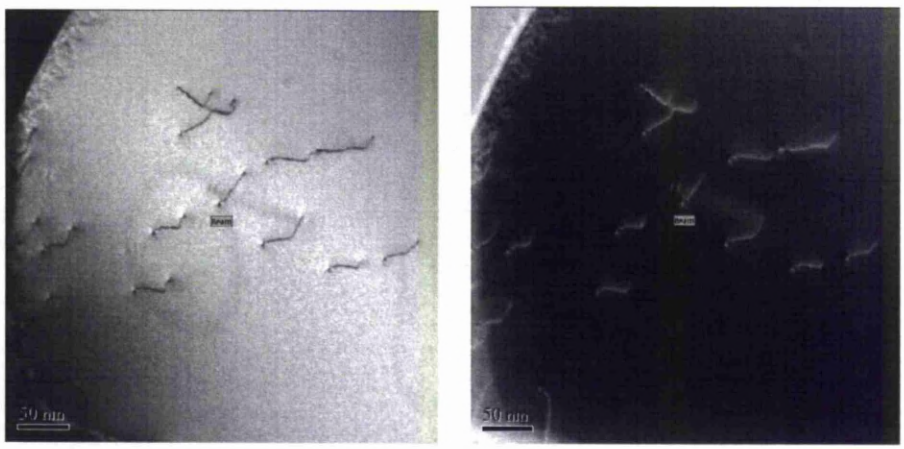

Figure 5.14 STEM bright field (left) and high angle annular dark field (HAADF) image of dislocations parallel to the surface of foil.

The dislocation density from this figure 5.14 is,

$$[12 / (16 \times 10^{-8})]\ \text{mm}^{-2} \qquad = 7.5 \times 10^{7}\ \text{mm}^{-2}.$$

This is close to the value of the prior calculation, which suggests that the distribution of dislocations is reasonably uniform in most of the areas. There were certain areas in the samples that were heavily deformed and the dislocations were too complex to analyse for any useful information. Examples are shown in the figure 5.15.

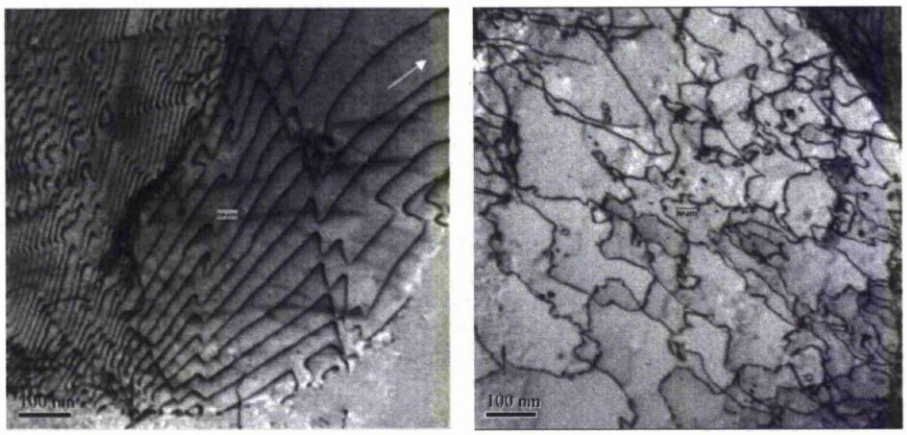

Figure 5.15 Bright field STEM images of dislocation networks near grain boundary (left) and in a heavily deformed (bend contour) region (right).

The polycrystalline samples were initially analysed in STEM for any changes in low loss spectrum and thickness variations along the regions with near end-on screw dislocations before they were transferred for SuperSTEM experiments. Bright field and annular dark field (ADF) images of a screw dislocation in a [111] grain are shown in figure 5.16.

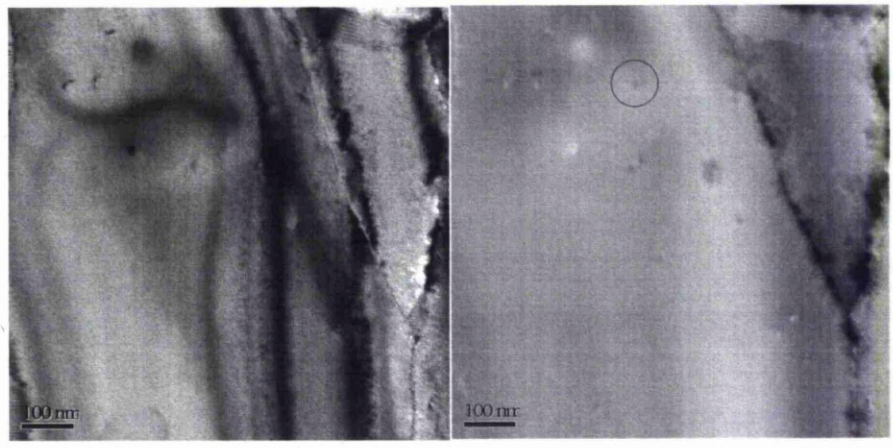

Figure 5.16 STEM bright field (left) and annular dark field (right) images of end-on screw dislocations (in circle) recorded at 100kX magnification.

It can be observed that the screw dislocation shown in the circle in ADF image of figure 5.16 is faint and almost invisible in the bright field image. This dislocation was chosen specifically for collecting EEL spectrum due to that reason. All other dislocations in the field of view were either close to the grain boundary or were clearly visible at the specified magnification which meant they had a considerable projected length. If the dislocations were close to the grain boundary, thickness variations and any seggregants near grain boundary could contribute to the recorded EEL spectrum making analysis difficult to interpret. Dislocations with significant projected length are not end-on and were not the type of interest for this research. A higher magnification 200kX ADF image of the screw dislocation with the region of interest (ROI) of the acquired spectrum image (SI) is shown in figure 5.17.

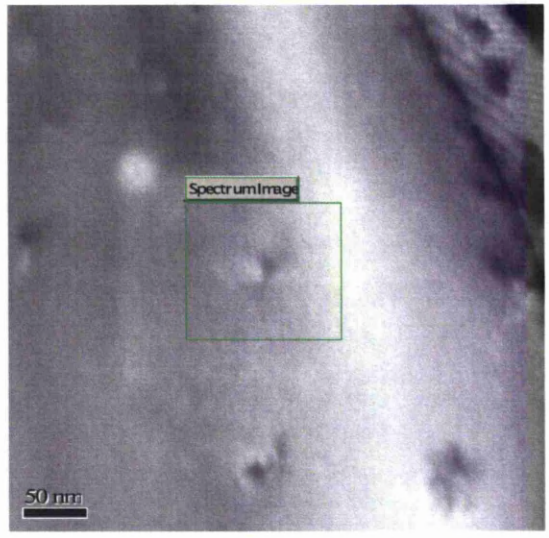

Figure 5.17 STEM ADF image (200kX) showing the ROI for EELS SI.

The contrast from the ADF image recorded at 500kX was used to measure the approximate area over which the dislocation region is distributed as shown in figure 5.18.

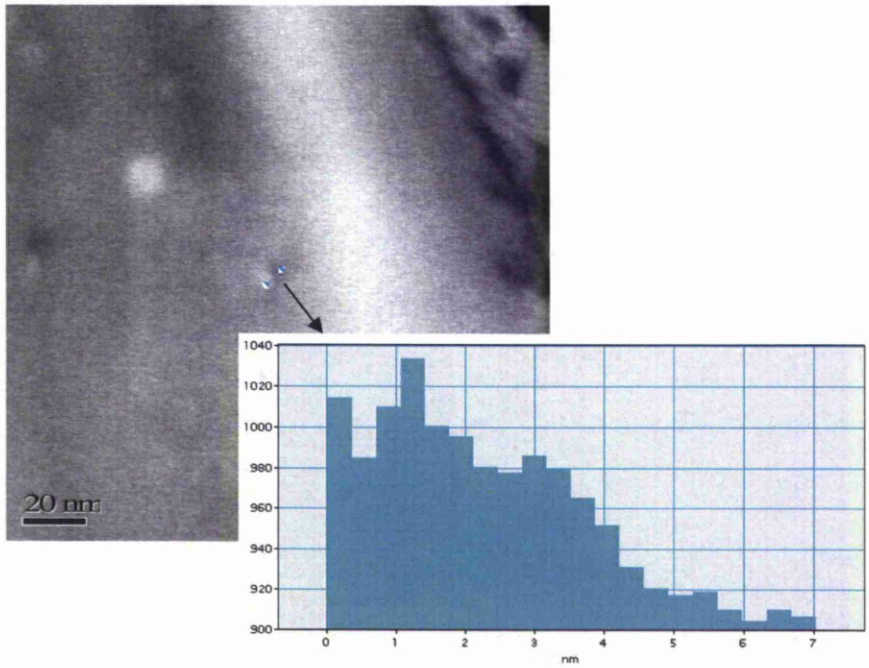

Figure 5.18 STEM ADF image showing screw dislocation and the line profile measuring the extent of dislocation region.

It can be observed from figure 5.18 that the extent of dislocation region measured as the contrast change from bright to dark in the ADF image is approximately 5 nm. This was calculated by the difference between the maximum and minimum intensity from the profile, the maxima occurring at 1 nm (brighter region of dislocation) and minima at 6 nm (darker region). The EELS SI image acquired at 0.001 seconds per pixel from the dislocation is shown in figure 5.19. All EEL spectra presented in this thesis were acquired in parallel dispersive mode with 0.3 eV per channel dispersion.

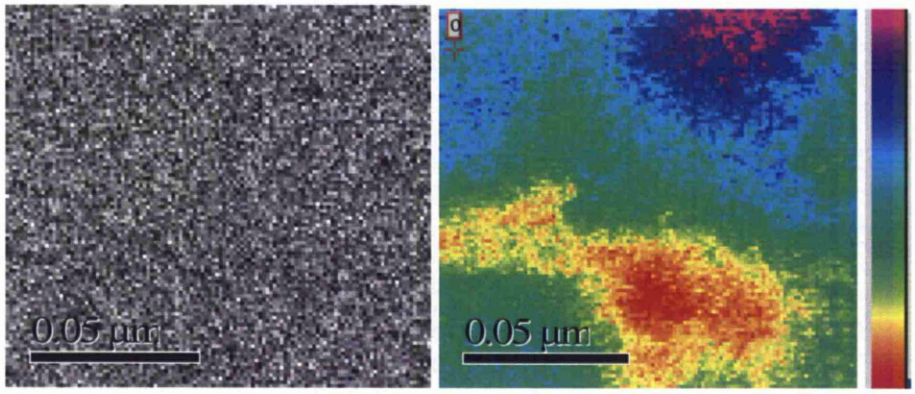

Figure 5.19 Low loss spectrum images from screw dislocation in STEM; original SI (left); energy slice (5 – 80 eV) applied to it (centre); intensity variation shown with colours (right).

The spectrum images collected from the screw dislocation were for low loss region which included zero loss peak, plasmon peaks. Apart from these, any other elements, if present, reveal their characteristic peaks at their respective energy loss edges. The number of counts variation is shown in the image 5.19 (right) with the colour at the top representing maximum number of counts and the colour at bottom representing minimum. The central image in figure 5.19 shows the distribution of intensity over the SI according to these colours. The dislocation region was at the centre of this spectrum image.

In figure 5.21 the low loss spectrum shown in red is the spectrum from the centre of SI containing the dislocation and the spectrum in black is from a region far away. The locations of the pixels in SI from which the spectra are generated are shown in figure 5.20.

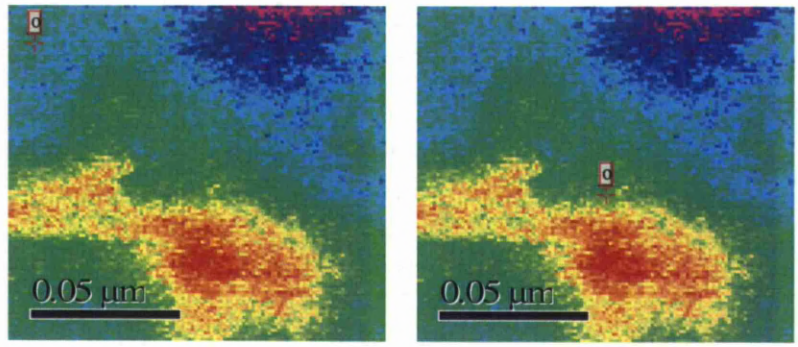

Figure 5.20 Spectral images showing the selection of spectra used for comparison in figure 5.21.

Low loss EEL spectra acquired from the dislocation and from a region far away were compared and are shown in figure 5.21.

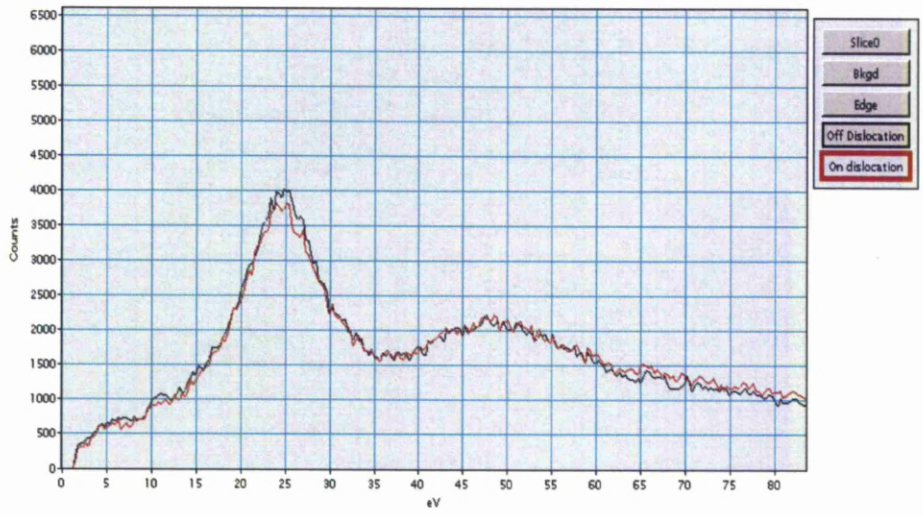

Figure 5.21 Comparison between low loss spectra from screw dislocation region (red) termed as "On dislocation" and from region away from dislocation (black) termed as "Off dislocation" in the figure.

It can be observed from figure 5.21 that the two spectra appear to be essentially same and no significant changes are apparent in the low loss region of the spectra. Although only two individual spectra are presented

here, all the spectra were compared during analysis of the SI and no changes were observed. The relative thickness from each spectrum is computed using the option provided in Digital Micrograph® and is found to be between 1.3 and 1.4 λ, where λ is the total inelastic mean free path.

The changes in bond lengths and angles at a screw dislocation core in transition metals were thought by many researchers to affect the fine structure near the characteristic energy loss edges. Hence ELNES region instead of low loss region was studied from cores of screw dislocations and mixed dislocations using high resolution EELS at SuperSTEM.

5.3.7 SuperSTEM

SuperSTEM based at Daresbury laboratories was used for ultra-high resolution electron microscopy involving high angle annular dark field (HAADF) imaging with a sub angstrom probe (< 1.0 Å) and atomic column resolution electron energy loss spectroscopy (EELS) (~0.5eV). It satisfies all requirements essential to do lattice imaging and high resolution EELS of a dislocation core, and therefore was used to study dislocation cores in Mo and Fe.

HAADF imaging at atomic resolution in a SuperSTEM characterises the structure around a dislocation core and is an efficient method for studying electronic structure at defects in transition metals. The reciprocity principle governs the relation between image characteristics of a conventional TEM and STEM. Although the BF images in TEM using the direct beam are similar to on-axis detector BF image in STEM by the reciprocity principle, HAADF intensity is low in STEM due to large scattering and in proportion to Z of the elements present.

BF and HAADF lattice imaging methods were used to identify the screw dislocations in molybdenum and bcc iron. Bright field and high angle annular dark field images were recorded from a region of the sample with no dislocations (termed as *perfect crystal* in this thesis) and from a region with a dislocation core in proximity. EEL spectra were recorded from both perfect crystal and from the dislocations, the spectral features of which were used to connect them with inter-band transitions and density of unoccupied states.

The EEL spectrometer fitted to SuperSTEM has a magnetic prism with 90 degrees bending angle and was interfaced with post-specimen detector chamber. A schematic diagram of an EEL spectrometer used in the STEM is shown in figure 5.23. The scintillator charge coupled device (CCD) detector in SuperSTEM was approximately 30 times better and more sensitive than previously used photo diode array detector.

The resolution of EELS is determined by the collection semi-angle of the spectrometer β given by:

$$\beta = d / 2h \qquad (5.1)$$

where h is the distance between the specimen and the aperture, while d is the diameter of the spectrometer's entrance aperture (shown in Fig 5.22).

Collection angle affects the signal to noise and signal to background ratios in EELS and hence is an important factor for EELS analysis. The collection angle of SuperSTEM is 19 milli radians and is different to STEM at Liverpool, due to the presence of post-specimen lenses. Due to this reason, the effective diameter of the spectrometer's entrance aperture (d_{eff}) projected onto the diffraction plane determines the value of β in STEM diffraction mode.

The scanning transmission electron microscope (STEM) based at Liverpool, was a VG HB601 UX operating at 100 kV with approximately 8 Angstrom diameter spot size and cold field emission gun as electron source.

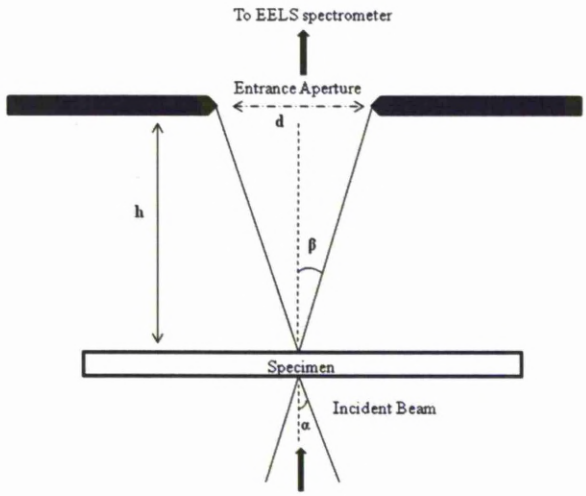

Figure5.22 Schematic diagram of collection angle in STEM assuming no lenses between specimen and spectrometer[7].

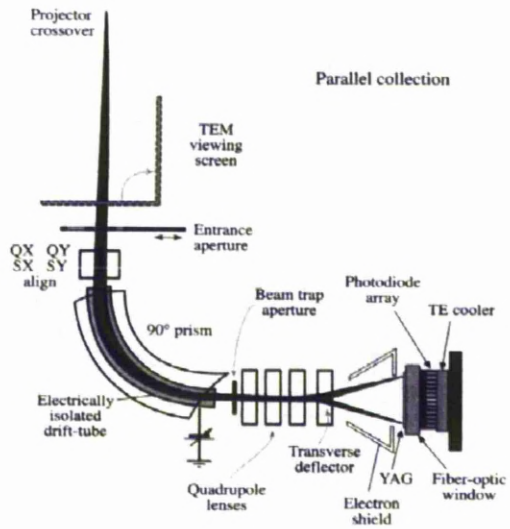

Figure5.23 Schematic diagram of an EEL spectrometer in a STEM[7]

5.3.8 Electron Energy Loss Spectrum acquisition

The electron energy loss spectrum is a plot of the electrons detected after they pass through the microscope column. The features of an EEL spectrum were discussed in chapter 3. An EEL spectrum contains contributions from inelastically scattered electrons, elastically scattered electrons and from those electrons that retain their energy[7]. A general EEL spectrum with its three main regions can be useful tool before the actual spectrum image is acquired (as shown in figure 5.24). Zero loss peak (ZLP) is essential for knowing the resolution (by Full Width Half Maxima- FWHM) of the spectrometer before EEL spectrum can be acquired. Since the acquisition of the spectrum including the zero loss peak can saturate the detectors, the spectra were collected without ZLP. When an electron from the beam interacts with a core electron in the sample, it can transfer energy and lose energy up to 25eV, but interaction with molecular orbitals can cause characteristic peaks in the low loss spectrum, the intensity of which can be used for elemental identification.

Electrons that have undergone inelastic scattering with inner shells of an atom and have lost energy greater than 50eV constitute the high energy loss region of EEL spectrum. The excitation of electrons in the K, L, M or N shells by an electron from the beam can result in them being transferred to higher orbitals accompanied by significant energy loss to the transmitting electron. This process is known as inner shell ionisation of the atom and the ionised atom restores itself to the ground state by releasing the excess energy in the form of an x-ray[8]. Thus the x-ray methods and EELS techniques are analogous suggesting that measurement is made with different aspects of the same process.

ELNES (30 - 40 eV above edge threshold) and EXELFS (100's of eV above ELNES region) are part of this high energy loss spectrum. The

edges that are studied in this research include the near edge structure of Mo $M_{4,5}$ and Fe $L_{2,3}$ which extend up to a few 10's of eV above the edge threshold and are characteristic of the ionisation of those shells. ELNES of perfect crystal region and dislocated crystal region are collected and interpreted using techniques which will be discussed in the next sections.

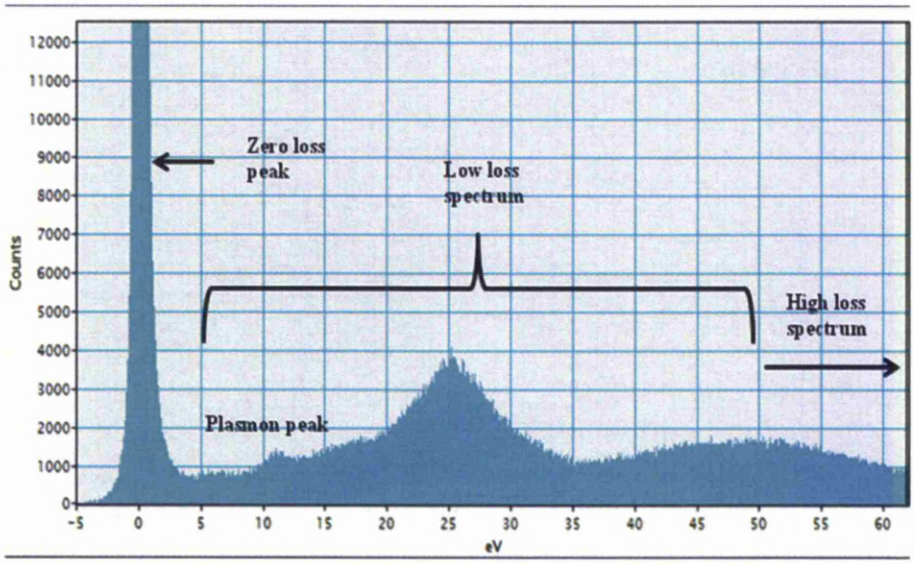

Figure 5.24 EEL spectrum collected at SuperSTEM with 100 keV electron beam showing different energy loss regions in molybdenum.

5.3.9 Background subtraction

The outer shell interactions are attributed to the plural scattering events that cause the background intensity in the EEL spectrum. The background in an EEL spectrum is a continuously changing continuum with maximum at 20-30eV just after the plasmon peak to a minimum at 0 eV. The background subtracted signal starting at 35 eV after background subtraction is shown as a part of the EEL spectrum in the figure 5.25.

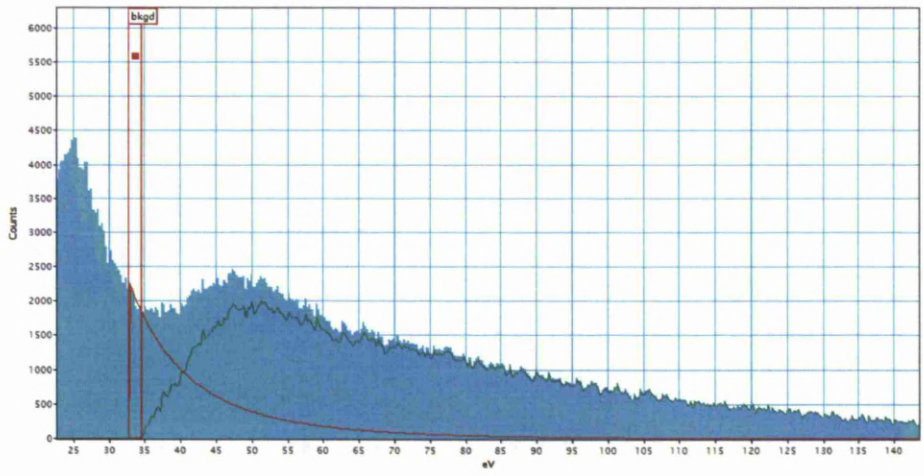

Figure5.25 Background (bkgd in red) and background subtracted signal (green) in an EEL spectrum showing decrease in intensity from maximum to minimum.

5.4 Contamination affecting Mo - ELNES

Carbon contamination is a common hindrance for analysis of samples in microscopes, particularly in STEMs. This is noticed during the EELS analysis of Mo $M_{4,5}$ edge as intense carbon K edge starts at 285eV shown in figure 5.27. The intensity of the focused electron beam on the sample can increase the carbon contamination and often tends to build-up carbon over the regions which are being analysed. Hence, during the EELS acquisition and while images are being collected, samples are always monitored for carbon contamination. Carbon contamination can occur as a result of poor vacuum in the electron microscope, untidy sample holders or surface contaminants on the sample. Carbon content in the sample may also be an affecting factor for contamination to a certain extent. Most precautionary measures were followed while handling, storing and transferring the samples between different microscopes. Additional procedures like plasma cleaning and baking the sample were followed as and when the need was felt. Carbon contamination on the sample after EELS acquisition from a dislocation is shown in figure 5.26.

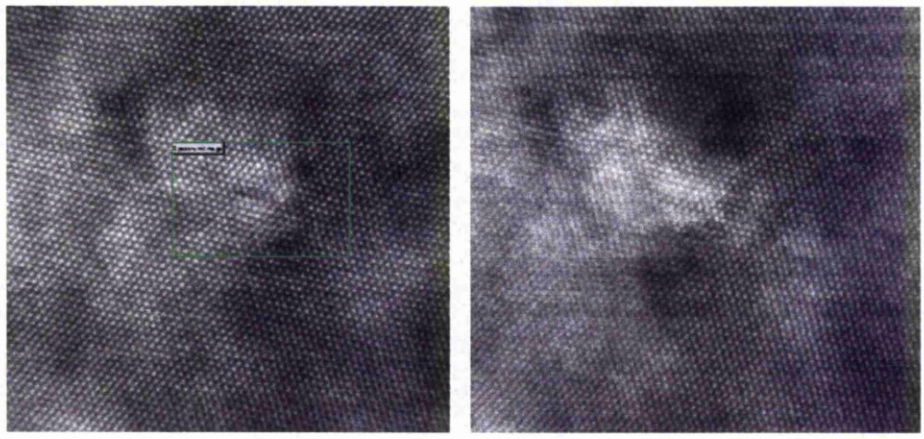

Figure 5.26 Pre-EELS (left) and post-EELS (right) HAADF images of mixed dislocation showing carbon contamination as white feature.

Solution: The energy window was chosen typically between 150 to 800 eV and dispersion was 0.3 eV per channel. The on-set for molybdenum $M_{4,5}$ edge is 227 eV with a delayed maximum of about 80eVabove the edge threshold. The carbon K-edge starts at 285eV and can interfere with Mo $M_{4,5}$ ELNES spectrum if there is carbon contamination. Typical energy loss spectrum for molybdenum is shown in figure 5.27

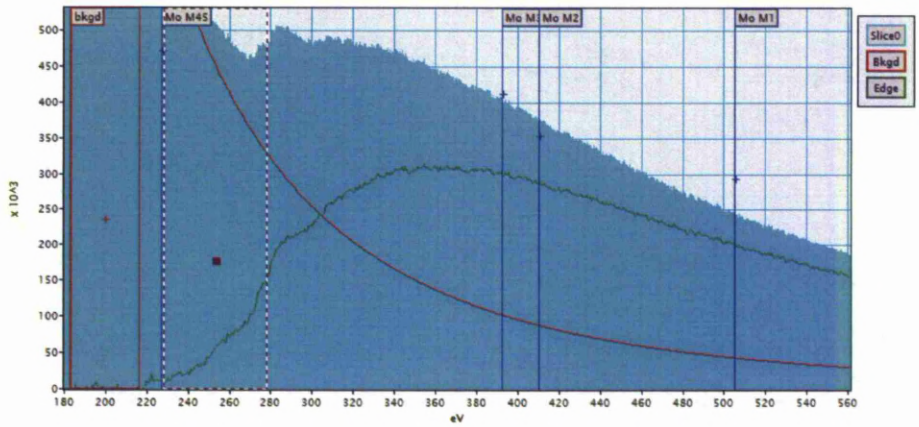

Figure 5.27 Energy Loss Near Edge Structure (ELNES) spectrum for pure molybdenum showing M shell edges and background subtracted.

The energy loss region for Mo shown in dashed line box (227 – 275eV) is the energy window of interest for the work described in this thesis.

5.5 Magnetism in iron samples

Thin iron samples were examined in the microscopes with supporting grids and anti-twist washers in place to prevent flipping and ensure that the sample had enough support when it experiences magnetic field from lenses.

The dislocations in iron samples were examined by TEM (JEOL 2000 FX) and then in SuperSTEM. The magnetic field effects were reduced as much as possible by careful correction of astigmatism for every angle of tilt and translation in the TEM after which the images were recorded. The objective lens strength was reduced to as low as possible and the eucentric height change was taken care of for every tilt. Tilting of the sample necessary to identify the Burgers vector was done so that the tilting range was set to one side of zero position. Other standard techniques for magnetic correction[7] were used to image dislocations in the iron sample.

The effect of magnetic field from the sample on the beam was noticed by the random shift of the electron beam in SuperSTEM. The sample experienced strong magnetic effects from the lenses and the change in tilt angle was observed after every translation and so care was taken to maintain sufficient *z*-height between the pole pieces and the specimen in SuperSTEM.

After the aberration corrections were done, atomic resolution image from a perfect crystal region of pure iron sample was taken. Although the corrections for astigmatism were made as good as possible, the images were still affected by some residual astigmatism. The images of

dislocations were taken at appropriate *z*-height followed by EELS at high resolution. An alternative method to extract useful information from the dislocation core was the use of spatial difference technique. It was used to reveal spectral changes in the ELNES obtained from a dislocation core and a perfect crystal. The next section will deal with spatial difference technique and its application for this research work.

5.6 Spatial difference technique

Electron microscopy equipped with high resolution EELS can provide detailed information from a localised region of the sample to a few nanometres scale. Spatial difference technique is a method of obtaining essential information from near edge structure by subtracting ELNES spectrum of a perfect crystal region from ELNES spectrum of a dislocation core or vice versa. This technique provides a resultant spectrum that can be used to monitor the changes in intensity of ELNES with respect to changes in spatial coordinates.

Spatial difference technique is often used to study defects, interfaces and grain boundaries at high spatial resolution. It can reveal changes in the local bonding as well as chemical composition. EEL spectrometer fitted in SuperSTEM is able to resolve spectral features to an atomic level in the EEL spectrum. The spatial difference spectrum of high resolution spectra can provide vital information about electronic structure from each atomic column. The use of scanning probe for acquisition results in overlap of ELNES information from adjacent atomic columns. In order to reduce the percentage error in quantitative information, ELNES regions are selected so that a maximum number of spatial coordinates are included the ROI.

In this research, the spatial difference technique is used to identify the ELNES changes by determining the difference between spectra collected from a dislocation core and a perfect crystal.

Spatial difference (SD) technique can be written simply as follows:

$$I_{SD} = I_{core} - m \times I_{perfect} \qquad (5.2)$$

where I_{SD} is the ELNES intensity from spatial difference spectrum, I_{core} is the ELNES intensity from dislocation core, and $I_{perfect}$ is the ELNES intensity from perfect crystal. Since the two spectra are collected from different spatial coordinates which could affect the background contribution, factor m provides allowance for background of I_{core}. A schematic diagram of the spatial difference technique is shown in figure 5.28.

The effects of thickness and surface variations were taken into account while choosing the areas for perfect crystal region to acquire EELS. Apart from the factor that decides how well the two spectra can be used for spatial difference techniques under identical experimental conditions, the changes observed in the difference spectrum can provide vital information about the bonding and density of states.

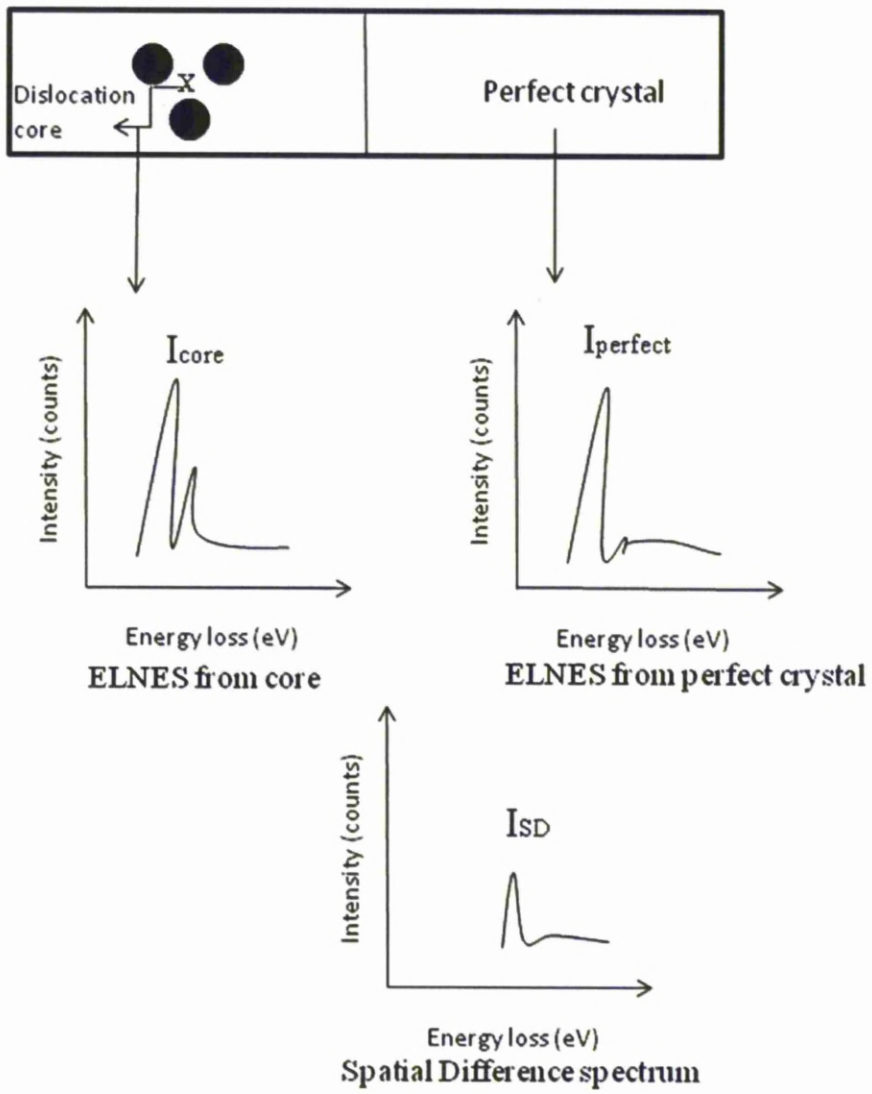

Figure 5.28 Schematic diagram of spatial difference technique for ELNES at a dislocation core. SD spectrum has fewer counts since it is a difference spectrum but has same energy loss points.

5.7 TEM and STEM analysis

The study of dislocations in TEM revealed their character (edge, screw or mixed). Dislocations perpendicular to the foil surface were identified by the faint contrast from them when viewed in the dislocation line direction [111]. The texture of the surface for some molybdenum samples examined in the TEM showed the presence of thin oxide layer. The dislocation line direction and **g** vector were determined from the TEM micrographs as shown in figure 5.11. Low magnification images were used to identify the dislocation regions in the sample. <111> screw dislocations were identified and recorded. TEM study was helpful in observing the thickness of the sample to be used for EELS analysis. It was also observed that the dislocations moved within the single crystal sample due to small deformations caused by handling of the sample with tweezers or during transferring. This was not experienced in polycrystalline samples and the reason could be the presence of grain boundaries that would pin the dislocations and avoid their further movement.

STEM images revealed the presence of complex dislocation networks that could interfere with the screw dislocations in polycrystalline samples. Dislocation density for different kind of samples was determined using the images from STEM and TEM and was found to be in multiples of $10^7 mm^{-2}$. This agrees approximately with a general value of dislocation density reported in deformed metals (10^9 mm^{-2})[9, 10] . The values of dislocation density calculated by the methods discussed earlier could be less than the actual dislocation density. This is because of the non-consideration of dislocations that lie perpendicular to the foil that show no contrast in the image and the dislocations that exist under the surface of the foil that do not have their ends projected on to the surface of the foil. A schematic diagram of such dislocations is shown in figure

5.29. The complex dislocation networks revealed in STEM images (refer to figure 5.15) along with the impurities present in polycrystalline samples were the key reasons for switching to single crystal Mo samples with ½[111] screw dislocations.

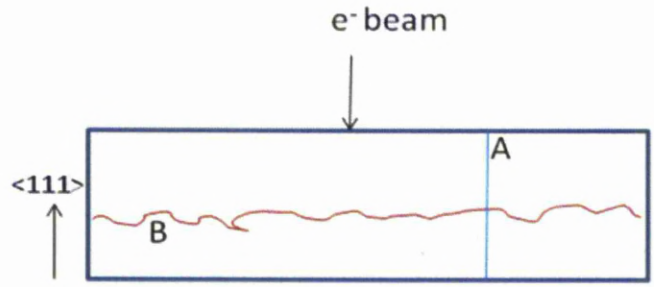

Figure 5.29 Schematic diagrams of two types of dislocations that cannot be accounted in dislocation density calculations. A is the dislocation perfectly perpendicular to the foil surface; B is the dislocation parallel to the surface but lying inside the crystal.

The low loss spectra of screw dislocations collected in STEM did not show any changes in the spectra as shown in figure 5.21. Hence the ELNES at $M_{4,5}$ edge for molybdenum was chosen to investigate changes from a screw dislocation core.

References:

[1] L. Hollang, M. Hommel, A. Seeger, Physica Status Solidi a-Applied Research 160 (1997) 329-354.
[2] P. J. Goodhew, Thin foil preparation for electron microscopy, Elsevier, Amsterdam ; Oxford, 1985, p. xiii,206p.
[3] P. B. Hirsch, Electron microscopy of thin crystals, Butterworths, London, 1965, p. 558p.
[4] ASM, ASM handbook - Textured Structures: Metallography and Microstructures, Materials Park, Ohio : ASM International, c1990-, 2004, p. v.
[5] J. a. W. Weertman, J. R. Weertman, Elementary Dislocation Theory, pp. ix. 213. Macmillan Co.: New York; Collier-Macmillan: London, 1964, p. 8º.
[6] D. Hull, D. J. Bacon, Introduction to dislocations, Butterworth Heinemann, Oxford, 2001, p. vii, 242 p.
[7] D. B. Williams, C. B. Carter, Transmission electron microscopy : a textbook for materials science, Plenum, New York ; London, 1996, p. xxvii,729p.
[8] U. Mizutani, Introduction to the electron theory of metals, Cambridge University Press, Cambridge, 2001, p. xii, 590 p.
[9] ASM, ASM handbook - Plastic Deformation Structures: Metalworking - Bulk Forming, Materials Park, Ohio : ASM International, c1990-, 2005, p. v.14A, 539–551p.
[10] G. K. Williamson, R. E. Smallman, Philosophical Magazine 1 (1956) 34 - 46.

Chapter 6

Theoretical Techniques

Chapter 6

THEORETICAL TECHNIQUES

This chapter presents detailed discussion about all the parameters that were used to simulate ELNES spectra for both Mo and Fe bulk crystals. The simulated theoretical ELNES of perfect crystal is then compared with experimental ELNES results of perfect crystal to assess and confirm the accuracy of the modelling technique for both Mo and Fe systems. The parameters that have been used for simulations and their values are then justified in conjunction to the requirements of experimental setup and the processes involved in practice. The presence and absence of certain parameters on the final ELNES spectra will be presented and discussed.

6.1 EELS calculations with FEFF8

The comparison of experimental EELS with theoretical calculations had been very challenging for over a decade. Band structure methods used for calculating electronic structure were dependent upon crystal symmetry in reciprocal space. Real Space Multiple Scattering (RSMS) approach can be used to calculate EEL spectra theoretically and compare with experimental spectra.

While experimental spectra suffer from peak broadening due to the core-hole lifetime and instrumental resolution, theoretical spectra from RSMS approach could be less precise due to spherical muffin-tin potentials and defined cluster size[1]. Since the total density, Fermi energy and charge transfer do not vary with fine details in the DOS, and are accurately calculated by FEFF, the comparison between experimental and theoretical spectra is justified to a preferable level of accuracy. Hence the

electronic structure measured from the experiment can be compared with FEFF8 EEL spectra and quantitatively interpreted in terms of DOS.

6.2 FEFF8 Procedure and Strategies

This section discusses the practical procedure of FEFF calculation and the strategy to be adopted with prerequisite parameters in the input to yield an error free output. It will also explain necessary and optional input commands which can generate ELNES spectra from a given central atom in the cluster.

A sample input is presented and the parameters used in the calculation are discussed. The output files generated are also listed. Further sections refer to the technique of making a calculation converge, and to check for important parameters like Fermi energy and core-hole effects. A more detailed discussion on the each of the parameters used for FEFF calculations is presented.

6.2.1 FEFF Input

An example of the input file that was used in FEFF for calculating ELNES of a perfect crystal is shown in figure 6.1. The commands and the parameters used in the input file are explained with reference to the selected cluster of atoms.

1. TITLE: This card contained the label of the metal cluster that was used as input in FEFF. In this example a molybdenum cluster with 300 atoms was used. Any other relevant information about the cluster can be added into this card.

2. EDGE: This instructs FEFF to calculate molybdenum M_4 edge. If a core hole was intended, an instruction for it can be included in this card.

```
TITLE  Molybdenum
EDGE    M4
NOHOLE
CONTROL 1 1 1 1 1 1
PRINT   0 0 0 0 0 0

POTENTIALS
      0   42   Mo   3   3
      1   42   Mo   3   3

IORDER -70202
SCF 11.0
XANES 8 0.07 0.0
LDOS   -20  50  0.3
FMS 11.0
RPATH 0.1

ATOMS
0       0       0       0       Mo0     0
-2.725302       0       0       1       Mo1     2.725302
-0.9085389      -2.5695255      0       1       Mo1     2.725418175
-0.9085389      1.2846054       -2.2252437      1       Mo1     2.72531897
0.9085389       -1.2846054      -2.2252437      1       Mo1     2.72531897
```

Fig.6.1. Sample FEFF input file for Mo perfect crystal system listing the commands, parameters and their values.

3. NOHOLE: This was an optional advanced card intended to perform multiple scattering calculations in the presence of a completely "screened" core hole (preferable for metals due to the presence of highly mobile valence electrons screening the core-hole)[2, 3].

4. CONTROL: This card instructed FEFF to run the modules that were necessary for error-free calculations. It was altered to choose the sequence of the modules that were intended to run for each calculation.

5. PRINT: The output files generated by FEFF calculations were dictated by this card and the input into this card was chosen so that required output files were written separately with appropriate names to them.

6. POTENTIALS: A unique potential index was designated to each type of atom specified in the cluster. In this example both the absorbing atom (potential index 0) and scattering atoms (potential index 1) were Mo with Z = 42. Angular momentum cut-offs were also given (a value of 3 for s, p, d and f states)

7. IORDER -70202: This is an optional advanced card used to perform calculations without error in the case of shells above M_3[4]. The absence of this card generated an error "Lambda array overfilled" and since the M_4 shell was calculated this was added into input.

8. SCF: This card instructed FEFF to perform calculations of potentials, Fermi energy, charge transfer and LDOS using self consistent field loop within a radius of 11.0 Angstroms.

9. XANES: This was an important card necessary to perform near edge structure calculations at molybdenum M_4 edge and beyond until a value of k = 8 $Å^{-1}$. The remaining values were necessary for grid specification. Default XANES parameter values specified in FEFF user manual are taken for calculations in this thesis as they suit the requirements.

10. LDOS: Angular momentum projected density of states were calculated when this card was used with an energy range of -20 to 50 eV, with 0.3 eV energy step. Fermi energy was also calculated with in this calculation. Finite cluster size may broaden the ℓ-DOS for crystals and has to be taken into account while comparing.

11. FMS: Full multiple scattering calculations were done within a radius of 11.0 Angstroms (4 atomic shells in cluster) around the central absorbing atom.

12. RPATH: This card restricted the FEFF to perform only ELNES calculations and avoid any path expansion calculations for EXELFS. The value 0.1 makes the path expansion negligible and even the use of any negative number (like -1) would perform the same calculations[5].

13. ATOMS: Atomic positions (first three columns in example) in the cluster with their x, y and z coordinates were listed. The potential index value (0 or 1) for each atom type (Mo0 for absorbing atom; Mo1 for scattering atoms) and the distance between the central atom and each scattering atom (last column) was given as input for FEFF.

14. END: Any instructions or CARDS present after this card were not to be included for FEFF calculations and this card was used to indicate the end of input for all calculations.

6.2.2 FEFF output

FEFF calculations were done for both perfect crystal Mo and Fe as well as dislocated crystal Mo and Fe. FEFF output files were generated in the same folder which contains the input files and the executable. Each calculation was done in a different folder to avoid overwriting of the output files.

Two important files generated by FEFF calculations were called "xmu.dat" and "ldos01.dat". The first file contains all the information about the ELNES data μ (E), smooth atomic like background μ_0(E), the number of atoms used for calculations, Fermi energy E_f, wave number (k), the energy loss (ω) and structure factor (χ). The second file contains the angular momentum projected density of states data for each orbital(s, p, d and f).

6.3 FEFF program modules

FEFF calculation follows six sequential steps as follows:

1. A self-consistent field approach is applied to the atoms in the cluster and self-consistent scattering potentials are calculated using an automated loop. At the end of this module (called **pot** module), absolute edge energies are estimated.

2. The second module called as **xpsh**, calculates absorption cross-section, dipole matrix elements ad scattering phase shifts. This module can also calculate the angular momentum projected density of states in addition, but is optional and will be run if LDOS card is specified in the input file.

3. The third module called as **fms** module performs full multiple scattering Near Edge Structure calculations for a cluster of atoms within a given size in angstroms.

4. In the fourth module called **path**, the leading multiple scattering paths for the cluster are listed for further calculations.

5. Fifth module calculates the effective scattering amplitudes f_{eff}, and other fine structure parameters for each scattering path listed by the above module. This module is called **genfmt.**

6. **ff2x** is the final module which combines the fine structure parameters from all the paths to calculate a total ELNES or EELS spectrum.

   DOS and ELNES data obtained from the calculated spectrum will help connect spectral features to transitions to particular states. Furthermore they can give direct information about the unoccupied states and occupied states which can be used to obtain the oxidation states of the

metal as well as the electronic configuration. In the next sections, important parameters that are useful in obtaining error-free EEL spectra will be discussed.

6.4 Convergence checklist

An important list of checks has to be performed before proceeding from one calculation into another. The first one of importance is self-consistent well-converged potentials. After the potentials are calculated the output file must be checked to examine how well the SCF loop has converged. A small cluster of about 20 atoms around the absorbing atom could yield well-converged potentials. Depending upon the radius of the cluster and the interatomic distance, more number of atoms can be used for achieving convergence, but it will not affect the output from potentials module and the final EEL spectrum.

The second important check to be done is the value of Fermi energy at the end of the first module. The SCF loop must converge the Fermi energy to a constant value in the last iteration. It can also be compared by plotting LDOS against energy E and checking if the lowest value of DOS with respect to energy is the same as the reported Fermi energy by the calculation.

The third optional check that can be done is the population density of different angular momentum states like s, p, d, f orbitals. The values of electronic configuration produced at the end of the first module for both the absorbing atom and the scattering atoms can be checked for justifying the orbital occupancy for the elements that are labelled as absorbing atom and scattering atom. If the absorbing atom is different in Z from the scattering atom then the orbital occupancy at the end of potentials

module can give an idea of the reasonable values of DOS for each atom type.

There are angular momentum cut-offs for calculating potentials and full multiple scattering. The probability of partially filled states in some systems as a result of hybridisation will affect any FEFF calculation. Hence additional angular momentum states have to be provided in the input for such systems. It is helpful also for other systems to have an additional angular momentum state as it doesn't affect the DOS if there is no contribution from it. Apart from these the charge transfer can be checked that gives a rough estimate of the oxidation state though it will be a fraction of the formal valence state. Charge-transfer transition is described as the transfer of an electron from the absorbing atom to the excited central metal atom. The transition will not involve the real transfer of an electron, but only a considerable reorganization of the charge density distribution around the excited central atom.

6.5 Fermi Energy

The corrections to be done for observed errors also have to be described in the event of any incorrect values being reported at the end of potentials calculations. If the potentials do not converge satisfactorily, the convergence accelerator "*ca*" parameter can be reduced to achieve convergence. The other option is to run potentials module for a known system and check with convergence and then re-run potentials module till well-converged potentials are obtained. As reported by FEFF software user's guide, Fermi energy could have an error of about 1 eV due to large changes in E_f, especially in semiconductors[5]. For most metals, this is not a problem and accurate E_f is reported by FEFF8. If there is an error in Fermi energy, it can be corrected using CORRECTION or EXCHANGE card in the input file. The next section will discuss the effect of self

energy and core-hole on the EEL spectra calculated by FEFF. It will also discuss the use of EDGE and HOLE cards for computing the EELS at specific energy edges.

6.6 Self Energy and Core-hole

EEL spectra arise from inelastic interactions of a beam of electrons with a thin sample in the electron microscope[6]. FEFF calculates EEL spectra using SCF approach which is based on *final state rule.* According to final state rule, the initial states are those calculated for the ground state and final states are those that are calculated with a screened core-hole. FEFF8 uses a self-consistent fully screened core-hole[4]. Self energy Σ (E) arises from the inclusion of inelastic losses in the calculation of final EEL spectrum and is energy dependent. It can shift the fine features in the spectrum by a systematic amount of energy and hence is an important consideration at energies above 30 eV[7]. This is the reason why it has to be integrated into the automated program for calculating excited final states for EELS. FEFF8 uses Hedin-Lundqvist[8] (H-L) self energy by default and results in good spectral match with experimental data for solids except a minor setback of having more peak broadening as compared with experiment. In the case of complex systems, other models for self energy like Dirac-Hara[5] can be used which are integrated as options in FEFF8.

6.6.1 Application of core hole for calculations

The effects of core-hole and self-energy attain significance because of the interpretation of EELS through LDOS from excited final states rather than ground state configurations. Hence the effects of self energy and core-hole have to be included in the calculations and FEFF8 does it by default. Optionally EELS can be generated by FEFF even without a core-

hole. The work described in this thesis was computed with default FEFF (i.e. with core-hole) and also without core-hole to assess its importance and no change in the shape of the spectra was observed for Mo $M_{4,5}$ and Fe $L_{2,3}$. However the intensity in the spectra has varied in the selected energy edge region (228-280eV for Mo and 720-780eV for Fe). This is shown in the figure 6.2 and 6.3 respectively.

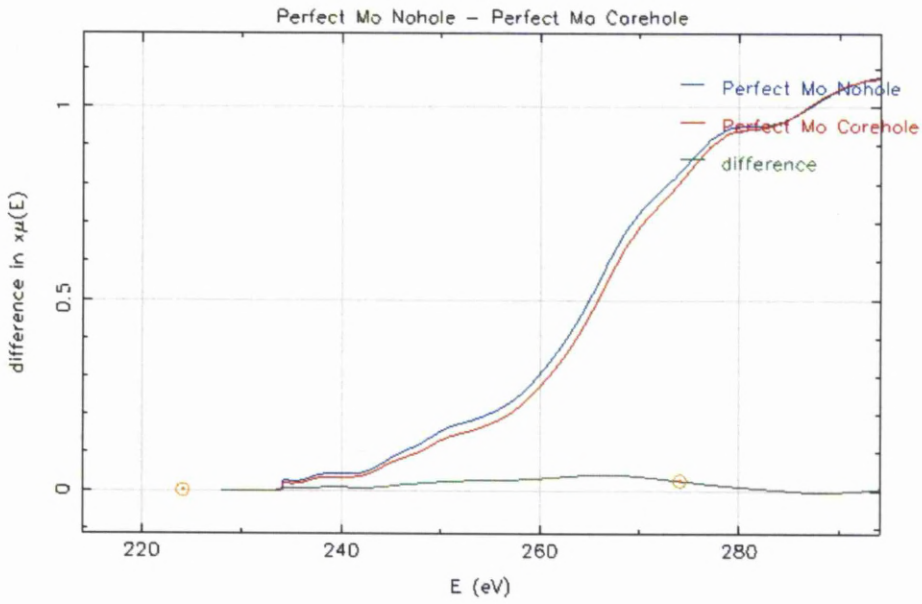

Fig.6.2. Comparison between Mo-$M_{4,5}$ ELNES spectra calculated with and without core hole.

The intensity decrease in the presence of a core-hole although appears in both Mo and Fe systems, the comparison between perfect crystal and screw core ELNES still holds good. This is because same parameters will be used for ELNES calculation for both perfect crystal and dislocation core i.e. either core hole or a screened core hole. Therefore any changes observed in the ELNES of dislocation core would be characteristic of the core configuration and not due to the presence of core hole.

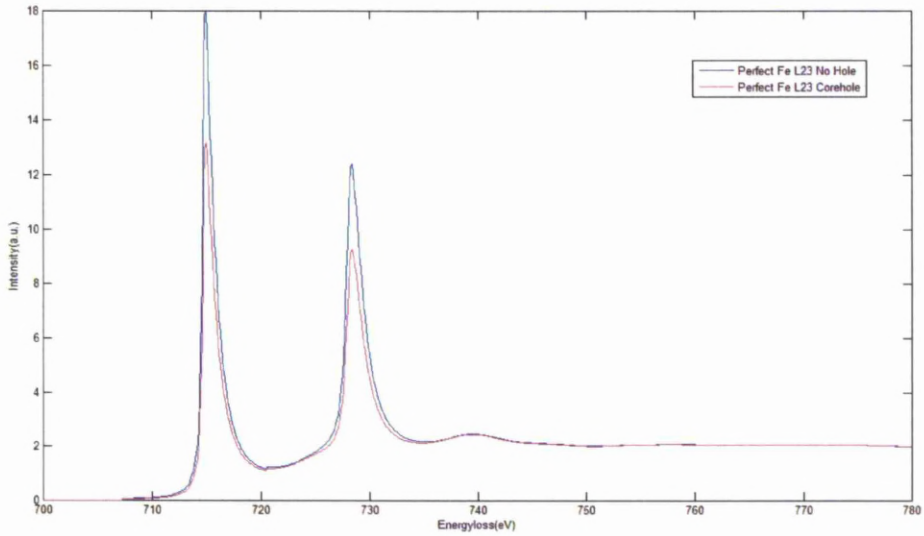

Fig.6.3. Comparison between Fe-$L_{2,3}$ ELNES spectra calculated with and without core hole.

This holds well even in the case of comparison of white line intensities for Fe $L_{2,3}$ edges. Hence the intensity ratio changes observed in the FEFF calculations for a dislocation core with respect to perfect crystal would be primarily due to the contribution from the electronic structure difference at the core.

An EDGE card is introduced in the input file for specifying the edge that has to be calculated by FEFF. Its arguments include edge or the core level (ex: "EDGE M4" calculates M_4 edge with M_4 hole). Instead of using EDGE card, HOLE card can also be used but the result is same as using the EDGE card. Calculations involving no core-hole should have NOHOLE card in the input file along with the EDGE card. Core-hole is important for EELS calculations of insulators and semiconductors.

In metals with EELS edges below 1000 eV, the core-hole potential can be completely screened out by the highly mobile electrons. This may be the reason NOHOLE often gives better results for such metal edges. The

metals to be discussed in this thesis are transition metals Mo and Fe and the edges of interest are Mo-$M_{4,5}$ and Fe-$L_{2,3}$ both of them well below 1000eV. Transition metals have extra available (unoccupied) states which make them good conductors which mean the mobility of electrons is quite high. Hence the core-hole may be completely screened at these metal edges and so EELS have to be calculated with NOHOLE card in the input file. Moreover, it is reported that better results with white line intensities were obtained for L_2 and L_3 edge when NOHOLE card is used[5, 9]. With core-hole in effect, the spectrum is shifted increasing the intensity near the edge and as a result the peaks appear sharp.

6.7 Calculation strategies

FEFF calculations need a prior plan for a desirable EEL spectrum to be produced. There are several options to choose from FEFF to get required output and therefore needs a calculation strategy. The prior information needed is the edge that is of interest and the atomic coordinates for the cluster to be used. The next step would be choosing all the necessary modules and output files from the standard cards. When these essential steps are finished, depending on the chosen energy range FEFF can calculate ELNES.

6.8 ELNES calculations

Near edge structure calculations can be highly time-consuming as discussed in theory. Full multiple scattering techniques are often preferred for ELNES over path expansion as the latter shows slow convergence near the edge. The cluster of atoms within a specified radius (in Angstroms) is used for ELNES calculations with the absorbing atom's position defined in it. All of the effective multiple scattering paths from the cluster are integrated into an infinite order by matrix

inversion. Given below is an example of the cards that are used for near edge structure calculations with in a finite cluster size:

```
SCF 6.0
XANES 8 0.07 0.0
LDOS  -20  50  0.3
FMS 6.0
RPATH 0.1
```

The SCF card will allow the self consistent approach for potential calculations along with Fermi energy using atoms within a radius of 6.0 Angstroms.

The second card (XANES) instructs FEFF to calculate near edge structure up to $k = 8\text{Å}^{-1}$, while the other two parameters in this card are used for specifying energy loss grid, with the size of the output k grid 0.07. The third parameter specifies the energy step of the grid at the edge. The default values for this card in FEFF are the same as shown above.

The density of states relates to the electronic structure of the metal and can predict the intrinsic properties of localised regions with in the sample. Therefore it is an interesting aspect studied in comparison with EELS experiments. FEFF8 calculates angular momentum projected density of states along with FMS.

The LDOS card specifies the minimum (-20eV) and maximum (50 eV) energies for ℓ-DOS calculation and the third parameter is the imaginary part of the potential (0.3) used in calculations. This card is useful when analysing the density of states for interpreting ELNES and when the self-consistency loop fails to converge. Angular momentum projected density of states calculated by FEFF in this example will have Lorentzian

broadening of about 0.3 eV and additional broadening due to effect of finite cluster size.

The FMS card will tell the FEFF8 program to perform full multiple scattering calculations for a cluster of radius of 6.0 Angstroms surrounding the absorbing atom. The radius of the FMS card can be different to SCF radius but cannot be less than the SCF radius. Instruction to avoid multiple scattering path expansion from being used in the FEFF calculations will be given by the last card RPATH.

6.9 Cluster size and convergence

Convergence is important factor even for ELNES calculations and is greatly dependent upon the cluster size. It is observed that increasing the number of shells for low Z materials like Si improves spectral features in ELNES and that spectral features contributing from a specific shell could be clearly distinguished [6]. This was shown for Mo $M_{4,5}$ in figure7.11 in chapter7. Repeated calculations could be performed with increasing cluster size till satisfactory convergence is obtained and until sharp structural features are visible in the spectrum. Comparison of LDOS with spectrum can help in attributing spectral features to electronic transitions.

6.10 Debye Waller factors

Thermal vibrations can affect the spectra by shifting the spectral features in the extended region of the EELS and broadening the peaks by a considerable amount. They have distinctive contribution to the EXELFS while their effect on near edge structure is subdued due to the absence of path expansion. Higher energy edges were said to be affected by temperature for ELNES [6]. When this standard card is introduced, it will approximate the effect of temperature by multiplying each free-electron propagator by a single scattering Debye-Waller (DW) factor exp ($-\sigma^2 k^2$)

when FMS calculations are done for ELNES. Since the EELS experiments are performed at specific microscope temperature and the energy edges discussed in this thesis lie beyond 1000 eV, the effects of temperature on ELNES calculated by FEFF could be ignored.

6.11 Other Parameters

Though other parameters have not been used for the work presented in this thesis, it will be useful to briefly outline the other parameters that could be used while calculating EELS by FEFF8. Collection and convergence semi-angles have not been accounted for by FEFF8. Only the EELS cross-section for forward scattering is calculated. FEFF can calculate the EELS for a given orientation of the sample. EEL spectrum from experiment shows changes in the fine ELNES features depending upon the orientation of the sample. Taking this into account FEFF input can be altered for sample orientation so as to match the experimental sample orientation. This can be done by introducing POLARIZATION card into the input file with the parameter being one of the x, or y, or z directions that relate to the beam direction in an electron microscope. An example is given below:

POLARIZATION 0.0 0.0 1.0

This card will calculate the EELS as if the beam is parallel to the z-axis of the Cartesian coordinate system of the cluster. In addition to all of the previously discussed cards, one other important adjustable card is CORRECTION. The life time of initial and final states added to the instrumental resolution can broaden the experimental spectra. The life times are taken care of automatically in FEFF8 while instrumental broadening can be added by CORRECTIONS card or EXCHANGE card. CORRECTIONS card adjusts Fermi energy and does a convolution that

tends to make the spectra smooth. EXCHANGE card adds Lorentzian broadening to the spectra by adding imaginary optical potential and sometimes can help convergence happen quickly. It is a better way to match the peaks with broadening by plotting the experimental and FEFF-calculated spectra together and then compare them for spectral changes.

6.12 Perfect crystal ELNES

The spectrum generated from a perfect crystal of molybdenum is compared with the experimental perfect crystal ELNES spectrum collected from a defect-free region of the sample. The spectra are shown in figures 6.4 and 6.5. The spectra are shown separately here since the tangential increase in intensity of one spectrum is variable with respect to other spectrum.

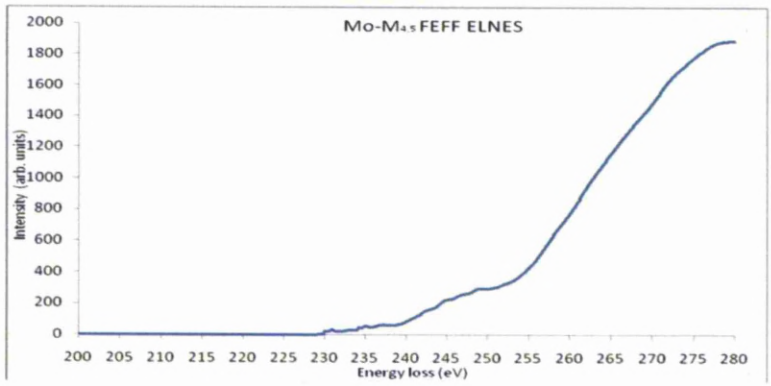

Fig.6.4. Mo-$M_{4,5}$ ELNES spectra for a perfect crystal of Mo calculated by FEFF.

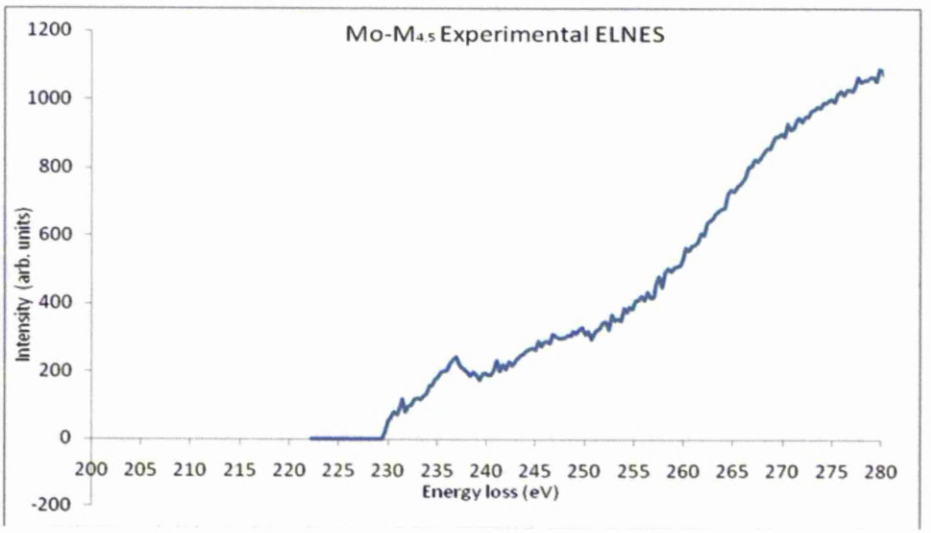

Fig.6.5. Experimental $M_{4,5}$ ELNES spectra of perfect crystal Mo.

It can be observed from figures 6.4 and 6.5 that M_4 edge onset is at 237eV and M_5 onset is at 229 eV. This agrees to the reported values of $M_{4,5}$ onset for perfect metallic molybdenum crystal[10]. In addition both spectra have similar changes in the shape in chosen energy windows. In the energy window 228 -240, both M_4 and M_5 peaks exist although in the FEFF ELNES spectra they cannot be distinguished clearly. Magnified image of this window from both ELNES spectra is shown in comparison in figure 6.6. Similarly there is a smeared small peak like region that extends between 240 and 250eV. There is a little dip in the intensity between 250 and 255 eV and further to 255eV there is a sharp increase tangentially until 280eV. The spectra have been limited to 280 eV in order to eliminate any contributions from the carbon K-edge at 285eV.

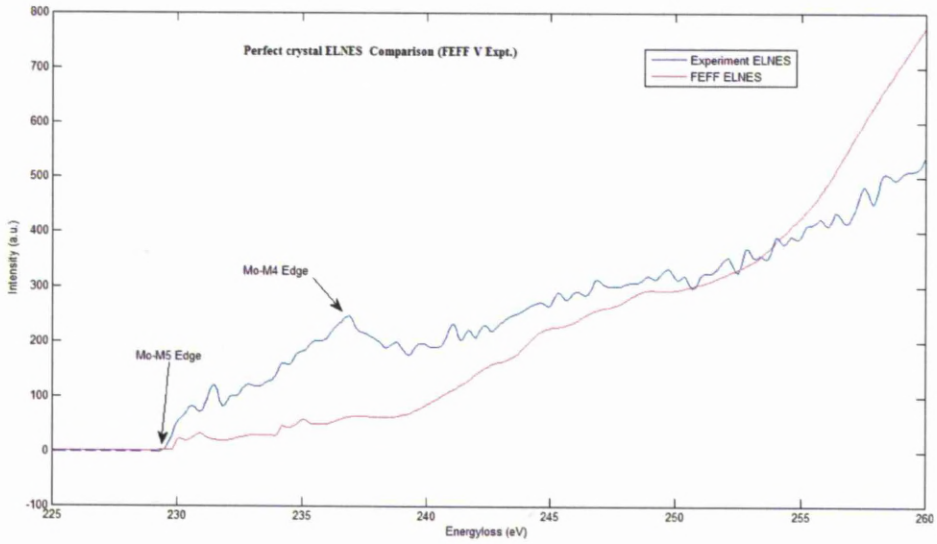

Fig.6.6. Comparison between Mo-$M_{4,5}$ ELNES of perfect crystal calculated by FEFF and ELNES from experiment.

Although the intensity is arbitrary in units, the important feature to note is the shape of the curves in both spectra that appear to be similar. Even though instrument resolution, noise and other factors like core-hole life time can alter the width of the peaks to a certain extent in experimental spectrum, it can be seen from figure 6.6 that the basic changes in the shape of spectra remain very much similar. Therefore the ELNES comparison between the spectra calculated from FEFF and the spectra obtained from experiment can be justified under the relevance of the above similarity. This will make it easy to identify that any changes to the spectra can only be from the additional presence of unoccupied states or their absence and investigating any big changes in ELNES hence can be directed to the changes occurring at screw dislocation core.

6.13 Summary

This chapter presented a detailed discussion of the practical aspects of calculating an electron energy loss spectrum by using *ab initio* code

FEFF8. The theoretical ELNES results from FEFF and the spectral comparison of perfect and dislocated crystals will be discussed in the next chapter.

References:

[1] A. L. Ankudinov, B. Ravel, J. J. Rehr, S. D. Conradson, Physical Review B 58 (1998) 7565.
[2] P. Rez, D. A. Muller, Annual Review of Materials Research 38 (2008) 535-558.
[3] M. Ohno, G. A. van Riessen, Journal of Electron Spectroscopy and Related Phenomena 128 (2003) 1-31.
[4] FEFF, FEFF wiki: http://leonardo.phys.washington.edu/feff/wiki in: 2009.
[5] FEFFTeam, FEFF8.4 User's Guide (provided with FEFF software), in: 2006.
[6] R. F. Egerton, Electron energy-loss spectroscopy in the electron microscope, Plenum Press, New York, 1996.
[7] J. J. Rehr, A. L. Ankudinov, Coordination Chemistry Reviews 249 (2005) 131-140.
[8] L. Hedin, S. Lundqvist, Solid State Physics 23 (1969) 1–181.
[9] S. Alam, J. Ahmed, Y. Matsui, Applied Surface Science 241 (2005) 199-204.
[10] F. W. a. E. Minni, Journal of Physics C: Solid State Physics 16 (1983) 6091.

Chapter 7

Theoretical results

Chapter 7

THEORETICAL RESULTS

7.1 Calculations using FEFF8.4

This section describes the theoretical calculation of ELNES spectra using FEFF8.4. FEFF is an automated *ab initio* code based on real space multiple scattering formalism that can calculate site specific symmetry projected local density of states as well as the ELNES spectrum[1]. In this research FEFF is chosen for theoretical calculations because of the reasons discussed in chapter 4.

The basis for ELNES calculations by FEFF is the inclusion of multiple scattering calculations. Full multiple scattering calculations in FEFF generate ELNES spectra from a cluster of atoms within a given radius. The central atom is the excited atom which initiates the scattering event and is surrounded by the neighbouring atoms which are responsible for scattering. Hence the calculations are property of local environment of excited atom and the surrounding atoms are divided into shells with specific orientation. Since the scattering is contained within specific radius (typically about 1 nm)[2] , only moderate number of shells are required.

A schematic diagram of multiple scattering and single scattering events is shown in figure 7.1.

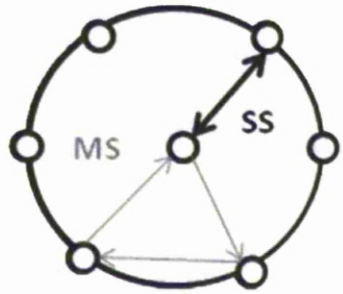

Fig. 7.1 Single and multiple scattering events from a central (absorbing) atom towards the scattering (shell) atoms.

Extensive computing power is necessary for large cluster FMS calculations. However, satisfactory results can be obtained by selecting optimum number of shells. For the ELNES calculations described in this thesis, 300 atoms sufficient enough to fill 4 shells around the central absorbing atom were included in the cluster. The number of atoms in the clusters of perfect crystal and dislocated crystal was same for both Mo and Fe. This was important to make the calculations interpretable and comparable.

7.2 Cluster generation

The starting point in FEFF calculations is the generation of a cluster of atoms separated by unit distances. They are later multiplied by the lattice parameter of the metal in order to convert them into a cluster of that specific metal. The input file of FEFF requires the Cartesian coordinates of atoms located at known distances from the central atom of the cluster[3]. While most common structures like bcc or f.c.c can be generated by ATOMS software[4], complex structures are difficult to generate like interfaces and defects. Due to the random distribution of atomic coordinates near the dislocation core, it is essential to use models generated by well accepted methods. However an already known simulated model can provide the coordinates for such a cluster.

The atoms coordinates used in this research were provided by materials modelling group based at university of Liverpool. These were generated from molecular dynamics model based on interatomic potentials known as Mendeleev (2000)[5] and Ackland (2004)[6] potentials. A description (in square brackets) of the procedure adopted by materials modelling group to generate co-ordinates is given below:

[A perfect bcc crystal with large number of Cartesian coordinates (in the range of a million) was produced and a dislocation was introduced into the crystal at specific coordinates close to the centre of the crystal. Interatomic potentials with periodic boundary conditions were then applied onto the crystal and the crystal was allowed to relax at finite temperature condition. The Cartesian coordinates of the relaxed crystal changed due to the displacement of atoms near the dislocation core.]

The changed coordinates were provided as input for the theoretical calculations described in this thesis. 300 atoms were extracted from a set of nearly a million Cartesian coordinates with the dislocation core atom at the centre of the cluster. This will ensure the dislocation core is effectively included in multiple scattering calculations. The extraction of 300 atoms neighbouring the central atom was done using a program written in FORTRAN and executed using g77 FORTRAN compiler. This extraction program is listed in the appendix.

The extraction program was given an input of total number of atoms, the number rows in which they were distributed, the Cartesian coordinates of the central atom and the radius of cluster for extraction. An example input file for extraction program is shown below:

```
2072847      : number of coordinates

12           : number of columns

52.2432098  60.6016006  38.6227798  : origin
x,y,z  ( must be in real number form)

4.0          : range  (real number)
```

300 atoms close to the given central atom were selected from the output. They will be referred by the name "*skeleton*" coordinates in this thesis.

Skeleton coordinates were multiplied by the lattice parameter of Mo (3.147Å)[7] and Fe (2.867Å)[7] to produce individual ATOMS models with dislocation core in the centre. ATOMS models were used to identify and alternate the dislocation core atoms for further FEFF calculations. Different core models for screw dislocation using different core atoms were generated. Apart from the dislocation model, a perfect bcc crystal model was also generated by entering the coordinates manually. ATOMS models of perfect crystal and dislocated crystal were checked for any missing atoms or repetition of atomic coordinates and were ensured that they were in the appropriate <111> orientation. The atomic coordinates were then used in the input file for FEFF. The ATOMS models of Mo and Fe that were generated using a cluster of 300 atoms with dislocation and perfect crystal are presented in the next sections. The FEFF input and output files were explained in the previous chapter. The ELNES and LDOS data contained in the output files was used to generate theoretical spectra.

7.3 Comparison

The plotted ELNES and DOS spectra from dislocation and perfect crystal were compared with each other to observe any changes in the spectra. ELNES spectra were subtracted the same way as the experimental spectra were done using spatial difference technique. This can be written as:

$$\mu_d(E) = \mu_{core}(E) - \mu_{perfect}(E) \quad (7.1)$$

where $\mu_d(E)$ is the difference spectrum, $\mu_{core}(E)$ is the ELNES spectrum from dislocation core and $\mu_{perfect}(E)$ is the ELNES spectrum from perfect crystal. This difference spectrum $\mu_d(E)$ is then compared with the spatial difference spectrum from experiments I_{SD}. FEFF calculations were done for different atoms around the dislocation core and the results were compared for changes in ELNES and DOS. The M_4 and M_5 edges for molybdenum and L_2 and L_3 edges for iron are calculated independently and then integrated into a single spectrum with common energy grid. Thus ELNES spectra at $M_{4,5}$ and $L_{2,3}$ edges were calculated theoretically using FEFF8.4. The observed changes from ELNES and DOS are reported in the next section.

Note: The FORTRAN source code for extraction program written by materials modelling group at university of Liverpool is given in the appendix section.

7.4 ELNES sensitivity to different core atoms

The FEFF calculations were an important part of this research work that helped to understand the effect of the dislocation core on the ELNES of various atoms around the core. ELNES calculations were performed for different atoms around the core and their results were analysed. It was evident from the results that the changes in the ELNES were diminishing as the atoms chosen for calculations were getting distant from the core. As the distance between the screw dislocation core and the atom chosen for ELNES calculations increased, the ELNES changes decreased. ELNES also varied from atom to atom around the core. This was shown in the series of figures from figure 7.2 to 7.5.

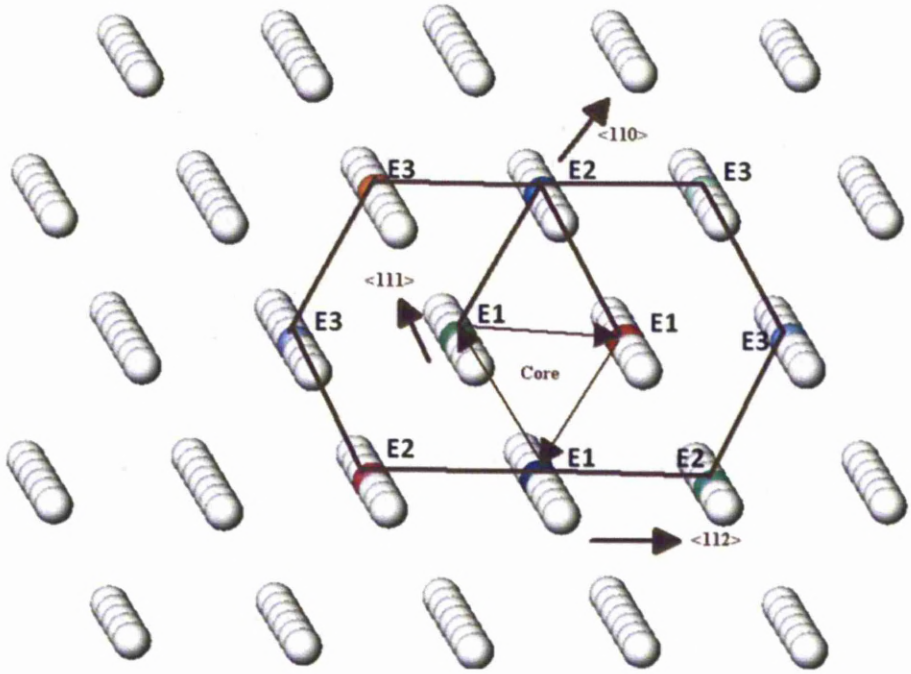

Figure 7.2 Screw dislocation easy core showing different atoms around the core for which ELNES calculations were performed.

The ELNES spectra shown in the figures below were with respect to the colour of the atoms shown in figure 7.2. E1, E2 and E3 were the types of ELNES observed at the respective atoms.

All atoms marked E1 exhibited same kind of spectra as shown in the figure 7.3. An atom exhibiting E2 type change was shown in figure 7.4 and E3 type was shown in figure 7.5. This demonstrated that atoms at the same distance from the core and with same configuration undergo similar transitions and hence similar near edge structure.

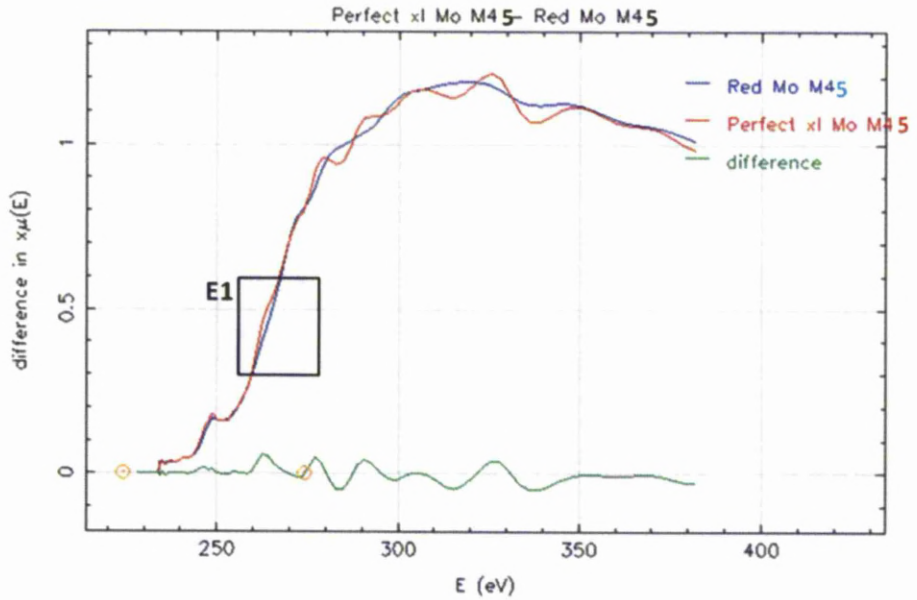

Figure 7.3 E1 type spectra showing changes in ELNES from screw core atoms. Green, red and blue atoms marked as E1 and connected by arrows in figure 7.2 exhibited this type of change in their spectra.

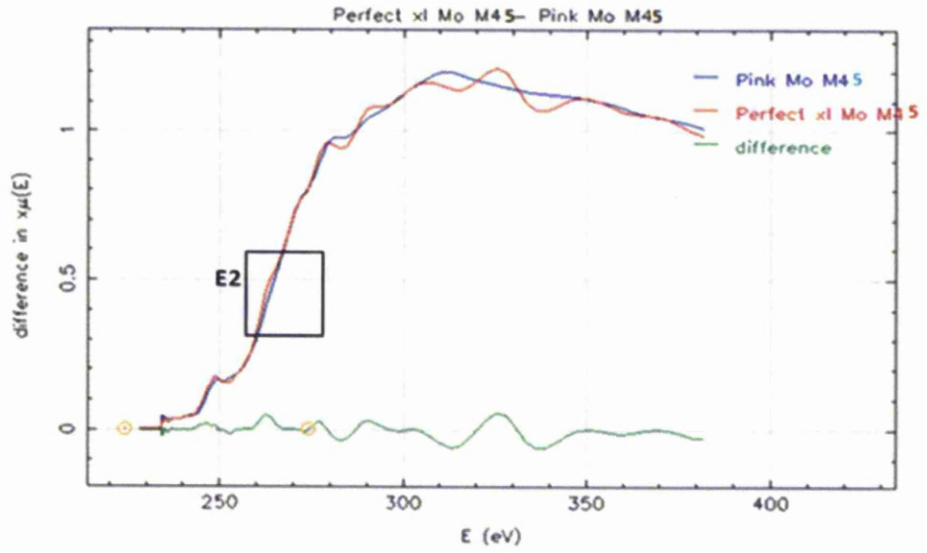

Figure 7.4 E2 type spectra showing smaller change than E1 and was exhibited by atoms marked E2 in figure 7.2.

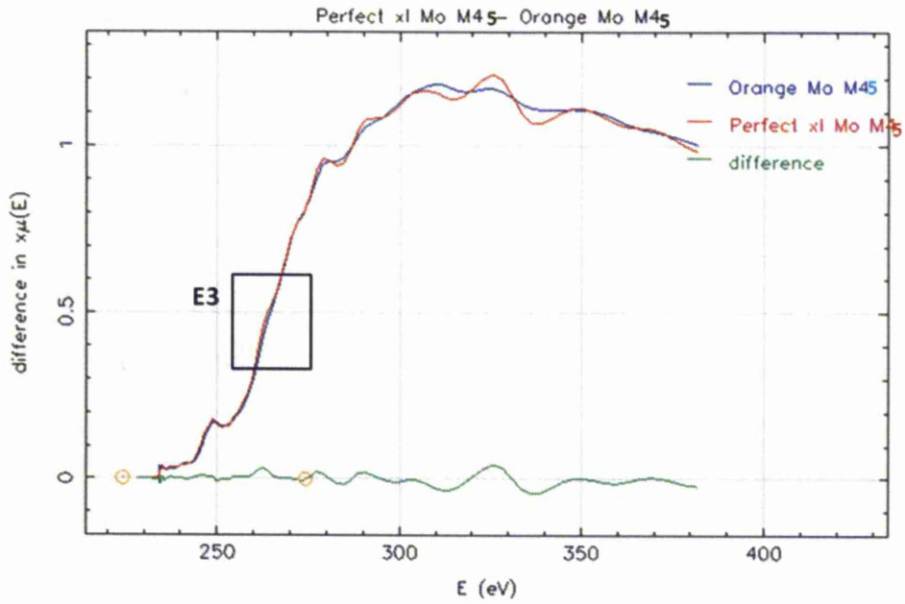

Figure 7.5 E3 type spectra showing smallest change compared to E1 and E2. This type of ELNES was exhibited by atoms marked E3 in figure 7.2.

The E1, E2 and E3 type changes can be studied by closely observing the spectra in the energy window of 224-274eV. These changes are shown clearly in the figures 7.6, 7.7, and 7.8. In these figures, it can be seen that the extent of changes observed between the screw dislocation core and the perfect crystal reduces as the distance between the central atom of the cluster and the core increases. The difference spectra for each type of ELNES (E1, E2 and E3) show a significant change in the shape of the spectra from 240eV to 270eV. As the peaks in this region appear sharp in the difference spectra for E1 and gradually reduce till E3, it can be said that the smearing of peaks in ELNES of dislocation core causes such a change when compared with perfect crystal.

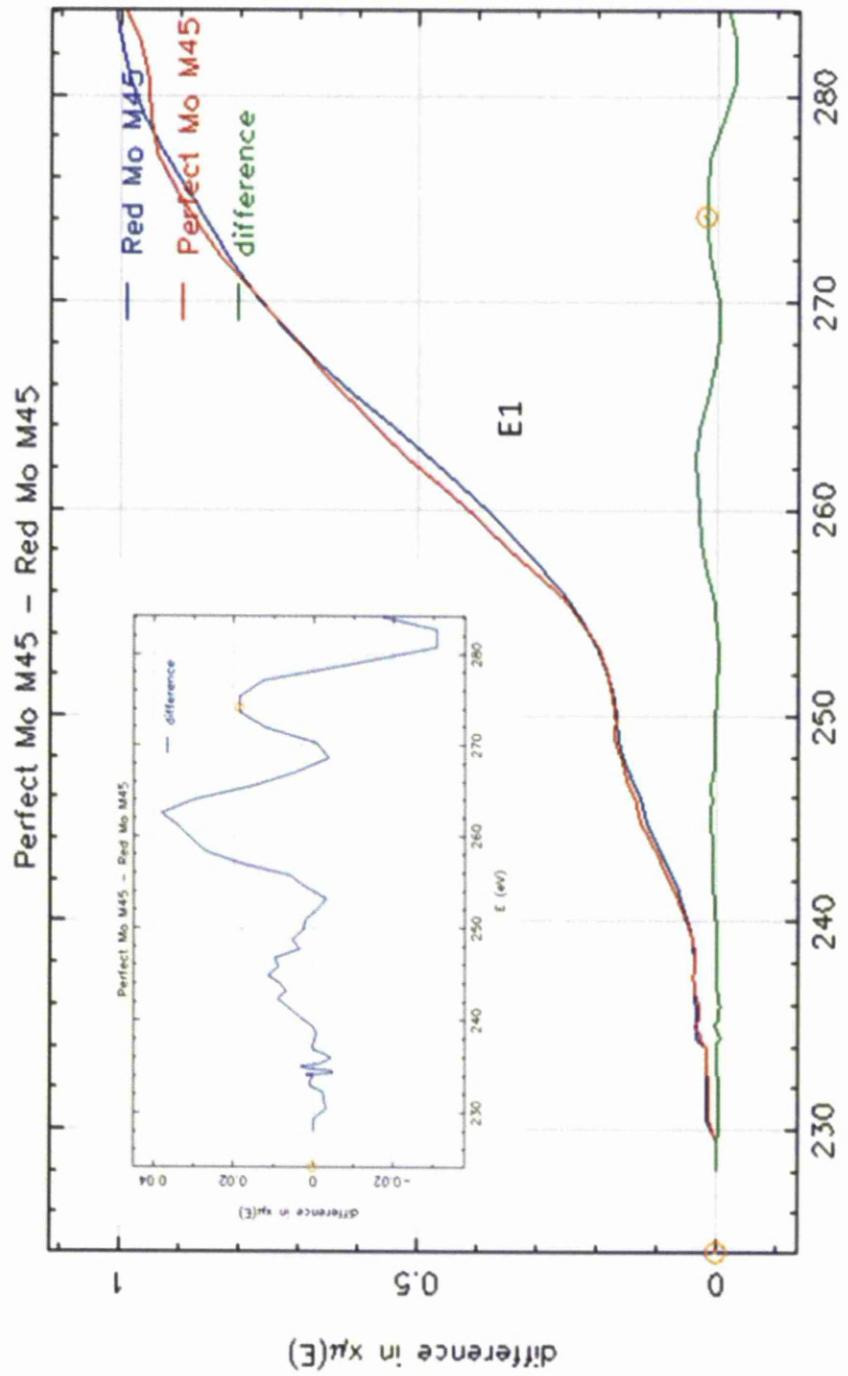

Fig.7.6. E1 type ELNES observed from the core atom (marked in red in fig.7.2). The difference spectrum is also shown with in the selected energy range.

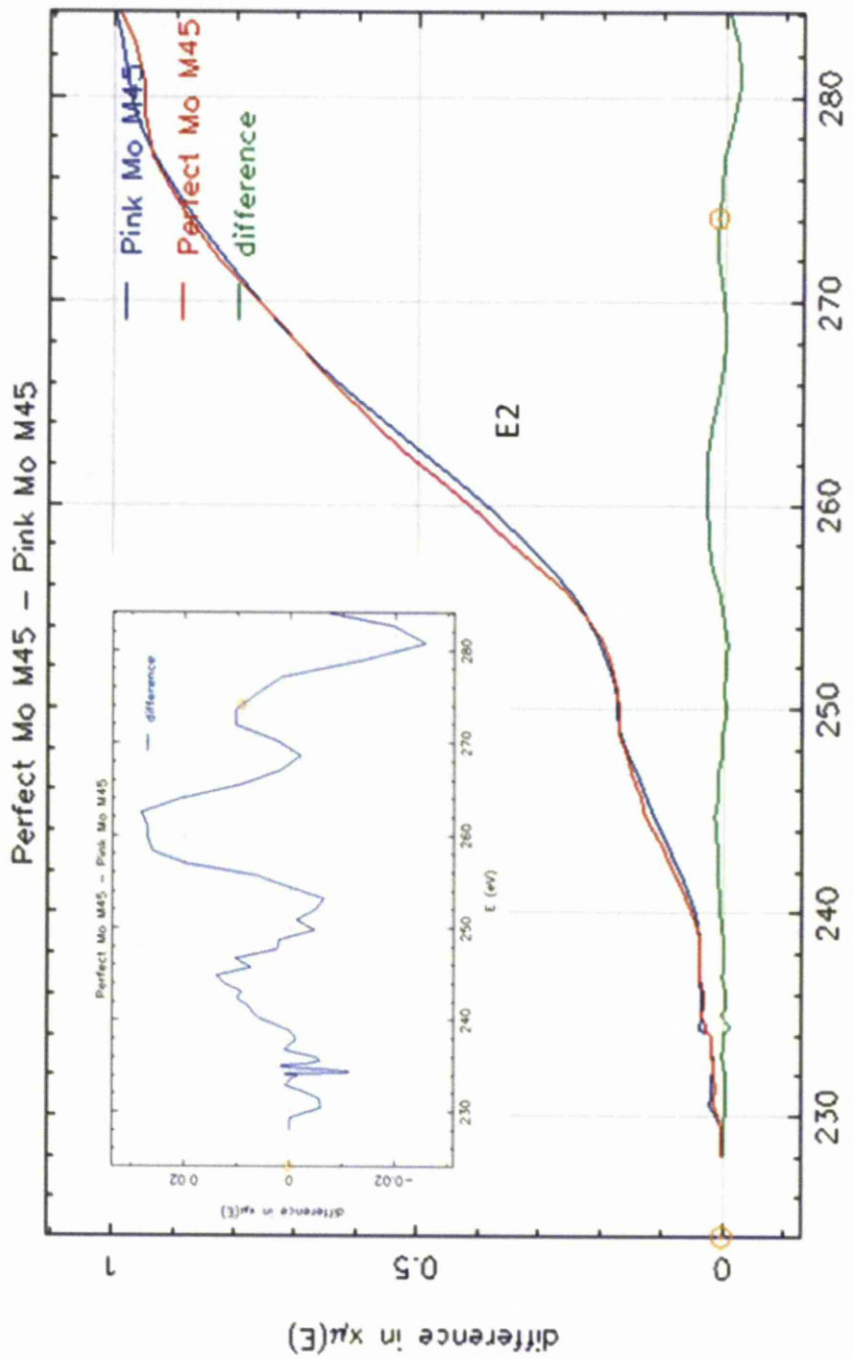

Fig. 7.7. E2 type ELNES observed from the core atom (marked in pink in fig. 7.2). The difference spectrum is also shown for the selected energy range.

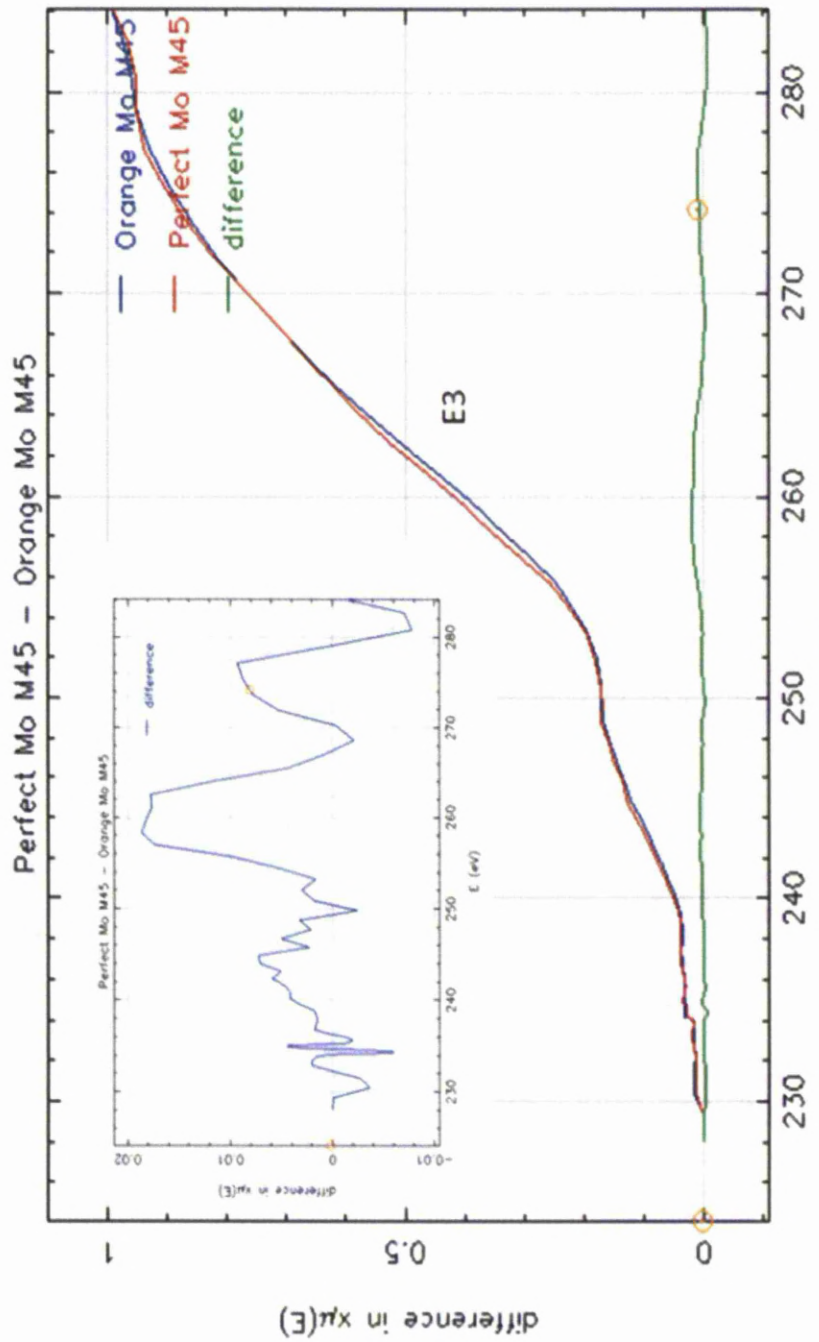

Fig 7. 8. E3 type ELNES observed from the core atom (marked in orange in fig 7. 2). The difference spectrum is also shown for the selected energy range.

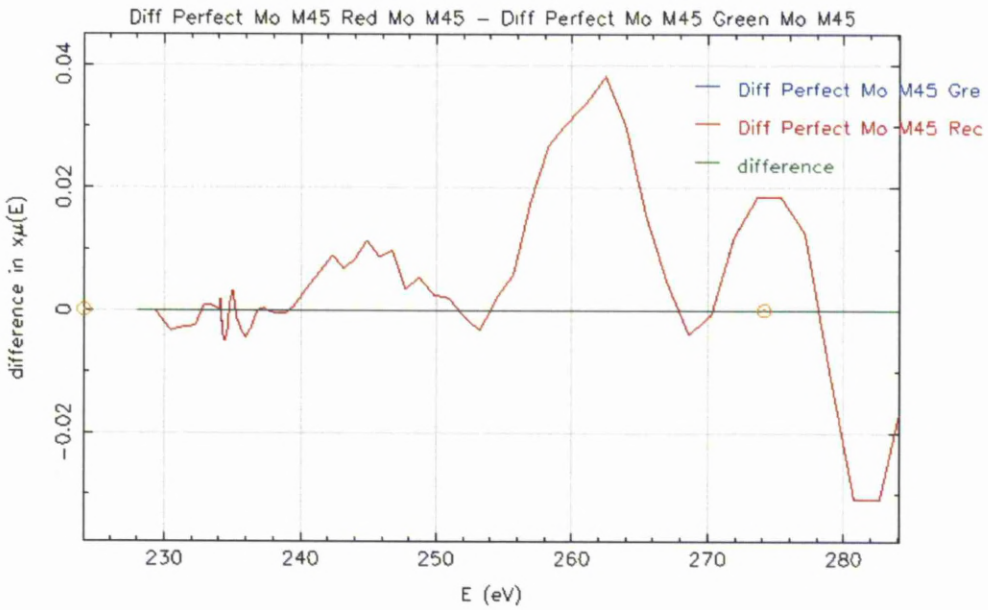

Fig.7.9 The difference spectrum of two E1 type ELNES spectra (calculated from red and green coloured atoms in fig.7.2.)

The core atoms marked in red and green colour in figure 7.2 are of equivalent configuration and they show similar changes with respect to perfect crystal. Figure 7.9 shows the difference spectrum between the E1 type ELNES changes at green atom and red atom. It can be seen from the figure 7.9 that the dislocation core atoms with equivalent configuration show same type of ELNES change and that the difference between these two difference spectra is negligible. The difference spectrum that is marked in blue (green atom E1) does not appear as it is masked by the shape of the spectra marked in red. However, close inspection of the difference spectrum of both E1 type spectra (shown in green in 7.9) was done to identify the minute changes of the order of 10^{-5} units. This difference spectrum is shown in figure 7.10. It could also give an estimate about the errors in calculations, if same type of spectral changes

were assumed to be observed from the three core atoms surrounding the core.

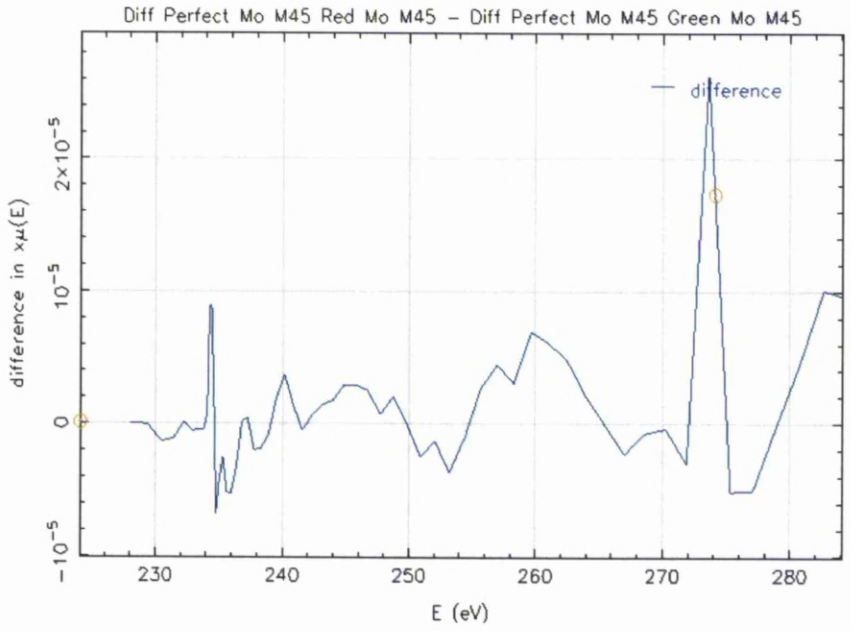

Fig.7.10. Difference in E1 type ELNES changes observed at different core atoms of equivalent configuration. These changes can be attributed to the characteristics of each core atom although they occupy equivalent atomic sites at the core. These changes are site-specific and unique to each core atom.

7.5 Convergence in FEFF calculations

The fine features of an ELNES spectrum calculated by FEFF are dependent on the size of the cluster. If the number of shells included in the calculations has increased, the fine details in the ELNES became much more evident. FEFF calculations were checked for convergence for different sized clusters with different number of shells. The spectra obtained by calculations with different shells are shown in figure 7.11.

The fine structural details in the spectrum started to show with the inclusion of more number of shells. The number of shells used for the calculations presented in this thesis was limited to 4 because more number of shells requires more time and better computing memory. A future recommendation would be fast parallel calculations using a big computing cluster that could generate spectrum with very fine structural details.

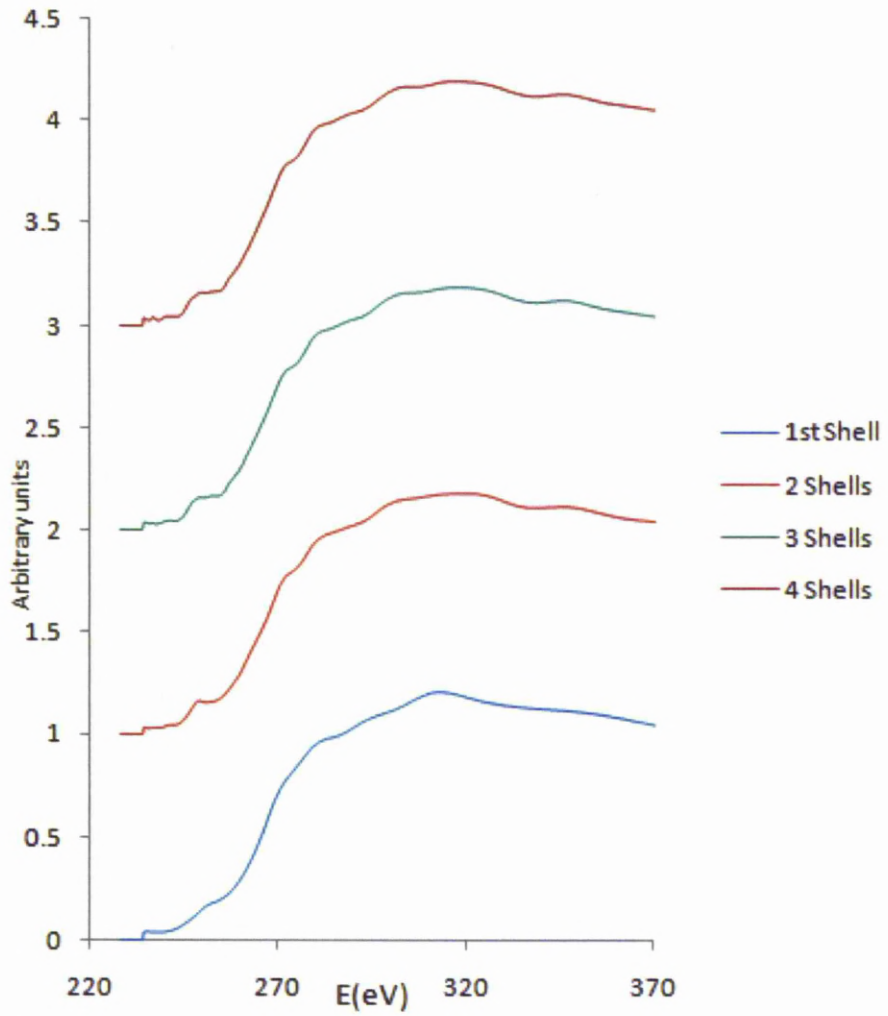

Fig.7.11.Comparison of Mo $M_{4,5}$ spectra calculated with different number of shells.

7.6 Theoretical calculations: Mo

FEFF 8.4 was used to calculate the theoretical EEL spectra for a cluster of 300 atoms of molybdenum. Basically two types of theoretical spectra were calculated.

1. EEL spectra for a perfect crystal of molybdenum.

2. EEL spectra for crystal containing dislocation (screw, edge or mixed).

FEFF calculations were done using a cluster of 300 Mo atoms with in a definite radius; their atomic co-ordinates and their distances from the centre were specified in the input. For the first type of spectra, the cluster was generated using standard bcc crystal structure coordinates. For the second type, co-ordinates were provided by the multi-scale modelling group at university of Liverpool. The crystal generated by these co-ordinates contains a relaxed dislocation (specifically screw or edge or mixed) at the centre of the crystal with different core configurations as specified by the modelling group. Dislocation co-ordinates generated by two different codes known as Mendeleev and Ackland were provided.

For many years ½[111] screw dislocations in molybdenum were studied for their core structure using different computer models[8]. Mendeleev and Ackland were two different interatomic potentials that were used by Materials Modelling Group based at University of Liverpool. The change in core configuration was thought to change the scattering conditions and hence could result in different ELNES and LDOS for different screw dislocation cores.

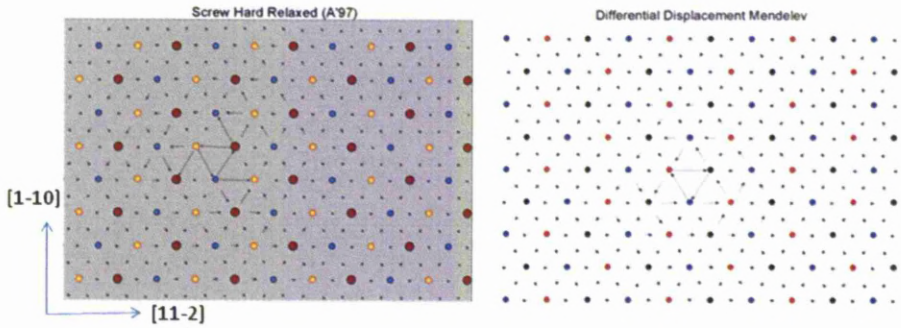

Figure 7.12 Differential displacement maps of screw dislocation core configurations provided by materials modelling group at university of Liverpool; image on the left was screw hard core generated by Ackland potentials and on the right was screw easy core generated by Mendeleev potentials. The circles represent the atomic positions while the arrows indicate the displacement of atoms along [111] direction.

The dislocation character and the code with which they were developed would be specified while presenting the theoretical calculation results in this section.

The input cards used for calculations and the calculation strategy were already described in the experimental techniques chapter and the input file containing the co-ordinates was added to the appendix.

Three types of dislocations were studied in the [111] orientation using FEFF calculations, screw (Mendeleev and Ackland potentials), edge (Mendeleev) and mixed dislocation (Ackland). Two types of screw dislocations were investigated, one with an easy and the second with a hard core. The input co-ordinates were sorted so that one of the atoms along the dislocation core was at the centre of the cluster. Full multiple scattering calculations in FEFF were done with the dislocation core atom as the central absorbing atom.

7.6.1 Screw dislocation Vs perfect crystal Mo FEFF results

FEFF calculations for perfect Mo crystal and dislocated Mo crystal were done using the same input cards but with different atomic co-ordinates. The changes in ELNES region of the EEL spectra were studied by choosing different neighbouring atoms of the dislocation core as the central atom in the cluster and comparing their ELNES spectra. Since the fine structure seen above the absorption edges relate to site-specific and symmetry-projected density of unoccupied states, the LDOS calculations were also done. ELNES changes at dislocation core were thought to be due to transitions occurring between different shells and were studied with respect to density of states in this research work.

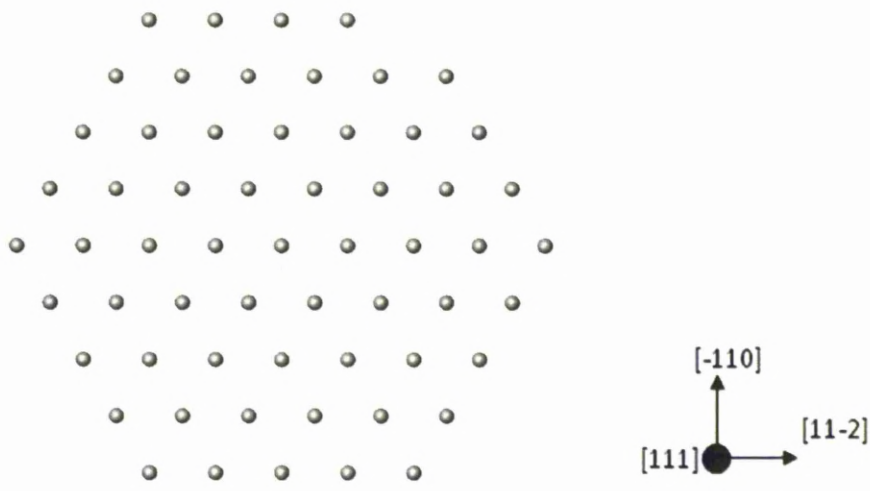

Figure 7.13 ATOMS© model of Mo perfect crystal with 300 atoms in [111] direction. The crystallographic axes are shown for [111] orientation.

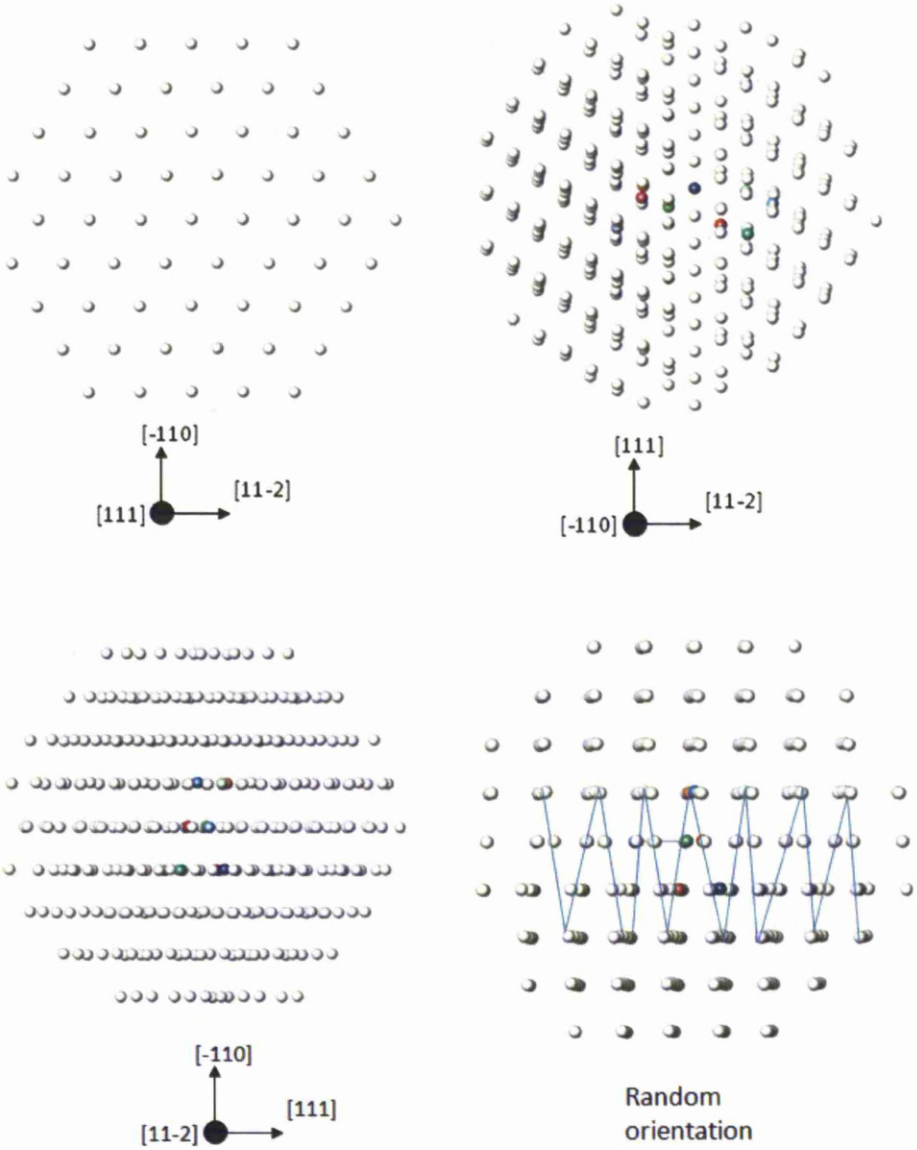

Figure 7.14 ½[111] Screw dislocation in 300 atoms cluster of Mo shown in various projections; Screw dislocation line direction was [111], hence the displacement of atoms were along the [111].Top left image is the [111] orientation which did not show any displacement of atoms. Top right projection is [-110] and the displacements are visible but the screw helix cannot be identified in this direction. Bottom left is [11-2] projection and the bottom right image is a random orientation of crystal

which shows screw helix. The shear displacements of atoms in the upper and lower half of the crystal are visible in this orientation.

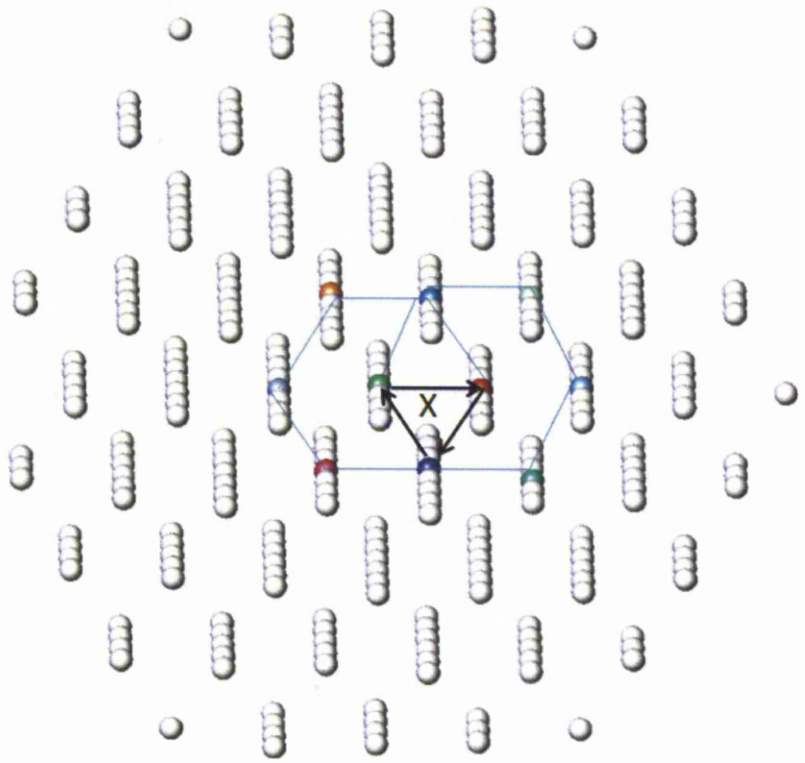

Figure 7.15 ATOMS© model showing the ½[111] screw dislocation in bcc Mo tilted slightly towards [-110]. The dislocation core atoms connected by black arrows were identified in this projection along with other surrounding atoms.

X was the relaxed easy dislocation core and the atoms connected by arrows have undergone maximum displacements along [111] direction. The green core atom was the centre of the cluster and the absorbing atom for FEFF calculations.

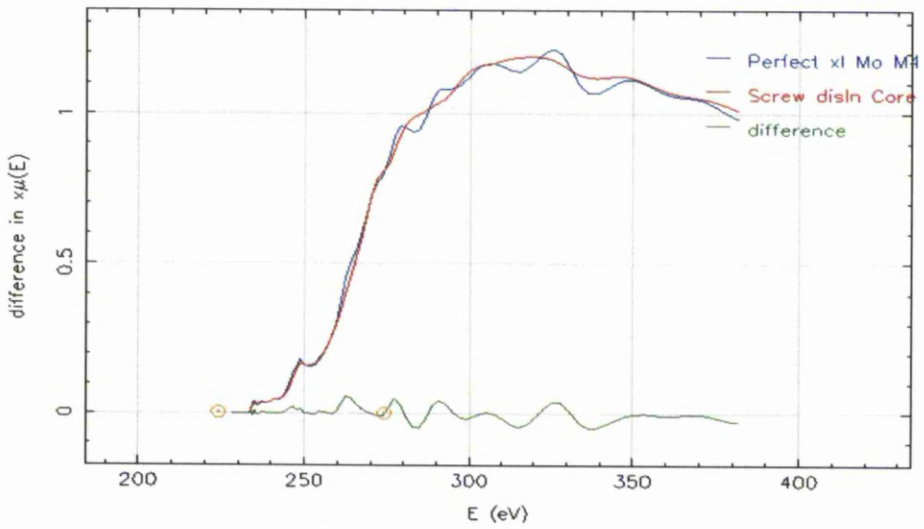

Figure 7.16 Comparison of theoretical ELNES at molybdenum $M_{4,5}$ edge between perfect crystal (blue) and screw dislocation easy core (red). The green spectrum is the difference between perfect crystal $M_{4,5}$ ELNES and screw core $M_{4,5}$ ELNES. The ELNES energy window used for comparison without carbon K-edge interference is located in between the marked orange points on the difference spectrum.

The changes observed before 260eV are comparatively small but major changes start from 260 eV and continue up to 350eV. However, the region of interest was only 227 to 285 eV since 285eV was the onset for carbon K edge. The changes observed in this energy range are shown in figure 7.17 and the difference spectrum between both spectra is shown in figure 7.18.

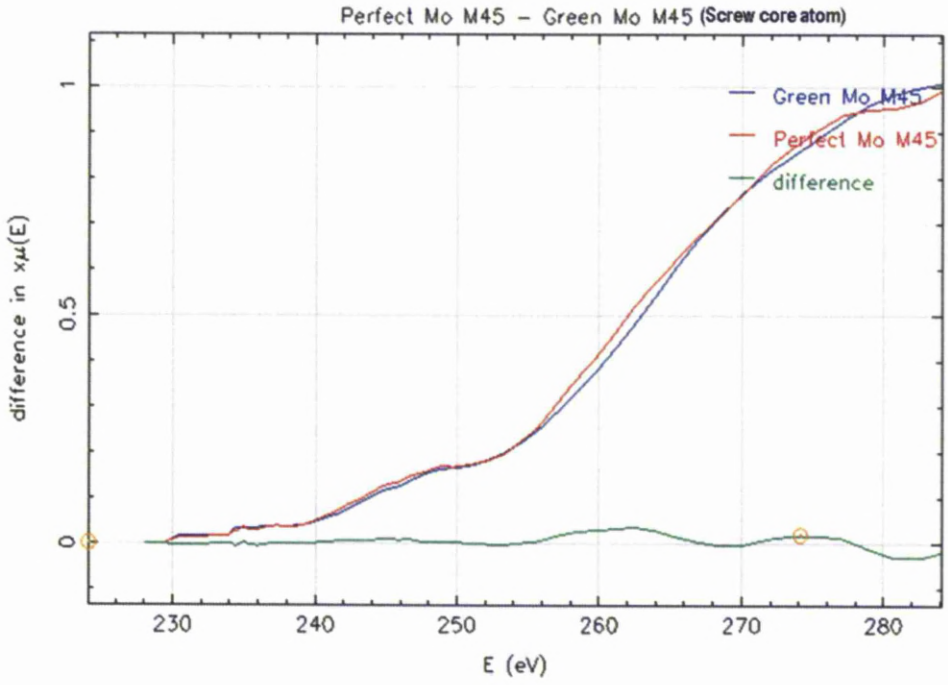

Fig.7.17 Comparison of Mo-$M_{4,5}$ ELNES of a screw dislocation core with that of a perfect crystal in the energy window 220-280eV.

The spectrum in blue is the screw dislocation core ELNES obtained from one of the three core atoms (atom marked in green) in figure 7.15. The red spectrum is from an atom in the perfect crystal. The green spectrum is the difference spectrum of dislocation core with perfect crystal.

The changes that occur in the selected energy region are very small and hence detailed observation of difference spectrum can help identify them. The energy range in which the changes are being investigated is shown by the circles at the onset and after the delayed threshold of $M_{4,5}$ edge.

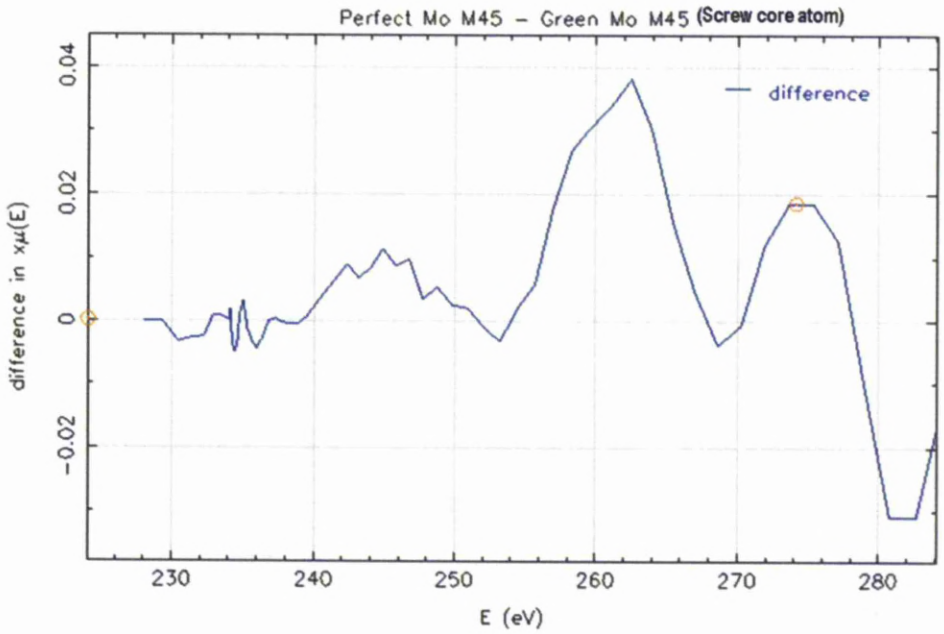

Fig.7.18 The difference spectrum of screw dislocation core and perfect crystal Mo $M_{4,5}$.

The shape changes observed in the difference spectrum shown in figure 7.18 and 7.19 can be used as a reference to check if similar changes are observed in experimental spectra on and off the dislocation core. Figure 7.19 is a magnified image showing the region which contains the changes in fine structural details of a dislocation core with respect to perfect crystal. It can be noticed in figure 7.18 that the M_5 peak of screw core dominates the perfect crystal thereby showing negative difference between 230 and 240eV.

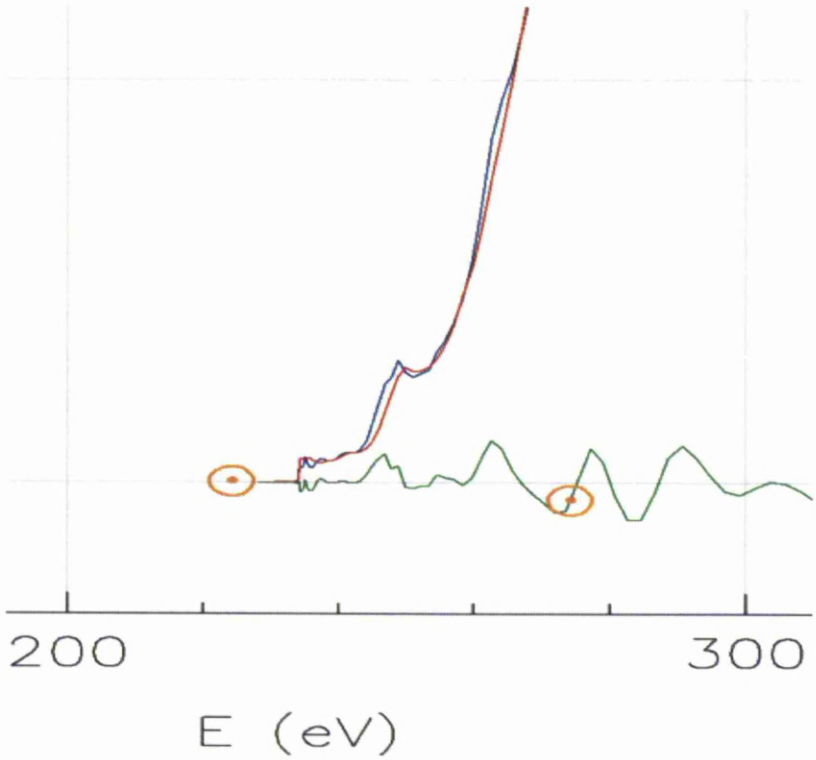

Fig.7.19. Mo $M_{4,5}$ Near edge structure of a screw dislocation core (red curve) with reference to perfect crystal (blue curve). Changes in $M_{4,5}$ peaks are observed at 244eV, 262eV and 270eV respectively.

Angular momentum projected density of states (ℓ-DOS) were also calculated by FEFF8.4 for each distinguishable atom. DOS and ELNES data helps connecting spectral features to transitions to particular states[9]. $M_{4,5}$ edge corresponds to $3d^{3/2}$ (M_4) and $3d^{5/2}$ (M_5) transitions to unoccupied states and hence M corehole. The unoccupied angular momentum states probed by EELS for Mo- M edge are p and f and hence theoretical (p+f) DOS will be investigated here for dislocation core and perfect crystal to estimate the d-band occupancy in either case.

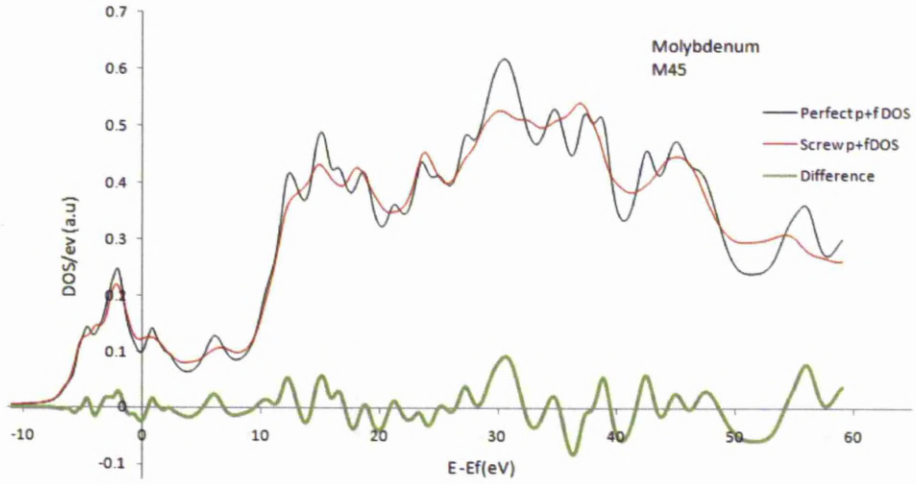

Figure 7.20 Figure showing the site-specific symmetry-projected density of states (LDOS). Comparison of (p+f) DOS between perfect crystal molybdenum and screw dislocation core at $M_{4,5}$ edge.

In figure 7.20, significant changes in the LDOS of screw dislocation were observed. Perfect crystal LDOS had sharp peaks while the screw dislocation curve had short and blunt peaks at most energies. The Fermi energies for perfect and screw dislocation calculations (-9eV) were corrected from energy scale and then plotted onto the grid for comparison. The extended width of the peaks in the case of screw dislocation suggest the availability more empty states at a given energy level. The loss of symmetry of the shells at the core region also might contribute to this effect. The difference spectra in figure 7.20 and figure 7.19 reveal common features regarding the fine structure and those are the changes occurring beyond the edge threshold. The previously mentioned changes in $M_{4,5}$ peaks in figure 7.19 can be directly compared with differences noticed in figure 7.20. The hard core screw dislocation model used for ELNES simulations is shown in figure 7.21 in different orientations. The screw helix can be clearly seen and is marked.

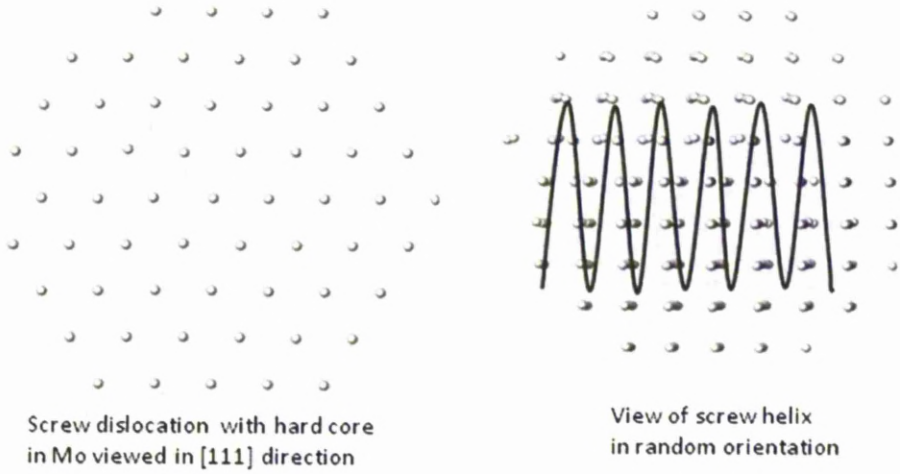

Figure 7.21 ½[111] screw dislocation with a hard core configuration in molybdenum and the screw helix visible at random tilt towards [11-2].

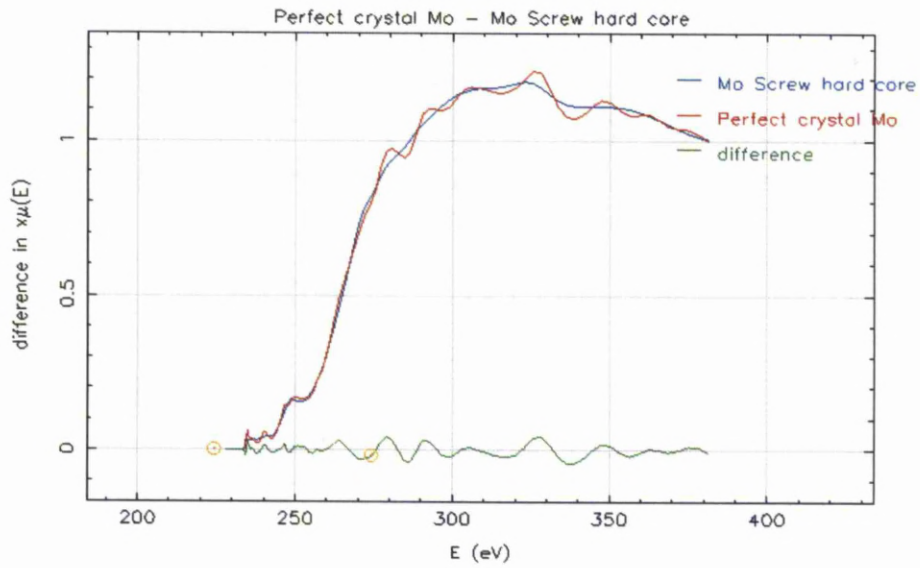

Figure 7.22 a) Comparison between computed Mo $M_{4,5}$ ELNES spectra of perfect crystal and screw dislocation with hard core configuration.

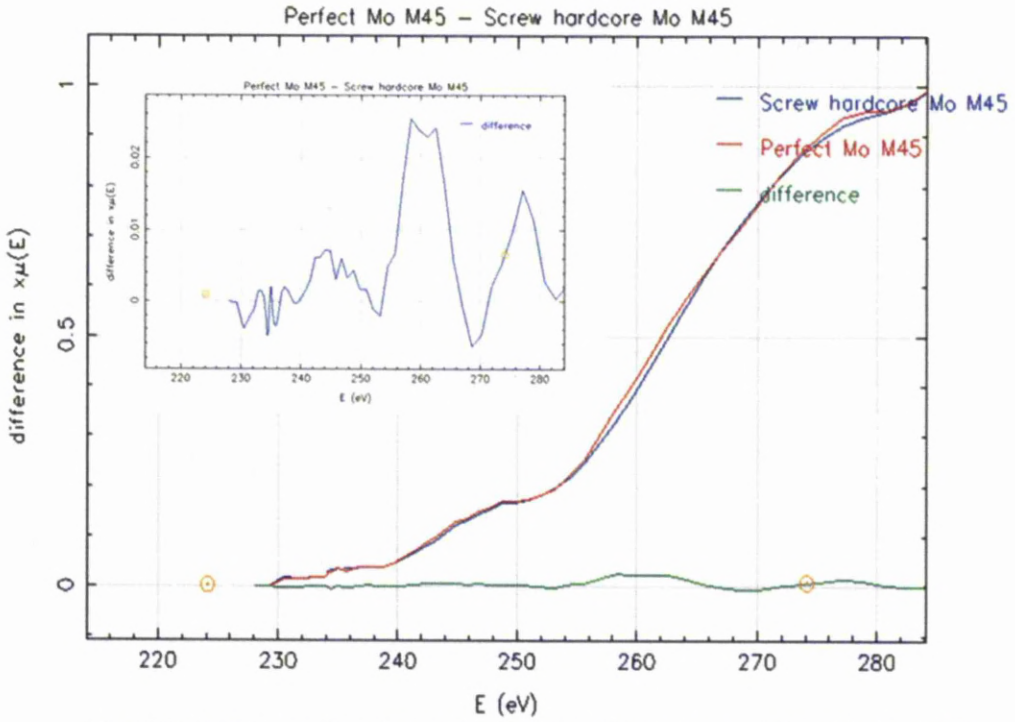

Fig.7.22b) ELNES observed from the screw hard core. The difference spectrum is shown for the selected energy range.

Careful observation of difference spectra in figure 7.22 revealed that small and fine structural changes remain in the energy window 227 – 270eV while relatively big ELNES changes started after 250 eV. ELNES from screw hard core and easy core configurations are compared in figure 7.25. A noticeable change was visible at 250 – 270eV energy loss for easy core while hard core ELNES appeared to have negligible change in that energy window. However, the difference spectrum shows that there are considerable amount of changes in the above considered energy window but are unnoticeable due to the slope of the curves that rise sharp at 260eV for both screw hardcore and perfect crystal Mo.

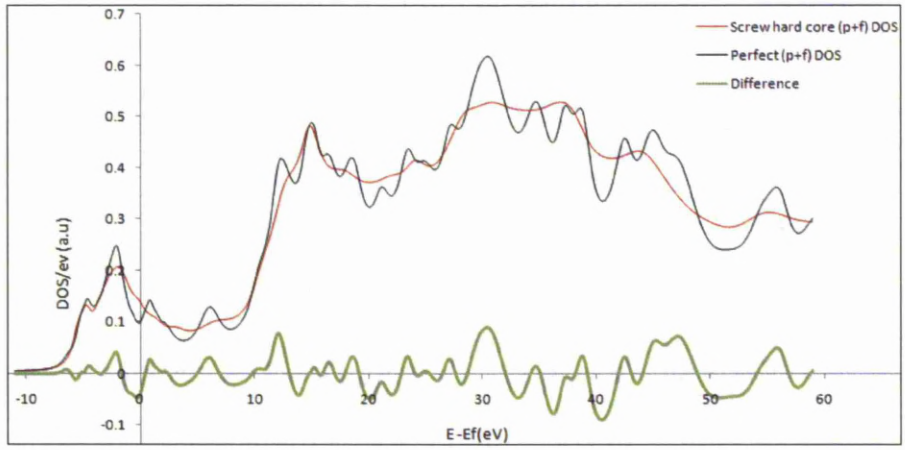

Figure 7.23 (p+f) DOS comparison between perfect crystal Mo and screw dislocation with hard core. The difference curve represents the LDOS changes and was helpful in determining the unoccupied states.

The density of states difference between the hard core and easy core can distinguish the ELNES changes clearly in each case since partial DOS can be extracted from these FEFF calculations. If they are compared with each other, like p+f DOS, the contribution of DOS changes to the theoretical ELNES changes can be easily determined.

Hence in figure 7.24 (p+f) DOS for both screw dislocation cores (easy and hard) are compared to assess the contribution of partial DOS to their ELNES respectively for each core configuration.

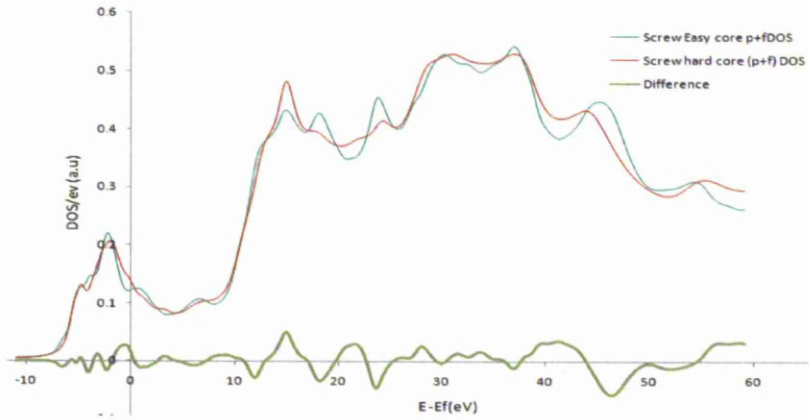

Figure 7.24 (p+f) DOS from screw hard core and easy core were plotted with the difference between them showing the existence of unoccupied states relative to each other.

In figure 7.24, (p+f) DOS curves are corrected for the Fermi energy and are plotted to compare with each other. The hard core was reported to be metastable and not energetically favourable to exist by previous atomistic simulations as mentioned earlier in literature review[5, 10]. The sum of p and f density of states for hard core appears similar to easy core up to 10eV beyond Ef and there is a single sharp peak in between 10 and 20eV.The rest of the curve stays fairly smooth and the peaks are much more smeared than the easy core. This is due to the heavy loss of symmetry at the hard core than the easy core configuration as explained in chapter 2. It is much easier to understand the basic ELNES changes by plotting the ELNES of both easy core and hard core with reference to perfect crystal in one single plot. This is shown in figures 7.25a and 7.25b. The ELNES of perfect crystal shows clear peaks and much fine structural details all through the curve which can be explained by the symmetry and well-defined density of states. The hard core lies intermediate between the near edge structures exhibited by perfect crystal and screw easy core.

a)

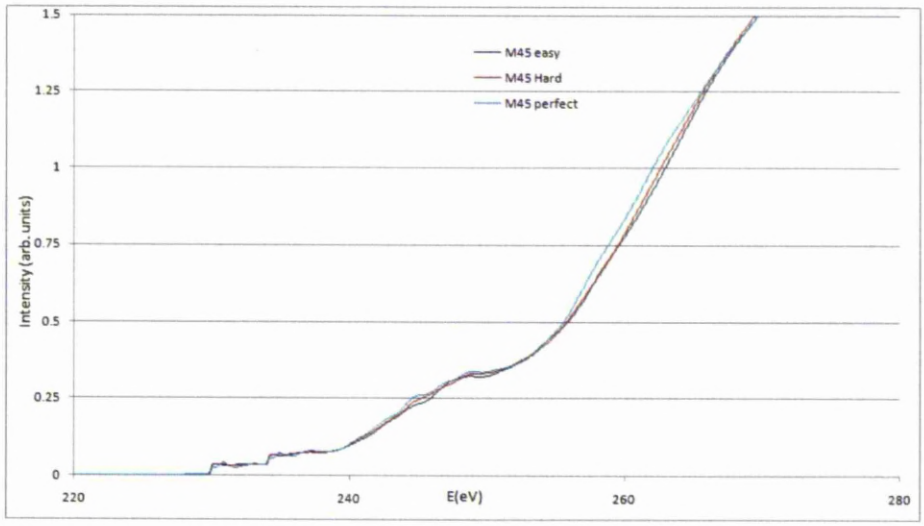

b)

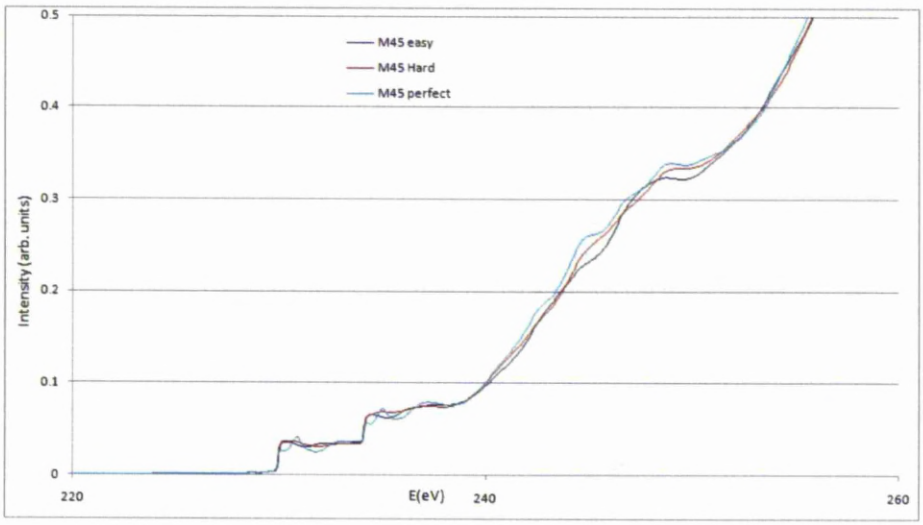

Fig.7.25. a) Mo- $M_{4,5}$ ELNES comparison between perfect crystal, screw dislocation easy core and hard core. b) A magnified image of the $M_{4,5}$ peaks region for the three different curves.

The easy core shows more changes in near edge structure than hard core as noticed in the figures 7.25a and 7.25b. It can be observed in figure7.25 that the easy core suffers most due to the loss of symmetry near the core

and hence the peaks are smeared to a maximum in comparison with hard core ELNES. In the energy range of 230-240eV, the hard core $M_{4,5}$ retains the peaks although they suffer a change, while the easy core have the peaks completely smeared and the structure at those peaks looks almost like a straight line. The ELNES differences of easy core and hard core with respect to perfect crystal are plotted in figure 7.26.

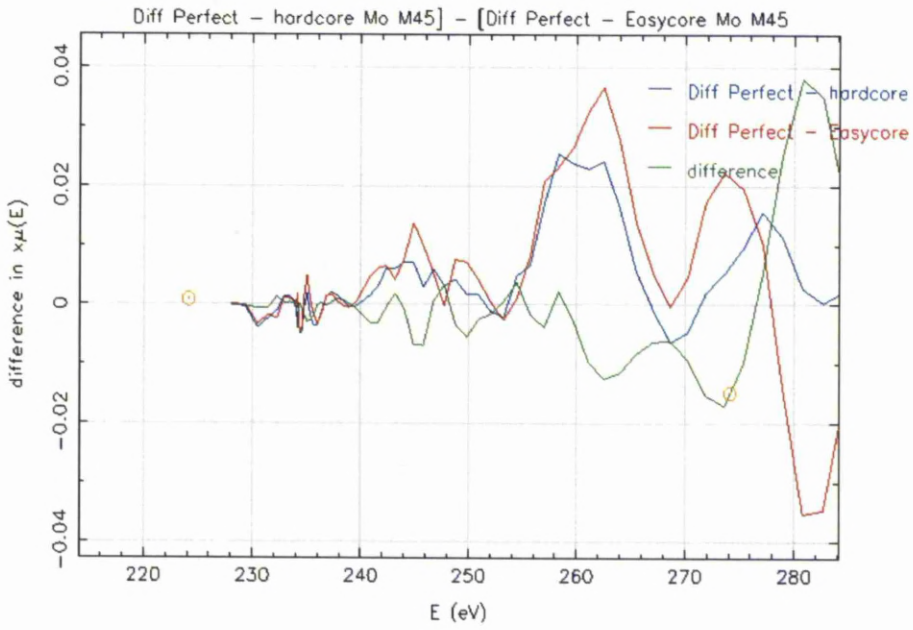

Fig.7.26. Mo-$M_{4,5}$ ELNES differences observed in the case of screw hard core (blue) and easy core (red) with respect to perfect crystal are shown.

In figure 7.26, the near edge structure differences in the easy and hard cores to perfect crystal are compared to identify the core structure that exhibits major differences. This can be helpful in assessing the probability of matching the ELNES changes observed in experimental spectra. The changes seen in both the curves above 0 on y-axis signify that the perfect crystal had more ELNES than the respective core

configuration. In other words this means that such a core configuration has exhibited more smearing of the peaks in a chosen eV range. Even in figure 7.26 the easy core configuration undergoes bigger changes in ELNES in the energy range 240-270eV.

7.6.2 Edge dislocation Vs perfect crystal Mo

ELNES calculations of $M_{4,5}$ edge are done for pure edge dislocation in the [111] direction. In practice, pure edge dislocations are not energetically favoured to exist in [111] orientation in bcc metals[8, 11]. The extra half plane is visible when viewed in [11-2] orientation which is the original as-provided orientation of the crystal co-ordinates. This is shown in figure 7.27. The ELNES of pure edge dislocation is calculated in [111] orientation to understand the spectral changes at edge dislocation core. These results were helpful in investigating the contribution of the edge component to the overall mixed dislocation ELNES.

Figure 7.27 Figure showing edge dislocation in molybdenum crystal and the extra half plane.

It was thought that the edge dislocation core contributes significantly to the changes in ELNES as the bond lengths and symmetry vary near the core. FEFF calculations were performed using the same parameters used for screw dislocation and perfect crystal. The $M_{4,5}$ ELNES spectra of edge dislocation and perfect crystal of Mo were then plotted on the same energy grid and examined for any changes in the difference spectrum. LDOS was also compared with respect to perfect crystal and any observations made were then carried to the study mixed dislocation ELNES.

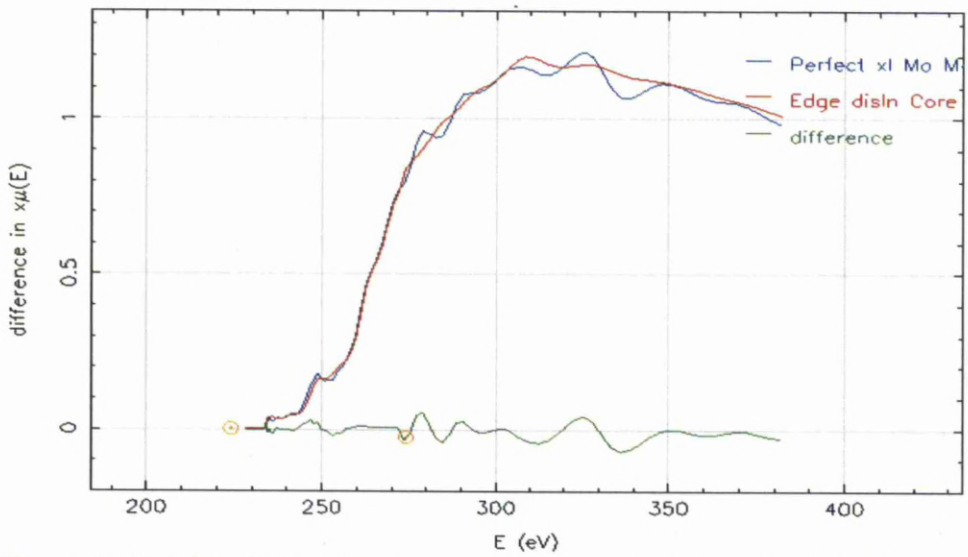

Figure 7.28 Edge dislocation core spectrum in comparison with perfect crystal spectrum.

In figure 7.28, the edge dislocation core spectrum shows small changes in ELNES within the energy range 230-255eV. Another big change is seen in the energy range 275-285eV. In comparison to the screw core, the changes seem to be fairly small within 250-270eV, mainly because the orientation of the crystal used for FEFF calculation does not contain the edge dislocation line. In addition, the peaks at 228-240eV also appear to have widened and then became smooth as compared to perfect crystal.

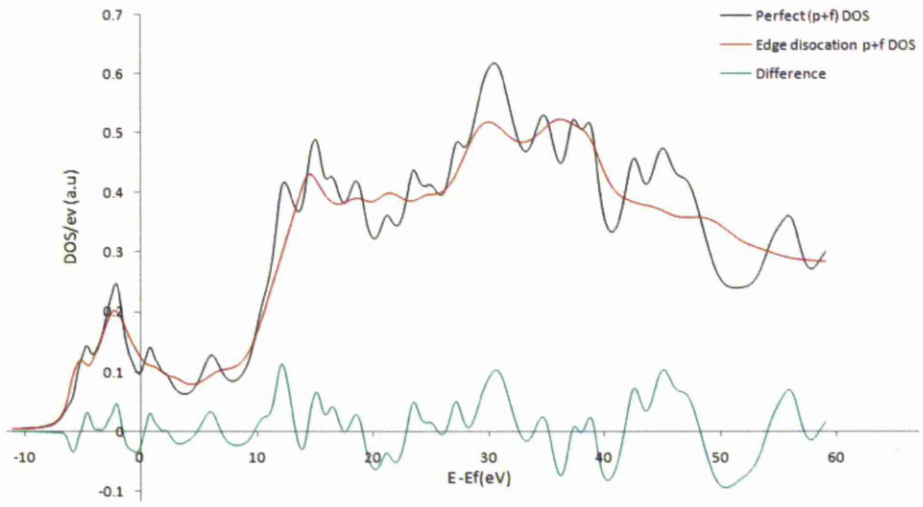

Figure 7.29 LDOS comparison between edge dislocation and perfect crystal.

The difference spectra as shown in the figure 7.28 revealed that edge dislocation core does not contribute significantly to the ELNES in [111] when the edge dislocation is in [11-2] direction. This result also suggested that ELNES must always be calculated along the dislocation line direction in order to study the complete effect of dislocation core on the electronic structure.

7.6.3 Mixed dislocation Vs perfect crystal Mo

A 70^{o} mixed dislocation in [111] direction was studied for ELNES by FEFF calculations. This mixed dislocation in a cluster of 300 atoms is shown in figure 7.30. In [111] direction the extra-half plane is shown and the other two orientations are shown to identify the core of the mixed dislocation. The randomness of the atomic distribution around the core can be observed and hence the edge component vectors attain significance in this case.

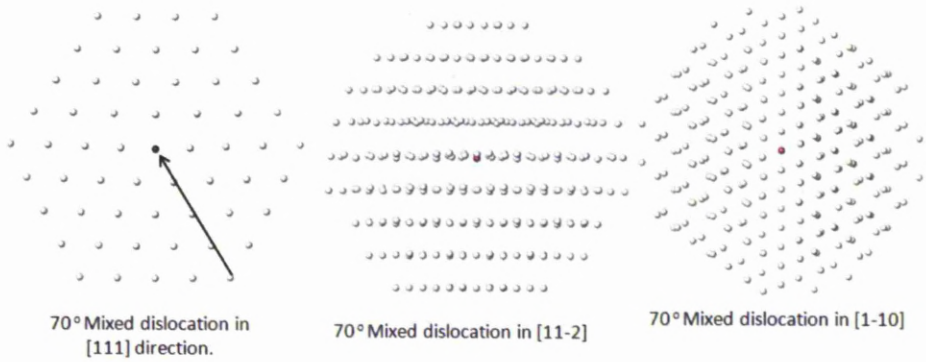

Fig.7.30 ATOMS© model of 70° mixed dislocation with screw components along [111] and edge component shown by arrow, projected in three different directions.

The mixed dislocation co-ordinates as provided were from relaxed crystal model including all the other models in this thesis. This mixed dislocation had an easy core configuration, the edge component of which was shown in figure 7.30. These results are compared with perfect crystal and analysed with respect to edge dislocation. In figure 7.30 the central atom (black in left figure and marked in red in the other two) is the absorbing atom in the cluster and was from the mixed dislocation core.

The $M_{4,5}$ near edge structure of molybdenum at the mixed dislocation core is compared with that of a perfect crystal in figure 7.31. The difference spectrum is shown enclosed in the left corner of the image. ELNES changes in the case of mixed dislocation are bigger than either screw or edge dislocation cores described earlier. The difference spectrum shows major changes in the positive y-axis indicating that the peaks and the fine structure details of the mixed easy core have diminished extensively with respect to perfect crystal ELNES. The symmetry loss at the core and its surroundings is believed to have caused the change in the structure of peaks from sharp to smooth.

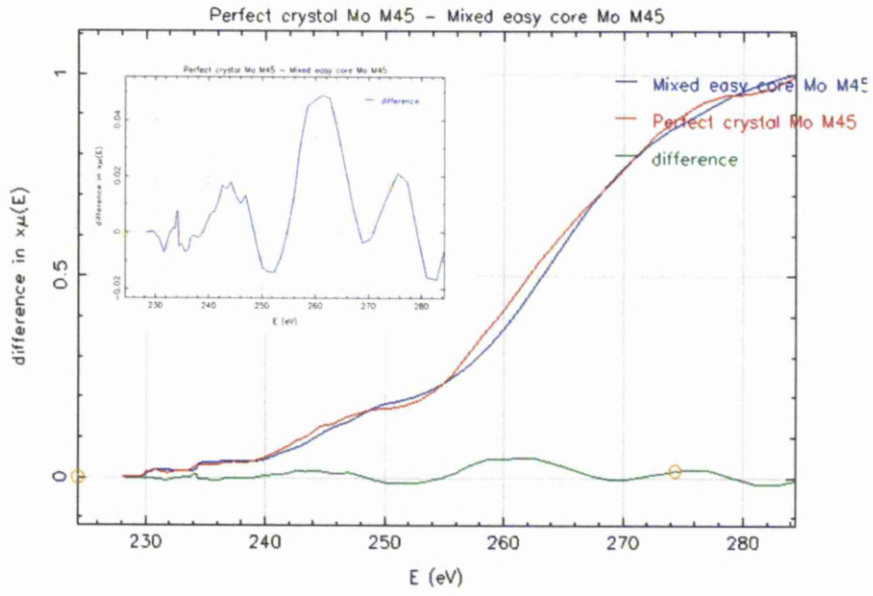

Fig.7.31. Theoretical $M_{4,5}$ ELNES comparison between mixed easy core and perfect crystal molybdenum.

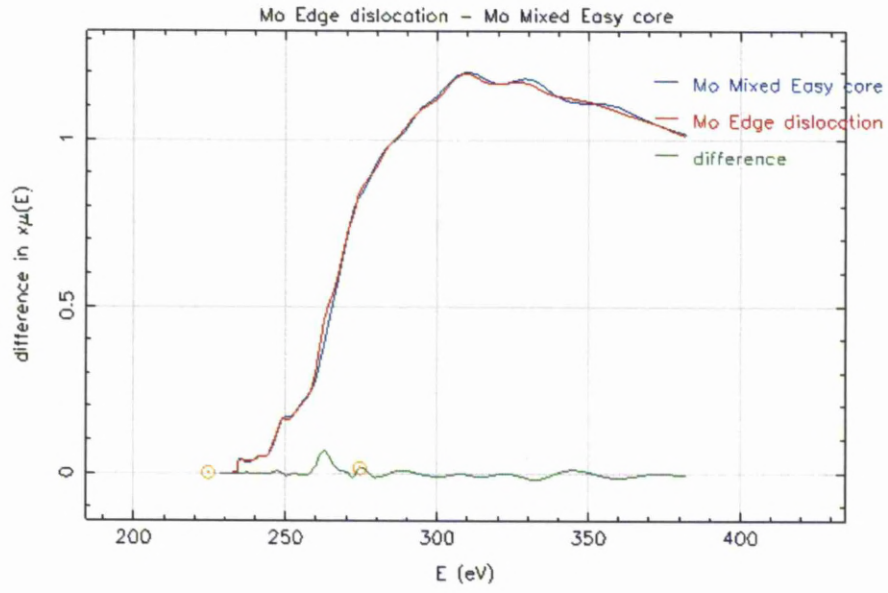

Fig.7.32 Theoretical $M_{4,5}$ ELNES comparison between edge and 70° mixed dislocations in [111] direction in molybdenum.

The ELNES from mixed dislocation easy core is compared with that calculated from edge dislocation core to investigate the effect of edge component on the ELNES changes. It can be noticed in figure 7.31 that the structural change noticed in screw dislocation core ELNES between 250 and 270eV also exists for mixed dislocation while this was absent in edge dislocation ELNES. Furthermore, the change in this energy range for mixed dislocation seems to have increased than compared to that exhibited by screw dislocation core.

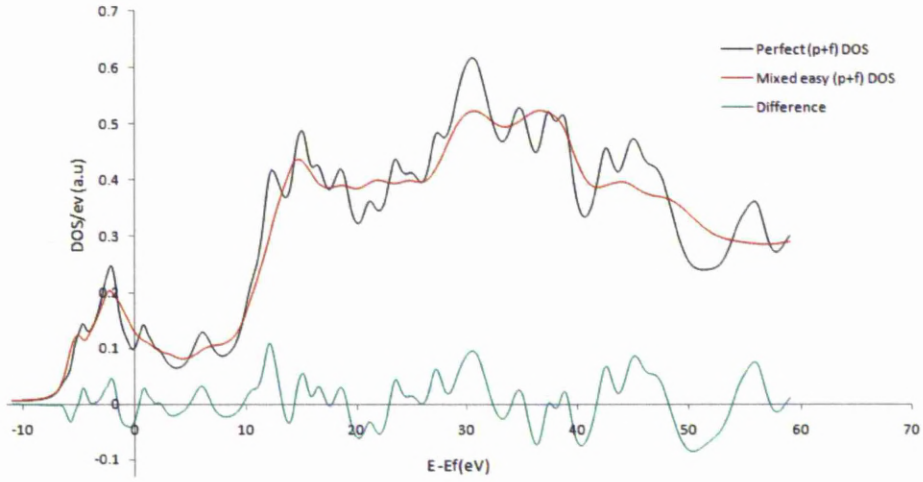

Figure 7.33 Mixed dislocation (p+f) DOS for $M_{4,5}$ in Mo compared with that of perfect crystal.

The angular momentum projected local density of states (p+f) calculated for 70^{o} mixed dislocation are compared with those of perfect crystal. The difference spectrum shows that number of unoccupied states in the case of a mixed dislocation relative to the perfect crystal.

7.7 ELNES calculations of iron

Dislocations in iron samples were investigated with reference to perfect crystal through theoretical calculations. Electronic structure calculations of bcc iron were of interest to this project because iron undergoes plastic deformation by a different process (pencil glide) compared to other bcc metals[12]. Therefore the ELNES at dislocation cores in iron was thought to be influential in predicting the physical properties of iron.

ELNES at $L_{2,3}$ edges was calculated initially for a perfect crystal. These results were confirmed by changing the central absorbing atom and repeating the calculations using the same input cards. The convergence of potentials was taken into consideration for different sized clusters and 300 atoms were found to be sufficient for Fe $L_{2,3}$ ELNES calculations.

In the FEFF calculations for iron, spin orbit splitting is taken into account and the calculations included a card known as SPIN card. This card is not intended for common materials that are not affected by spin. In order to perform spin dependent calculations, the source code had to be changed with spin inclusion in the header file containing essential parameters and was then compiled to generate a new executable FEFF program that can perform spin dependent ELNES calculations.

FEFF can automatically take care of most of the spin up and spin down calculations and is shown to be accurate with Fermi levels for different materials including metals like Fe[3]. The importance of spin in calculating the appropriate electronic structure in transition metals was explained in chapter 4. While identifying the transitions could play a significant role in explaining the changes in electronic structure, the ability to differentiate transitions based on spin dependence could make the ELNES more precise.

7.7.1 Screw dislocation calculations

ELNES calculations at $L_{2,3}$ edge were performed for ½[111] screw dislocation in iron. The co-ordinates for Fe crystal containing screw dislocation as provided by the materials modelling group were relaxed but contained about 30,000 atoms and the screw dislocation had an easy core configuration. 300 atoms were chosen with the central atom of the cluster being the screw dislocation core atom. ELNES and LDOS calculations were then performed for Fe $L_{2,3}$ edge. Same input cards were used for both perfect crystal and screw dislocation. The ELNES and LDOS results of both were compared to observe any significant changes in the spectra.

Figure 7.34 ATOMS© model of iron perfect crystal in different orientations. This confirmed no irregularity in the crystal.

Figure 7.35 ½[111] screw dislocation in iron shown in different orientations.

The atoms marked in different colours in figure 7.35 are screw dislocation core atoms that have retained maximum displacement along [111] direction after relaxation of the crystal. ELNES calculations were performed as if the electron beam travels down the crystal interacting with <111> atomic columns.

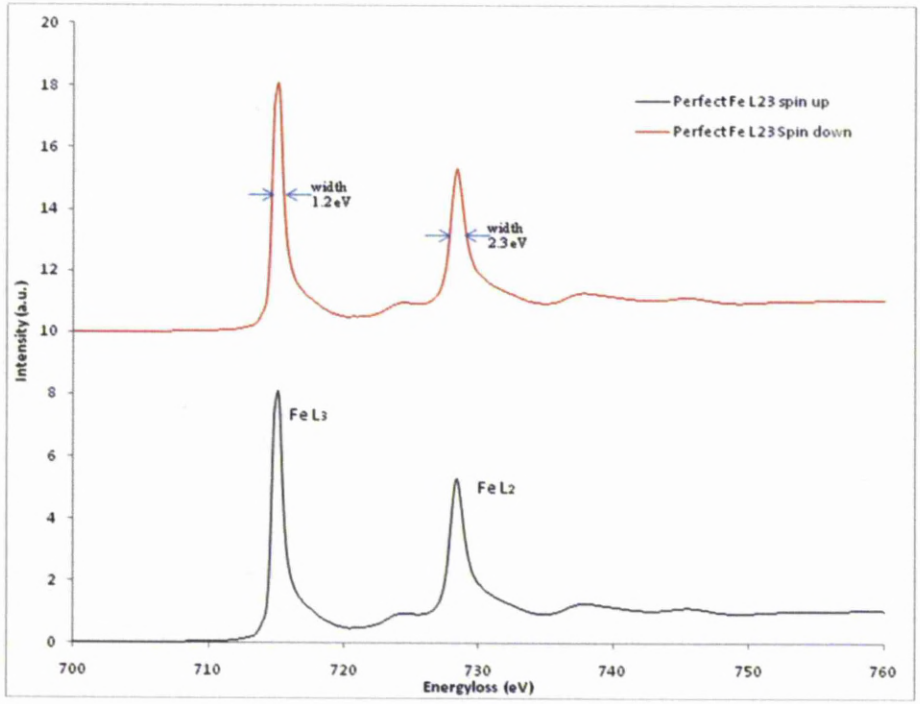

Fig.7.36. Spin up and spin down Fe $L_{2,3}$ ELNES calculated from a cluster of 300 atoms depicting the perfect crystal of iron shown in 7.34.

In figure 7.36, spin dependent ELNES calculated by FEFF for Fe-$L_{2,3}$ is shown. The spectra are shown one above the other than overlapping onto one another because the two ELNES are exactly similar. It is useful to compare the structural changes by overlapping ELNES spectra in the case of Mo-$M_{4,5}$, but if the changes happen to be variation in ELNES peaks width and intensity then this method can be useful. It can be seen from the figure that the ELNES spectra of spin up and spin down calculations are similar because of the perfect crystal's symmetry and no

variation in fine structure is noticed. This observation can serve as a reference for further ELNES calculations for a screw and mixed dislocation core models. Another important technique to identify the change in fine structure is the variation in L_2 and L_3 peaks width and height. The peak width can be measured by the full width half maxima of each individual peak and can be compared with the reference perfect spectral peak widths and heights.

As mentioned in the literature review, the white line intensity ratios are a direct method to determine the d-band occupancy by estimating the unoccupied local density of states and the number of electrons in each angular momentum state[13]. The white line intensity ratios determined from theoretical ELNES of a dislocation core can be compared to standard ratios in reference and with the perfect crystal ratios. The other factors that can affect the width are the core hole and the instrument resolution. A general set of core-hole life times and the resultant widths are written into FEFF code and it automatically takes care during initial calculations as it is incorporated with the complete data of core-hole life times for different metals[14].

The instrument resolution is dependent upon the energy spread of the electron source in the electron microscope[15]. Effects like channelling which can add up to the scattering events among the atoms of the material being probed, can further make the structural features appear fuzzy in the final spectrum. Nevertheless instrument broadening and the core-hole life times can be added to the calculation as corrections to the parameters. This will make the final spectra smoother and the peaks broadened which make the spectra more appropriate for comparison with experimental results. Theoretical Fe-$L_{2,3}$ spectra presented in the thesis are calculated with and without spin dependence and an instrumental broadening of 1eV added to the spectra while the core-hole life times

were automated and taken care of by FEFF during calculations. The spin up Fe-$L_{2,3}$ spectra calculated of a perfect crystal is taken as a reference for comparing the spin up and spin down screw dislocation core spectra. The intensity of the peaks from screw core has increased and if the difference between perfect spectrum and screw core spectrum is considered, this intensity difference lies below zero axis as shown in figure 7.37. The changes observed are the increase in intensity of white line peaks for a screw dislocation and a shift in corresponding energy range of the peaks. The Fe-$L_{2,3}$ ELNES calculated without spin are compared and are shown in figures 7.37 and 7.38.

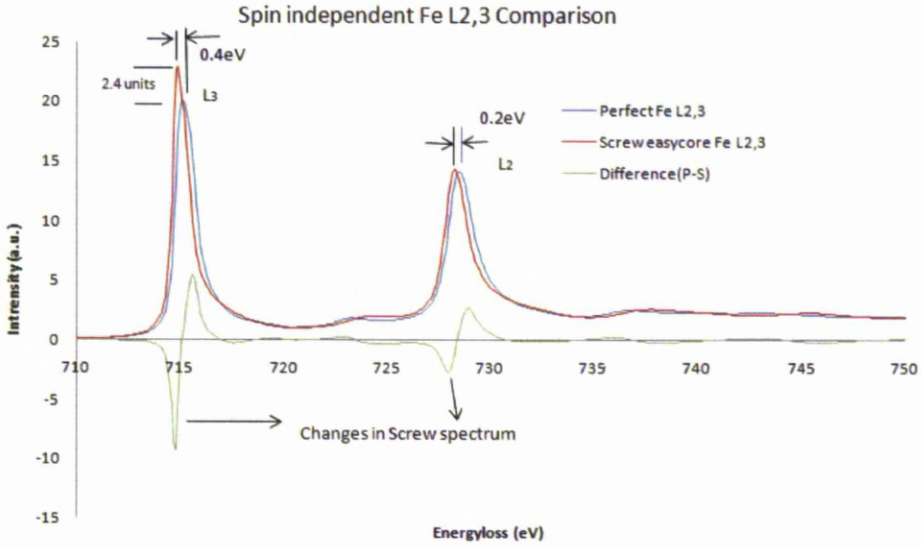

Fig. 7.37 Comparison of Fe-$L_{2,3}$ ELNES of screw dislocation and perfect crystal. The difference spectrum relate to the changes in ELNES of screw with respect to perfect crystal.

It can be observed that there is a shift in energy peaks along the energy axis (0.4eV for L_3 and 0.2 eV for L_2) that caused the differences noticed in the difference spectrum apart from the change in intensity. The intensity of the L_3 peak had increased significantly by 2.4 units for screw

dislocation core while the L_2 peak showed clear but relatively small changes. In order to confirm this shift in peaks both L_2 and L_3 edges were calculated independently. They were then plotted onto a common energy grid using a script (refer to appendix) written in MATLAB© software and then compared with perfect crystal spectrum.

The comparison of perfect and screw dislocation ELNES at $L_{2,3}$ was shown in figure 7.38. The L_3 peaks were magnified and shown on the right side of the spectrum. The spectra appear much sharper in figure 7.38 in the energy range of 720 -750 eV, where the shoulder peak just before L_2 edge shows apparent change.

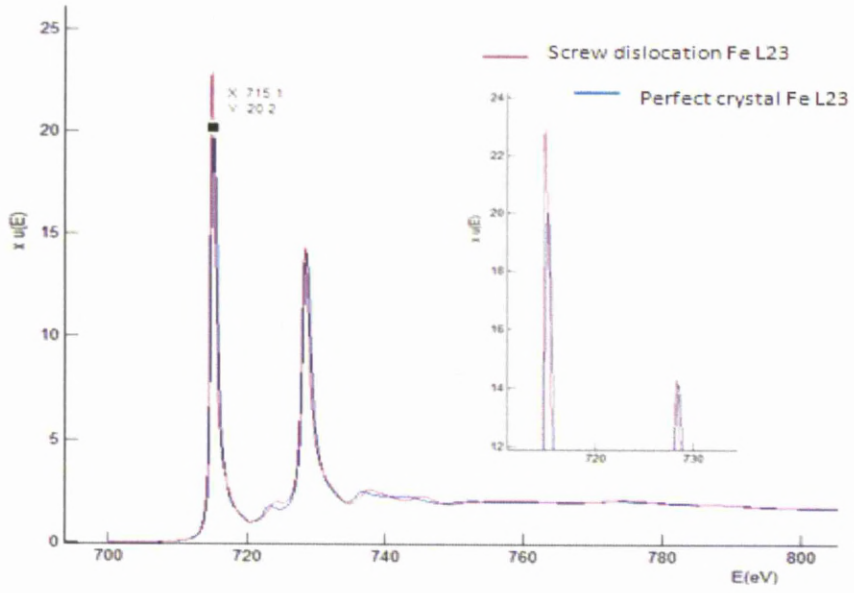

Figure 7.38 Variations in ELNES of Fe $L_{2,3}$ at screw dislocation core as compared to perfect crystal, both calculated without specifying spin.

It is interesting to notice that the variations are different when the calculations are done using spin. These variations are shown in figures7.37, 7.39 and 7.40. In addition to perfect crystal, the spin up and spin down calculations for screw easy core are also similar to each other.

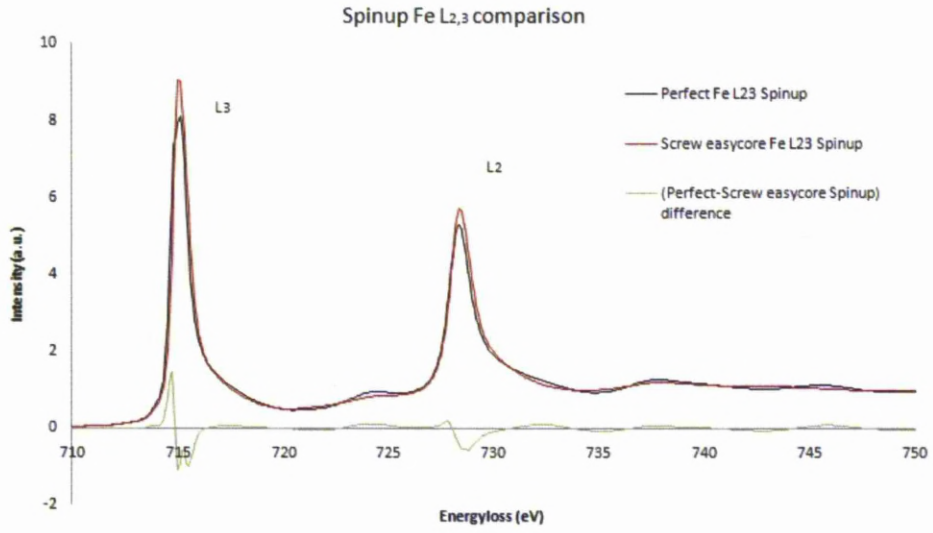

Fig.7.39a. Spin up Fe-$L_{2,3}$ comparison between perfect crystal Fe and screw dislocation easy core and their difference spectrum.

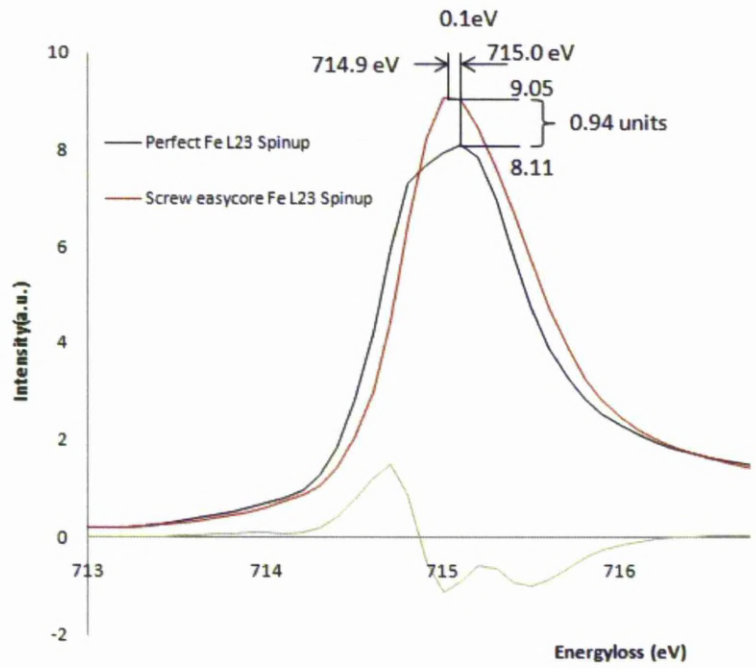

Fig.7.39b. Variation in intensity and the peak shift of L_3 edge for a screw dislocation easy core. The peak shifts by 0.1eV and intensity varies by 0.9units. L_3 peak is magnified from 7.39a to show the differences clearly.

The lower half of the difference spectrum indicates the changes from screw easy core while the upper half corresponds to the perfect crystal ELNES. The variations of L_2 peak for screw core and perfect crystal are shown in figure 7.39c.

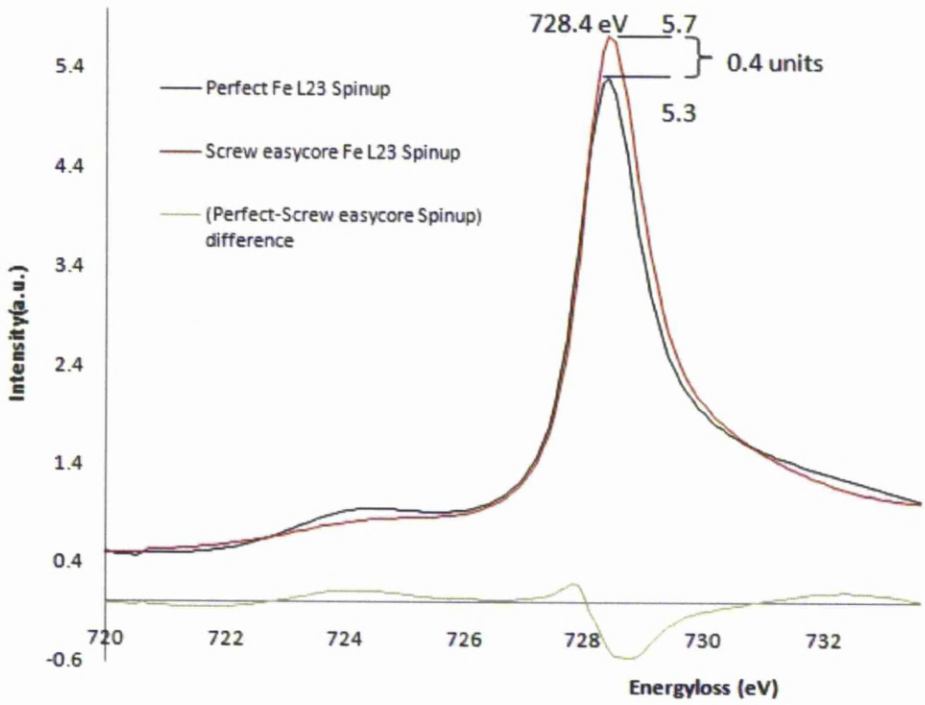

Fig.7.39c. L_2 peak magnified from 7.39a showing variation in intensity of L_2 edge for a screw dislocation easy core. The L_2 peaks in both spectra appear at 728.4eV and peak intensity from screw core increased by 0.4 units.

The observations made in Fe $L_{2,3}$ ELNES in figures 7.39a,b and c, confirm that for a screw dislocation core, the L_2 and L_3 peaks exhibit increased peak intensity while the L_3 peak shifted by 0.1eV with respect to perfect crystal. The spin down Fe $L_{2,3}$ ELNES spectra are shown in figure 7.40.

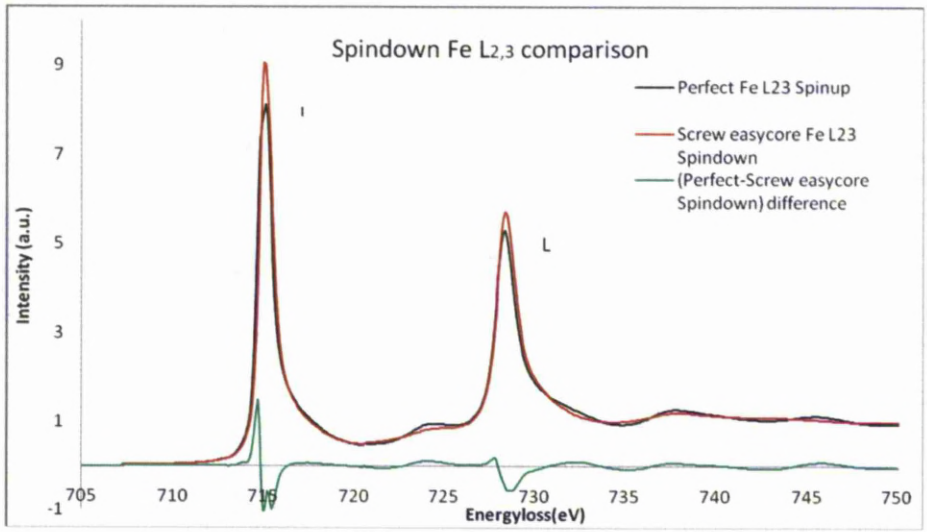

Fig.7.40 Spin down Fe-$L_{2,3}$ comparison between perfect crystal Fe and screw dislocation easy core and their difference spectrum.

The analysis of peak positions and the energy shift of spectra in figure 7.40 revealed that they look similar to the spin up calculation spectra in figure 7.39 and no changes are observed between spin up and spin down calculations for screw easy core with reference to perfect crystal. The spin up and spin down Fe- $L_{2,3}$ spectra for different core configurations with respect to perfect crystal are shown in figures 7.41 and 7.42.

The L_3 peaks of screw easy core and hard core are separated by 0.1eV and the easy core L_3 peak by itself is 0.1eV distant from perfect crystal L_3 peak. It can be observed in figures 7.41 and 7.42 that the L_3 peaks of both easy and hard core have same change in peak heights of 0.94 units with respect to perfect crystal. In contrast, the spin up L_2 peak of screw easy core varies approximately about 1 unit {i.e. (0.43-0.34)} in height with hardcore L_2 peak. The spin down L_3 peak varies by 0.5 units [0.41-0.36]. The energy at which the L_2 peaks reach maximum is 728.4 eV for both easy core and perfect crystal while the hard core L_2 peak shifts by 0.1 eV to 728.3eV.

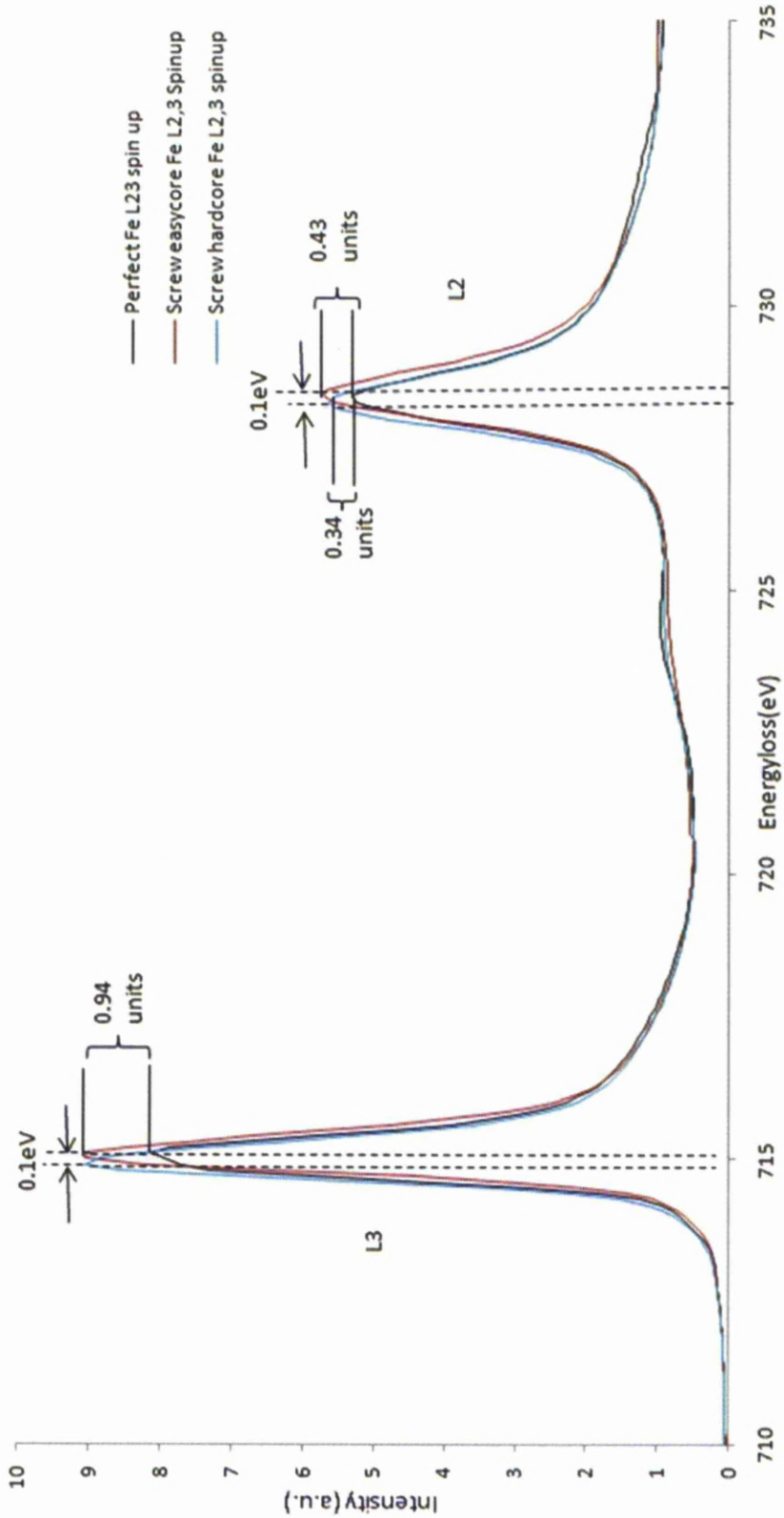

Fig.7.41. Spin up Fe-$L_{2,3}$ ELNES spectra for perfect crystal, screw easy core and hard core configurations shown in comparison. The relevant energy shift of 0.1 eV and the intensity variations are highlighted in the figure.

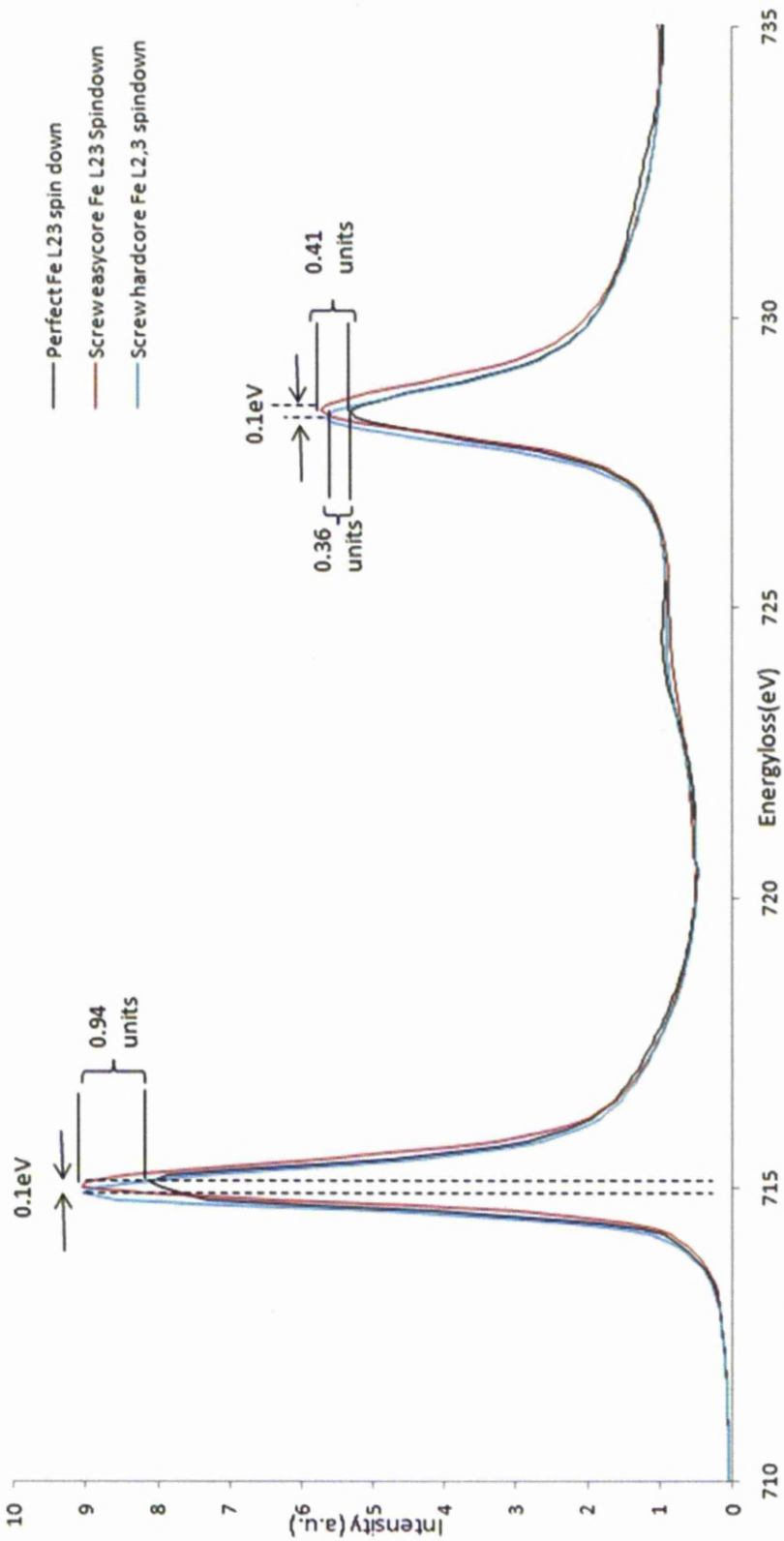

Fig.7.42. Spin down Fe-$L_{2,3}$ ELNES spectra for perfect crystal, screw easy core and hard core configurations shown in comparison. The relevant energy shift of 0.1 eV and the intensity variations are highlighted in the figure.

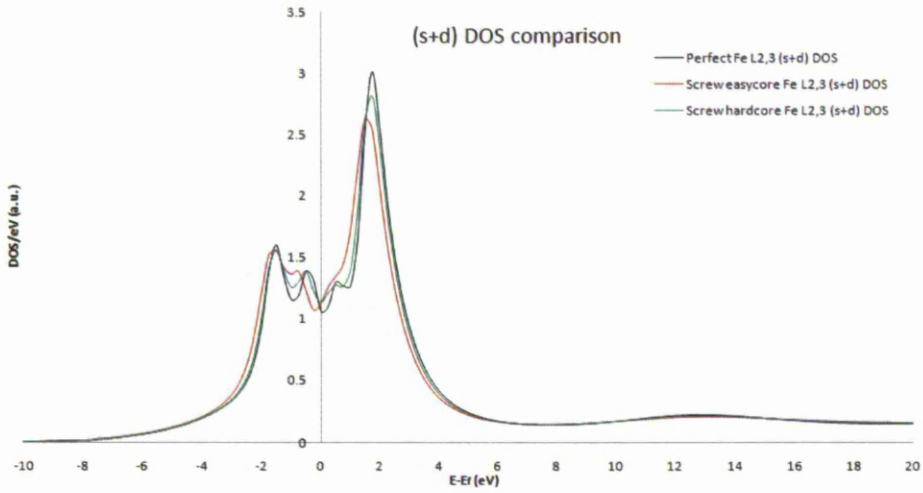

Fig.7.43 Figure showing changes in Fe (*s*+*d*)-DOS at screw dislocation cores with respect to perfect crystal. The Fermi energy is corrected by -20.25eV and the electron counts for each orbital momentum as reported by FEFF calculations are shown in table 7.1.

Electron counts for each orbital momentum			
Orbital	perfect Fe $L_{2,3}$	Screw easy core Fe $L_{2,3}$	Screw hardcore Fe $L_{2,3}$
(s)	0.617	0.634	0.626
(p)	0.748	0.746	0.747
(d)	6.635	6.62	6.627
(f)	0	0	0
(s+d)	**7.252**	**7.254**	**7.253**
Total	8	8	8

Table7.1 The number of electrons per each orbital momentum for easy and hard core configurations with reference to perfect crystal.

It can be seen from figure 7.43 that the (*s*+*d*) DOS at screw dislocation core changes significantly at 1.75 eV. There are less number of *s* and *d* states at dislocation cores than in perfect crystal. The peaks occur at 0.5 and 1.75 eV (peak maximum) above the edge threshold and the (s+d) DOS of screw cores increase between 0 and 1 eV above the edge and then decrease at 1.75 which can be noticed by the difference in peak

maximum. The electron counts for each orbital momentum infer the transitions occurring at the screw cores when compared with their values for perfect crystal. It can be observed that the *s* orbitals of screw cores have more electron count than the perfect crystal while the electron counts for *d* orbitals have reduced. The charge transfer for all the three spectra is 0eV and the Lorentzian broadening applied to the curves while calculation is 0.3eV. The shapes of the DOS curves suggest that the hard core is more perfect-like than the easy core. The total number of states remains constant as in general case but there are more (s+d) electron counts at the easy core than hard core and perfect crystal. These changes are analysed in comparison with experimental spectra to understand the changes occurring in the Fe $L_{2,3}$ ELNES at screw dislocation cores.

7.7.2 Mixed dislocation calculations

Apart from screw dislocation, 70° mixed dislocation in [111] orientation was also investigated for its electronic structure at the core calculated by FEFF. The mixed core was noticed from the ATOMS model generated from a large cluster and 300 atoms enclosing the core were chosen for FEFF calculations with core atom at the centre.

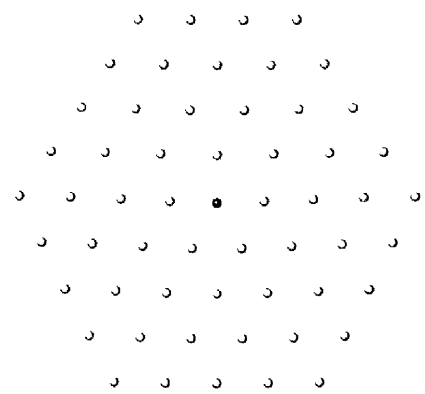

Fig.7.44. ATOMS model of a mixed dislocation in Fe showing the core atom (black atom at the centre). The edge component of the mixed

dislocation can be easily identified from this figure with the black atom at the end of the extra half plane. The screw components are in [111] and invisible when viewed in [111] orientation

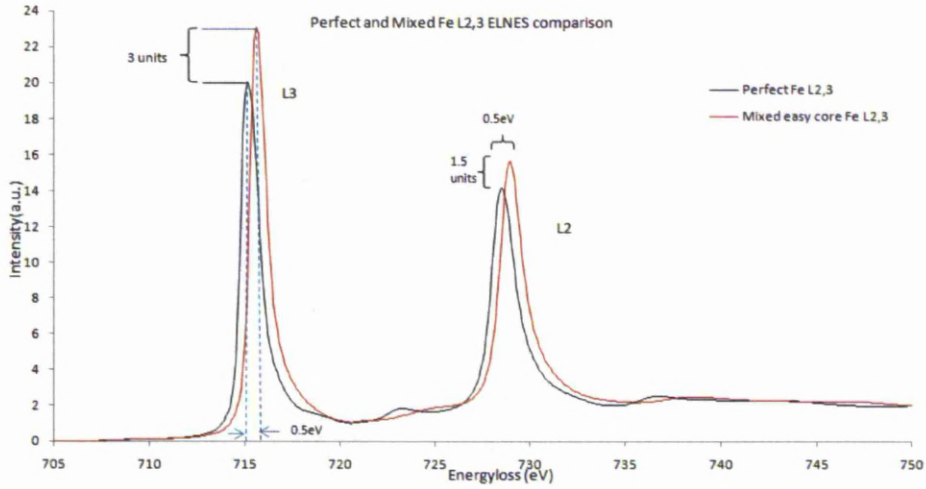

Fig.7.45. Fe $L_{2,3}$ ELNES comparison between mixed dislocation and perfect crystal.

In figure 7.45 the L_2 and L_3 peaks from mixed dislocation core show a consistent change in the intensity by 1.5 and 3 units respectively. There is an energy shift corresponding to the energy of perfect crystal peaks by 0.5 eV for both peaks. It is interesting to note that both L_2 and L_3 peaks showed apparent change in their heights while in screw dislocation core, the changes in L_2 peak are very small. The relatively big differences in energy shift and intensity of mixed dislocation core could help in differentiating the screw core from mixed dislocation while examining the changes visible in the experimental spectra. The local density of states of a mixed dislocation in comparison with a perfect crystal is shown in figure 7.46. A difference of about 1.5 DOS/eV between the peaks of perfect spectrum and the mixed dislocation easy core is observed and the peaks are separated by 0.25eV.

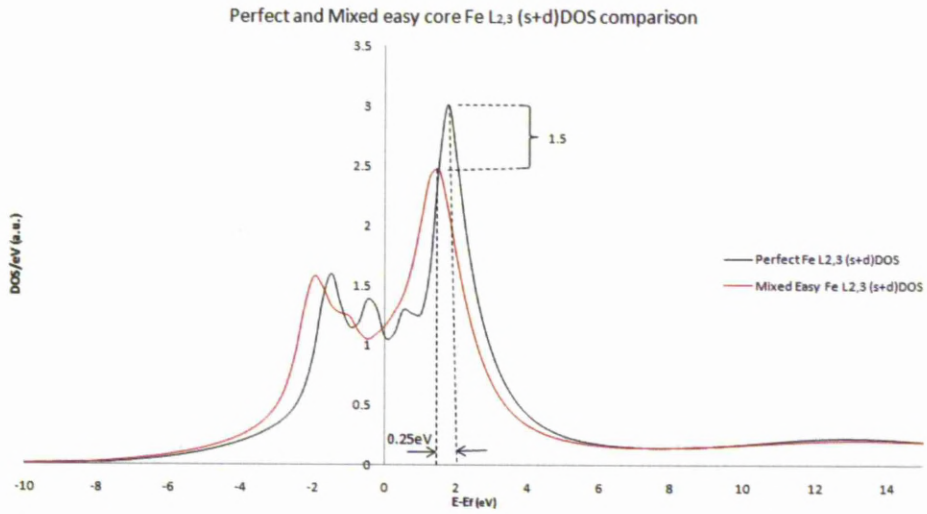

Fig.7.46. Comparison between (s+d) density of states of mixed dislocation and perfect crystal. The difference between the spectral peaks (1.5 DOS/eV) and their energy shift (0.25eV) are shown.

7.8. Approximations

The FEFF calculations are done using a single atom at the centre of the cluster as absorbing atom and the multiple scattering from surrounding atoms is calculated with respect to that absorbing atom. However in practice, in an electron microscope there are many number of atoms under the probe and the spectrometer records ELNES from column of atoms rather than a single atom. The inelastic scattering intensity accounts to the signal from the atoms and a contribution from the surrounding atoms which causes peak broadening.

The advantage of experimental spectra is that it can increase the signal from many dislocation core atoms under the probe, and the changes might be more pronounced than the theoretical spectra calculated from a single atom. It is important to note here that theoretical ELNES varies

from one core atom to the other since FEFF performs real space site-specific calculations of density of states and ELNES. An example of this aspect is shown in figures 7.47 where different core atoms can cause the changes in the intensity of $M_{4,5}$ peaks in molybdenum.

Another important factor to be considered when attempting to study theoretical ELNES with experimental ELNES is the state of the core atom. Experimental EELS records the structure from the core atom that is excited by the electron interaction, stays in a metastable state till the core hole life time and finally returns to ground state.

Theoretical ELNES calculations are done for the crystal that is relaxed to a lowest energy structure to allow the core atoms reconfigure and stabilise. However the basic differences between the ELNES from dislocation core and perfect crystal should provide information regarding the transitions that cause the electronic structure to change for different core configurations.

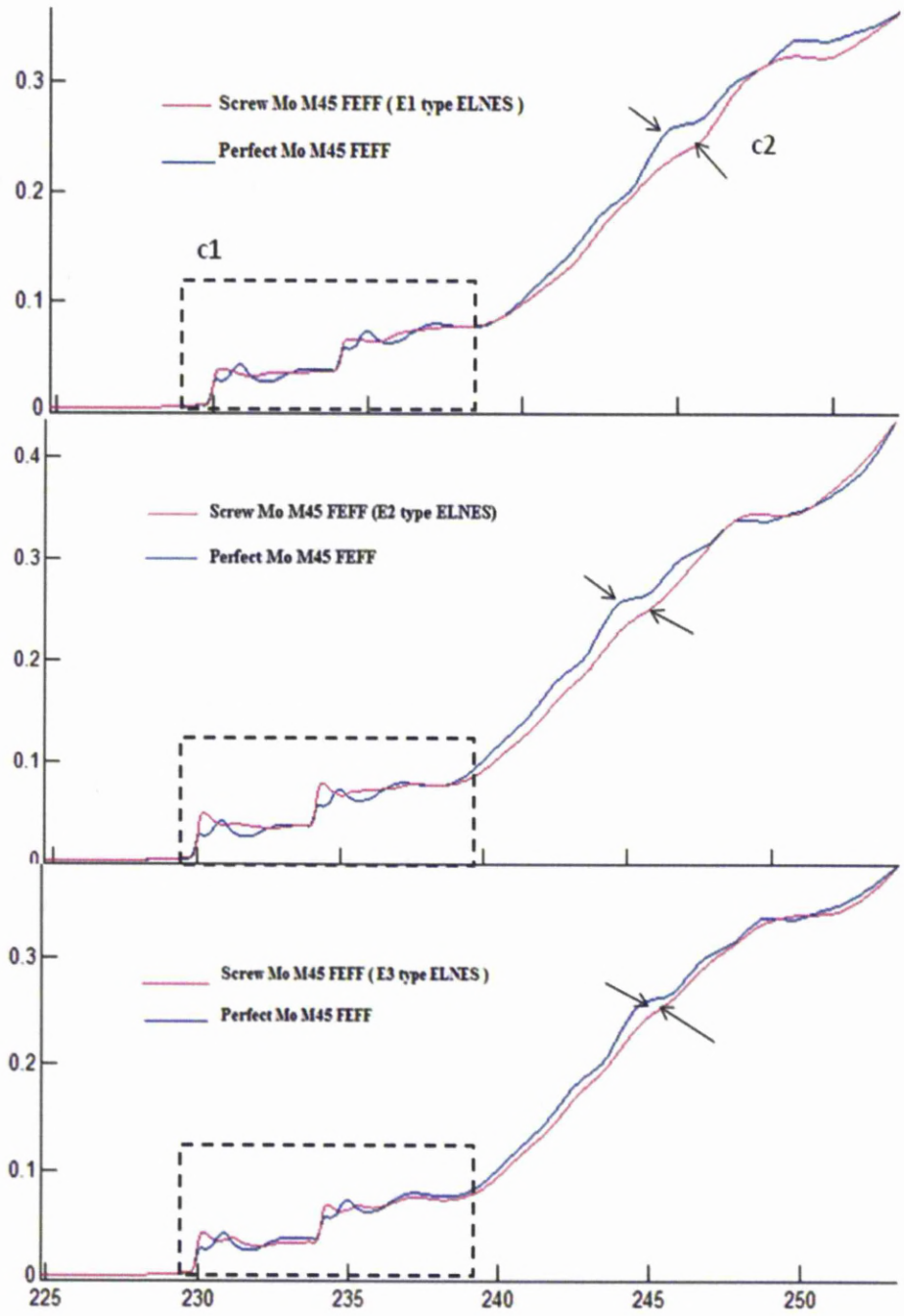

Fig.7.47. Theoretical ELNES of Mo-$M_{4,5}$ calculated from different core atoms (E1, E2, E3 in fig.7.2) showing variations in peak heights (marked c1 and enclosed in dotted box) and the relative change with respect to perfect crystal (marked c2 indicated by arrows).x axis is energy loss(eV).

7.9 Calculated Fe $L_{2,3}$ ELNES

The Fe $L_{2,3}$ edge is investigated for ELNES changes at the cores of screw and mixed dislocation and compared with that of prefect crystal. Fe $L_{2,3}$ edges are characterised by two strong white line intensities Fe L_2 at 728.5 eV and Fe L_3 at 715.1eV for perfect crystal from FEFF calculations. The ELNES exhibited at these edges is a characteristic of Fe valence state and the changes in ELNES of $L_{2,3}$ edge at screw dislocation core would provide information about the electronic structure at the core. Clear changes are observed in Fe-$L_{2,3}$ edge white line intensity ratios as shown in figures 7.38 to 7.42. The L_3 edge had increased counts at screw dislocation core and a chemical shift of 0.1eV for both peaks was observed when compared to prefect crystal. The intensity increase was also observed at the shoulder just before L_2 edge at 725 eV. L_2 edge is a resultant of $2p^{1/2}$ electron transition to unoccupied 3d states of high density while $2p^{3/2}$ electron transition causes L_3 edge. Therefore $L_{2,3}$ edge provides information about the electron transitions occurring between 2p and 3d states. The information contained in the ELNES was reported to be sensitive to chemical composition and the local symmetry of the region[15]. The white line intensity ratio of L_3/L_2 was reported to be in the ratio of 2:1 for perfect crystal from the x-ray absorption study done on transition metals and EELS studies by Leapman *et.al* reported the ratio to be 3.4[13]. The ratio was suggested to be sensitive to the valence state and site-specific[13, 16, 17]. This is the reason for the changes in the intensities of L_3 and L_2 at the screw dislocation. The changes noticed at core are site-specific because core atoms are at different bond lengths due asymmetry prevailing at the core. They are also valence dependent because the binding energies between the atoms of the core are different with respect to the perfect crystal. Therefore the interaction of electrons with core atoms causes transitions that change the electronic structure.

The maxima of Fe L_3 and L_2 peaks from screw dislocation core are compared with those of perfect crystal.

ELNES	L3 max. Energy (eV)	L3 max. Intensity (eV)	L2 max. Energy (eV)	L2 max. Intensity (eV)	L3/L2 ratio
Perfect crystal	715.1	20.07	728.5	14.16	1.417372881
Screw dislocation core	714.9	22.89	728.3	14.33	1.597348221

Table 7.2 L_3/L_2 maxima ratio comparison between screw dislocation core and perfect crystal taken from figure 7.38.

The L_3/L_2 intensity maxima ratio for screw dislocation (1.6) was a larger value than for perfect crystal (1.4) suggesting the changes occurring in the ELNES region of screw dislocation core.

The (s+d) density of states of $L_{2,3}$ edge at screw dislocation core in α-iron are compared with perfect crystal as shown in the figure 7.43. It can be inferred from table 7.1 that when compared to perfect crystal, the electron population of s and d states at screw cores is more in the bound (or occupied) states. In other words, this suggests that at the screw cores there are more unoccupied (or freely available) states. This could be the reason for the ELNES $L_{2,3}$ peaks to show an increase in intensity at dislocation cores. The unoccupied (s+d) states on an average at screw dislocation core were higher than those in perfect crystal, suggesting that there are more occupied d states, henceforth confirming that more transitions from 2p to 3d occur at the core. The Fe $L_{2,3}$ edge was showing increased intensity at screw dislocation core suggesting that more 2p electrons were undergoing transitions at the core than at the perfect crystal which agrees with the changes observed in local DOS.

References:

[1] M. S. Moreno, K. Jorissen, J. J. Rehr, Micron 38 (2007) 1-11.
[2] B. Ravel, http://feff.phys.washington.edu/~ravel/, in: 2004.
[3] FEFFTeam, FEFF8.4 User's Guide (provided with FEFF software), in: 2006.
[4] B. Ravel, ATOMS on the Web, in: vol 2005, University of Chicago, 3 February, 2005.
[5] J. Chaussidon, M. Fivel, D. Rodney, Acta Materialia 54 (2006) 3407-3416.
[6] M. I. Mendelev, S. Han, D. J. Srolovitz, G. J. Ackland, D. Y. Sun, M. Asta, Philosophical Magazine 83 (2003) 3977-3994.
[7] M. Winter, WebElements: the periodic table on the web in: WebElements Ltd, UK, Sheffield, UK, 2009.
[8] D. Hull, D. J. Bacon, Introduction to dislocations, Butterworth Heinemann, Oxford, 2001, p. vii, 242 p.
[9] D. B. Williams, C. B. Carter, Transmission electron microscopy : a textbook for materials science, Plenum, New York ; London, 1996, p. xxvii,729p.
[10] S. Ismail-Beigi, T. A. Arias, Physical Review Letters 84 (2000) 1499-1502.
[11] F. R. N. Nabarro, M. S. Duesbery, J. P. Hirth, Dislocations in solids v. 8, Amsterdam ; Oxford, 1989, p. 67
[12] A. H. S. Cottrell, Dislocations and Plastic Flow in Crystals, pp. ix. 223. Clarendon Press: Oxford, 1953, p. 8º.
[13] R. D. Leapman, L. A. Grunes, P. L. Fejes, Physical Review B 26 (1982) 614.
[14] FEFF, FEFF wiki: http://leonardo.phys.washington.edu/feff/wiki in: 2009.
[15] R. F. Egerton, Electron energy-loss spectroscopy in the electron microscope, Plenum Press, New York, 1996.
[16] J. Taftø, O. L. Krivanek, Physical Review Letters 48 (1982) 560.
[17] K. M. Krishnan, Ultramicroscopy 32 (1990) 309-311.

The EELS spectra taken from EELS ATLAS of molybdenum $M_{4,5}$ core loss edge and iron $L_{2,3}$ core loss edge are shown below for reference.

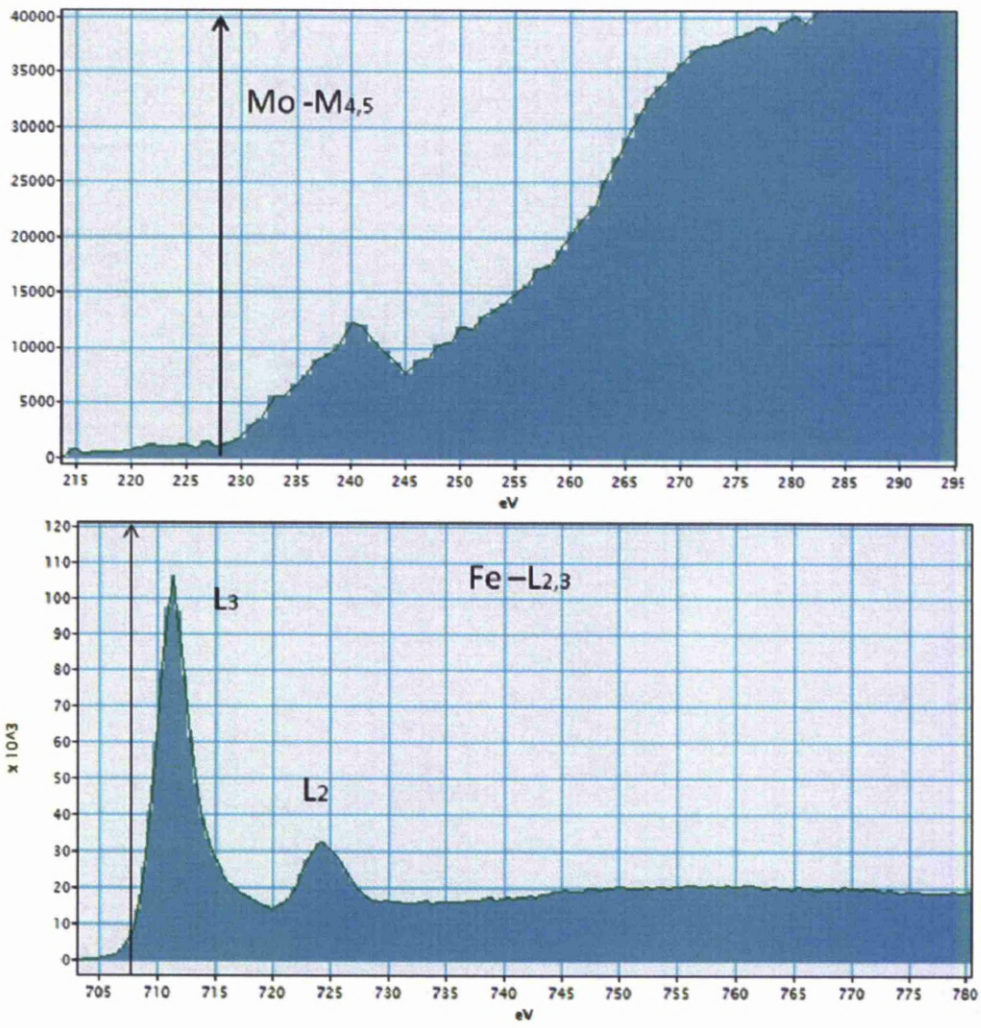

EELS ATLAS reference spectra obtained from Digital Micrograph.

Chapter 8

Results and Discussion: Molybdenum

Chapter 8

RESULTS AND DISCUSSION: MOLYBDENUM

This chapter includes the results obtained using SuperSTEM from single crystal and polycrystalline molybdenum samples. These results consist of atomic resolution images of perfect crystal, screw and mixed dislocations in grains with [111] orientation. The electron energy loss spectra obtained from dislocations and perfect crystal regions without dislocations are presented along with the experimental conditions under which they were obtained.

The experimental results are compared with theoretically calculated EEL spectra for pure molybdenum cluster of atoms, theoretical results from ½[111] screw dislocation core and mixed dislocation in [111] orientation. The observed differences are discussed.

8.1 SuperSTEM results

Molybdenum polycrystalline samples were examined at SuperSTEM for screw dislocations in [111] grains after they have been studied using TEM and STEM at Liverpool. Low magnification micrographs recorded using TEM were used to quickly identify the regions containing dislocations in SuperSTEM as shown in figure 8.1. In figure 8.1 dislocations can be observed near the centre of the grain and the grain is relatively thin with respect to the adjacent grain.

A common aspect observed in polycrystalline molybdenum samples prepared by electropolishing was the presence of bend contours at relatively short distances near the edges the sample while some thin areas were prone to curling. In the bright field image in fig 8.1 these bend contours are clearly visible. Heavy bending of the grains in thinner areas

restricted the use of high angles at which the samples could be tilted for analysing the dislocations. This was one more factor added to the difficulty of working with polycrystalline molybdenum samples in the microscopes in this research.

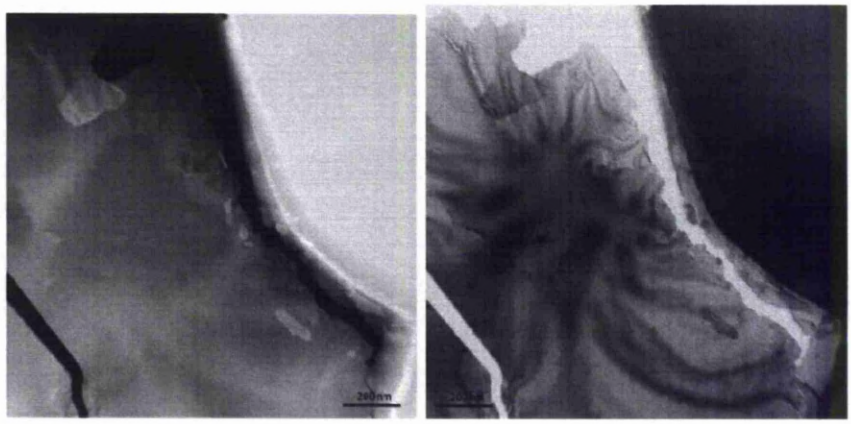

Fig. 8.1 SuperSTEM bright field (left) and high angle annular dark field (HAADF) (right) images of a grain with <111> orientation containing dislocations in a polycrystalline Mo sample.

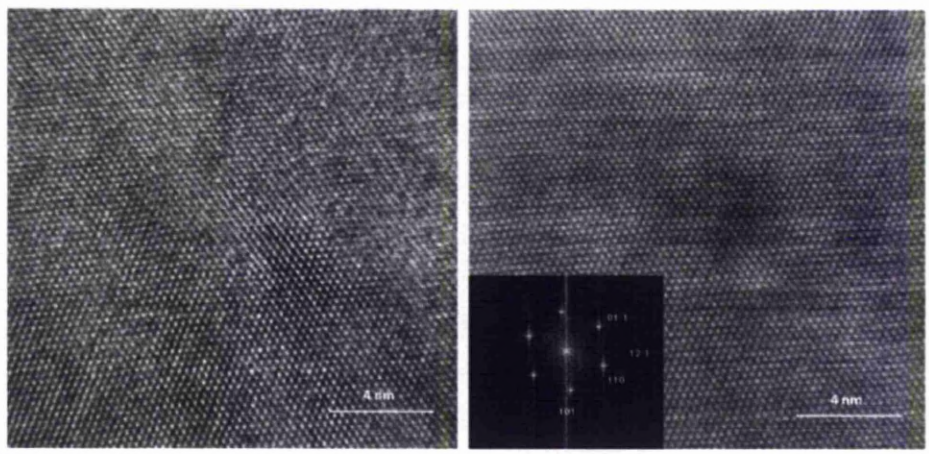

Fig. 8.2 Bright field (left) and high angle annular dark field (HAADF) (right) lattice images of perfect molybdenum [111] grain with the corresponding FFT image with indexed diffraction patterns.

8.2 Identification of dislocation core in SuperSTEM

A series of low magnification TEM images are used to identify the location of screw dislocations in the sample and the bright field and HAADF images of dislocations were recorded in SuperSTEM at different magnifications.

8.2.1 Geometric phase analysis by IFFT

Lattice images of perfect crystal region (region without defects) were taken at atomic resolution, followed by the images of dislocations. The HAADF image gives better resolution of the lattice contrast and can be used to identify the crystal orientation by performing a Fast Fourier Transform (FFT) of the HAADF image. The FFT is an analogue of the information contained in the image taken in real space converted into Fourier space[1]. The FFT of HAADF image generates the diffraction pattern for the crystal orientation. The distance between the diffraction spots and the angles between them were measured and compared with standard data to confirm the <111> crystal orientation. The FFT was also used to identify the alignment of the optic axis with respect to the crystal zone axis and was helpful for identifying any astigmatism or coma after the initial aberration corrections were done.

Each set of the bright spots in the FFT image contains information about the corresponding set of planes with specific orientation from which they were generated. Therefore each set of diffraction spots in the FFT image was studied to check for any distortion or discontinuity in those planes that are responsible for generating them. This was done by masking a set of diffraction spots and taking an inverse FFT followed by displaying phase. The resulting image contains the planes that were responsible for the set of diffraction spots. This procedure is repeated for each set of first order

diffraction spots in the FFT image. This method is shown with images in the figure 8.3.

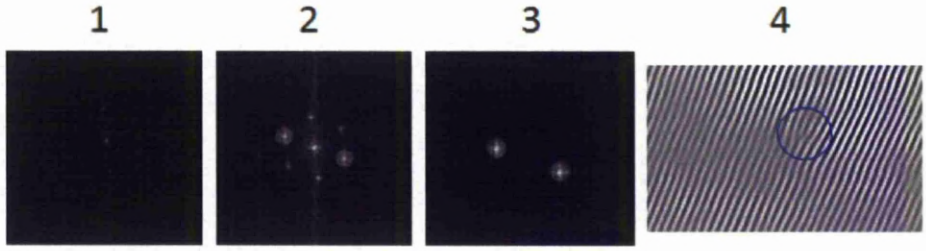

Fig. 8.3 1) FFT of HAADF from mixed dislocation 2) Masking a set of reflections 3) Masked image 4) IFFT of masked image showing extra half-plane in the marked circle.

The resultant inverse FFT image (termed as 'IFFT') reveals the distortion in the planes with respect to each set of diffraction spots and the presence of any extra-half planes in the case of mixed dislocations in 111 crystal sample. This was used to identify the core region where there is maximum distortion or discontinuity accompanied by the change in contrast.

8.2.2 Geometric phase analysis by Live FFT

Geometric phase analysis is a popular technique used to identify any structural change in the information contained in the image taken from defects. This is based on the fact that changes in the periodicity and orientation of the lattice near defects cause changes in the scattering of electron beam from the defect region. This results in the change in phase information that can be observed by examining the diffraction spots in the FFT image. Geometric phase analysis in this research was used to identify the character of the dislocation (screw or mixed dislocation) and involves the step by step procedure given below:

1. A HAADF image of the dislocation was taken at atomic resolution and care was taken to fit whole contrast change from the dislocation within the image.

2. FFT analysis explained above was done for each set of diffraction spots to identify the planes that are responsible for lattice distortion and dislocation contrast.

3. A single diffraction spot of that set was chosen in the FFT image using ROI marker box with a size of $2^n X 2^n$.

4. A first live FFT of the selection in the ROI was taken. This was followed by selection of first FFT and generating second FFT from it. This was repeated until a third FFT is generated from the second. The third FFT image was changed to display the phase information.

5. The changes in phase were observed by moving the ROI marker box slowly around the diffraction spot in the FFT image that has diffraction spots.

6. When the ROI box was located at the centre of the diffraction spot the phase information remained constant and when it was moved slightly away from the centre of the diffraction spot, a phase ramp was observed which provided information about the orientation of the planes corresponding to that diffraction spot.

7. The phase changes were expected and observed in the case of a screw dislocation due to Eshelby twist and the distortion of atomic planes surrounding the screw dislocation core. A mixed dislocation was identified by the presence of an extra half plane in one of the orientations of the lattice planes in the image as discussed in previous section. Thus the character of the dislocations was identified from atomic resolution images using Geometric Phase Analysis (GPA). The GPA for screw dislocation is

shown in figure 8.4. The identification of dislocation character was followed by electron energy loss spectroscopy (EELS) of the dislocation core region and perfect crystal region.

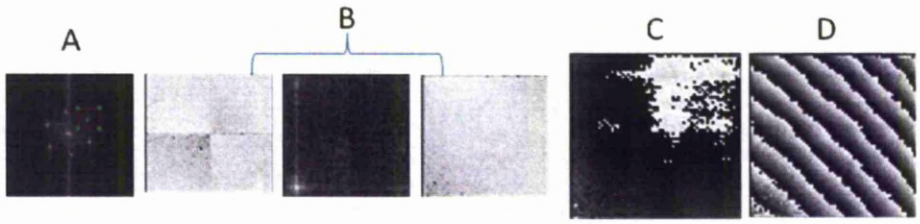

Fig. 8.4 A) Live FFT showing the selected diffraction spot B) First, second and third live FFT's of diffraction spot in A. C) Phase display for third live FFT with ROI on the diffraction spot D) Phase display for third live FFT away from the diffraction spot.

8.3 Drift tube Correction

While the spectra were being collected, the electron beam moves across the atomic columns collecting information column by column. It was observed that the spectrum moves along the energy axis as the spectra was collected. This led to a considerable shift in individual spectra from the first pixel in the row of pixels to the last pixel. This was corrected using a script specifically written and installed into Digital micrograph known as "drift tube correction".

When this script is used, it controls and corrects the movement of drift tube at random using a specific number of channels used for EELS acquisition. It also contains the section that allows the removal of dark current that arises from noise when the beam is blank. The program code for this script is added in the appendix section of thesis and the process dialogue is shown in figure 8.5. The spectra were collected using this script from the dislocation (termed as DT shift SI) and was followed by collecting spectrum image of dark current noise (termed as background

noise SI). This was done by blanking the beam and collecting spectrum image. This background SI was then subtracted from the DT shift SI to obtain background removed SI. Then the spectra were realigned to their correct energy scale by clicking "SI realign" button shown in figure 8.5. The resultant SI was named background removed and realigned SI and was used for further EELS analysis. An example of this procedure is shown in figure 8.5.

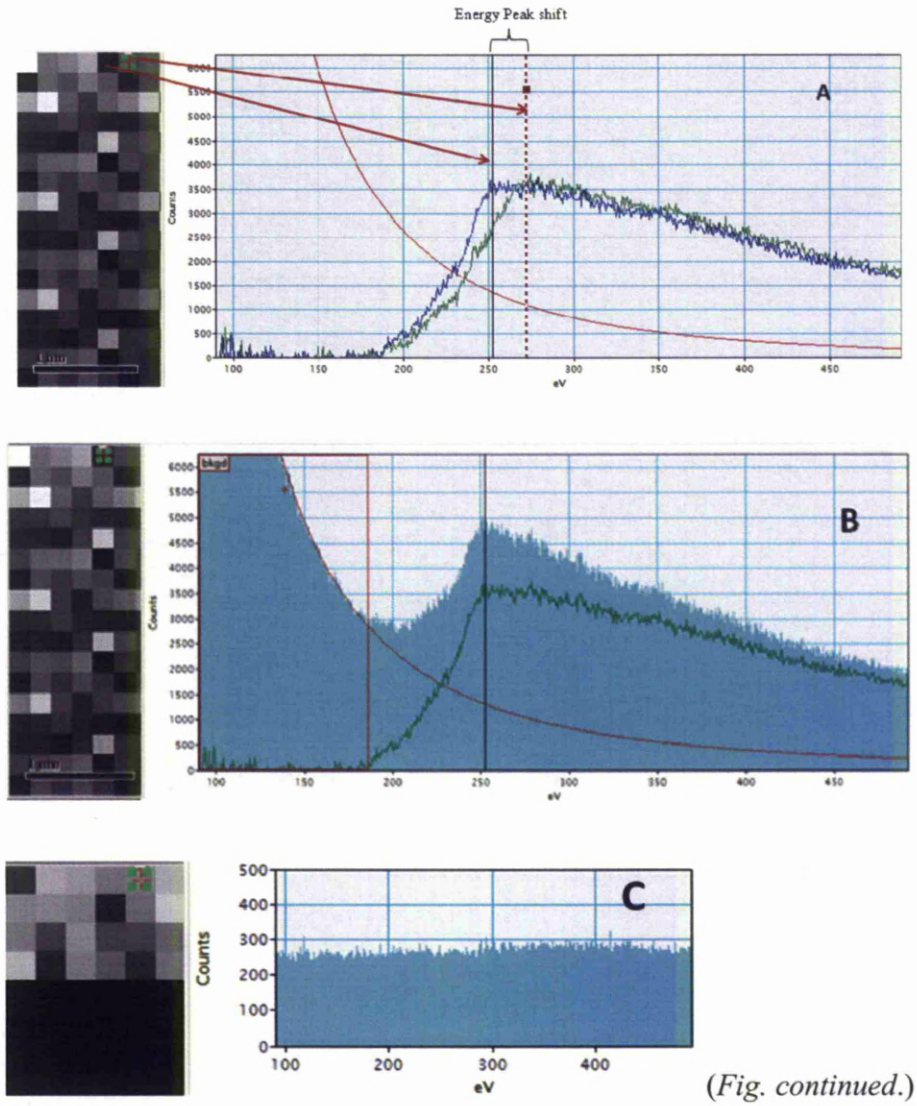

(*Fig. continued.*)

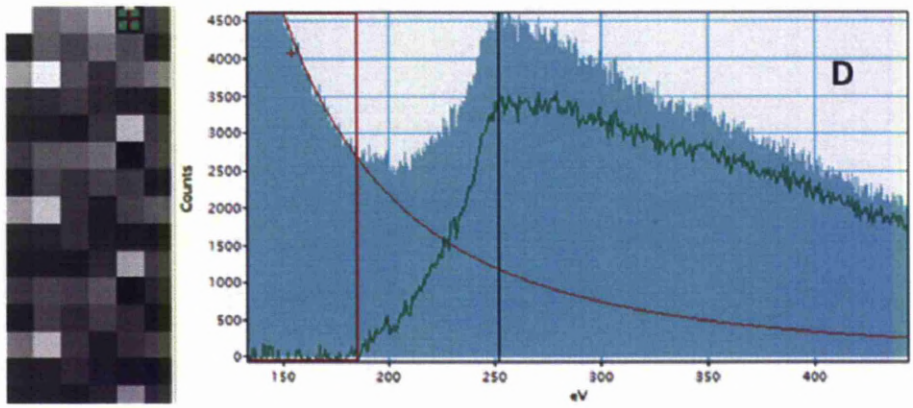

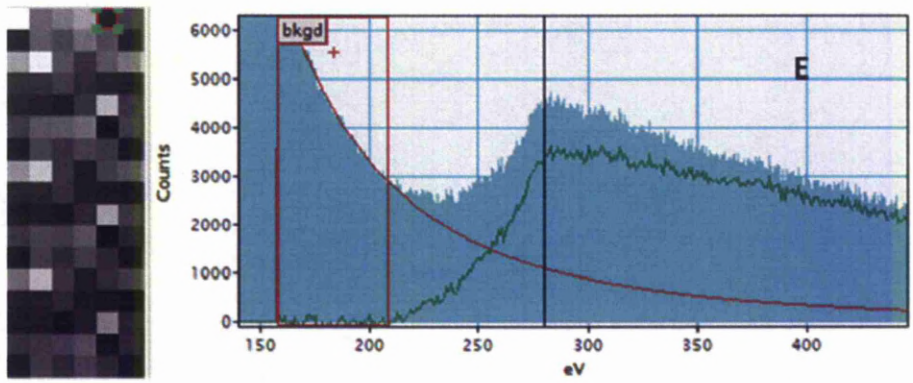

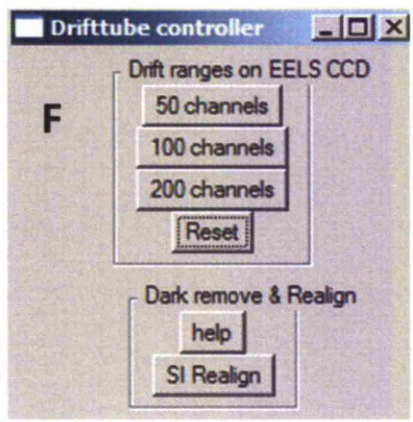

Fig. 8.5 Drift tube correction and dark current removal and realigning method followed during EEL spectrum acquisition. Figure A is the DT shift SI that shows the pixels from which respective spectra are collected and the shift in energy peak as beam acquires SI from one pixel to its adjacent one. Figure B shows the DT shift SI with the carbon K-edge at 250 eV rather than its actual value of 285eV. Figure C shows the

background SI which records the dark current noise. Figure D is the background removed SI and it can be observed that the peaks and the spectral features become sharp and clear in the spectrum. It can be seen that the carbon K-edge still shows maximum at 250eV in this spectrum. Figure E is the background removed and realigned spectrum image which shows the carbon K-edge at 285eV and the spectral features sharp and clear. Figure F is the dialogue that the "drift tube correction" script generates in Digital Micrograph. The options to choose the number of channels to be used for correction are also shown.

8.4. Identification of spectral changes using Chi squared Image

The spectrum images acquired from dislocation region are analysed pixel by pixel for any spectral changes near the molybdenum $M_{4,5}$ edge. The number of pixels is large in most cases (typically 700 to 900) and examining each individual spectrum proved to be a tough task. As the spectra were collected, the signal and noise levels varied for each pixel and are non-uniform throughout the spectrum image. This can lead to the variations in the fine structure observed above the edge threshold and could be misinterpreted for changes in near edge structure. This non-uniformity was taken care of by a script named "chi square" written and installed into digital micrograph.

For this script to run, it required background from every pixel to be removed in the spectrum image, and creating a background subtracted spectrum image. This was done using the option provided in digital micrograph for generating a background subtracted SI. It was followed by the summation of all spectra with in the background subtracted SI, selection of ELNES region from the summed spectra and then normalising the spectra with a selected energy window far from ELNES region. The result of this script was a "chi squared" image which has the same number of pixels as the original SI, but the pixels that contain

spectral changes in the selected ELNES region were highlighted as bright pixels. The rest of the pixels appear dark. The idea of this script was to highlight the pixels that correspond to changes in ELNES as compared to the rest of the pixels. These pixels were then located in the background subtracted SI and were carefully examined for the spectral changes near the energy edge.

The chi squared script served two purposes.

1. Reduction of time and effort to examine each individual spectrum out of large number of spectra contained in the SI.

2. Identification of pixels that contain variations in near edge structure.

The program code for "chi squared" script is added to the appendix section of this thesis. As changes in ELNES were expected from the spectra that correspond to dislocation core, they would be revealed as bright pixels in the chi squared image.

The position of the bright pixel in chi squared image was noted and the spectrum at the same position in background subtracted SI was analysed. The spectra from those bright pixels were compared to the average background subtracted spectrum. This revealed the changes in near edge structure at the dislocation core.

The application of chi squared script for this SI is shown sequentially in figures 8.8A to 8.8H. Molybdenum $M_{4,5}$ edge was studied for ELNES changes from mixed dislocation core in comparison to a perfect crystal region of the sample. A region of interest with sufficient width and height to include the dislocation core was chosen and EEL spectra were acquired from mixed dislocation with shortest projected length along the surface of the foil as shown in figure 8.6.

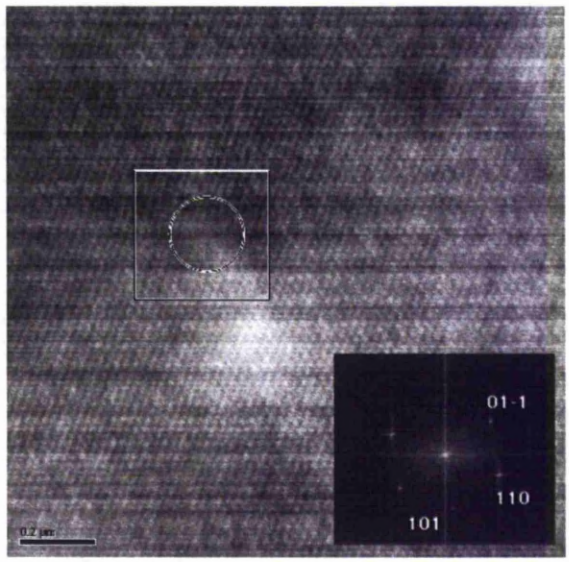

Fig. 8.6 HAADF image of mixed dislocation in polycrystalline molybdenum with diffraction pattern indexed FFT. Dislocation core is in the circle and EELS spectrum image is collected from the rectangular selection. The Fourier filtered image from HAADF of this dislocation that can be helpful in identifying the core is shown in figure 8.12.

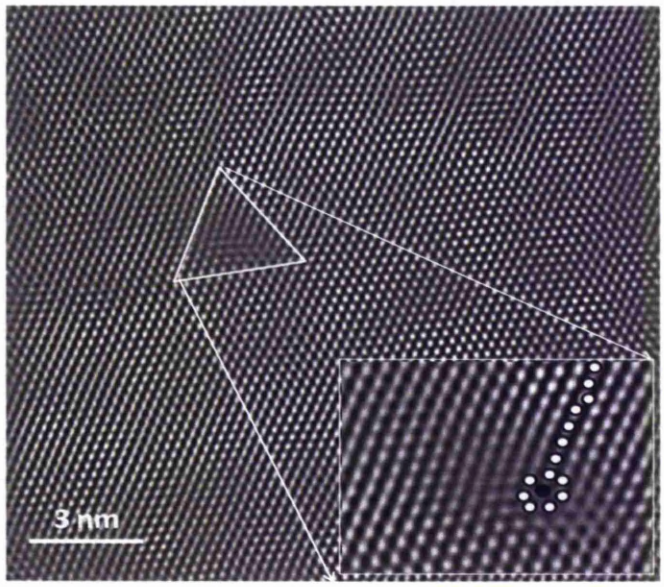

Fig. 8.7 Fourier filtered image showing the extra-half plane that arises from the edge component of a mixed dislocation.

In figure8.7 the triangle region contains the core of the mixed dislocation and the displacement of atoms around the core is apparently visible in the image. Mixed dislocation core region separated and magnified from the filtered image shown in the bottom corner. The dislocation core atom represented in black colour is where the half plane ends and it can be seen here that there are 7 atoms surrounding the black core atom rather than 6 atoms for [111] orientation. EELS is acquired from this core and the chi square script is applied to it as shown in figure 8.8.

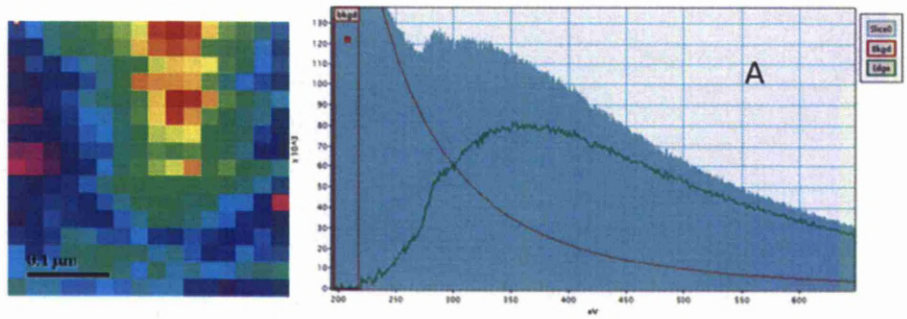

Fig. 8.8 A) Dark current removed and realigned SI is on the left and background subtraction for the spectrum from first pixel of SI is shown on the right.

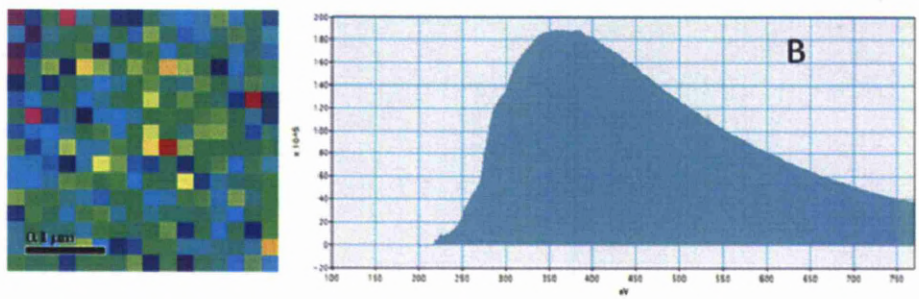

Fig.8.8 B) Figure showing background subtracted SI (left) and the summed spectra of all 256 pixels in SI (right).

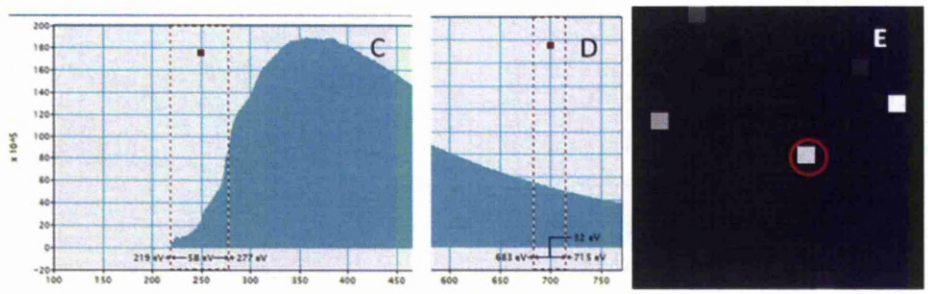

Fig. 8.8 C) Figure showing selected ELNES region on the summed spectra; D) figure showing the normalisation energy window used to generate chi squared image; E) chi squared image showing bright pixels that correspond to ELNES changes.

The pixel enclosed in the red circle is the spectrum that shows ELNES changes and could be from dislocation core. This can be confirmed by comparing the position of this pixel with the pixel in the original SI as shown in figure 8.8F. Moreover it can be verified if the position of this pixel corresponds to the core atom in the post SI HAADF image. This will be discussed with the results obtained from mixed and screw dislocations.

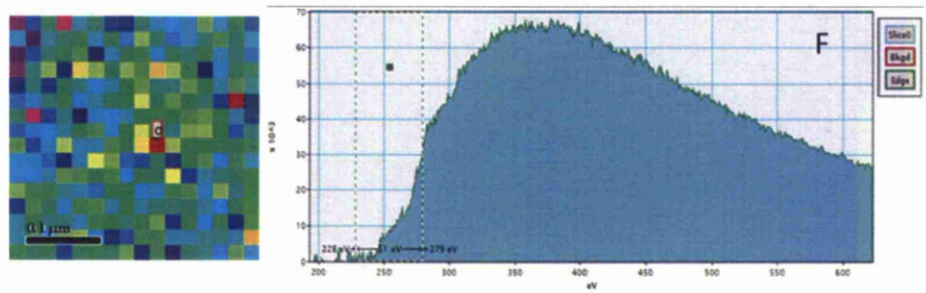

Fig. 8.8 F) Figure showing the spectrum image (left) with the central red pixel being the supposed dislocation core region. The spectrum shown on the right is from the central red pixel with marked ELNES energy window.

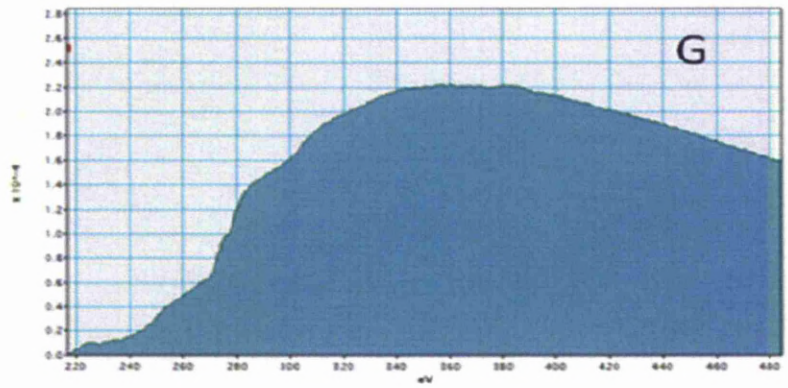

Fig. 8.8 G) Figure showing the average spectrum of 16 background subtracted spectra selected from the perfect crystal region.

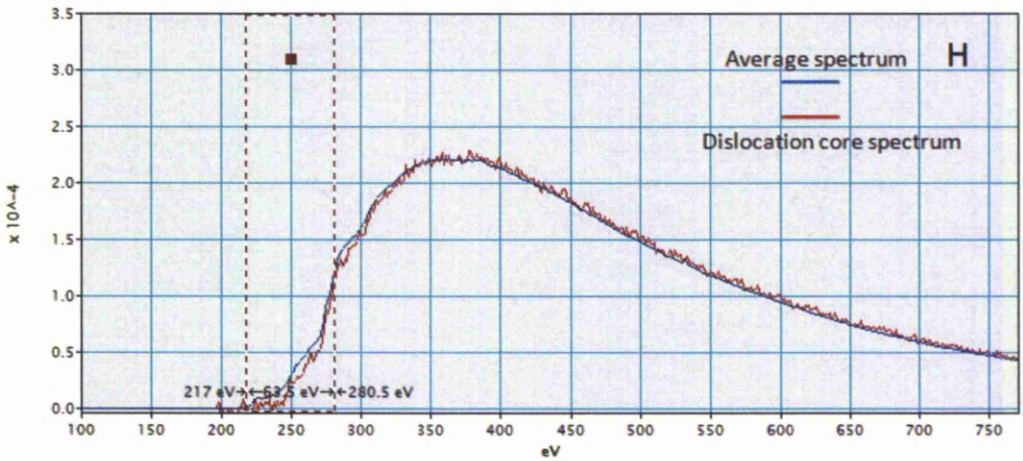

Fig. 8.8 H) Comparison of average (fig G) and the expected mixed dislocation core (fig F) spectra. It can be observed from figure 8.8 H that the ELNES of dislocation core is different from ELNES of perfect crystal. The variation in ELNES peaks are clearly noticed within the selected energy window. The factors that could contribute to these ELNES changes will be discussed along with the results in the next sections of this chapter.

8.5 Reason for studying single crystal Mo

The difficulty of finding end-on screw dislocations within a thin area of [111] orientation in polycrystalline specimens was one of the reasons for

the decision to consider the study of screw dislocations in a [111] molybdenum single crystal. Contamination from the polycrystalline sample due to the presence of <20 ppm carbon in the bulk samples was responsible for further problems while analysing Mo $M_{4,5}$ ELNES edges (edge onset at 227eV with delayed 80 eV) close to carbon K-edge (285 eV). The single crystal samples were prepared in exactly the same way as the polycrystalline samples by standard metallographic and electropolishing techniques. The difference between both the samples was the bulk material purity, crystal orientation and the deformation of single crystal so as to generate ½[111] screw dislocations. This is summarised in table 8.1.

Sample	Purity (%)	Orientation	Deformation	Dislocation density (mm^{-2})
Polycrystalline Mo foil	99.95%	Most grains with <110>	Not deformed	~5 x 10^7
Single crystal Mo	99.99%	[111]	Under high strain rates	~4.3 x 10^7

Table.8.1. Comparison of single crystal and polycrystalline Mo samples studied in this work.

8.6 Mixed dislocation results

8.6.1. Mixed dislocations in polycrystalline sample

Most of the dislocations observed in these samples were 70° mixed dislocations while screw dislocations were of the desired type. Atomic resolution images were taken from dislocations exclusively from [111] orientated grains of the samples using SuperSTEM followed by high resolution EELS experiments. These images were then checked for screw

character by performing geometric phase analysis. Geometric phase analysis reveals the presence of any extra half-plane from the lattice image of a dislocation. The extra-half plane is a general characteristic of an edge dislocation but it is also observed as the contribution of the edge component from a mixed dislocation[2]. The particular case of interest for this work is the mixed dislocation with [111] line direction normal to the foil surface and Burgers vector equal to one of the other three 1/2<111> types, i.e. a 70° mixed dislocation.

In most cases, mixed dislocations were observed in polycrystalline molybdenum samples with a very short range of lattice distortion around the core. These small distorted regions with electron beam along [111] direction were observed at 1000kX magnification in SuperSTEM and could easily be misinterpreted for screw dislocations when they were observed in TEM and STEM for their dislocation contrast.

Due to the presence of such mixed dislocations it was necessary to check the absence of any extra-half planes in the atomic resolution images recorded from dislocations that were thought to be of screw character. Hence, as a part of this research, some mixed dislocations were also studied for their electronic structure near the core. The core structure of mixed dislocations was much complex as compared to screw dislocations due to the partial contributions from both edge and screw components. Therefore the work on mixed dislocations described in this thesis is limited to the study of their electronic structure at the core in comparison to screw dislocations.

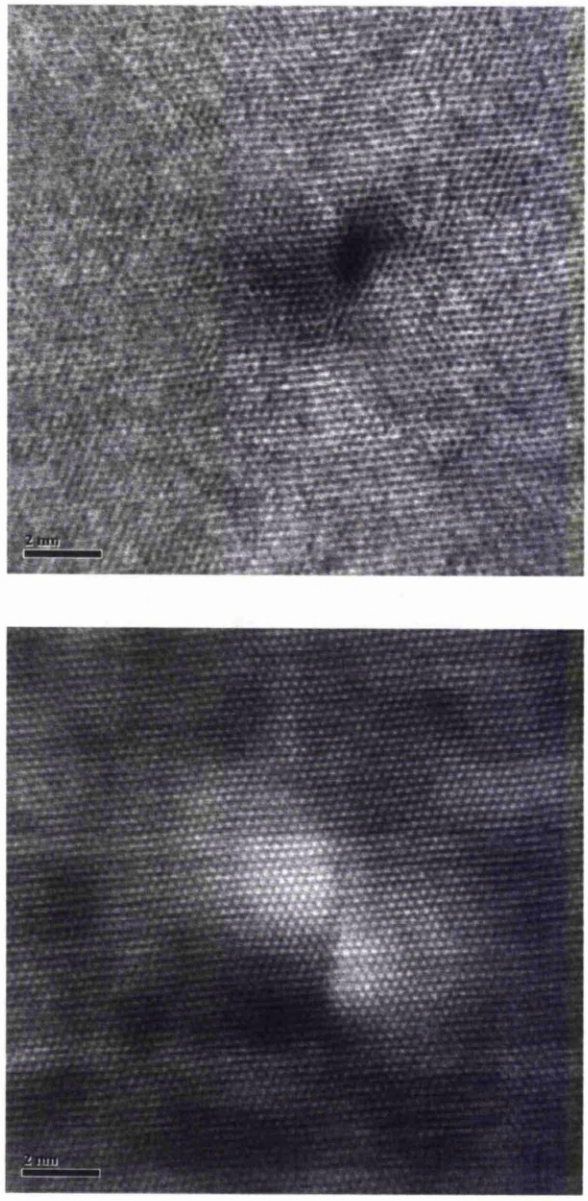

Fig. 8.9 Mixed dislocation in [111] orientation with a small region of contrast arising from the destruction of symmetry around its core.

The figure above is a bright field image and below is the corresponding HAADF. A mixed dislocation with short range of lattice distortion is shown in figure 8.9. The contrast arising due to bending of lattice planes around the dislocation core can be clearly seen from the bright field image.

In figure 8.9, scan noise from the instrument can be seen as fine lines running horizontally across the dark field image. The brighter areas in the HAADF image are better resolved as compared to the darker areas revealing the presence of deformation of the planes surrounding the dislocation. The location of the core of this dislocation using geometric phase analysis is shown in figure 8.10.

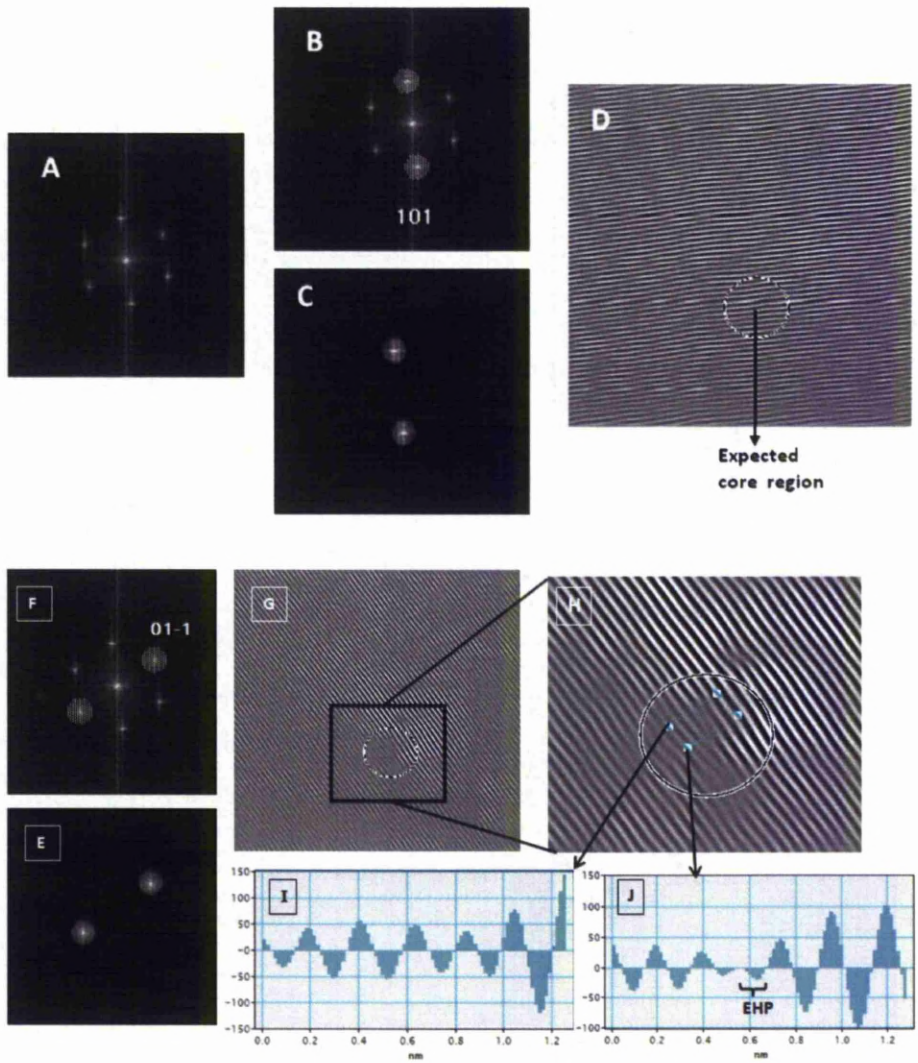

Fig. 8.10 Identification of mixed dislocation core and extra-half planes by geometric phase analysis.

The FFT of HAADF image of mixed dislocation in figure 8.7 is shown in image A of figure 8.10. This was used to identify the reflections and index them accordingly. Masking using <101> reflection is shown in images B and C. The planes responsible for <101> reflections are shown in image D, which is the inverse FFT of image C and careful examination of these planes should reveal any extra-half planes if present. The circle marked in image D is the region that corresponds to the area that has the dislocation contrast in the HAADF. Hence the circle area was the expected core region. From the image D it is obvious that no extra-half planes were present for <101> reflection. Therefore <01-1> were masked as shown in images E, F and G respectively.

The dislocation core region is magnified to show the extra-half plane encircled clearly in image H. The alternative white and dark lines in images D, G and H are a representative indication of the successive 2π phase changes that occur between planes. The two green lines inside the circle are the ROI's for a line profile; the first one was along the region containing extra-half plane and the second one was for dislocation core. The corresponding line profiles are shown in figures I and J. Figure I is the same as a perfect region of the crystal and hence has symmetry which is evident from alternative positive and negative intensity values plotted against the distance in nanometres, and are representative of alternate dark and bright lines in inverse FFT.

Figure J is the line profile along the mixed dislocation core and it can be seen that there are two negative peaks between 0.4 and 0.6 nm. The width of each peak is 1.03 Å. The extra negative-valued peak at 0.6 nm with less intensity in comparison to other peaks represents the extra-half plane and is indicated in the figure as "EHP". Thus the mixed dislocation core was identified and examined for changes using high resolution HAADF images. Some of the recorded mixed dislocations were analysed for ELNES changes by acquiring spectra from their cores.

In order to record ELNES from dislocations, primarily it was essential to find the location of the core on the HAADF image so that the spectrum collected from the selected ROI on the HAADF image contains ELNES from the core. The core was identified by performing Fast Fourier Transforms of HAADF images of dislocations.

Fig. 8.11 shows the Fourier filtered image of the mixed dislocation and figure 8.12 shows the core region magnified and displayed in colour contour map for easy identification. In both of these images, the core is situated inside the marked circle.

Fig. 8.11 Mixed dislocation core clearly identified inside the circle from Fourier filtered image.

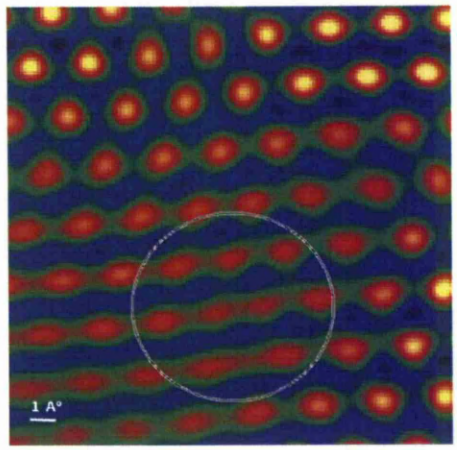

Fig. 8.12 Colour contour image of mixed dislocation core blown up from Fourier filtered image shown in figure 8.11.

The red features in figure 8.10 are the atomic positions as recorded in a HAADF image. Careful observation of the atomic rows from top to bottom in the image reveals the extent of displacement along horizontal and vertical directions. Though the atoms will be displaced in the dislocation line direction, this image cannot reveal the relative z-displacements i.e. along [111] direction.

8.6.2 Mixed dislocations in single crystal Mo

The results obtained from mixed dislocations in polycrystalline molybdenum samples were showing ELNES changes in the spectra obtained from core region as shown in figure 8.8. However the presence of the constituent elements as impurities in polycrystalline samples raised questions as if the changes noticed were due to their presence. It was well known and often reported phenomenon that the existence of impurity atoms in the sample might possibly lead to their segregation at the dislocation cores. One such phenomenon is the presence of Cottrell atmospheres at dislocation cores in iron. Hence it was important to ensure that ELNES changes are caused due to the damage to local symmetry at dislocation rather than due to the presence of impurity

atoms. This eventually led to the study of dislocations in molybdenum single crystal that is ultra pure. Mixed dislocations in samples prepared from single crystal molybdenum were analysed for ELNES changes and will be presented in this section. The experimental techniques and EELS analysis procedures followed for single crystal samples are same as those described for polycrystalline samples. Hence, the results from single crystal Mo samples are presented with short and concise description and any modifications done in the procedure are highlighted with relevant results.

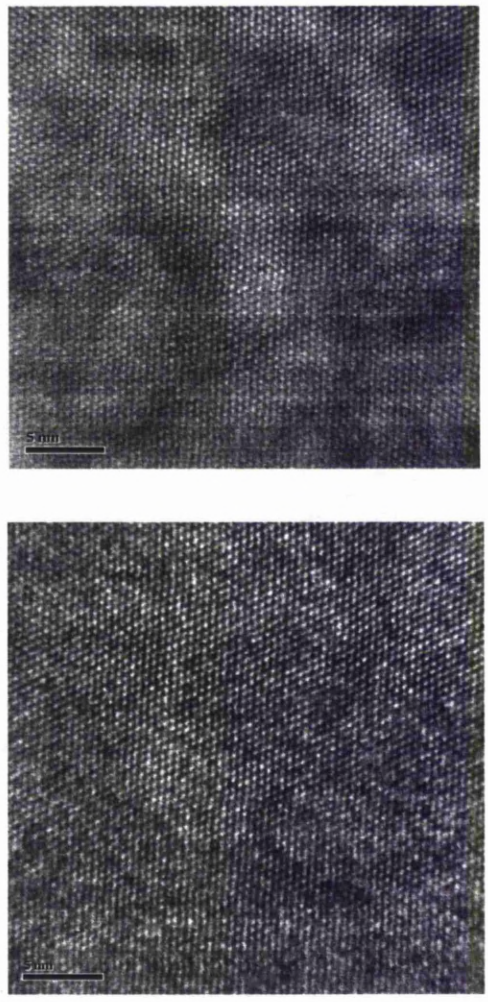

Fig. 8.13 HAADF lattice image (above) and BF (below) images of perfect crystal region in a single crystal molybdenum sample.

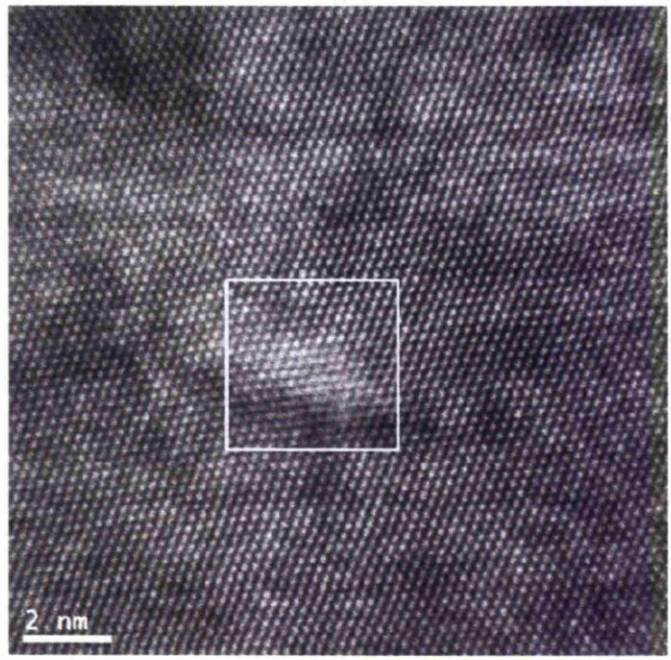

Fig. 8.14 HAADF image of a mixed dislocation showing the region of interest from which the EELS spectrum image was acquired.

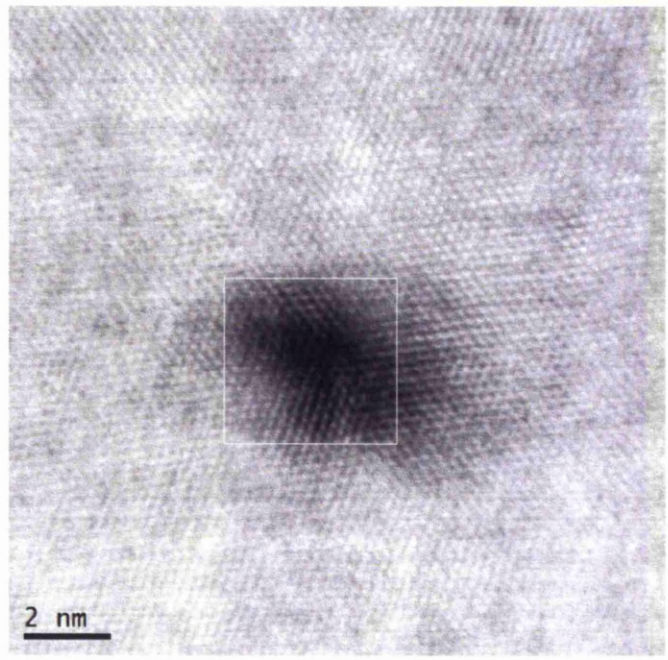

Fig. 8.15 SuperSTEM Bright field image of the mixed dislocation shown in figure 8.14.

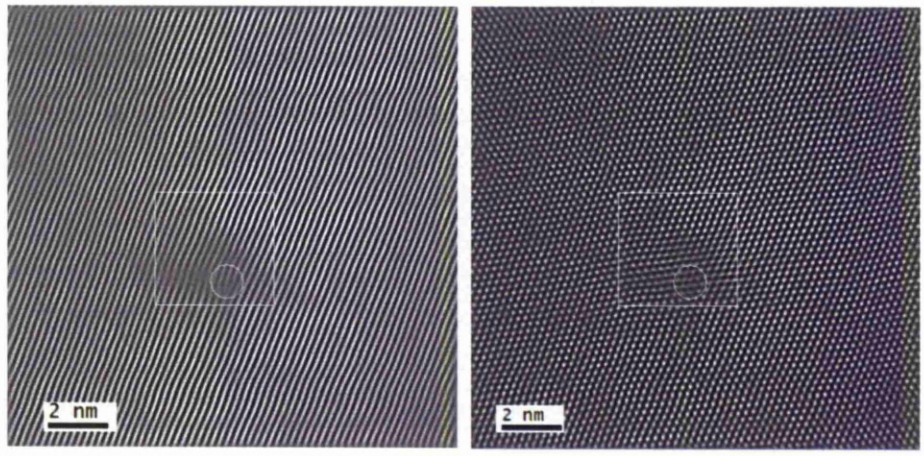

Fig. 8.16 Inverse FFT of HAADF (left) revealing the extra half plane and Fourier filtered image (right) with dislocation core enclosed in circle.

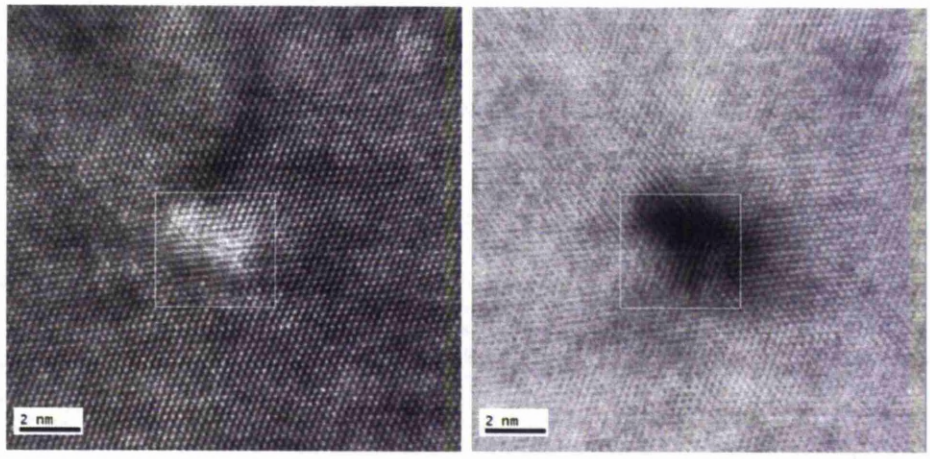

Fig. 8.17 HAADF and BF images recorded after the EELS acquisition from the dislocation. The region of SI acquisition is shown in square box.

It can be observed from figure 8.17 that there was not much carbon contamination in this sample after EELS acquisition. Bright field and HAADF images recorded after EELS acquisition in polycrystalline samples showed carbon contamination while in single crystal samples it was reduced to a minimum. This meant that the ELNES changes at Mo $M_{4,5}$ edge would be much vivid and almost free from the interference of carbon K edge signal.

Sample drift is a common problem encountered in electron microscopes and it can be either upwards, downwards or a diagonal drift. If the sample is drifting while EELS is being acquired, then it can lead to a situation where the atoms of the core are probed at a different position than their original position in the pre-SI HAADF image. For example if we assume the sample drifts at 1.0 Å/min (i.e. 0.016 Å/sec) and a spectrum image of 16x16 pixels (since it has to be 2^n x2^n) is being collected at a rate of one second per pixel, then it would take 4.2 minutes (i.e. 256/60) for the SI acquisition to complete and the sample would have drifted by 4.2 Å at the end of the SI acquisition. Applying the movement of core atoms to this case, they would have moved by 4.2 Å in the direction of the drift at the end of acquisition which is a bigger value than the interatomic distance in Mo (3.14 Å)[3]. This suggests that the core atoms in the pre-SI HAADF image have moved to the position of their neighbouring atoms in the direction of drift at the end of acquisition.

If the acquisition is linear and along horizontal axis in a square box of 16x16, then at the end of acquisition of the first row of 16 pixels, the atoms would have moved by 0.2 Å (i.e. 16/60) in the direction of drift. If it is assumed that that there are 16x16 atoms in a SI image of 16x16 pixels (i.e. an atom per pixel) and assuming the core is at the centre of the SI image according to pre-SI HAADF image, then by the time the beam reaches the core pixel position of 8x8 at 120^{th} second (7 rows with 16 pixels +7pixels in 8^{th} row=119 pixels at 1s/pixel acquisition time), the core would have already moved 1.9 Å (i.e. 119/60) far away from its original position.

This suggests that the beam would experience only a fraction of the atomic column and the signal will hence be much reduced from the core atoms. In reality the drift rates can be higher than the above example and in that case the neighbouring atoms can move completely to the position of core atoms. This would mean the core atoms according to their

position in the pre-SI HAADF image do not match the pixels in same position in the SI image. However the pixels that are from the dislocation core atoms can be found by comparing the positions of the core atoms in both pre-SI and post-SI HAADF images assuming there is no carbon contamination. In practice the contrast from dislocation in post-SI HAADF image is masked with a heavy white contrast from carbon contamination that also affects the identification of core in the IFFT of post-SI HAADF image. However, the Fourier filtered image of post-SI HAADF is not affected extensively and can still be used to identify the core. The drift associated with the mixed dislocation core in figure 8.14 is shown in the IFFT of its post-SI HAADF in figure 8.18.

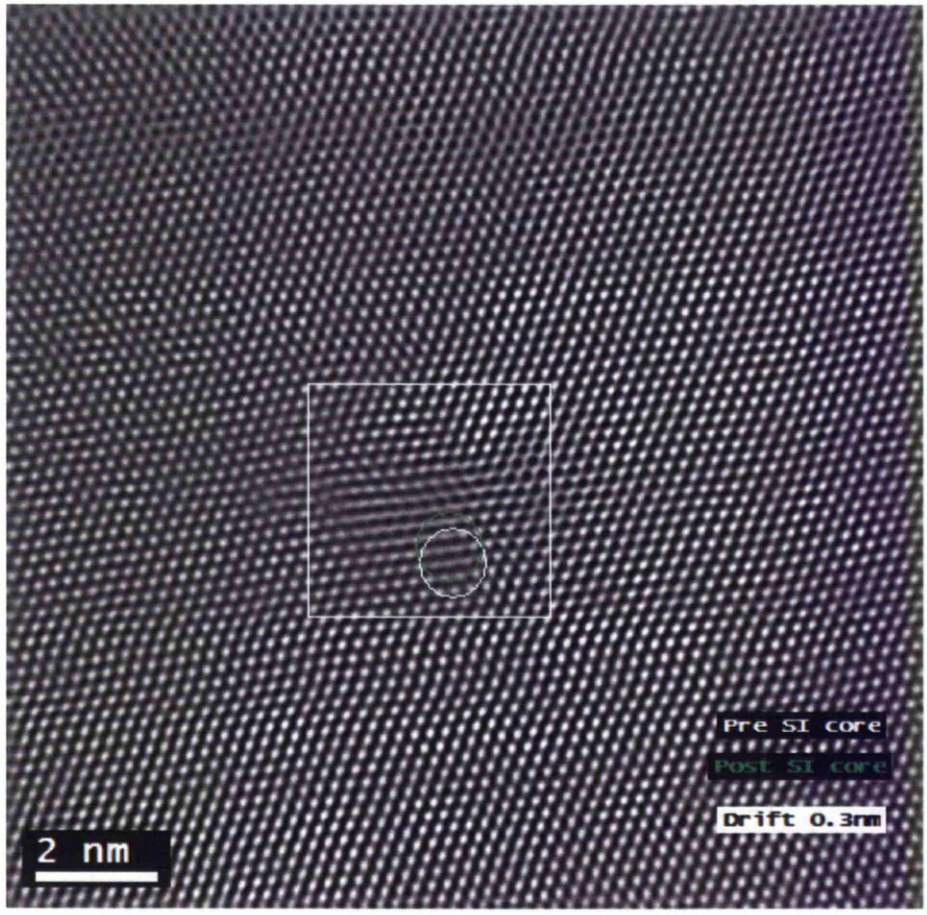

Fig.8.18.Fourier filtered image of post-SI HAADF image showing that the sample experienced diagonal drift and the core moved by 0.3 nm.

A magnified image of the dislocation core shift between SI start and finish from figure 8.18 is shown in figure 8.19.

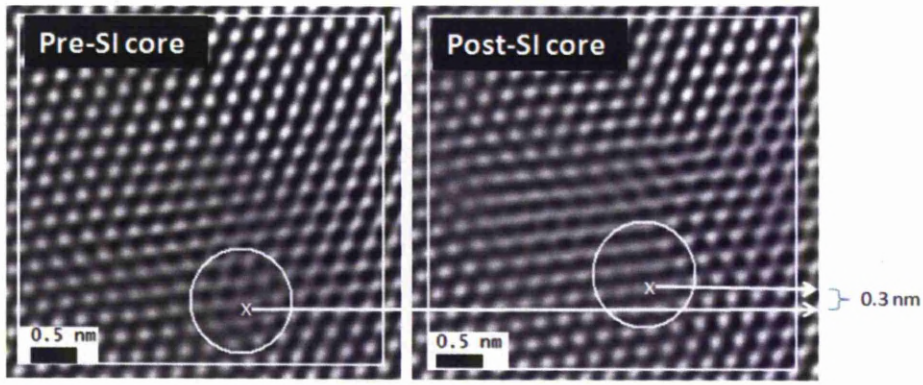

Fig.8.19. Mixed dislocation core (marked as X in the image) from its original position in the pre-SI HAADF Fourier filtered image to post-SI HAADF Fourier filtered image moving diagonally by 3 Å. The white square represents the selected region for SI acquisition; the core is at X enclosed in the white circle.

The EELS SI acquired from the region shown above is given in figure 8.20. The EELS is acquired in parallel dispersive mode by choosing energy range of 100 -500eV at a rate of 0.3 seconds per pixel and at a dispersion of 0.3eV/channel. The EELS aperture is 3mm; the collection semi-angle is 19 milli radian while the convergence semi-angle is 24 milli radian. The total acquisition time is 128seconds with 400 pixels acquired at 0.3 seconds per pixel (approximately ~400x0.3) and the size of the acquired SI is 3.87nmX3.87nmX400eV.

The time elapsed between the pre-SI HAADF and post-SI HAADF is 230 seconds. This suggests that the core had moved 0.3 nm in 230 seconds as shown in figure 8.19, but the time taken for SI acquisition is only 128 seconds according to the image properties of the EELS SI. Therefore the core should have moved 0.167 nm or 1.67Å in 128 seconds. This is important to estimate the position of pixel in the SI image that

corresponds to the core in the HAADF image. If the core position can be mapped in the SI then the pixels that correspond to the core can be studied for ELNES changes.

A single pixel in the SI is collected in 0.3 seconds and the drift of the core in this time will be 0.0004nm i.e. {(0.3s x 0.3nm)/230s}.The position of the core in the EELS SI is mapped with respect to the pre-SI and post-SI IFFT images as shown in figure 8.20.

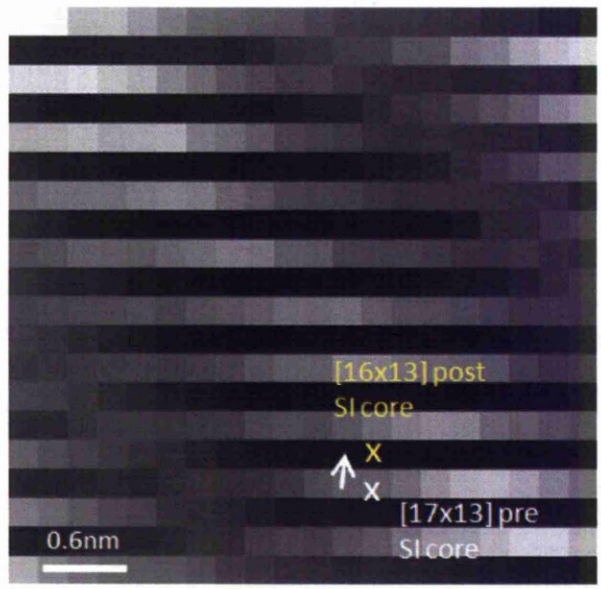

Fig.8.20. EELS image of the mixed dislocation showing core position before and after SI acquisition and the drift direction indicated by arrow.

The time lapse between the collected pre-SI HAADF image and the start of SI acquisition is 88 seconds. In order to calculate the drift of the core, this time has to be added to the time taken for the total number of pixels collected before the probe reaches the pre-SI core position. It can be observed from figure 8.20 that there are 16 rows with 20 pixels each and another 12 pixels in the 17^{th} row (i.e. 332 pixels in total) before the pre-SI core position can be reached. Since there is a drift of 0.0004 nm in the time a single pixel is collected, the drift of the core after the collection of

332 pixels is 0.1328nm (i.e. 0.0004nm X 332 pixels). The drift that occurs in 88 seconds is 0.117nm {i.e. (88s X 0.0004nm)/0.3s}.Therefore the total drift of the core before the electron beam reaches the pre-SI core position is 0.25nm i.e. (0.1328+0.1172). In figure 8.20 the size of each pixel is 0.2nmX0.2nm and it can be said that the core must have moved one pixel position up since the drift is in the upwards direction. Hence the spectrum from the dislocation core must be the pixel located at (16x13) position as indicated in figure 8.20 which also corresponds to the post-SI core position.

The EELS spectrum image shown in figure 8.20 consists of spectra that have been drift tube shift corrected, dark current noise removed and realigned in energy calibration. The EELS SI is corrected with a linear drift range of 100 channels on EELS CCD. The dark current or background noise is removed and the spectra are realigned according to the procedure shown in figure 8.5. The spectrum from the first pixel of a drift tube corrected SI is shown in figure 8.21. In this image the energy window of interest for Mo-$M_{4,5}$ core loss edge is shown with the edges on correct energy scale.

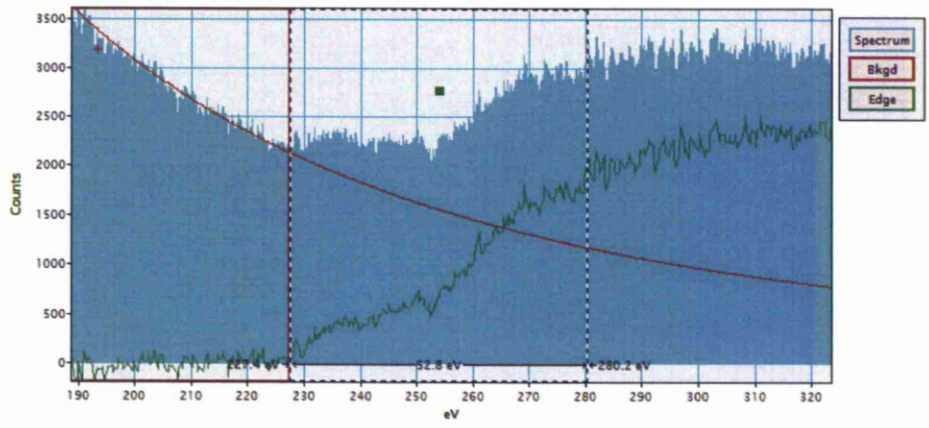

Fig.8.21. Mo-$M_{4,5}$ EEL spectrum from the drift tube corrected SI. The background correction is shown along with a selected edge region between 228 and 280eV.

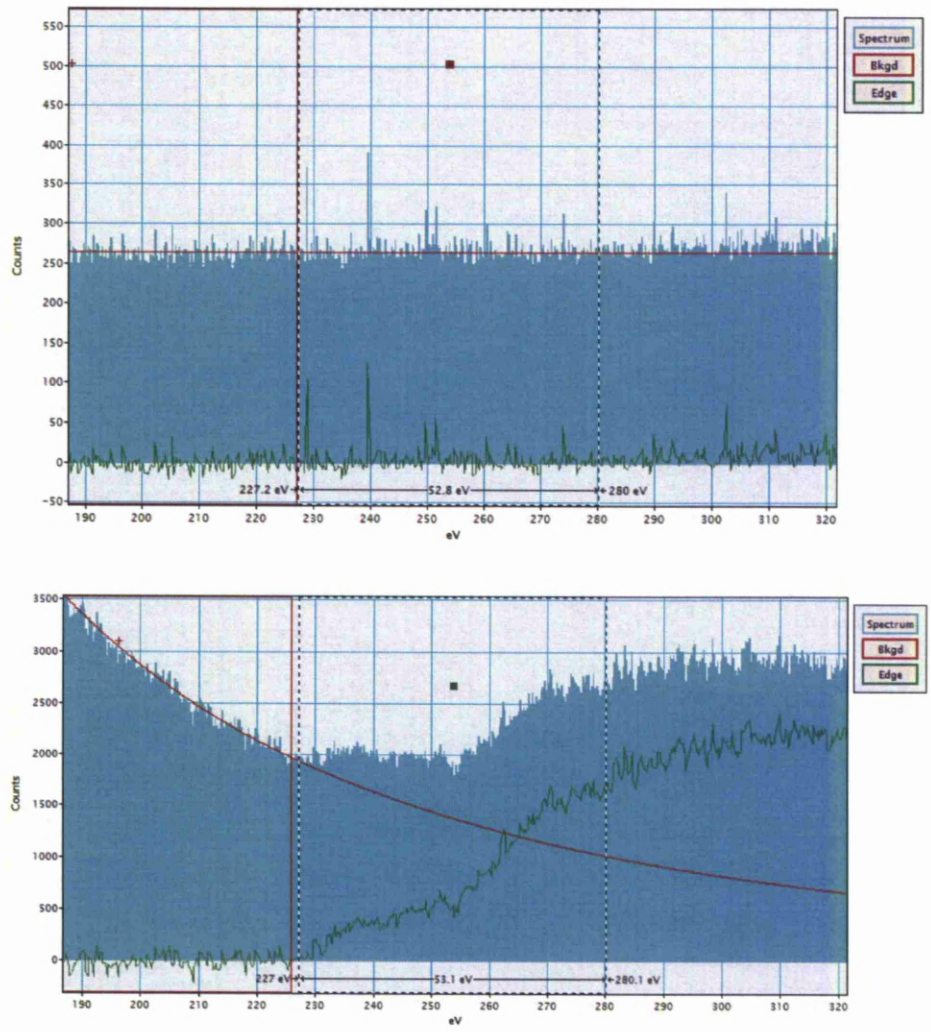

Fig.8.22 The above figure shows dark current noise in the spectrum recorded with beam blanking in the energy window 227-280eV. The below figure shows the EEL spectrum from the first pixel of a dark current noise removed SI showing Mo-$M_{4,5}$ core loss edge onset at 227eV and the background.

For the chi square script to be applied to this SI image the background has to be subtracted and the EELS signal has to be extracted. The background subtraction done for the EELS SI is shown in figure 8.23. When the chi square script is applied to background subtracted spectra, it reveals the spectra that change in ELNES in the chi square image.

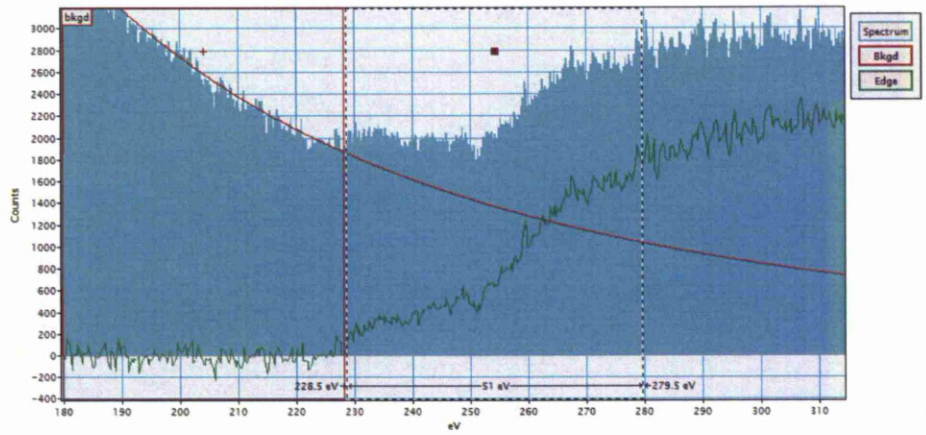

Fig.8.23. Figure showing the background subtraction to extract signal from the first pixel spectrum of SI image.

The background removed signal is then checked for any traces of remaining background features and if present they are removed by repeating background subtraction with those features included. The background is removed for all the spectra in the SI and their sum spectrum is generated. In this sum spectrum, the ELNES region is chosen as required by the script i.e. between 227 and 280eV and a normalisation region is chosen a few 100 eV away from the Mo-$M_{4,5}$ core loss edge. These energy windows are shown in figure 8.24. CCD Channels used for ELNES are 227 to 280 and for normalisation are 285 to 300. The chi square script then generates a chi square image which reveals bright pixels that have changes in ELNES in the selected energy window with respect to the normalisation energy window.

Many trials were taken with same ELNES energy window but different normalisation windows. The chi square image shown on the right side in figure 8.25 is the resultant chi squared image when the normalisation window is chosen from 285 to 300 eV, while the image on the left is its corresponding ELNES signal SI. The positions of the spectra that show ELNES changes revealed in chi square image are identified with in the white circle in the ELNES signal SI and they remained significant

irrespective of different normalisation windows. The location of these bright pixels is shown on the chi square image as [16x11] and [16x12] which meant that these pixels are in the 16th row and 11th, 12th columns in the SI image. These were approximately identified to be [16x13] in figure 8.20. However, figure 8.25 reveals that the core is located in the same area but in the 11th and 12th column rather than 13th column.

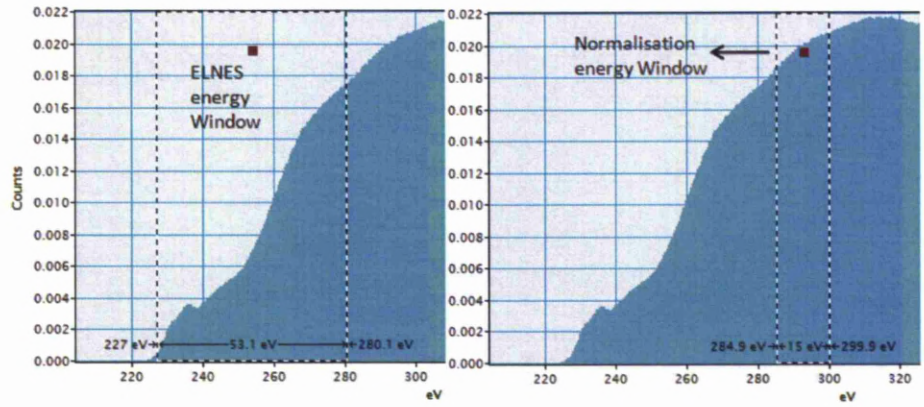

Fig.8.24. Mo-$M_{4,5}$ ELNES window (227-280.1eV) and the normalisation energy window (284.9-299.9eV) used for chi square trial of mixed dislocation core.

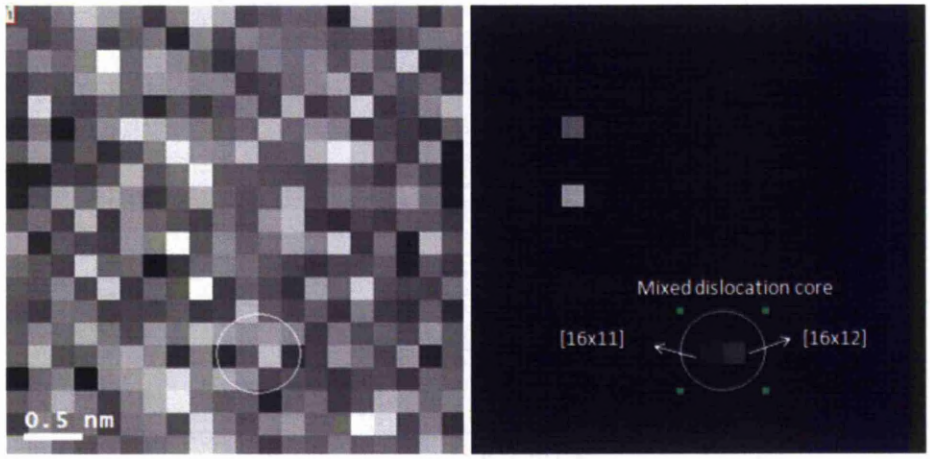

Fig.8.25. Chi squared image showing the pixels that contain ELNES changes from a mixed dislocation core. The other two pixels were showing higher intensity because their spectra included an x-ray at

252eV and 278eV respectively. In both cases the spectrum that contains ELNES variations was shown in white colour but they are far from the expected dislocation core region. Therefore they are discarded. The ELNES from the signal SI from a perfect crystal region (i.e. 1st pixel in the SI shown in fig.8.25) was taken and is compared with the ELNES from the dislocation core spectra. The difference is shown in figure 8.26.

In fig.8.26 the ELNES at dislocation core remains very much similar to the perfect crystal except in the region 225 to 235eV where the peaks show greater intensity than the perfect crystal peaks. The ELNES from the pixel at (16x12) is shown in figure 8.27. In this figure the ELNES of mixed dislocation core increases between 250 and 260eV. However, the intensity of the peaks between 225 and 235eV remains the same as that of perfect crystal spectrum.

The theoretical ELNES changes between perfect crystal and mixed dislocation core are compared with the experimental ELNES in figures 8.28 and 8.29. In figure 8.28 experimental ELNES changes from a dislocation core pixel at 16x12 are compared to theoretical ELNES with respect to perfect crystal.

In figure 8.28, for mixed core the peaks at 230 and 235eV remain subdued and the changes start between 240 and 250ev in both theoretical and experimental ELNES with respect to perfect crystal. The increase in intensity mixed core between 250 and 260 eV is evident in both comparisons. The intensity gap observed between perfect and mixed core theoretical ELNES after 260eV does not appear in experimental comparison. Hence, changes observed through the theoretical and experimental comparison agree to a certain extent in the energy ranges of 230 to 260eV for a mixed dislocation core.

In figure 8.29, experimental ELNES changes from a dislocation core pixel at 16x11 are compared to theoretical ELNES with respect to perfect crystal. Two sharp peaks are observed at 230 and 232 eV from the experimental mixed core ELNES spectrum while no such sharp peaks exist in the theoretical dislocation core spectra. This could suggest that this core atom is occupying a different or inequivalent site with respect to the other core atom. Beyond these sharp peaks, the spectrum is similar to the perfect crystal in experimental spectra.

Careful observation of the spectra in figures 8.28 suggest that a similarity of spectral changes to some extent exists between experimental and theoretical results although majority of the ELNES region is masked by the noise. In figure 8.29 the changes do not seem to occur after the initial sharp peaks. In both cases, the signal is not strong enough to dominate the noise that masks the fine structural details in the experimental results. While theoretical results have shown clear changes between the ELNES of mixed dislocation easy core compared to perfect crystal, the experimental results do not tend to show the changes prominently due to background noise and weak signal.

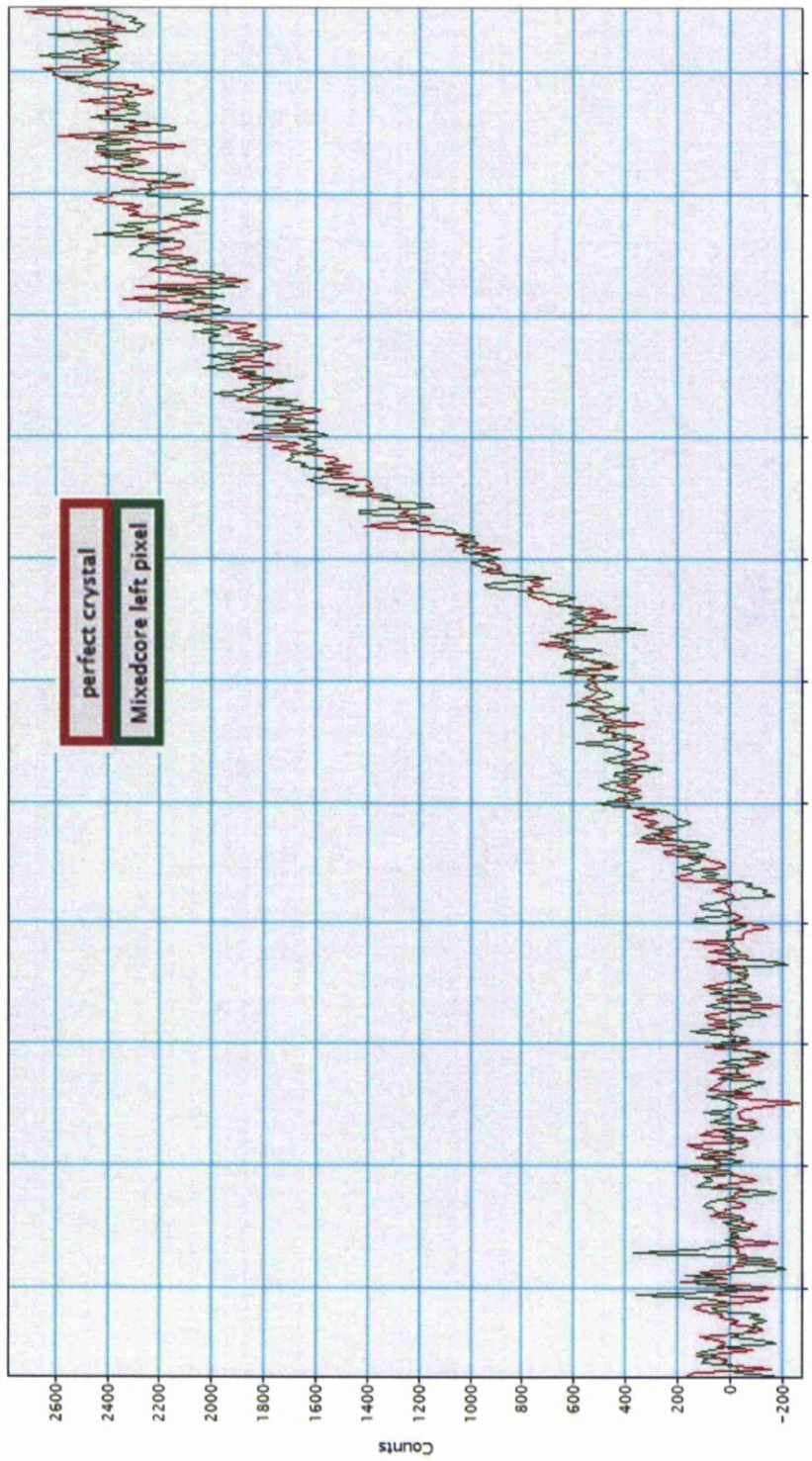

Fig.8.26. Mixed dislocation core spectrum from pixel (16x11) in fig.8.25 compared with perfect crystal spectrum taken from the first pixel in signal SI.

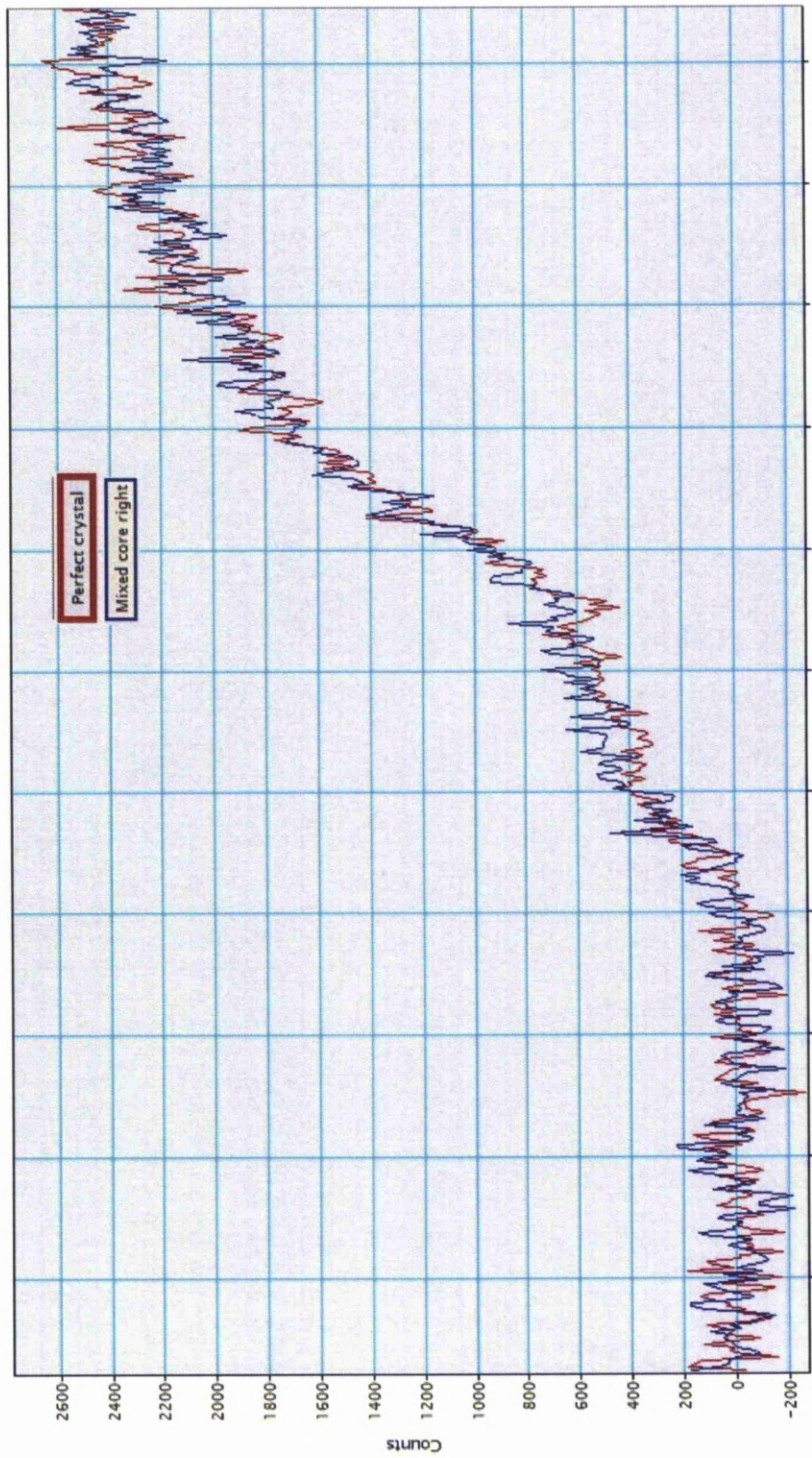

Fig.8.27. Experimental Mo-$M_{4,5}$ ELNES comparison between perfect crystal and mixed dislocation core located at (16x12) pixel.

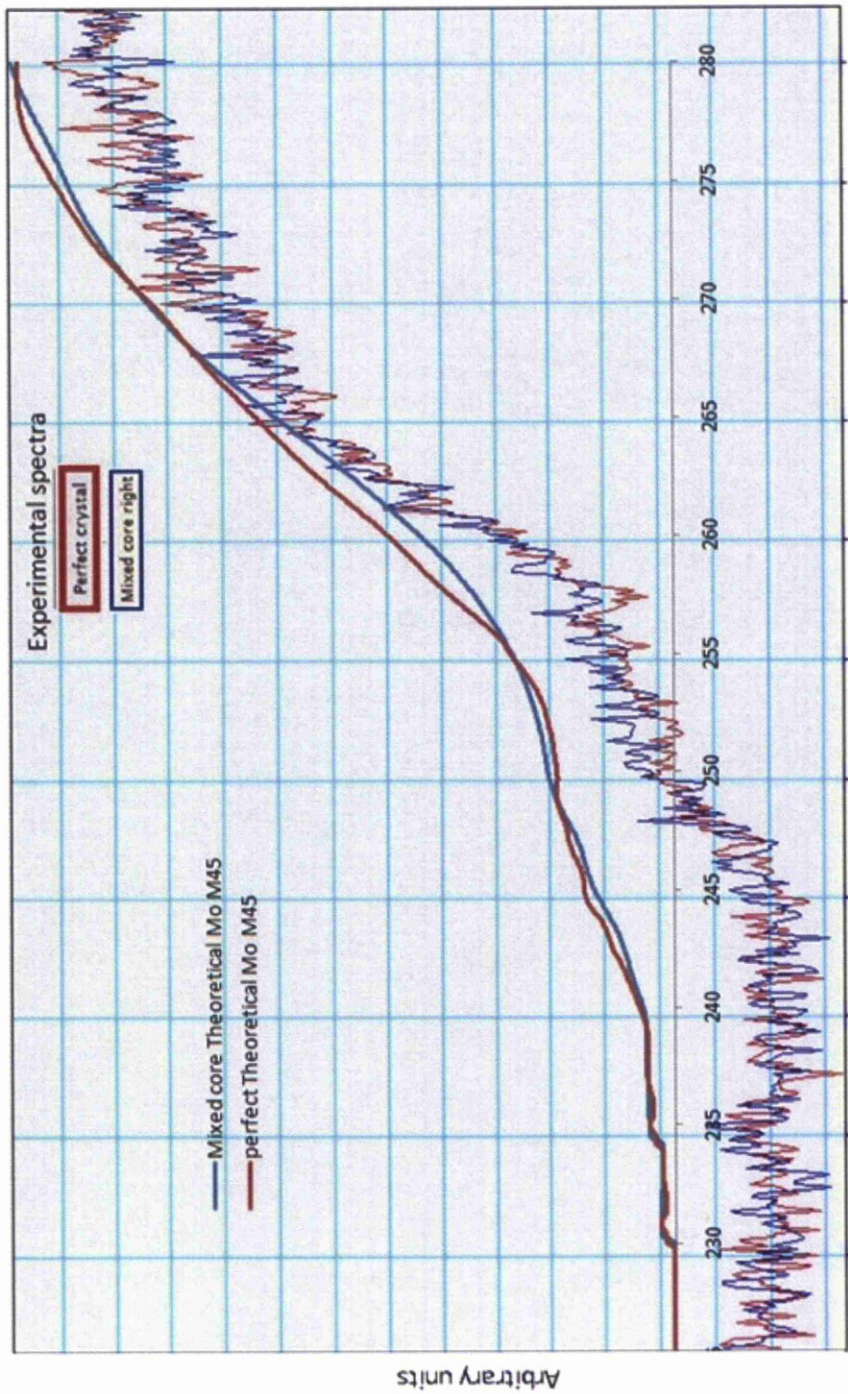

Fig.8.28. Comparison between theoretical and experimental Mo- M4,5 ELNES changes observed at a dislocation core (16x12 pixel in chi square image)with respect to perfect crystal.

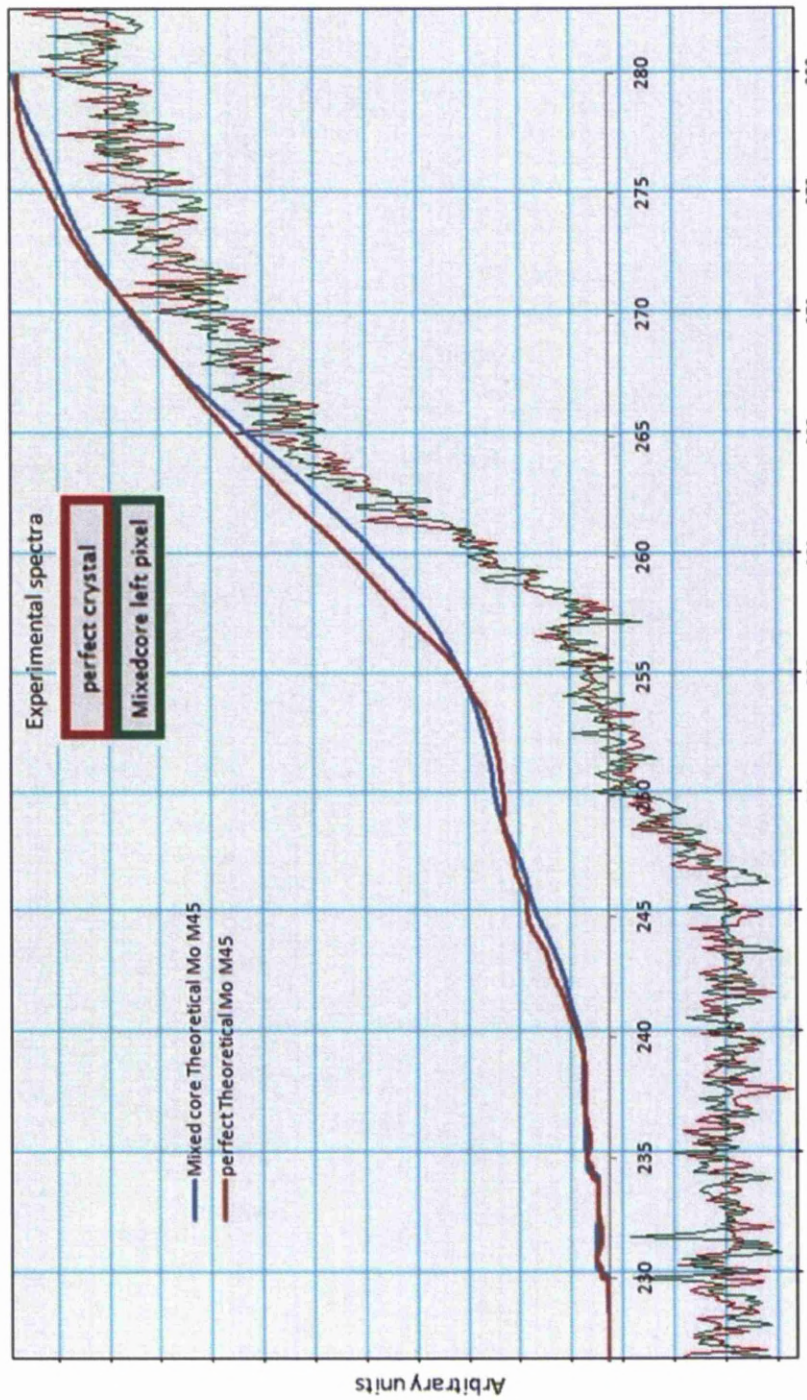

Fig.8.29. Comparison between theoretical and experimental Mo- $M_{4,5}$ ELNES changes observed at a dislocation core (16x11pixel in chi square image) with respect to perfect crystal.

8.7. ½ [111] Screw dislocations in Mo

8.7.1. Screw dislocation core identification

½[111] screw dislocations in polycrystalline as well as single crystal molybdenum samples were investigated for ELNES changes at $M_{4,5}$ edge. The EELS analysis procedure followed for screw dislocations was same as that for mixed dislocation but the geometric phase analysis was different. This was due to the reason that screw dislocation core was difficult to identify in [111] direction. In the case of mixed dislocation geometric phase analysis revealed extra half plane and the core was located easily.

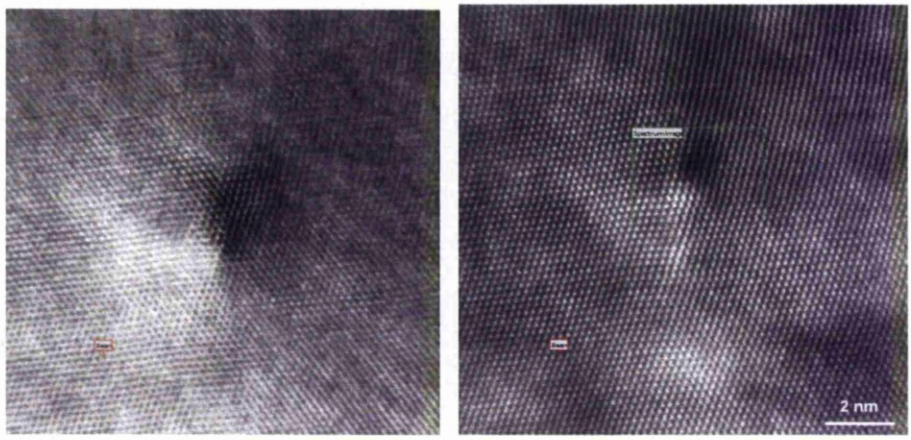

Figure 8.30 Bright field (left) and HAADF (right) images of screw dislocation in a polycrystalline sample, showing the well-known bright and dark contrast around the dislocation core.

For a screw dislocation the lattice distortion on the surface was used to estimate the position of dislocation core. The Eshelby twist characteristic to screw dislocations can cause surface relaxation which generates short edge components along the surface of the foil[4]. This kind of lattice distortion at screw dislocation was evident from the contrast of HAADF and BF images and the absence of extra half planes indicated their screw

character. The screw character was confirmed by performing live geometric phase analysis which was different from the analysis performed for mixed dislocation. After confirming the screw character, EEL spectra were acquired from the screw dislocation and from perfect crystal region. These were analysed for ELNES changes using the chi squared script and then compared with each other. The observed ELNES changes were then compared with theoretical ELNES changes. These changes are then analysed taking into consideration factors that can affect ELNES results obtained from experiments and simulations.

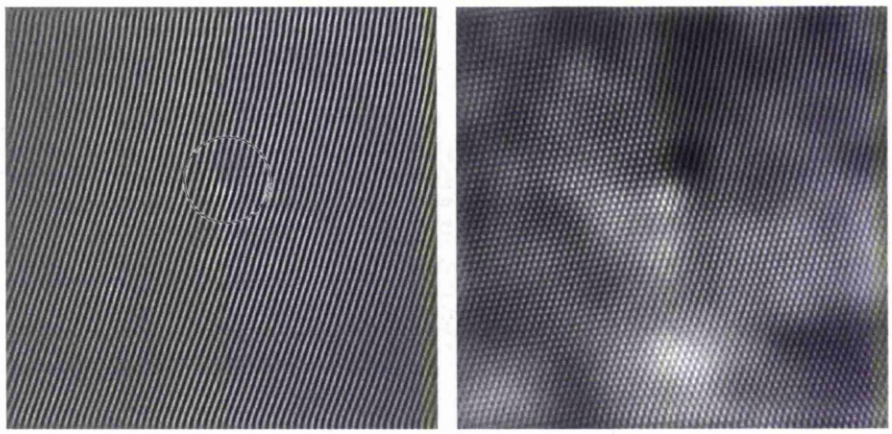

Fig. 8.31 Inverse FFT (left) and Fourier filtered image (right) of screw dislocation shown in figure 8.30. Dislocation core is enclosed in circle.

In figure 8.31 the contrast from screw dislocation can be observed clearly in both inverse FFT image of HAADF and Fourier filtered image. Another screw dislocation is shown in figure 8.32 and confirmation of screw core using live geometric phase analysis is shown in figure 8.33.

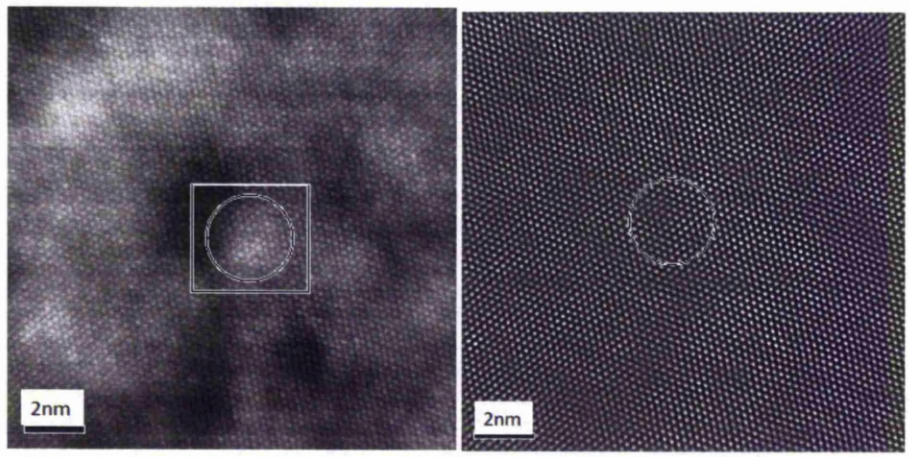

Fig. 8.32 HAADF (left) and Fourier filtered image (right) of screw dislocation; core is enclosed in the circle and the ROI box used for EELS SI acquisition is shown.

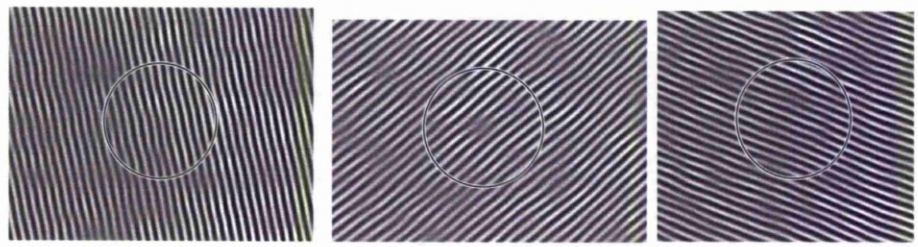

Fig. 8.33 Figure showing the absence of extra-half plane indicating screw character of the dislocation.

In figure 8.33 the planes that correspond to each set of reflections were examined and distortion of the planes in the central image was noticed which gave a fair estimate of screw dislocation core position. Live geometric phase analysis (GPA) was performed for confirming the screw character and core position. This was shown in sequential steps in figures 8.34 A to 8.35.

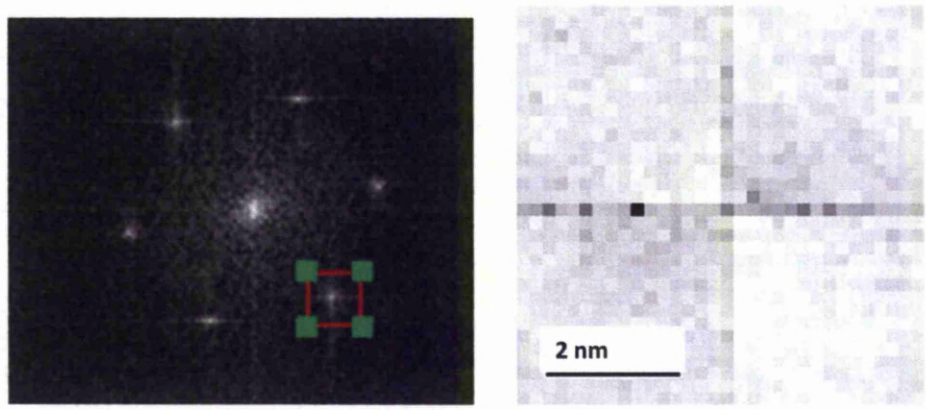

Fig. 8.34 A) Figure on the left is FFT of HAADF image of screw dislocation with a <110> diffraction spot selected for live GPA; the image to the right is the live FFT of the selected diffraction spot.

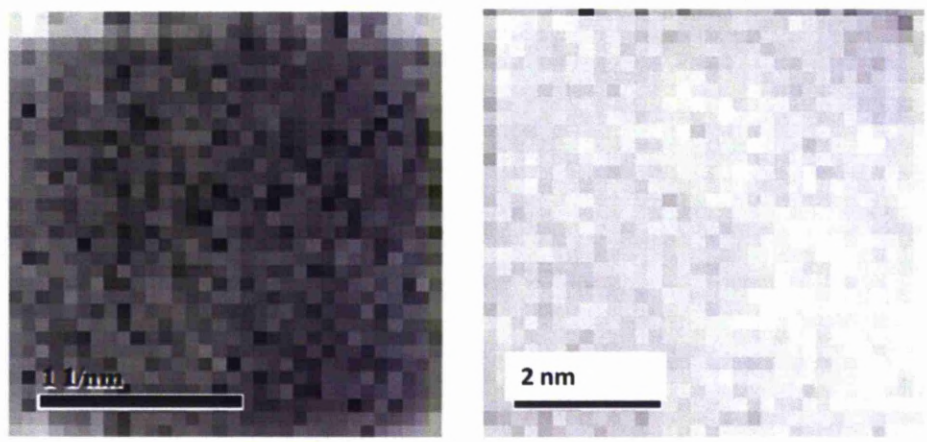

Fig. 8.34 B) Second live FFT (left) and third FFT (right) of the selected diffraction spot. The diffraction spots which bear the planes with lost symmetry appear to change their phase by losing continuity. This loss is observed in the phase ramp between the planes and is displayed in the third FFT image using the option "Display phase" provided in Digital Micrograph.

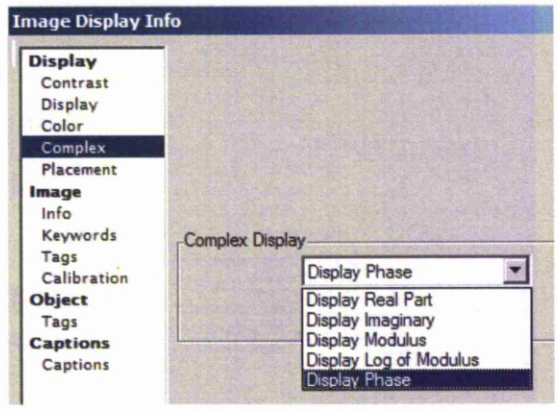

Fig. 8.34 C) Image of the menu that provides the option to choose "Display phase" in Digital Micrograph®.

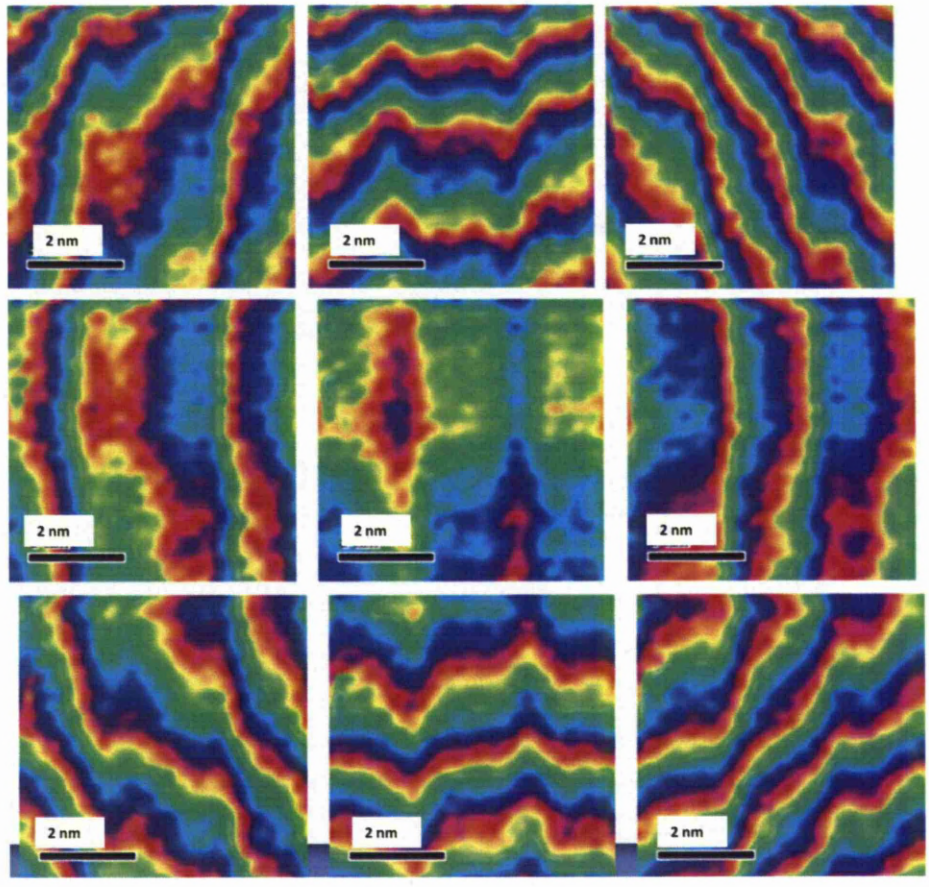

Fig.8.35 Geometric phase analysis for the selected diffraction spot shown in figure 8.34A.

In figure 8.35, the six images around the central image correspond to the position of the selected ROI around the diffraction spot. The central image is the geometric phase when the ROI is on the diffraction spot, and the surrounding six images shows phase ramp as the ROI is moved away from the diffraction spot. The features that appear as curves with different colours were analogous to the distribution of planes that are responsible for the selected diffraction spot. If there was any discontinuity in the planes like an extra-half plane in the case of a mixed dislocation, it was evident from these images.

Figure 8.35 is the geometric phase analysis for a screw dislocation; there was no extra-half plane but there was noticeable amount of distortion in the planes which supports the screw character. Since the planes have periodic symmetry of 2π separated by repetitive units of lattice parameter in a perfect crystal, any damage to symmetry due to a dislocation in a deformed crystal can be revealed by the geometric phase analysis. This procedure was followed for all the diffraction spots. The screw core was confirmed in the region where the planar symmetry was heavily disfigured and its position was noted in the EELS spectrum image for further analysis.

8.7.2 Screw dislocations in single crystal Mo

Screw dislocations in single crystal molybdenum are also studied in this research. 99.99% pure single crystal samples containing ½[111] screw dislocations were examined in TEM and SuperSTEM. Low magnification images were recorded to map the screw dislocations in TEM. It was followed by high resolution imaging and EELS experiments using SuperSTEM. ELNES changes were investigated on and off the screw dislocation core and compared with each other. Conclusions were drawn from the ELNES comparison results.

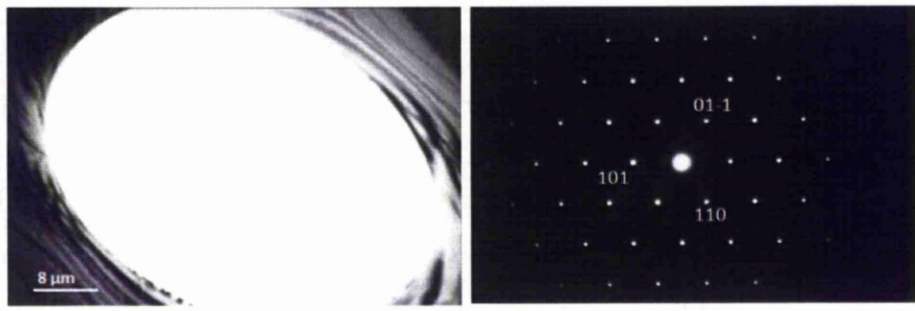

Fig.8.36.TEM bright field image of single crystal sample showing near hole regions and [111] diffraction pattern for bcc molybdenum.

Fig.8.37.TEM bright field image of screw dislocations in [111] direction recorded at 20kX magnification. Screw dislocation shown in the red circle is visible with a faint contrast. The dislocations that are visible in the TEM are recorded and the location of them is mapped using low magnification images. The single crystal samples were much cleaner than the polycrystalline samples without oxides or deposits on the surface. This made the identification of screw dislocations much easier in the TEM.

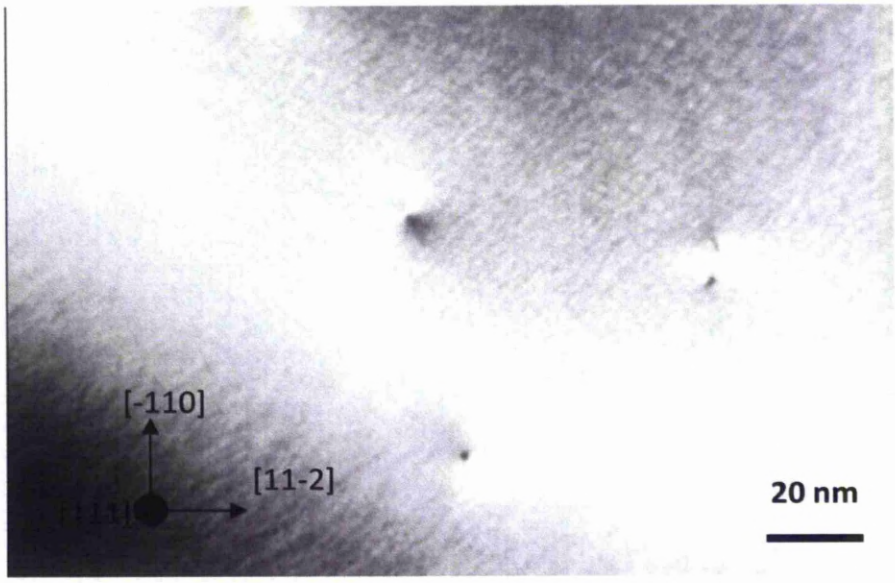

Fig.8.38.End-on screw dislocations in a single crystal Mo sample; bright field image recorded at 120kX magnification in TEM.

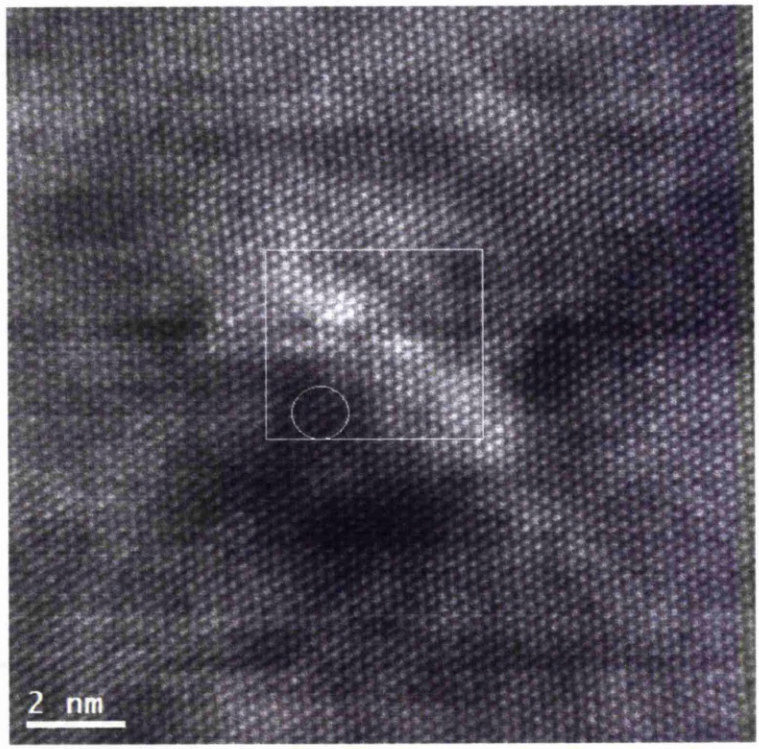

Fig.8.39. HAADF image of ½[111] screw dislocation with its core in the marked circle; EELS SI was acquired from the ROI box as shown.

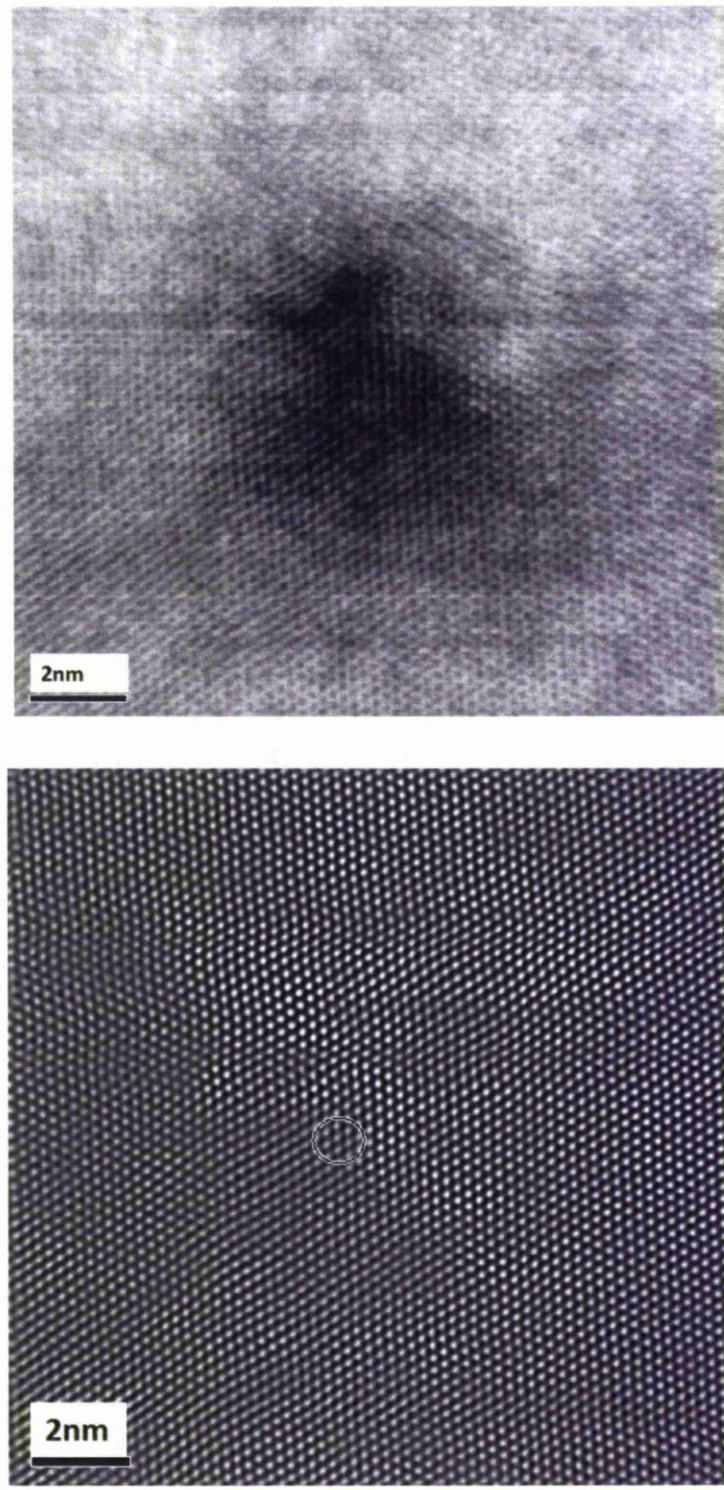

Fig.8.40.SuperSTEM bright field image (above) and Fourier filtered HAADF image (below) with screw dislocation core in the marked circle.

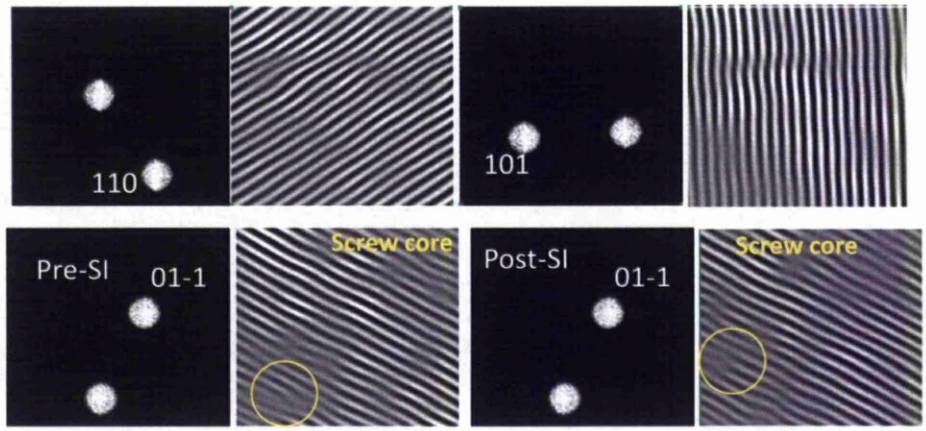

Fig.8.41.Geometric phase analysis showing the masking of different diffraction spots in order to reveal the presence of any extra-half planes.

It was evident from figure 8.41 that there are no extra half planes from the dislocation but some distortion along the plane of the paper was noticed at the core which supports the screw character. The position of screw core in pre-SI and post-SI Fourier filtered images is marked in the yellow circle. The screw dislocation core in pre-SI and pos-SI Fourier filtered images with in the spectrum image are shown in figure 8.42. An EELS SI is acquired from the selected box region shown in figure 8.39 with a drift tube correction linear shift of 100 channels on EELS CCD. The dark current noise is collected and is removed from the EELS SI, and the spectra are realigned by using the drift tube correction script.

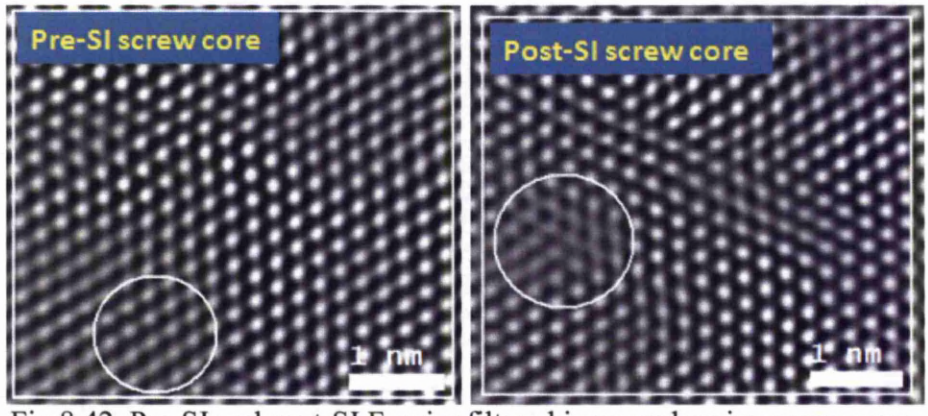

Fig.8.42. Pre-SI and post-SI Fourier filtered images showing screw core.

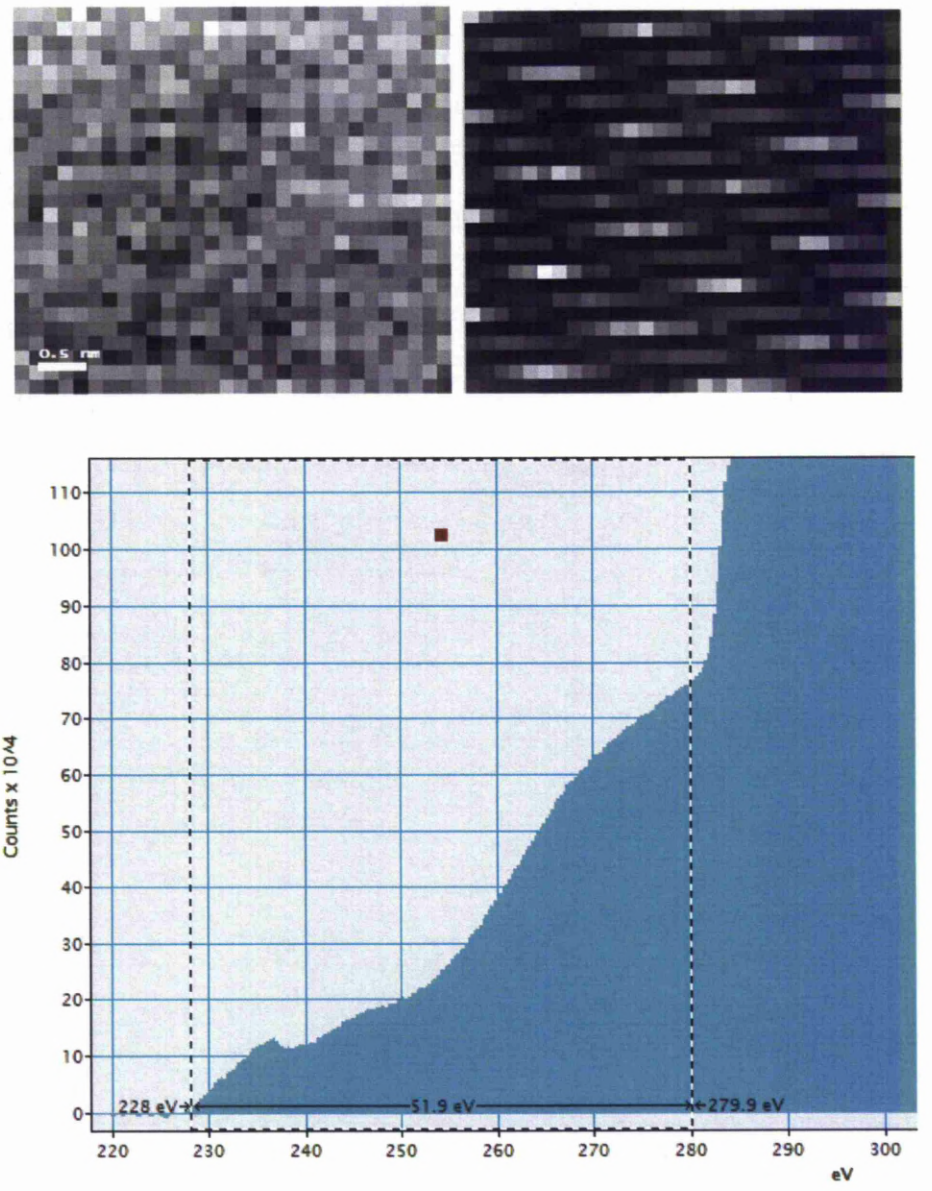

Fig.8.43.EELS SI acquired from screw dislocation core (left); background subtracted SI (right) and its sum spectrum (below).

After the background was removed from the SI and the spectra are summed, the chi squared script was run to detect ELNES changes from the screw dislocation core. The SI consisted of 810 pixels (30 x27) out of which a group of pixels appeared to have ELNES changes when $M_{4,5}$ was normalised with an energy window of 280 -300 eV close to the expected

core position. Since chi squared was only an image, the bright pixels from chi squared image were marked and their corresponding pixels in background subtracted SI were used to generate individual spectra.

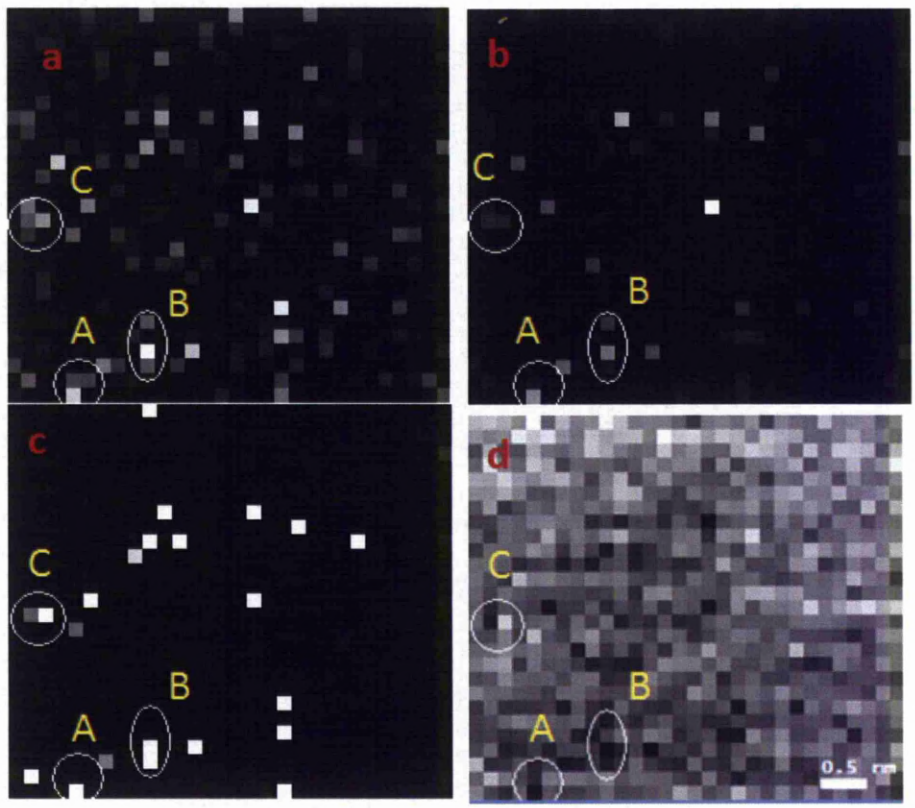

Fig.8.43a, b and c) Chi squared images generated by three individual trials showing pixels A, B and C that exhibit ELNES changes; d) Spectra A, B, C are marked on original SI.

In above figure, three chi squared images generated by three individual trials were compared with one another. This was done to ensure that the chi squared script was detecting spectral changes that were genuine to the ELNES at $M_{4,5}$. The energy window chosen for normalisation in figure 8.43a is from 285-300eV, in 8.43b it is from 320 to 360 eV and in figure 8.43c it is from 480-520eV. It needs to be identified as to which spectra actually correspond to the core in relevance to the post-SI core position.

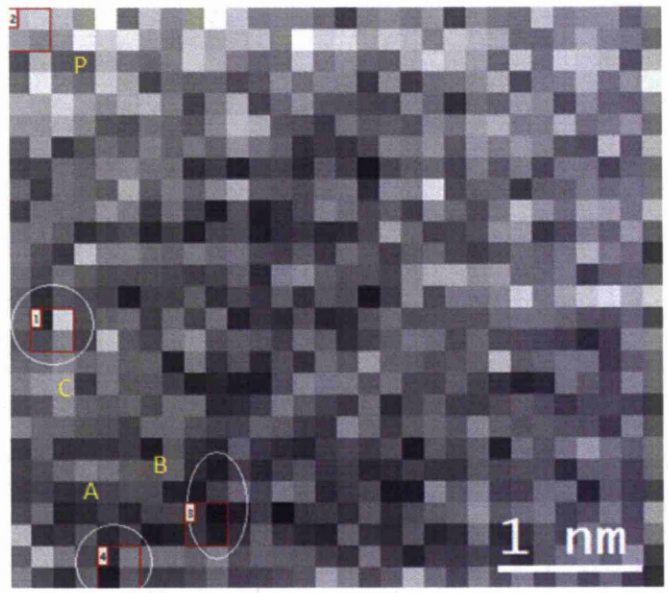

Fig.8.44. ELNES spectra in the signal SI used for comparison between perfect crystal and screw dislocation core.

A, B, C are the four spectra identified from chi square image that show ELNES changes at $M_{4,5}$ edge. P represents 4 spectra from the perfect crystal region. The average spectrum taken from these 4 spectra are compared with the average spectrum from regions A, B, and C to reveal any changes in the ELNES. The four pixels chosen for calculating average spectrum from each region are shown in the red boxes enclosed in white circles at A, B, C and P. Only A, B, and C were chosen for studying ELNES changes because they are the bright pixels that appeared in the chi square image which are in close proximity to the estimated dislocation core region shown in figures 8.41 and 8.42.

Four pixels near the region marked as C are selected from the background subtracted signal SI shown in figure 8.44 and an average spectrum is calculated from them. Similarly four pixels in the perfect crystal region as shown in figure 8.44 are selected from signal SI and an average perfect crystal spectrum is calculated. These two average spectra are compared with each other in figure 8.45. Similarly the comparison of

average spectra between perfect crystal and region A is shown in figure 8.49 and from region B in figure 8.50.

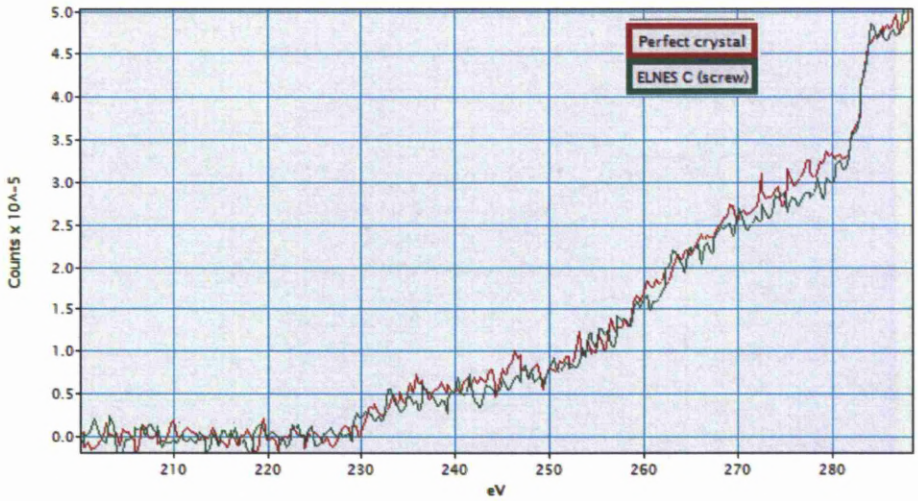

Fig.8.45. Comparison between ELNES from spectrum C reported in chi square image as correspondence to screw dislocation core and a perfect crystal spectrum. Small change in the shape of the curve can be seen where the intensity of $M_{4,5}$ edge drops between 230 and 250eV and 260 and 280eV. It can be observed that the relative intensity of the $M_{4,5}$ edge for perfect crystal is higher than the spectrum C (i.e. average spectrum obtained from region C) in the energy windows 230-250eV and 260-280eV. This suggests that ELNES changes are very small but still noticeable in the experimental spectra only at higher energies up to 50eV above edge onset.

The spectra shown in fig 8.45 are compared with the easy and hard core spectra calculated by theoretical FEFF simulations and the comparison is shown in figure 8.46. Although the Mo-$M_{4,5}$ edge signal levels in the experimental spectra are perturbed by the background noise, careful examination of the spectra along the energy axis still reveal an optimistic level of changes that are seen in the theoretical spectra.

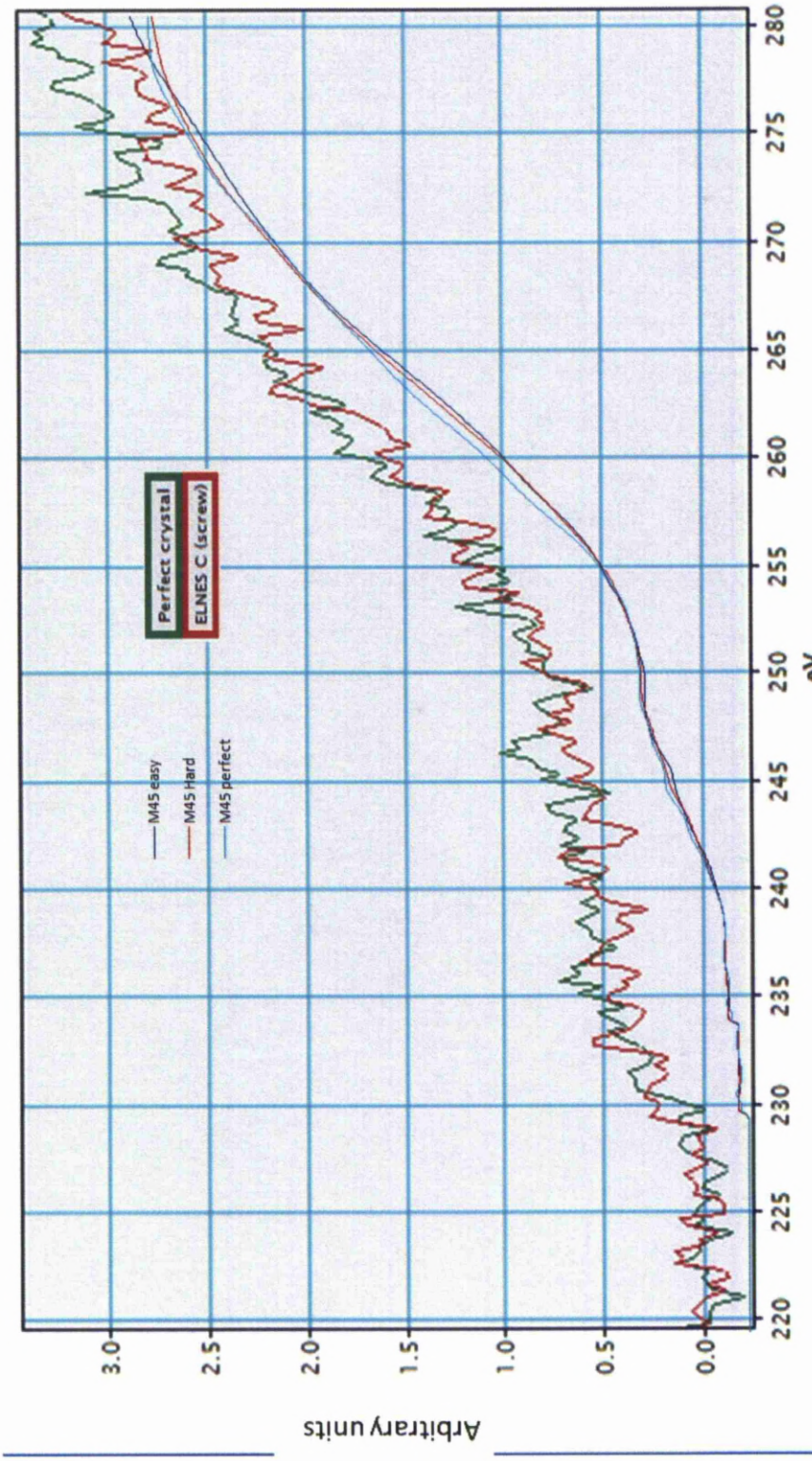

Fig.8.46. Comparison of theoretical and experimental ELNES of Mo- M4,5 core loss edge from a dislocation core and perfect crystal.

In figure 8.46, it can be observed in the experimental spectra that the height of the peaks vary between 240 and 250 eV to a very small extent. In the energy window of 250-260eV where the theoretical spectra show no difference, the experiment spectral peaks start to collapse and show a similar change. The signal from dislocation core region in experimental spectrum reduces after 260eV till 280eV. The theoretical ELNES also have similar change at dislocation core. The theoretical hard core and easy core spectra vary in their edge structure with respect to perfect crystal, but it is difficult to identify the type of core structure from the experimental ELNES. The theoretical hardcore ELNES is much closer to the perfect crystal in its ELNES than easy core as evident in figure 8.46. However the difference between the experimental screw core ELNES and perfect ELNES shown in figure 8.46 does not reveal a significant change in features. Therefore the energy window of 225 to 240eV has been magnified in order to study the spectral changes within that energy region. This energy window comparison is shown in figure 8.47.

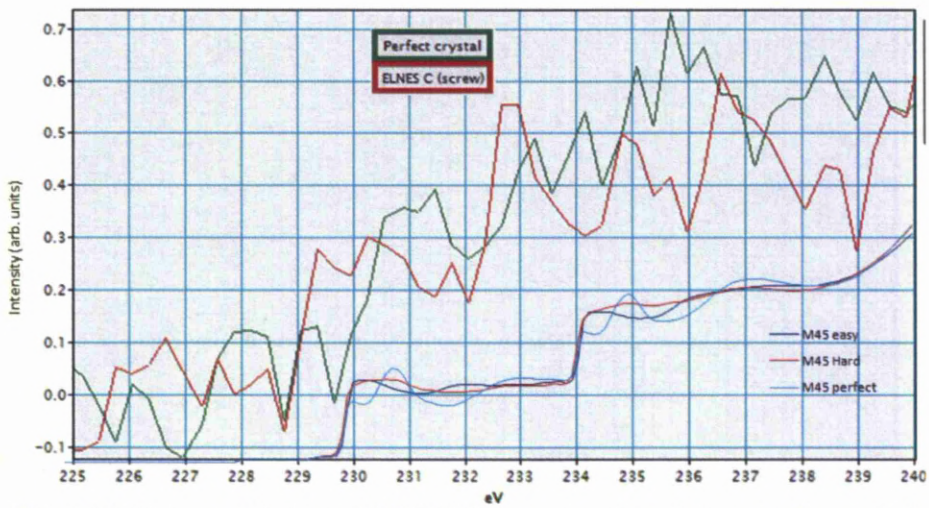

Fig.8.47. Energy window (225-240eV) comparison between theoretical and experimental ELNES changes of a screw dislocation core with respect to perfect crystal.

It can be seen in figure 8.47 that the hard core and easy core theoretical ELNES spectra differ in the peak positions at 231eV and 235eV. A similar change in the peaks is observed in experimental spectra. The difference between the peaks of experimental screw ELNES and perfect ELNES if compared with difference between peaks of theoretical screw and perfect ELNES suggest the changes are much similar to easy core than hard core, especially between 230-232eV and 234-237eV. The ELNES changes beyond 250eV are shown in figure 8.48 which also match the theoretical ELNES spectra except between 262 to 265eV. However, comparing all the changes seen in the experimental spectra with theoretical ELNES changes, it can be said the changes are similar to each other. Hence it can be said that the screw core ELNES spectra observed could be of easy core configuration.

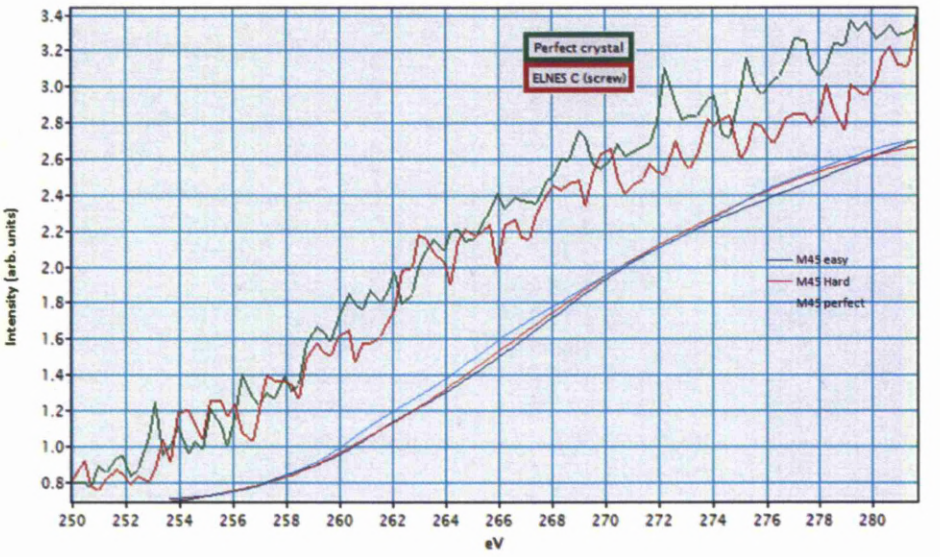

Fig.8.48. Energy window (225-240eV) comparison between theoretical and experimental ELNES changes of a screw dislocation core with respect to perfect crystal.

It is also important to examine the spectra A and B to confirm if they constitute any ELNES changes that are similar to the dislocation core. They are shown in figures 8.49 and 8.50 respectively.

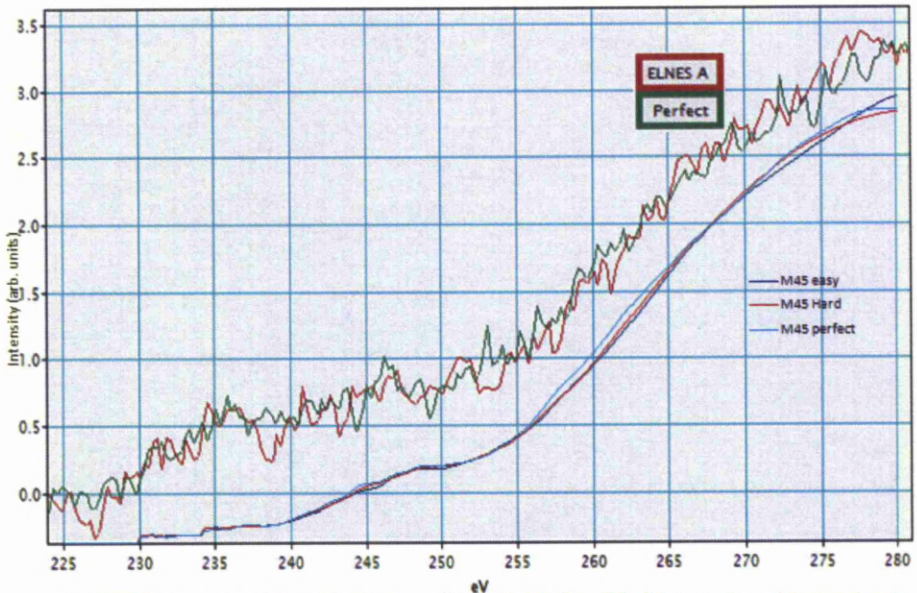

Fig.8.49. Comparison of theoretical and experimental ELNES of Mo- M4,5 core loss edge at region A in chi square image and perfect crystal.

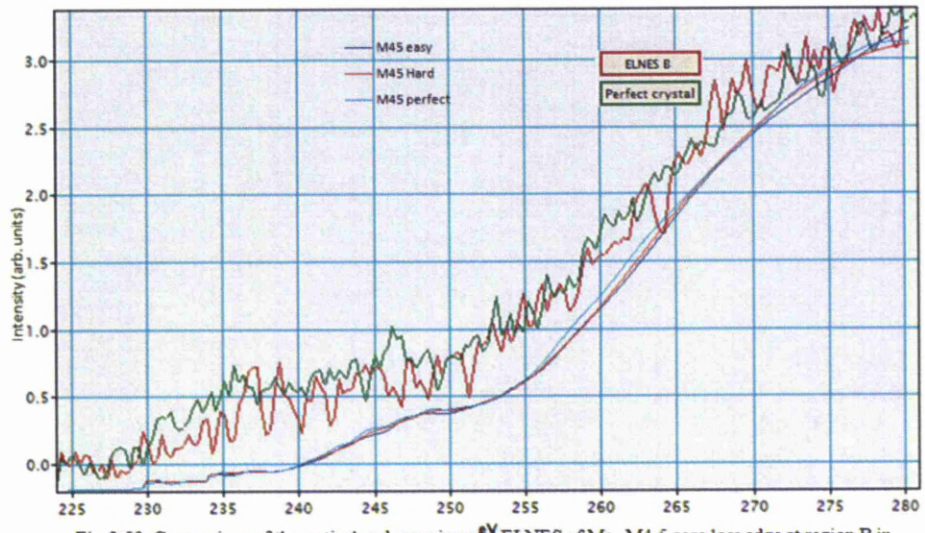

Fig.8.50. Comparison of theoretical and experimental ELNES of Mo- M4,5 core loss edge at region B in chi square image and perfect crystal.

It is observed that the spectra from region A and region B resemble the perfect crystal spectra at all energy levels. However the noise levels in these spectra (especially in ELNES B) with respect to perfect spectra are so high enough that they could be shown in the chi square image as bright pixels although they do not contain ELNES difference in the shape of the edge. This would mean that the region C is the dislocation core region and it confirms with the estimated core position in the Fourier filtered images presented earlier.

Since the screw dislocation core in bcc metals exists between three atoms of same configuration on the {111} plane, a bright patches of pixels were observed in the chi squared image and also because the number of pixels are not equal to the number of atoms probed by the electron beam. Upon observation, the average spectra at A, B showed same kind of ELNES as average perfect crystal spectrum while spectrum C showed small but clear variation compared to perfect crystal.

Spectra A and B are exhibited in the chi square image mainly due to the variation in noise levels with respect to perfect crystal spectrum in the $M_{4,5}$ near edge region while the extent of ELNES change in spectrum C is relatively small but genuinely due to the change in shape of the peaks at $M_{4,5}$ edge. Therefore from the spectral comparison it was understood that A and B were the spectra with different noise levels compared to perfect crystal spectra and spectrum from region C is from the dislocation core atoms, as their position matches with the core marked on post-SI HAADF image. In summary, the screw dislocation core is mapped using different analysis techniques, the ELNES variations in spectra from different regions in the SI that contained the core were critically discussed and the experimental ELNES changes were compared with theoretical simulations.

8.8. Problems encountered during EELS analysis

Three types of problems were often encountered during EELS analysis.

1. Problems with noise: Comparison between spectra from dislocation core and the average spectrum always meant that there was considerable amount of noise included with the signal. This noise had to be removed or reduced so as to compare effectively the signal from dislocation core to average spectrum. Since the number of atoms the electron beam interacts with, was not equal to number of pixels in SI, the signal from one core atom might be included in several different pixels nearby each other in a matrix. Hence it was necessary to extract information from surrounding pixels before comparing with average spectrum. This was achieved by rebinning the pixels in the SI by a factor of 2. Though the noise from each pixel added up, the signal also increased due to the contribution from four pixels. Thus rebinning was used effectively to extract ELNES information.

2. Problem with carbon contamination: Most of the analysed samples, especially polycrystalline samples suffered carbon contamination. This was evident in the spectra with high intensity of carbon K edge at 285eV. The overlap of carbon K edge with Mo $M_{4,5}$ edge in some of the EEL spectra made them difficult to analyse. In such cases, the ELNES had to be extracted pixel by pixel and the spectra had to be readjusted according to correct energy scale. Carbon contamination restricted the investigation of dislocations in samples since the area that had been analysed once could not be used for any further analysis. However, the problem with carbon contamination was less significant with single crystal molybdenum samples.

3. Sample Drift: When the samples were examined in SuperSTEM, during some experiments, sample drift was experienced that made EELS

analysis difficult. In this research work, the acquisition of EEL spectra from dislocation core region was vital. The drift of the sample meant that the second row of spectra would be collected far away from the region where the first row of spectra was collected. In some experiments, sample drift caused the dislocation core to move out of the assigned region of interest. Careful observation of drift was done before acquiring EELS and comparison of pre-EELS and post-EELS HAADF images roughly determined the extent of drift experienced by the sample during EELS acquisition. The EELS results presented in this thesis were acquired when there was no sample drift.

8.9. Alternate methods for extracting ELNES

Alternate methods considered for extracting ELNES changes from dislocation core are:

1. **Spatial difference method:** Background was subtracted from EELS SI of screw dislocation core and from that of perfect crystal region. The background subtracted spectra in each case were summed and an average spectrum was calculated. The subtraction of average spectra from each other gave a difference spectrum which consisted of ELNES changes.

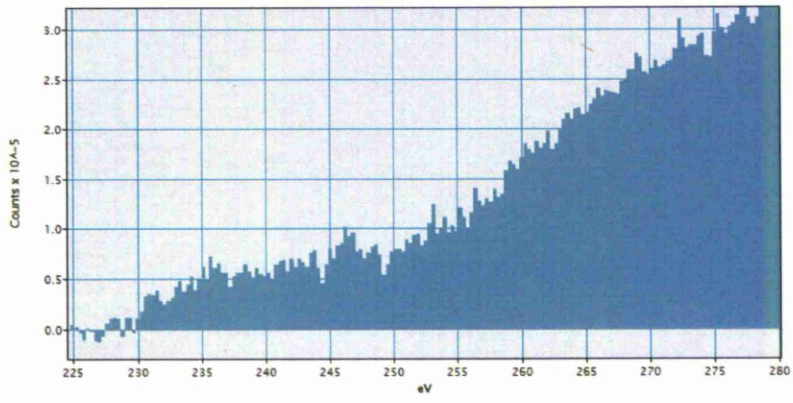

Fig.8.51 Figure showing average spectrum of perfect crystal marked as P in the background subtracted SI shown in figure 8.44.

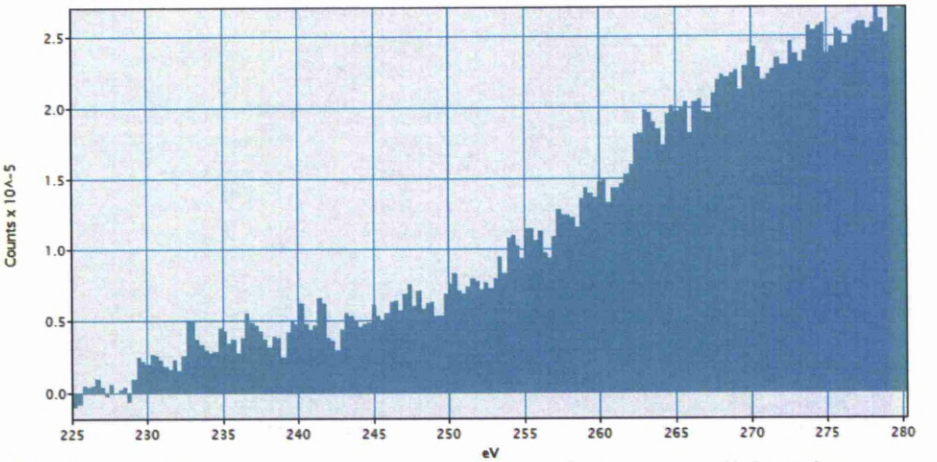

Fig.8.52 Figure showing average spectrum from screw dislocation core marked as C in the background subtracted SI shown in figure 8.44.

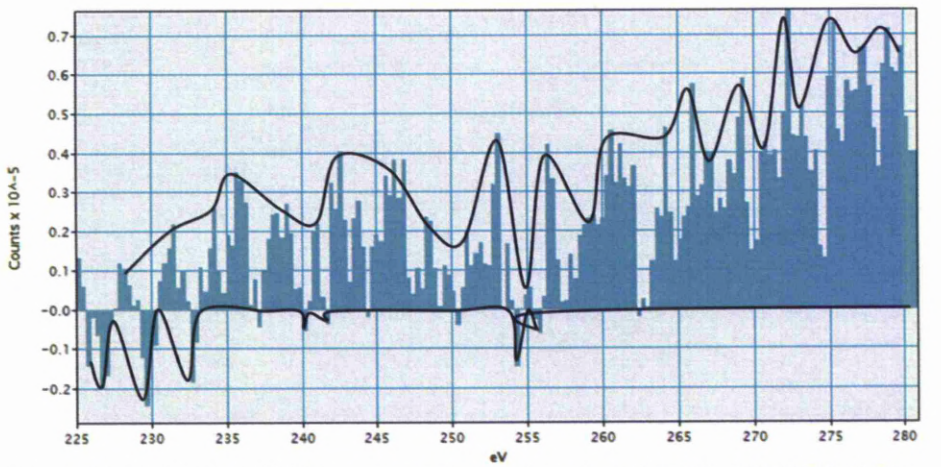

Figure 8.53 Spatial difference spectrum showing the $M_{4,5}$ ELNES (227–280eV) changes, obtained by subtracting perfect crystal spectrum from that of screw dislocation.

The ELNES changes at $M_{4,5}$ were much clearer by this method than by spectral comparison. The variation in the thickness of the specimen is one factor that could affect this spectrum, so care was taken to acquire the spectra form a perfect crystal region close to screw dislocation. The part of the spectrum below zero represents the ELNES of screw core while the above part represents the perfect crystal. It can be noticed in figure 8.53 that no major changes after 235eV occur at the screw

dislocation core with respect to perfect crystal except the reduction in the number of counts which was considered as ELNES change previously that arises only due to the loss of symmetry at the core.

2. Rebinning of SI: This method was considered to add and project ELNES changes from the neighbouring pixels that account to every atom the beam interacts during EELS acquisition. Rebinning the EELS SI by a factor of 2 produced a new SI in which the first pixel is the sum of information contained in the first 2 x 2 pixels of original SI.

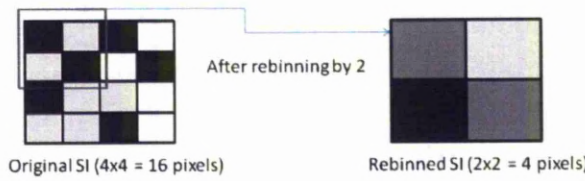

Fig.8.54 Diagram (left) showing the 4 x4 pixels of EELS SI before rebinning. Fig.8.55 (right) Rebinned EELS SI with 2 x2 pixels.

The 4 spectra shown in the enclosed box will be added to generate a single spectrum that contains all the information from the four spectra. Depending upon the number of pixels that constitute the information from a single atom, the rebinning can be done by factors of 2^n. This was taken as an approach to gain better signal to noise ratio at times when the ELNES signal had to be extracted from an SI with a greater number of spectra. Rebinning was performed by the option provided in Digital Micrograph and chi squared script was later applied to the rebinned SI the same way as explained in previous sections. Rebinning also served the purpose of better background subtraction before executing chi squared script.

The rebinned signal SI and the chi squared image generated from it by choosing an ELNES energy window of 227-280eV and normalisation window of 285-300eV are shown in figure 8.56.

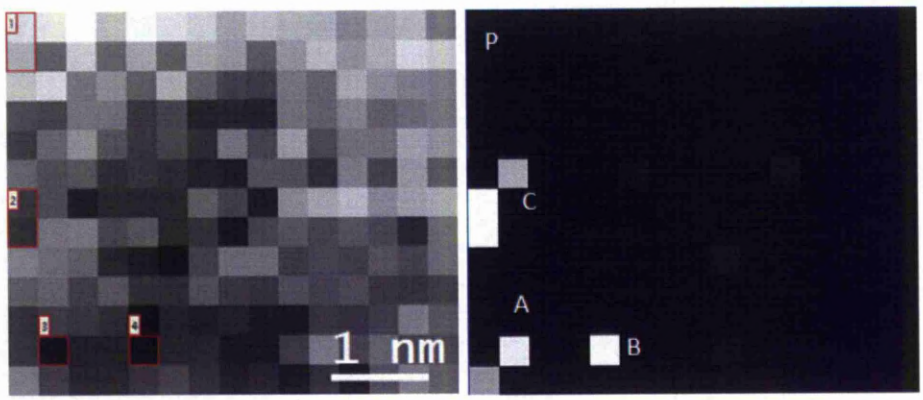

Fig.8.56. Rebinned ELNES signal SI is shown on the left and its chi square image on the right showing bright pixels that have differences in the ELNES spectra. P represents the average perfect crystal spectrum; A, B and C represent ELNES spectra from pixels that appear bright in chi square image.

The spectra from the regions marked in figure 8.56 are compared with perfect crystal spectrum and are shown in figure 8.57, 8.58 and 8.59 for regions C, A and B respectively.

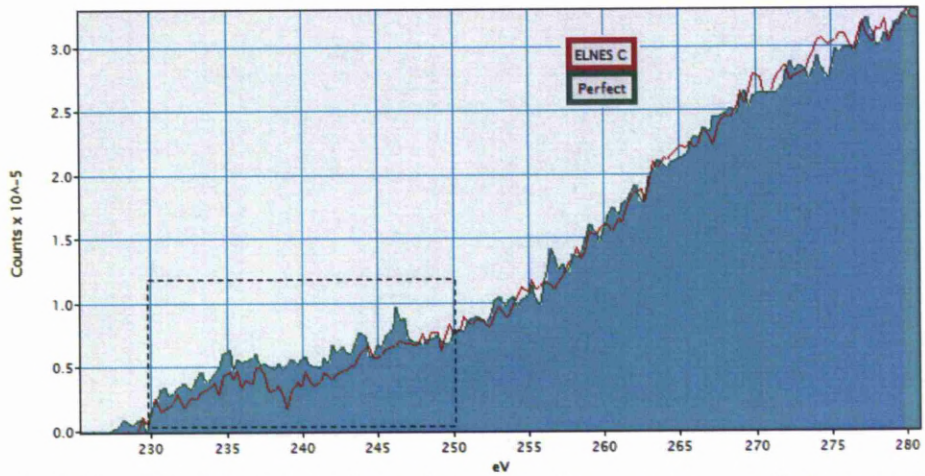

Fig.8.57. ELNES comparison between the average perfect crystal spectrum and average spectrum from region C, where the dislocation core is located in post-SI Fourier filtered image.

It can be observed in figure 8.57 that the ELNES peaks between 230 and 250 eV change in shape and intensity while the rest of the spectral regions remain similar. This change in the energy window 230- 250eV is shown enclosed in the dotted box.

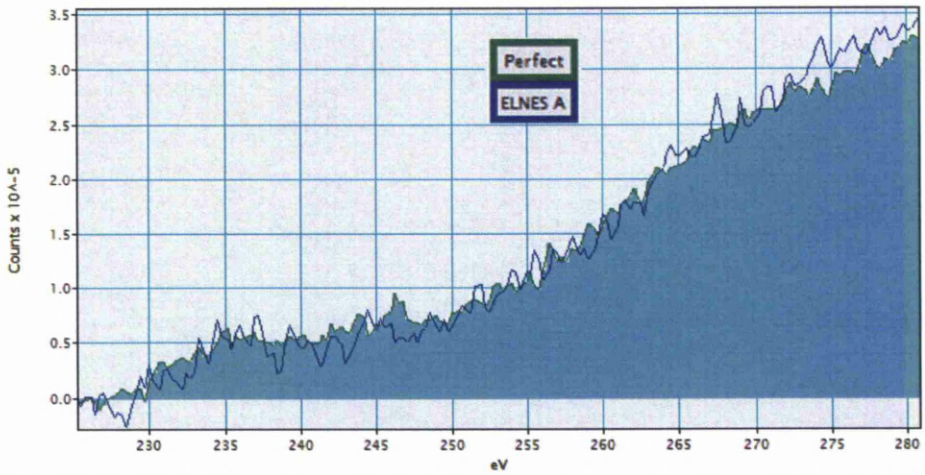

Fig.8.58. ELNES comparison between the average perfect crystal spectrum and the spectrum from region A.

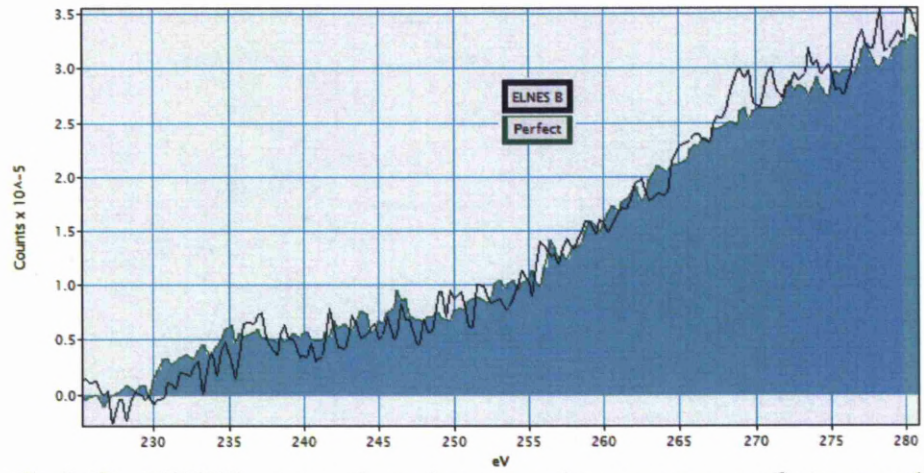

Fig.8.59. ELNES comparison between the average perfect crystal spectrum and the spectrum from region B.

In figure 8.58, the noise levels are high enough to cause this spectra appear different from the perfect crystal spectra and this is the reason for this spectrum to appear in the chi square image. Moreover, the error with

respect to the background between 225 and 230eV also can contribute to this effect. Therefore spectrum from region C is considered to be the original spectrum from dislocation core that shows genuine changes in the ELNES peaks. ELNES C is compared with theoretical spectra calculated using FEFF and are shown in figures 8.60 and 8.61.

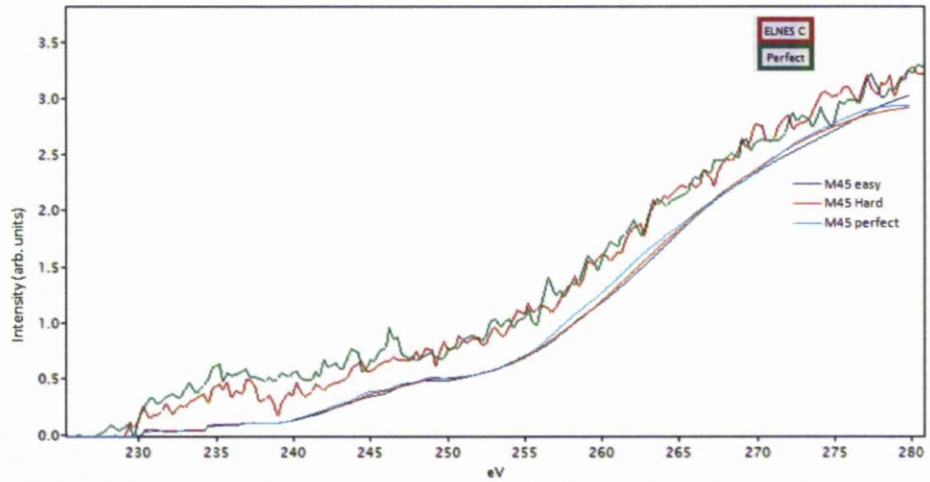

Fig.8.60. Experimental and theoretical ELNES comparison of Mo-$M_{4,5}$ edge at a dislocation core and perfect crystal region.

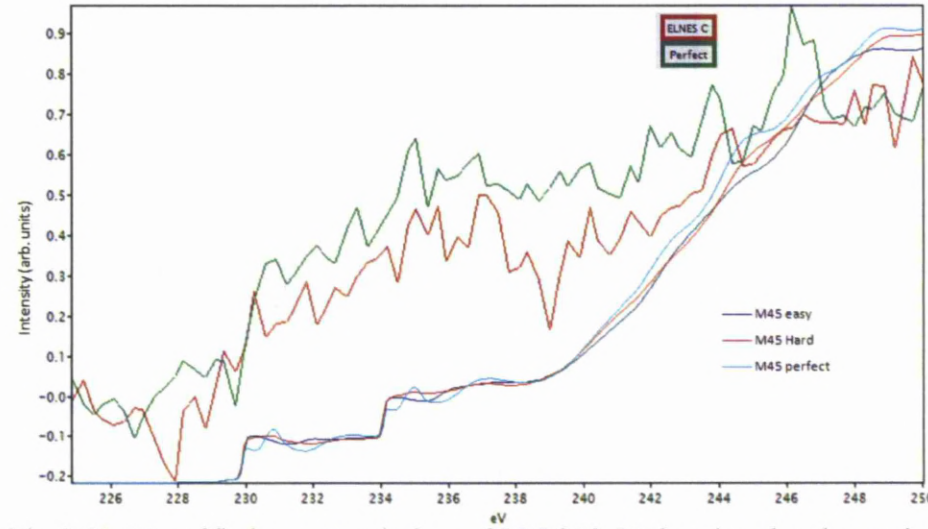

Fig.8.61. Magnified energy window of 225-250eV showing the change in the ELNES for a dislocation core both in theoretical and experimental results.

In figures 8.61 it can be seen that the experimental dislocation core (ELNES C) spectrum has a sharp drop in the intensity at 239eV and 247eV. If the theoretical and ELNES spectra are compared, the peaks at 231 and 235eV are smeared for both easy core and hard core screw dislocation with respect to perfect crystal while such a change is difficult to interpret from the experimental spectra. However the peak at 245eV in perfect experimental spectra is absent in screw core experimental spectra. The same change is observed in theoretical spectra and both spectra coincide at 248eV.

8.10 ELNES changes discussion

The ELNES changes observed at the screw dislocation core are explained by the following:

1. The high lattice strain observed at the screw dislocation core is the first reason. At the screw dislocation core the bond lengths and the bond angles were different to that of perfect crystal because the atoms from different planes bond together at the core, in other words screw core was non co-planar. The core atoms were displaced from their perfect crystal positions leading to bond length changes. Due to the change in the bond lengths and bond angles the symmetry of the crystal at the core is damaged. The core atoms need high binding energy to retain these bonds making the screw dislocation core a high energy region. The core atoms would be under severe lattice strain due to asymmetry and would be willing to lose energy and return to equilibrium energy configuration as perfect crystal.

2. The ELNES of screw dislocation core was also affected by the transitions of 3d electrons to higher or lower energy states. Molybdenum M_4 edge is the resultant of $3d^{3/2}$ electron transition while M_5 is the resultant of $3d^{5/2}$ electron transition. Non-dipole ($\Delta\ell \neq \pm 1$) 3d to 4d transitions were also reported to show sharp peaks before the $M_{4,5}$ edge

threshold at 227eV in molybdenum[5]. From the experimental spectra of a screw dislocation core, no peaks were observed before the edge onset (227eV) ruling out the possibility of dipole-forbidden transitions. Hence d→p or f transitions would be considered to explain the intensity drop in ELNES region of screw core spectrum.

Screw dislocation core is a region of different energy configuration with respect to rest of the crystal which might increase the chances of transitions to either p or f states from d state. The higher the number of transitions the larger would be the difference noticed in the spectrum. Hence (p+f) DOS plots of screw dislocation core and perfect crystal calculated by FEFF were compared which show the density of unoccupied states in both p and f states in either case. This was shown in figure 8.62.

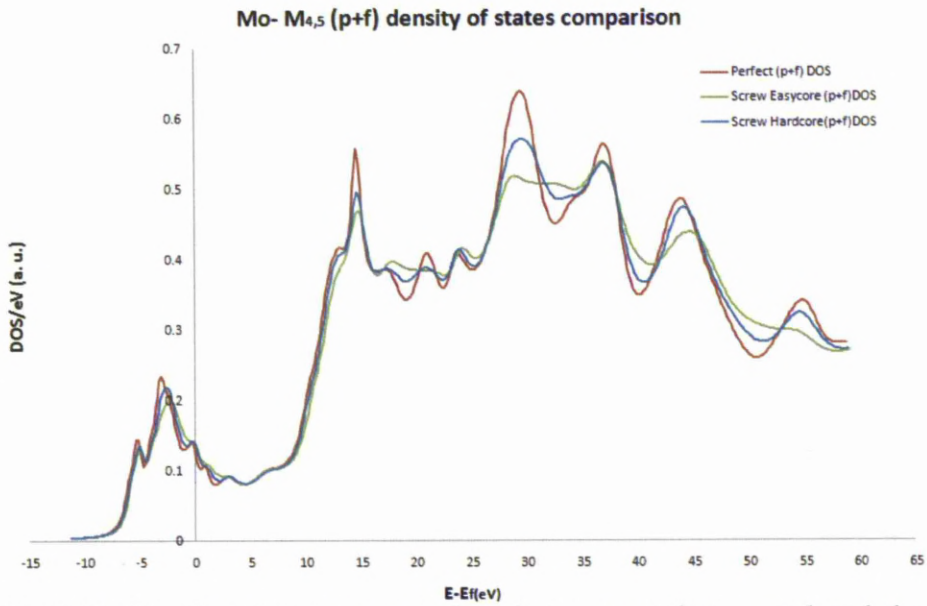

Fig.8.62. Density of states comparison between perfect crystal and the two types of screw dislocation cores.

In figure 8.62 it can be observed that there was a big change in the dislocation core spectra (blue and green coloured spectra) at 30 eV which corresponds to 30eV above the edge threshold (i.e. 227+30 eV = 257eV)

in ELNES spectrum. In the ELNES comparison spectrum shown in figure 8.60, this change can be noticed by the loss of sharp peak in experimental screw core spectrum(red) approximately about 257eV confirming the changes seen in (p+f) DOS. Therefore the changes in spectra occur both in LDOS and ELNES at the same energy range (257eV). This confirmed that the transitions from d to p and f states were responsible for the changes observed in ELNES of screw dislocation core.

The (p+f) DOS plot reveals the density of unoccupied states in p and f states. The reduction in the DOS for a screw dislocation core as compared to perfect crystal was evident from figure 8.62. This suggested that number of unoccupied p and f states in the case of screw dislocation core were less than those available in perfect crystal. This draws a direct inference that more p and f states were occupied at screw dislocation core, which meant that the transitions from d to p and f have occurred more in number at screw core than in perfect crystal. Hence there would be more electrons in the p and f states and less in d states. This would cause the $M_{4,5}$ edge to drop because the number of 3d electrons that were responsible for $M_{4,5}$ edge would be less. This was the reason for the drop in the number of counts at the ELNES region of screw dislocation core spectrum. From the comparison of screw hard core and easy core spectra with perfect crystal spectra in figures 8.60 and 8.61, it was confirmed that the theoretical screw dislocation core spectra match experimental spectra for easy core and hard core configurations. In order to identify the transitions, the p and f DOS can be compared for easy and hard core models with perfect crystal. These are shown in figures 8.63 and 8.64. It can be observed from these two figures that there is more unoccupied f-DOS contribution to the (p+f) DOS suggesting a d to p transition and screw easy core has more unoccupied DOS than hard core.

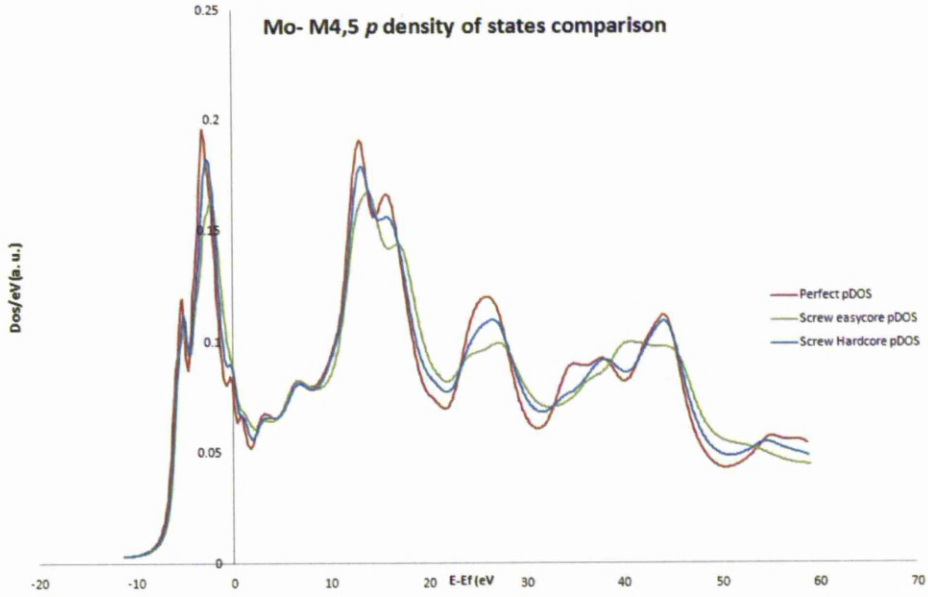

Fig.8.63. *p* density of states comparison between easy core, hard core and perfect crystal.

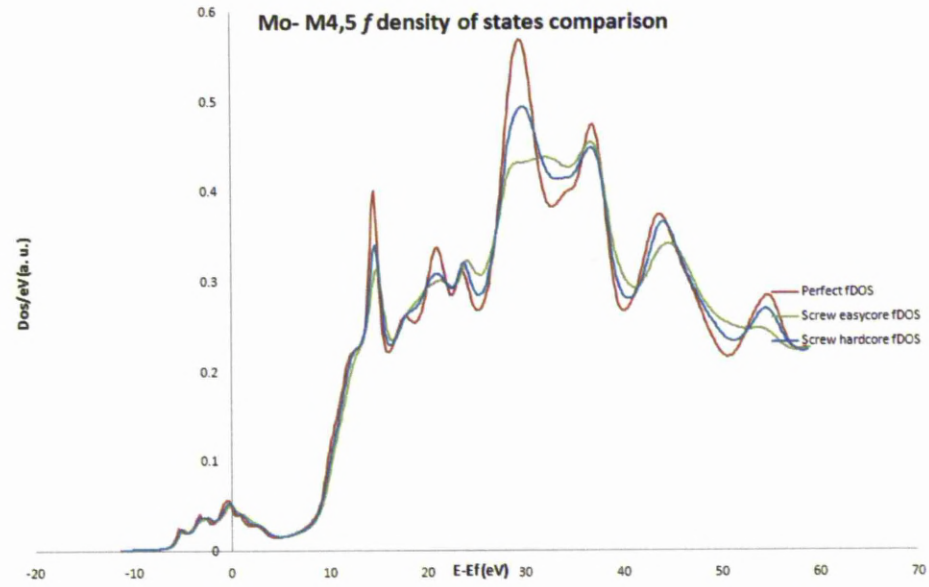

Fig.8.64. *f* density of states comparison between easy core, hard core and perfect crystal.

In summary even though the intensity reduces and the shape of the peaks change in experimental spectra from screw dislocation core supported by

the evidence from the DOS plots, it is still very difficult to identify which type of core is experimentally observed. The experimental results from SuperSTEM showed changes in ELNES while the FEFF calculation showed similar change in ELNES and the LDOS calculations provided the reason for the ELNES changes at screw dislocation core.

References

[1] D. B. Williams, C. B. Carter, Transmission electron microscopy: a textbook for materials science, Plenum, New York; London, 1996, p. xxvii, 729p.
[2] M. H. Loretto, R. E. Smallman, Defect analysis in electron microscopy, Chapman and Hall [etc.], London, 1975, p. ix,134p.
[3] M. Winter, Web Elements: the periodic table on the web in: Web Elements Ltd, UK, Sheffield, UK, 2009.
[4] J. D. Eshelby, A. N. Stroh, Philosophical Magazine 42 (1951) 1401.
[5] J. M. Auerhammer, P. Rez, Physical Review B 40 (1989) 2024.

Chapter 9

Results and Discussion: Iron

Chapter 9

RESULTS AND DISCUSSION: IRON

In this chapter the experimental results from dislocations in iron samples will be presented. This chapter consists of two parts. The first part consists of TEM and STEM results from magnetic iron samples followed by SuperSTEM results. The second part deals with the comparison and discussion of experimental ELNES differences with theoretical ELNES differences. The two screw dislocation core models are then assessed for their electronic structure differences supported by reasons for practical preference.

9.1 Experimental results

Experimental results obtained from TEM, STEM and SuperSTEM will be presented in this section.

9.1.1 TEM and STEM results

Thin samples were prepared for high resolution microscopy from bulk samples. Initially they were examined in TEM and STEM for screw dislocations in the <111> direction. Care was taken during tilting and translation because of the magnetic nature of the samples. Low magnification images were taken for the purpose of identifying the screw dislocations and are shown in the figure 9.1. A <111> grain with dislocations was recorded at various magnifications to accurately identify its location when the sample was used again in another microscope. The 3-fold symmetry patterns visible at bend contours were helpful in finding <111> grain[1].

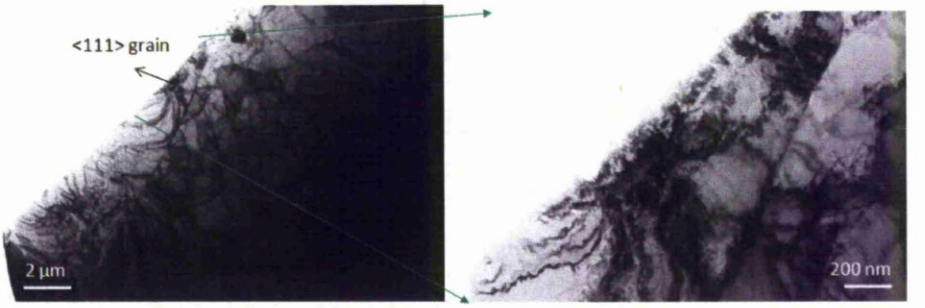

Figure 9.1 TEM bright field image of <111> grain near the edge in a polycrystalline iron sample. The bend contour region shown (right) at higher magnification was helpful to identify zone axis patterns.

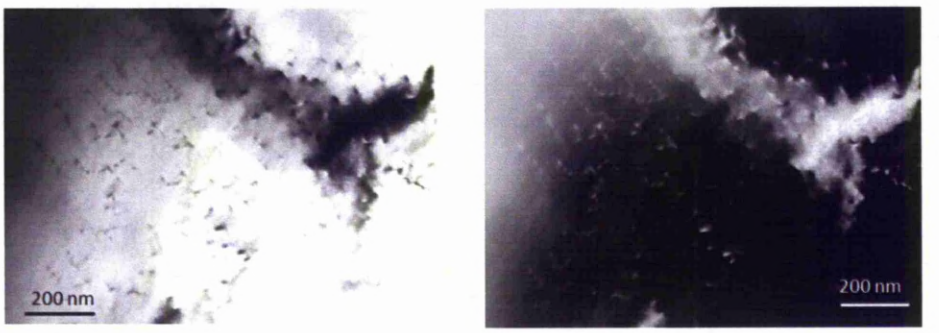

Figure 9.2 Bright field (left) and dark field (right) TEM images of dislocations in <111> grain of polycrystalline Fe sample.

Most of the dislocations shown in the images in figure 9.2 lie parallel to the surface of the foil. The heavily bent grain can also be seen clearly in the dark field image. The screw dislocations were identified by tilting the sample to see if the contrast in the image varies with respect to the length of the dislocation. Care was taken to correct the astigmatism for each tilt. The grains were deformed heavily and there were large number of dislocations near the grain boundaries. The bend contours added to the

problem of astigmatism and thickness fringes caused difficulty in identifying the dislocation character.

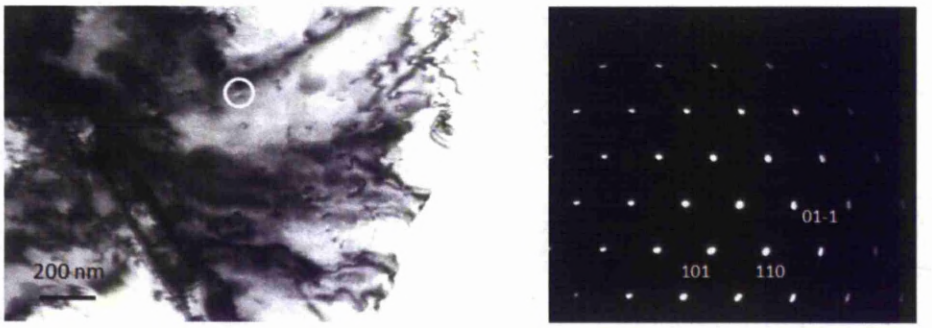

Figure 9.3 Bright field TEM image showing near end-on screw dislocation in the marked white circle; [-111] diffraction pattern recorded from the grain was shown on the right side.

It can be observed from the diffraction pattern that the electron beam was slightly off axis due to the magnetic field of the sample. The diffraction spots far from the central spot are blurred and smeared but they can help in astigmatism correction before recording images. Blurring of the image caused by severe astigmatism during the experiments in the microscope was another effect of magnetism of the sample.

TEM images of dislocations in single crystal iron samples were also recorded with better contrast by repeated astigmatism corrections. The diffraction conditions were also slightly better than those for polycrystalline samples. In polycrystalline samples, heavily bent grains with different orientations added to the problems of magnetism and made the experiments with polycrystalline samples much difficult than anticipated. Most of the polycrystalline samples also suffered oxidation as shown in figure 9.6. Hence [111] single crystal iron samples were examined for screw dislocations in TEM and STEM.

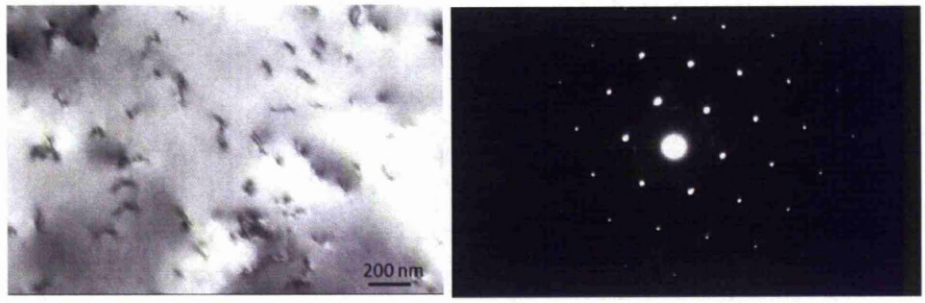

Figure 9.4 Bright field TEM image of dislocations in 111 single crystal sample and the diffraction pattern showing <111> zone axis pattern.

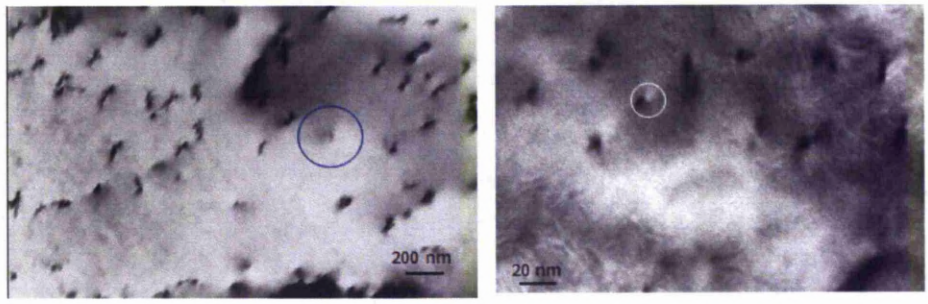

Figure 9.5 TEM bright field images showing end-on screw dislocations inside marked circle. The image on the right was recorded at 800kX.

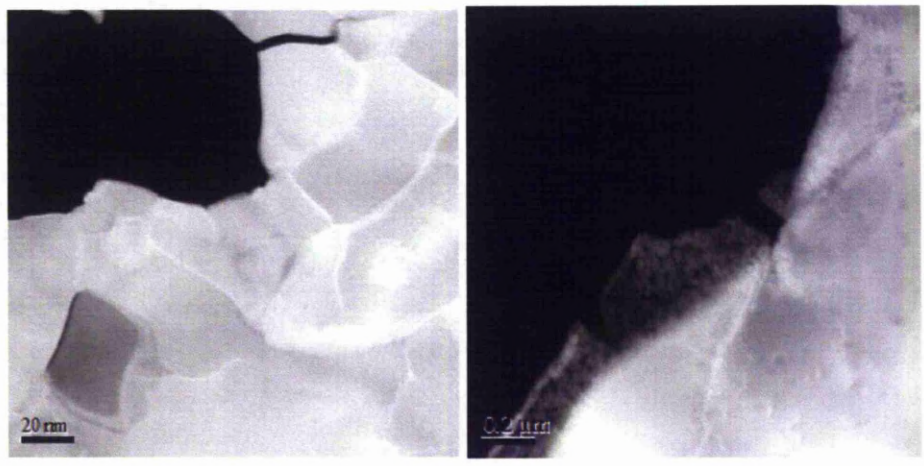

Figure 9.6 Low magnification STEM HAADF images of [111] grains with dislocations in a polycrystalline sample. The image to the right was

thin oxide growing at the edges of a one month old iron sample. Hence it was necessary to carryout experiments within a week of sample preparation to obtain better results with polycrystalline iron.

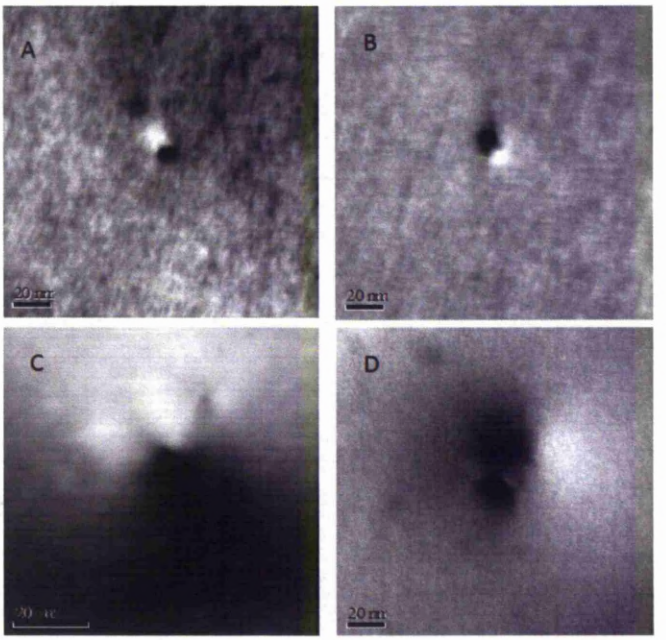

Figure 9.7 STEM HAADF (A, C) and BF (B, D) images of a screw dislocation in Fe [111] single crystal sample at 500kX and 1000kX.

The possibility of acquiring the HAADF and BF images was found to be limited by the sample's magnetic field in STEM. The magnetic field caused the sample-tilt to change continuously in STEM. The images in figure 9.7 were taken after the tilt correction and after acquiring these images the tilt changed again. Due to this reason, EELS acquisition could not be performed on these magnetic iron samples in STEM.

9.1.2 SuperSTEM results

After TEM and STEM examination, screw dislocations in single crystal iron samples were analysed for ELNES changes at $L_{2,3}$ edge using high

resolution EELS collected at SuperSTEM. The magnetic field of the iron sample kept the sample stage in SuperSTEM under strong torque. This was due to the sample's attraction towards the pole piece. This phenomenon restricted the usage of z-height required for increased magnification up to atomic resolution. Therefore HAADF and BF images were collected at lower magnifications. The aberration corrections were done before imaging dislocations, but the images still suffered from persistent astigmatism and direction-dependant aberrations. Dislocations were identified using BF images and EELS was acquired from them.

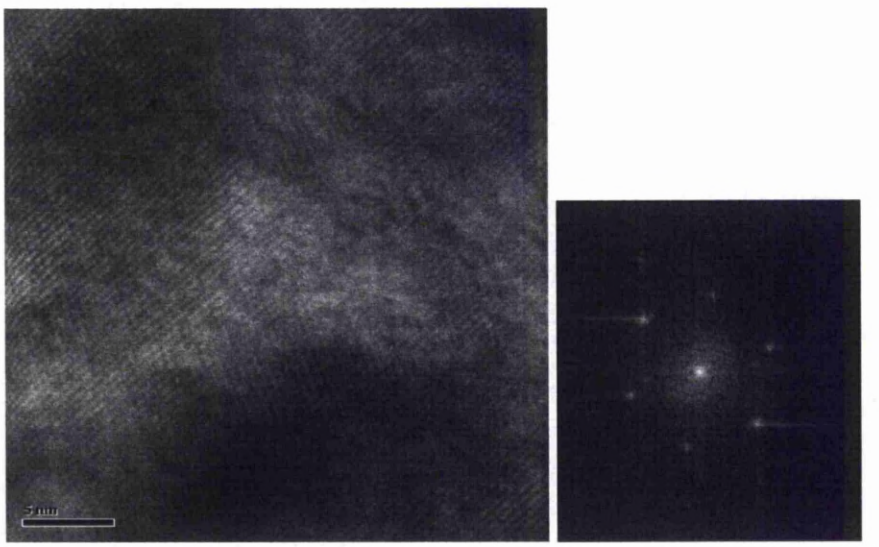

Figure 9.8 Bright field image of Fe <111> perfect crystal and its FFT.

From the FFT image it can be noticed that the sample is not aligned perpendicular to the zone axis direction when this image was collected. This is because the sample was at an angle to the beam and hence the resolution was poor in the image. In the BF image some areas of the sample especially at the corners, are well resolved than in the centre. The image shown in figure 9.8 was de-striped to improve the resolution in the

lattice image and was processed to generate a Fourier filtered image as shown in figure 9.9.

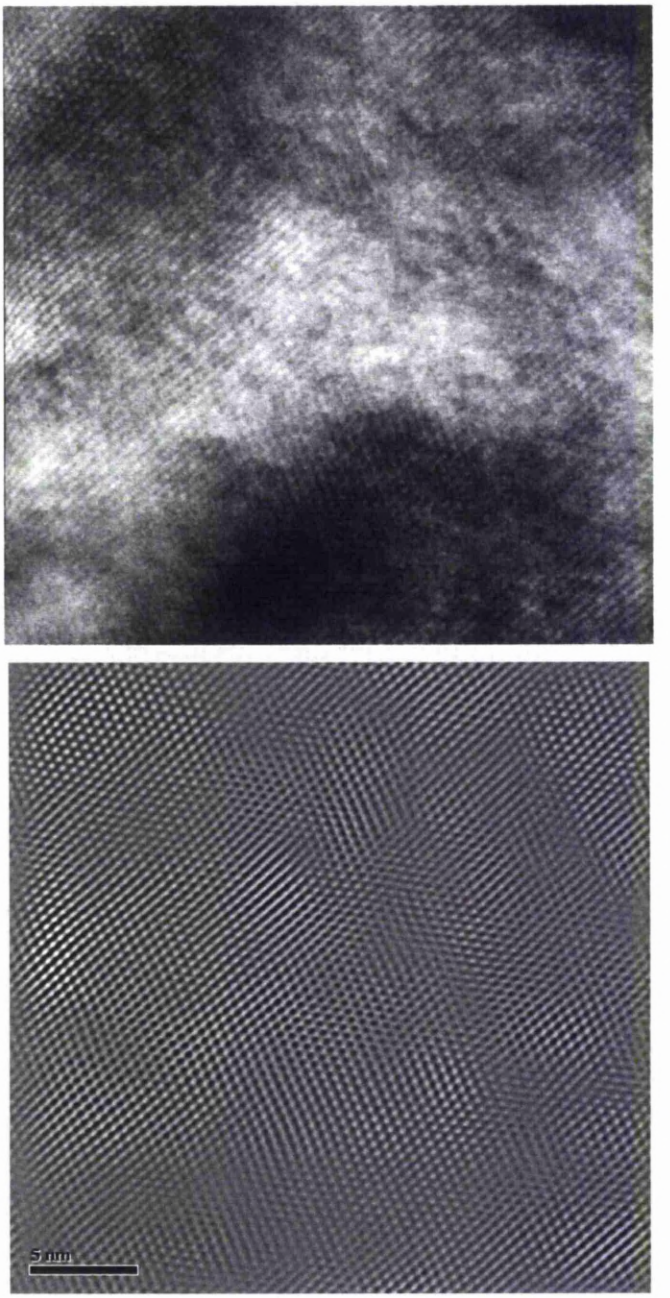

Figure 9.9 De-striped BF image (above) of perfect iron crystal at lattice resolution and its Fourier filtered image (below).

De-striping was done essentially to remove any scan noise recorded as horizontal lines on the BF image and to improve its overall resolution. The area with dislocations was relocated and aberration corrections were done for that area. This was followed by the EELS acquisition. One of the screw dislocations that were investigated for its electronic structure at the core is shown in figure 9.10.

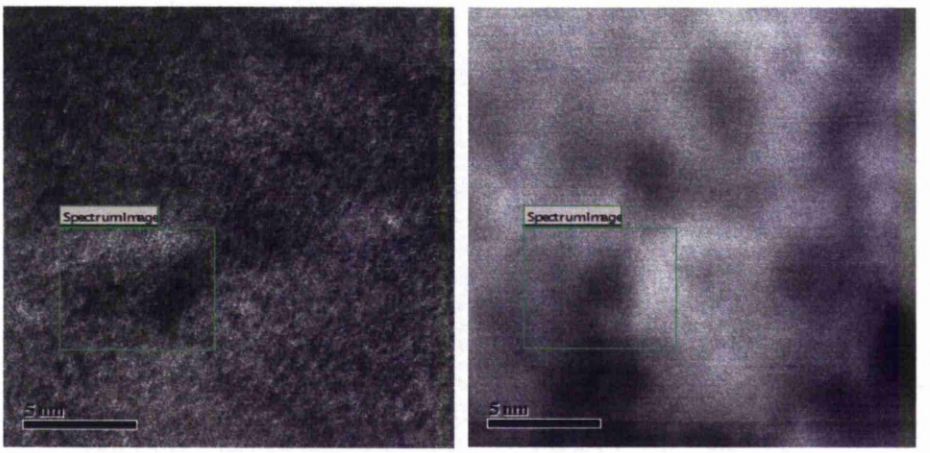

Figure 9.10 HAADF and BF images of a screw dislocation in [111] direction; the spectrum image was marked to show the region from which EELS was acquired.

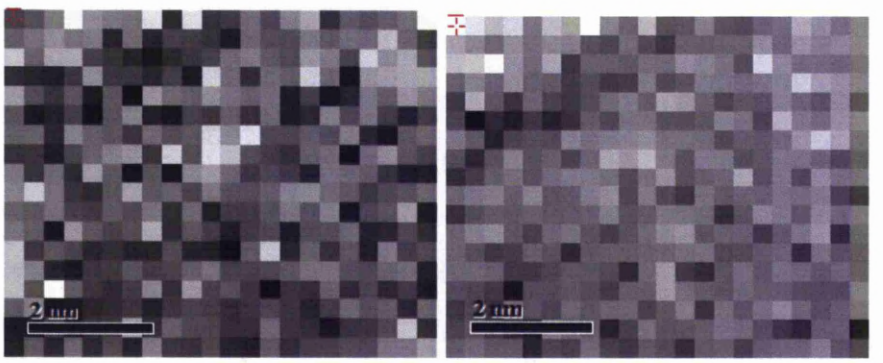

Figure 9.11 Spectrum image collected from screw dislocation shown on the left and its background subtracted SI shown on the right side.

The back ground subtracted spectra was summed and then chi square script was used to identify any $L_{2,3}$ changes at the dislocation. Determination of the screw core from HAADF images is complex in this case because of the lack of resolution in the images. Hence the spectra that represent the bright pixels in the chi squared image were used to analyse for ELNES changes by comparing it with perfect crystal ELNES. However the drift of the sample during EELS acquisition has to be taken into account before expecting the location of screw dislocation in the chi square image. The post SI HAADF is useful to identify if the sample had drifted during EELS acquisition. Comparing the features in pre-SI and post-SI, the drift could be estimated and hence the position of the expected core region is determined.

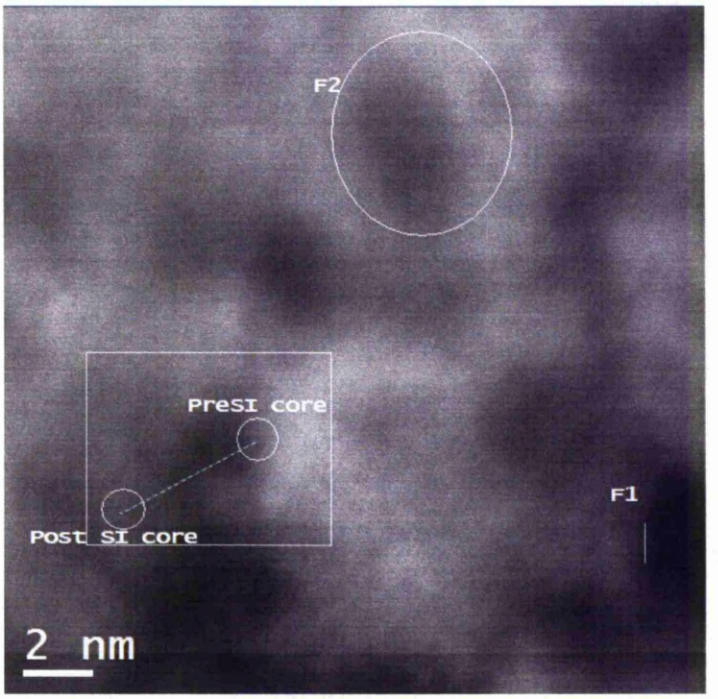

Fig.9.12. Pre-SI HAADF image showing an estimated dislocation core position and the features associated with the image. In figure 9.12, F1

and F2 are the features that could be used to identify the drift in the sample. The post-SI HAADF image is shown in figure 9.13

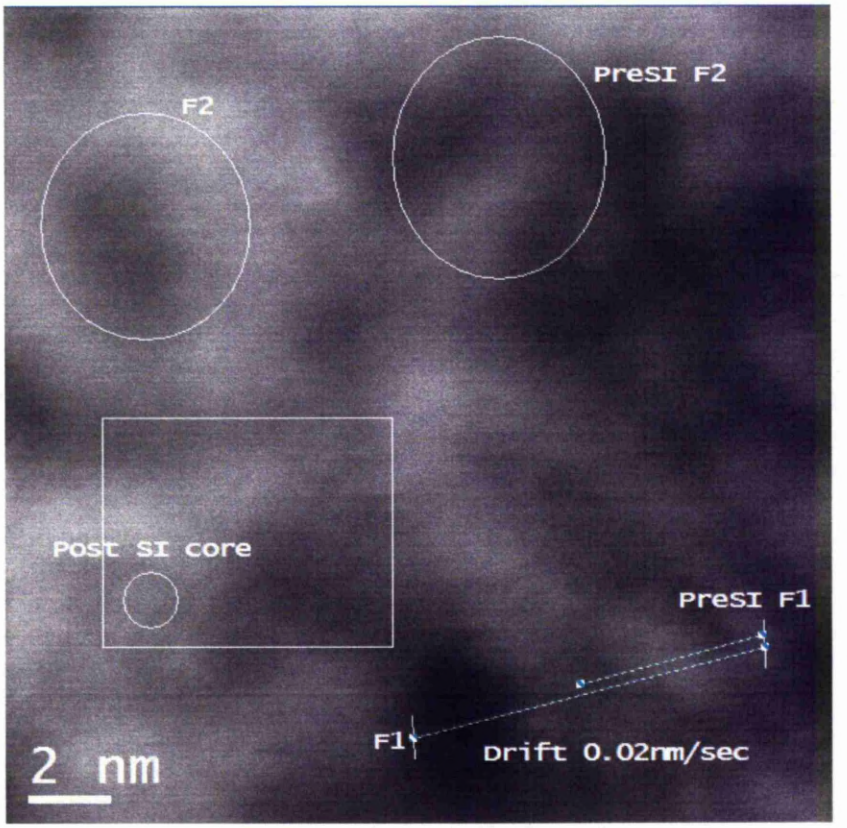

Fig.9.13. Post-SI HAADF image showing features F1 and F2 and their pre-SI and post-SI positions. The core is located in the ROI box even after the drift.

The feature F1 has moved by 8.5 nm in 6 minutes (i.e. 360 sec time interval between pre-SI and post-SI images), so the drift is calculated to be 0.02 nm/sec. The EELS is acquired at 0.5 s per pixel and a total of 396 pixels have been acquired, which meant that the total acquisition time is 198 seconds (i.e.3.3 minutes). The drift in that time will be 3.96 nm. The estimated core position with that value of drift is shown in figure 9.14.

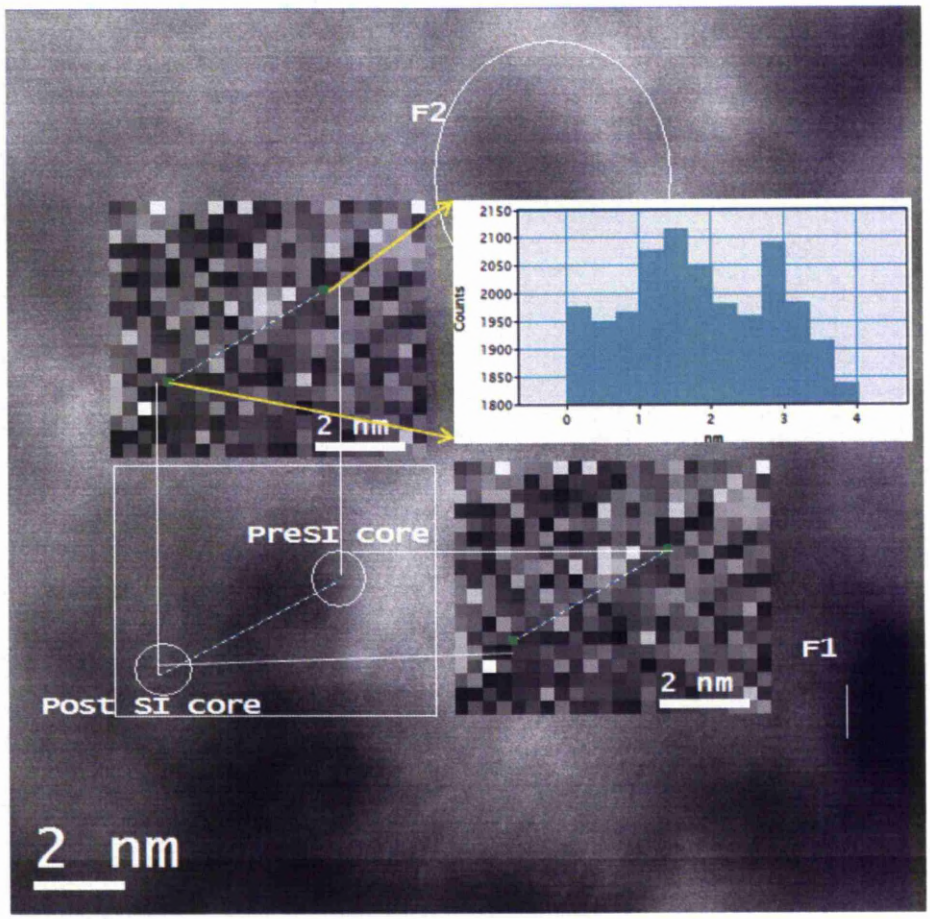

Fig.9.14.Expected screw dislocation core position shown in the SI by comparing the pre-SI and post-SI HAADF images and the value of drift of 3.96 nm applied to the core position.

In figure 9.14, the pre-SI HAADF image is shown with the position of the core located after the sample drift at the end of acquisition. It can be seen that the core still lies within the selected ROI at the end of acquisition and drift. The drift value of approximately 4 nm (~3.96 nm) is shown in the line profile connecting the pre-SI and post-SI core position. Fig.9.14 shows the expected core position in the SI image, but since the beam probes the core at some time in between the start and end of acquisition the core has to be situated at some point along the line

connecting pre-SI and post-SI HAADF. The chi square image is generated from the background subtracted SI and the bright pixels from the chi square image are identified in the ELNES signal SI. They are shown in figure 9.15.

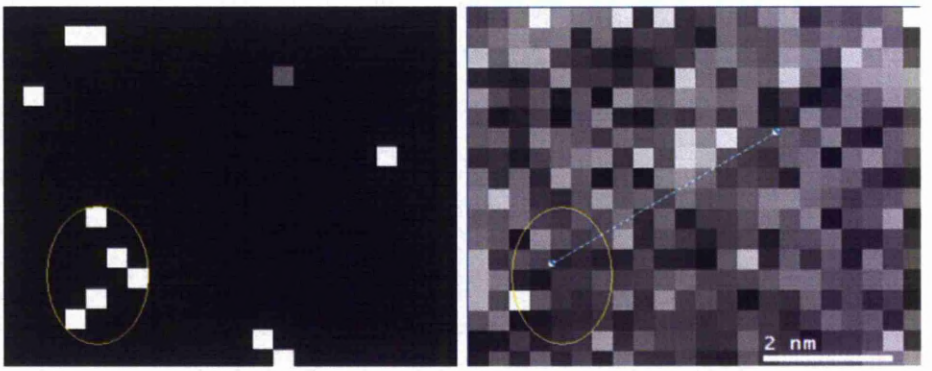

Fig.9.15. Chi square image (left) of the EELS SI showing the spectra that contain ELNES changes in the enclosed yellow oval region and identified on the ELNES signal SI (right).

The normalisation window chosen for executing the chi squared script was 960 – 1000eV and the ELNES region chosen was 700 to 760eV. The corresponding 16 spectra from bright patch in the chi square image are selected and an average spectrum is calculated from them for comparison with background subtracted SI. 4 pixels in the top right corner were used for comparison as perfect crystal since they do not show any ELNES changes in chi squared image. Average spectrum for both screw dislocation and perfect crystal are compared with each other as shown in figure 9.16.

The average spectrum is given by dividing the summed spectra by the number of spectra that were summed. This would result in increased signal but also the noise would be averaged[2]. If the spectral changes still appear when average spectra were considered, then it must be

understood that the original signal without noise is much intense and sharp. The average spectra comparison between screw dislocation and perfect crystal iron was shown in figure 9.16.

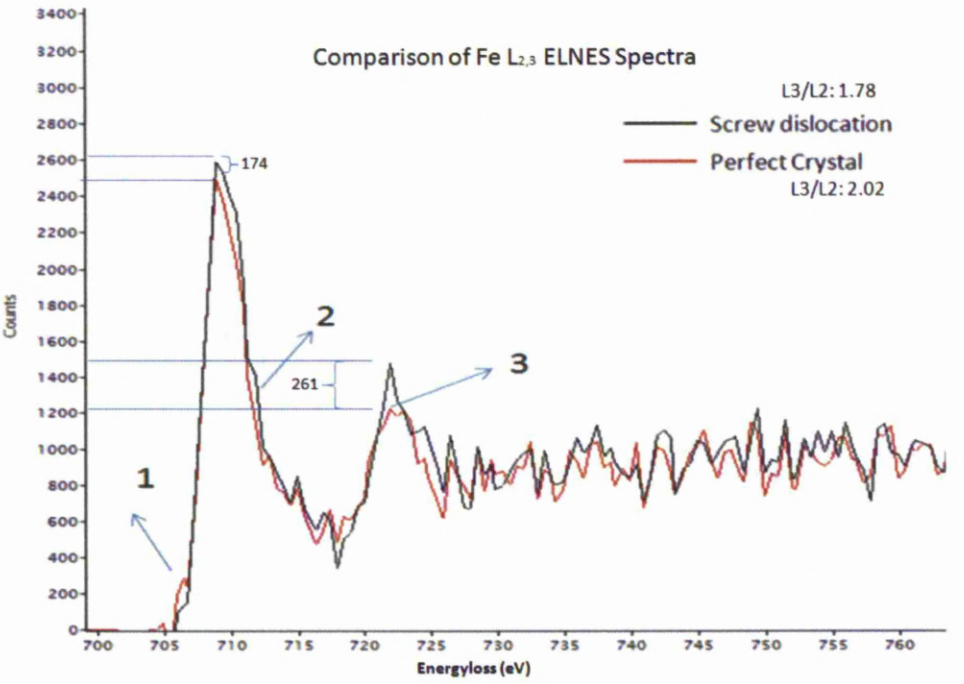

Fig.9.16.Comparison of an average experimental spectrum of a screw dislocation core to that of a perfect crystal region of iron.

The changes observed in the spectra were labelled 1, 2 and 3. The changes 1 and 2 were affecting the shape of the peaks while 3 was affecting the number of counts. To understand the changes in the spectra, the screw dislocation spectrum was subtracted from the perfect Fe crystal spectrum. The resultant difference spectrum was shown in figure 9.17.

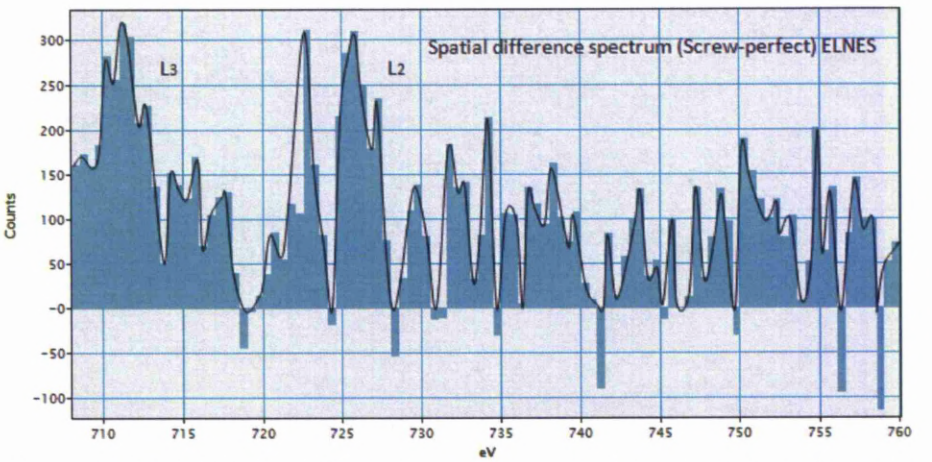

Figure 9.17 ELNES difference between perfect crystal and screw dislocation. The observed peaks in difference spectrum were confirming that the screw dislocation core would change the near edge structure in bcc iron.

These changes are matching to a certain extent with the changes observed in theoretical calculations. The reasons that can explain these changes will be discussed in the next section.

9.1.3 Fe $L_{2,3}$ ELNES discussion

The experimental spectra comparison shown in figure 9.16 suggests a different outcome. In this comparison, the tiny peak that existed just before perfect crystal L_3 peak was observed to have smeared for screw dislocation. This change is marked as 1 in the figure 9.16. The width of the screw core L_3 peak at about 708 eV started to show a very small shoulder as compared to perfect crystal, the change marked as 2. Finally the change marked as 3 was the reduction in intensity of screw core L_2 peak, which was not observed in the FEFF calculations.

The changes 1 and 3 were attributed to severe lattice strain associated with the screw dislocation core that tends to smear the fine spectral features in ELNES. Similar type of change due to symmetry damage was

reported in the LDOS of edge dislocations[3]. Change 2 was interesting and was assumed to be the effect of other elements present at the screw dislocation core. This could also occur due to different oxidation state resulting from different valences possible in transition metals (i.e. Fe^{2+} and Fe^{3+}). The changes observed in screw core spectrum and perfect crystal were similar to those reported by David Muller *et.*al [4]for Fe^{2+} and Fe^{3+}. Experimental screw core spectrum presented in this thesis was identical to Fe^{2+} spectrum and perfect crystal spectrum was identical to Fe^{3+} spectrum. This could suggest that Fe valence state might change at screw core from 3 to 2 associated by dipole mediated electron transitions.

The difference spectrum between perfect crystal and screw core showed in figure 9.17 revealed that L_3 from screw core increased in intensity by 174 counts while the L_2 peak increased by 261 counts. This was evident from the positive counts of screw core in difference spectrum observed at L_3 and L_2 respectively, since the difference was calculated by subtracting screw core from perfect crystal spectrum. The L_3:L_2 ratio for perfect crystal experimental spectrum is 1:2 and for screw dislocation core it is 1:1.7. This ratio is important because it relates to the density of states in the system.

The experimental ELNES is compared to theoretical ELNES and the changes are studied comparatively. This is shown in figure 9.18. The L_3:L_2 intensity ratios in theoretical ELNES are found to be 1:1.4 for perfect crystal and 1:1.6 for screw dislocation core. These values are much lower than the experimental ratios because the calculations are done with only one atom in the centre while in experiment there are a column of atoms under the probe.

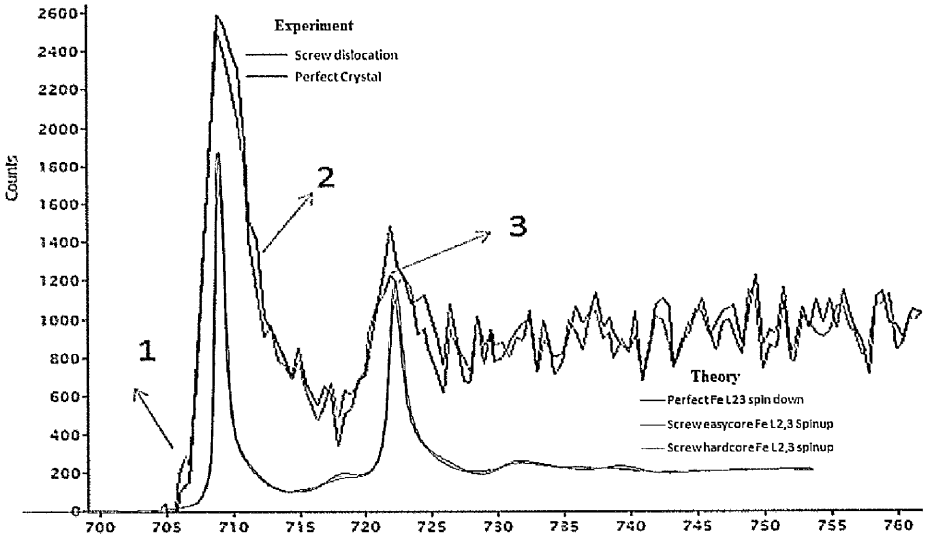

Fig.9.18. Comparison between theoretical and experimental ELNES of Fe-$L_{2,3}$ at a screw dislocation and a perfect crystal.

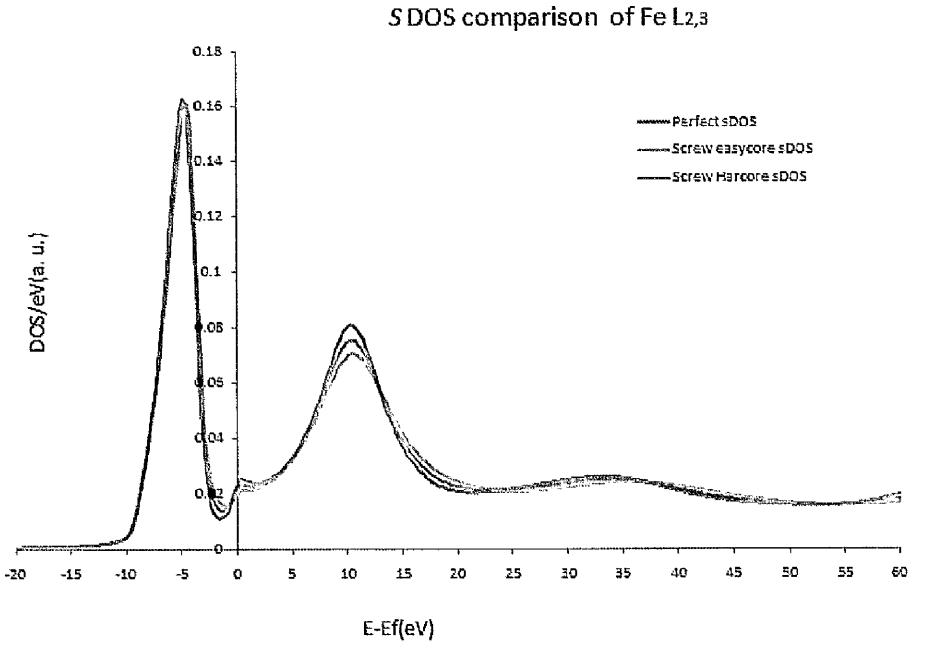

Fig.9.19 Comparison between the '*s*' density of states for a perfect crystal and the two types of screw cores.

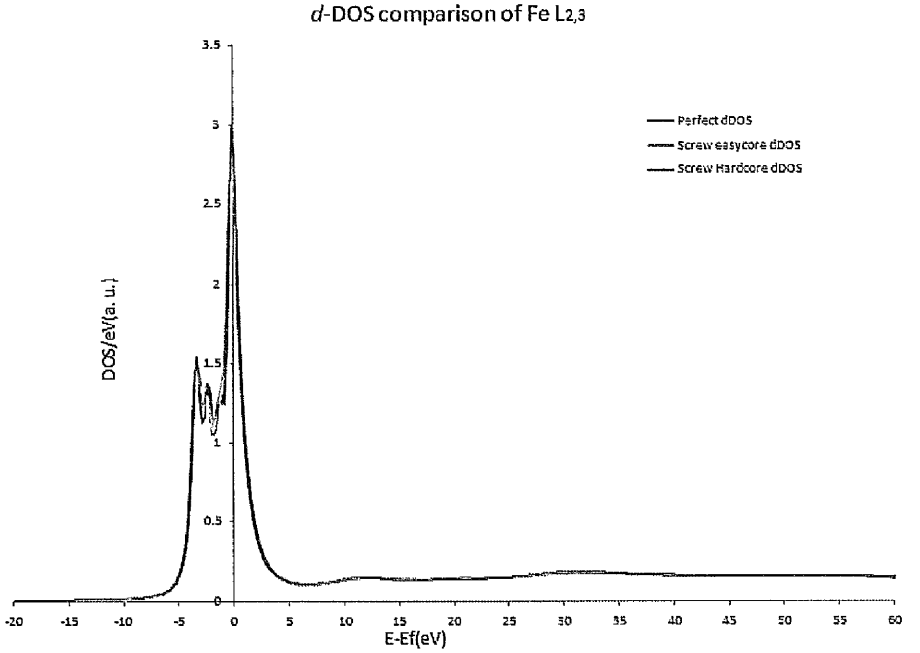

Fig.9.20 Comparison between the '*d*' density of states for a perfect crystal and the two types of screw cores.

It can be seen that the perfect crystal has more unoccupied s-states as compared to easy and hard core while the *d* states remain the same in shape but their number decreases for screw cores compared to perfect crystal. Hence it is understood that the *p* to *d* transition attains significance at screw cores as the number of unoccupied '*d*' density of states decrease compared to perfect crystal.

The conclusions drawn from theoretical and experimental results of both molybdenum and iron will be presented in the conclusions chapter.

References

[1] D. B. Williams, C. B. Carter, Transmission electron microscopy: a textbook for materials science, Plenum, New York; London, 1996, p. xxvii,729p.
[2] R. F. Egerton, Electron energy-loss spectroscopy in the electron microscope, Plenum Press, New York, 1996.
[3] L.-q. Chen, C.-y. Wang, T. Yu, Computational Materials Science 38 (2006) 39-44.
[4] D. A. Muller, Nat Mater 8 (2009) 263-270.

Chapter 10

Conclusions and Suggestion for future work

Chapter 10

CONCLUSIONS AND FUTURE RECOMMENDATIONS

This chapter consists of two sections. The first section contains conclusions from the work described in this thesis. Suggestions and recommendations for the future work to be done in this relevant field of research will be discussed in the second section. They include the techniques to make magnetic samples for electron microscopes. The presence of Cottrell atmospheres near screw dislocation cores and elemental mapping of impurities near the core will be discussed, followed by suggestions for the techniques to be used for such analysis highlighting the importance of this future research work.

10.1 Conclusions

The conclusions from the research work presented in this thesis are listed here:

1. Dislocations in transition metals molybdenum and iron were investigated with special interest in screw dislocation core. Transmission electron microscope, STEM and SuperSTEM examination of the dislocations are done in order to understand the dislocation density, their character and their location in the sample.

2. High resolution lattice images of mixed and screw dislocation in <111> direction were acquired at SuperSTEM and position of dislocation cores were determined from them. The dislocation cores of screw dislocation were difficult to be found in <111> direction and the screw character was determined by using the g.b criterion in TEM.

3. High energy resolution ELNES comparison between screw core and perfect crystal was done at $M_{4,5}$ edge in molybdenum and $L_{2,3}$ edge in iron.

4. Experimental near edge structure altered in spectral features at the screw dislocation core compared to perfect crystal in both molybdenum and iron. Significant reduction in intensity (counts) at ELNES region of molybdenum $M_{4,5}$ edge was evident from the spectrum. The peaks at $M_{4,5}$ edge onset change in their heights when a specific core atom is chosen for studying ELNES changes. Different core atoms around the core have different ELNES as evidenced by the E1, E2, E3 spectra in theoretical simulations. As the distance between the core and the central atom in the cluster increases, the ELNES varies accordingly from a completely screw to a complete perfect crystal. At screw core, the changes are relatively bigger compared to atoms a few atomic distances away from the core. This reduction in intensity was a combined result of the severe lattice strain at the core due to bond length changes between core atoms and the electronic transitions from *d* to *p* angular momentum states. This is because $3d \rightarrow 4f$ transitions are suppressed at the $M_{4,5}$ edge threshold due to the centrifugal potential.

5. Theoretical ELNES at $M_{4,5}$ edge when compared with experimental ELNES revealed similar changes to the edge through reduction in intensity in specific energy windows. While theoretical spectra were smooth, the experimental spectra had high levels of noise that masked majority of the genuine differences in the ELNES that were predicted by theoretical simulated ELNES spectra. Other factors like carbon contamination and statistical uncertainty made it difficult to identify the type of core structure that is exhibited in experimental results.

6. In iron, the intensity of screw core L_3 peak increased while L_2 peak intensity decreased. The total L_3/L_2 maxima ratio of screw dislocation core (1.6) was higher than that of perfect crystal (1.4) while in experimental results it was less than perfect crystal (1.7 for screw and 2.0 for perfect crystal). An extra peak was identified just after L_3 maxima of screw core while the peak observed just before L_3 maxima in perfect crystal spectrum, was smeared in screw core spectrum. Both these changes were attributed to the change in valence state of Fe. The reduction in the intensity of L_2 peak was the resultant of bonding changes at the screw core and the transitions from *2p* to *3d* states.

7. Theoretical ELNES calculations confirmed the reduction in intensity of $M_{4,5}$ edge in molybdenum but Fe L_2 and L_3 peaks increased in intensity with reference to the experimental result. A chemical shift of 0.4 eV to 0.9 eV between perfect $L_{2,3}$ and a screw core $L_{2,3}$ spectrum is noticed. LDOS results confirmed that screw core atom showed a decreasing unoccupied *p* and *f* states in Mo $M_{4,5}$ and increased unoccupied s and d states in Fe $L_{2,3}$. ELNES changes from screw core reduced as the distance from the core increased. The easy core seems to alter more in density of states while hard core has more lattice-strain associated ELNES changes. The ELNES peaks are heavily smeared for hard core while the easy core shows very fine structural changes at specific energy ranges.

8. The electronic structure at the cores of mixed dislocations showed changes that could be the combination of changes observed at screw and edge dislocation cores. The ELNES differences observed due to the edge component of a mixed dislocation dominate its screw character and hence does reveal changes similar to edge dislocation ELNES.

9. The electronic structure at the cores of dislocations in transition metals Mo and Fe was studied through experiments and by theoretical calculations and the changes observed in both support each other. However the experimental results suffer from inherent uncertainties in the way the spectra are collected and the noise is included in the spectra. The hard core remains elusive to be identified under these given conditions, since the changes revealed by theoretical simulations show that hard core lies much closer to perfect crystal ELNES than easy core.

10. Contrary to the assumption that big ELNES changes could be observed at the screw dislocation cores, the ELNES changes were comparatively small but were still resolved in theoretical results. The experimental results on the other hand did not provide satisfactory concluding evidence to support the genuine changes in ELNES from a dislocation core.

10.2 Suggestions for future work

The ELNES spectrum of Mo analysed in this research was a complex energy window which included molybdenum $M_{4,5}$ edge, carbon K-edge and molybdenum $M_{2,3}$ edge. Big changes in ELNES of Mo $M_{4,5}$ were shown by theoretical calculations after 280 eV but the carbon K-edge was a hindrance to work in that energy range. If ELNES of pure carbon K edge could be acquired and then subtracted from the overall $M_{4,5}$ edge that includes carbon K edge, this will result in pure Mo $M_{4,5}$ and $M_{2,3}$ ELNES. Care has to be taken with this type of analysis since thickness variation of different samples can affect the results.

In the case of iron the samples were magnetic and hence were difficult to work in the microscope. If the iron in the sample can be reduced to a thin and small area, it could be workable in the microscope after the initial

aberration corrections. The sample preparation methods for Fe described in this thesis were sufficient enough to carry out EELS analysis over a lower magnification than atomic resolution. The embedded iron samples analysed for this research work were prepared by ion milling, but electropolishing of the iron samples could also be done effectively by selecting correct electrolyte that would not attack the interface region of two metals. Electropolished samples are comparatively less likely to suffer carbon contamination with the added benefit of no mechanical deformation on the sample during electropolishing.

Fe samples can be analysed for ELNES at screw dislocation cores with an interest in the presence of other elements at the cores. Cottrell atmospheres were classical examples of segregation of low Z elements like C, N, and H at the screw dislocation cores. Elemental quantification of high resolution ELNES at the screw cores in Fe would reveal the existence of Cottrell atmospheres in Fe and therefore would be the next interest in this field of research. Alternative theoretical calculations to the experiments would also serve the purpose of understanding the electronic structure of bcc metals with specific type of dislocations in them.

10.3 Summary

The electronic structures at dislocation cores in b.c.c transition metals Mo and Fe are investigated in this thesis by high resolution imaging and EELS. Experimental results and theoretical results confirmed that electronic structures at screw dislocation cores alter due to electronic transitions between p (Fe) and d (Mo) angular momentum states to unoccupied states and are dominated by the bonding changes at the core. However it has to be said that the type of core exhibited in practice could not be identified from the experimental results and the ELNES variations are most likely due to the loss of symmetry at the dislocation core.

APPENDIX

This section includes the scripts and all other relevant information that are used for the research work presented in this thesis. The scripts and files listed here are referred in appropriate chapters.

SECTION 1

Extraction program

The extraction program code in FORTRAN used to extract 300 atoms from multi-scale model is given below:

Author: Dr. Andy.F.Calder at University of Liverpool.

```
.....................................................................

 implicit double precision(a-h,o-z)
real  ddx,ddy,ddz
 parameter (mk=4000000)
 dimension  ddx(mk),ddy(mk),ddz(mk)
 open(unit= 8,file='prefs.txt',status='unknown')
 open(unit=11,file='dislx.dat',status='unknown')
 open(unit=12,file='disly.dat',status='unknown')
 open(unit=13,file='dislz.dat',status='unknown')
 open(unit=9,file='allcoords.txt',status='unknown')
 open(unit=10,file='output.txt',status='unknown')
 read(8,*) nco
```

```
read(8,*) mkf
read(8,*) x0,y0,z0
read(8,*) range
write(6,*) 'number of input coords = ',nco
write(6,*) 'arranged in ',mkf,' columns'
write(6,*) 'origin coords    = ',x0,y0,z0
write(6,*) 'range            = ',range
        nr=nco/mkf
        mki=1
 write (6,*) 'no of rows', nr
 if (nco .gt. mk) then
    write (6,*) 'ERROR Too many input co-ords. max= ',mk
    write (6,*) 'edit source code. increase parameter mk'
 stop
 endif
c ********************************************
c READ COORD FILES
       do 21 ir=1,nr+1
c     write (18,*) mki,mkf,ir,nr,nco
```

```
      read (11,*) (ddx(i),i=mki,mkf)
      read (12,*) (ddy(i),i=mki,mkf)
      read (13,*) (ddz(i),i=mki,mkf)
           mki=mkf+1
           mkf=mkf+12
       if (mkf.gt.nco) mkf=nco
   21 end do
c ******************************************
      ncor=0
      xmaxx=-9999.0
      ymaxy=-9999.0
      zmaxz=-9999.0
      xminx=9999.0
      yminy=9999.0
      zminz=9999.0
c ******************************************
      do 22 i=1,nco
      if (ddx(i) .gt. xmaxx) then
      xmaxx=ddx(i)
      endif
```

```
if (ddy(i) .gt. ymaxy) then
ymaxy=ddy(i)
endif
if (ddz(i) .gt. zmaxz) then
zmaxz=ddz(i)
endif
if (ddx(i) .lt. xminx) then
xminx=ddx(i)
endif
if (ddy(i) .lt. yminy) then
yminy=ddy(i)
endif
if (ddz(i) .lt. zminz) then
zminz=ddz(i)
endif
dx=(ddx(i)-x0)*(ddx(i)-x0)
dy=(ddy(i)-y0)*(ddy(i)-y0)
dz=(ddz(i)-z0)*(ddz(i)-z0)

dd=dsqrt(dx+dy+dz)
```

```
c
c WRITE ALL COORDS TO ALLCOORDS.TXT

      write (9,*) ddx(i), ddy(i), ddz(i)

c WRITE ONLY REQUESTED COORDS TO OUTPUT.TXT
      if(dd .le. range) then
      write (10,*) ddx(i), ddy(i), ddz(i), dd
      ncor=ncor+1
      endif

   22  end do
c ***********************************************
      write(6,*) 'input data:'
      write(6,*)'x distr : ',xminx,' - ',xmaxx
      write(6,*)'y distr : ',yminy,' - ',ymaxy
      write(6,*)'z distr : ',zminz,' - ',zmaxz

      write(6,*) 'output data:'
      write (6,*) 'in requested range= ',ncor
```

```
    close(unit=10)

    close(unit=11)

    close(unit=12)

    close(unit=13)

    end
```

●●

SECTION 2

Chi squared script: written and installed into digital micrograph.

Author: Dr. B.G. Mendis, SuperSTEM research group.

●●

```
// $BACKGROUND$

number WaitOnUserDialog(string prompt, string buttonName)

{

number sem=NewSemaphore()

ModelessDialog(prompt,buttonName,sem)

try GrabSemaphore(sem)

catch return 0

return 1

}
```

```
//Script used for detecting changes in ELNES at each pixel in the SI raw
data

//*******************************************************

image SI

number xSI,ySI,zSI,scalex,scaley

OKDialog("Warning: SI must be Background subtracted!")

SI.getfrontimage()

get3Dsize(SI,xSI,ySI,zSI)

WaitOnUserDialog("Generate summed spectrum","OK")

WaitOnUserDialog("Select ELNES ROI","OK")

image EELS,winELNES,IMG,chi,temp

EELS.getfrontimage()

number
t,l,b,r,normMIN,normMAx,edgeMIN,edgeMAX,normSUM,value,\x,y

GetSelection(EELS,t,l,b,r)

edgeMIN=l;edgeMAX=r

result("CCD Channels used for ELNES are:"+"\n"\

  +edgeMIN+" to "+edgeMAX+"\n")

WaitOnUserDialog("Select normalisation ROI","OK")

GetSelection(EELS,t,l,b,r)

normMIN=l;normMAX=r
```

```
result("CCD Channels used for normalisation are:"+"\n"\
  +normMIN+" to "+normMAX+"\n")
normSUM=sum(EELS[])
EELS=EELS/normSUM
winELNES=EELS[0,edgeMIN,1,edgeMAX]
chi:=realimage("Chi-squared value",4,xSI,ySI)
for (x=0; x<xSI; x++)
for (y=0;y<ySI;y++)
{
IMG=slice1(SI,x,y,0,2,zSI,1)
normSUM=sum(IMG[0,normMIN,1,normMAX])
IMG=IMG/normSUM
temp=IMG[0,edgeMIN,1,edgeMAX]
value=(sum((temp-winELNES)/winELNES))**2
chi[y,x,(y+1),(x+1)]=value
}
showimage(chi)
```

.....

Drift tube correction script

// This script is drift tube control code which can be run directly in DM and create a float window at lower-right screen to control drift tube values. This script has started from the idea of Michel Bosman that EEL spectrum is linearly shifted back and forth on CCD by changing drift tube value to reduce systematic noise from CCD. SuperSTEM extended it by adding random shift of EELS to further eliminate the time-dependent noise. The script can be obtained with permission from SuperSTEM (www.superstem.co.uk).

MATLAB EELS interpolation script

This program combines two EELS plots M_4 and M_5 with different energy and intensity values into a single plot with common energy grid.

Author: Dr. B.G. Mendis, SuperSTEM research group.

……

```
clear;clc

[x1,y1]=textread('Mo_M5.txt','%f %f');

[x2,y2]=textread('Mo_M4.txt','%f %f');

xplot=[200:0.1:400]'; %%%%%%%%%change energy scale if required

a=size(xplot);n=a(1,1);clear a;

yplot=zeros(n,1);

min1=min(x1);min2=min(x2);
```

```
fL3=zeros(n,1);fL2=zeros(n,1);
for a=1:n
 energy=xplot(a,1);
 if energy<min1
    fL3(a,1)=0;
 else
  fL3(a,1)=interp1(x1,y1,energy,'spline');
 end
 if energy<min2
    fL2(a,1)=0;
 else
  fL2(a,1)=interp1(x2,y2,energy,'spline');
 end
end
yplot=fL2+fL3;
plot(xplot,yplot,'-b')
save('energy values','xplot','-ASCII')
save('intensity values','yplot','-ASCII')
```

MATLAB EELS comparison script

Two EELS plots with different energy grids can be plotted on same energy grid by running this script. This is intended for comparison purpose.

Author: Dr. B.G. Mendis, SuperSTEM research group.

```
clear;clc
[x1 y1]=textread('EELS_perfect.txt','%f %f'); %1st EELS spectrum
[x2 y2]=textread('EELS_dislocation.txt','%f %f'); %2nd EELS spectrum
Emin=220; %minimum EELS energy
Emax=400; %maximum EELS energy
step=0.1; %required dispersion
x=[Emin:step:Emax]';
y_a=interp1(x1,y1,x,'spline');
y_b=interp1(x2,y2,x,'spline');
plot(x,y_a,'-b');
hold on;
plot(x,y_b,'-m');
hold on;
```